T. Fransson

COMMUNICATION
DU LABORATOIRE DE THERMIQUE APPLIQUÉE ET DE TURBOMACHINES

DE L'ÉCOLE POLYTECHNIQUE FÉDÉRALE DE LAUSANNE
PROF. DR. A. BÖLCS

Nr. 13

# AEROELASTICITY IN TURBOMACHINES
# COMPARISON OF THEORETICAL AND EXPERIMENTAL CASCADE RESULTS

par

DR. A. BÖLCS ET DR. T.H. FRANSSON

LAUSANNE, EPFL
1986

# AEROELASTICITY IN TURBOMACHINES

## COMPARISON OF THEORETICAL AND EXPERIMENTAL CASCADE RESULTS

**Editors: A. Bölcs and T. Fransson**

June 30, 1986

This study is sponsored jointly by the United States Air Force under GRANTS AFOSR 81-0251, AFOSR 83-0063, AFOSR 84-0105 with Dr. Anthony Amos as program manager, and by the Swiss Federal Institute of Technology, Lausanne.

Communication de Laboratoire de Thermique Appliquée et de Turbomachines N°13, 1986

Ecole Polytechnique Fédérale de Lausanne, Switzerland.

## I. Preface

At the 1980 "Symposium on Aeroelasticity in Turbomachines [1-3], held in Lausanne, Switzerland[1], it became clear that it was virtually impossible to compare different analytical models for predicting flutter and forced vibration and establish their validity.

The Scientific Committee[2] of this meeting decided to initiate a workshop on "Standard Configurations for Aeroelasticity in Turbomachine-Cascades". The aim of this project is to establish a data base with some well documented experimental data, and to initiate and coordinate future experimental investigations in existing test facilities. The standard configurations to be compiled should also serve as test cases for present and future models for predicting aeroelastic phenomena in turbomachine-cascades. It was decided by the Scientific Committee that this study should be coordinated by the "Laboratoire de thermique appliquée et de turbomachines" at the EPF-Lausanne, and that Mr. T. Fransson should undertake the task under an United States Air Force Contract.

A first report with a set of standard configurations was distributed to all the participants at the end of 1983 [4][3]. Calculations were subsequently

---

1 Three symposia have been held in this serie (Paris, France 1976; Lausanne, Switzerland 1980; Cambridge, UK 1984) and a fourth is scheduled for 1987 (Aachen, West Germany).

2 Scientific Committee:

| | | |
|---|---|---|
| Germany | : | H. Förscher |
| Switzerland | : | A. Bölcs (P. Suter 1980, G. Gyarmathy 1976, 1980) |
| France | : | E. Szechenyi (R. Legendre, M. Roy 1976, 1980) |
| UK | : | D.S. Whitehead (+ J.E. Ffowcs Williams, D.G.M. Davis, R.J. Hill 1984) |
| Japan | : | Y. Tanida |
| USA | : | M. F. Platzer (+ M.E. Goldstein 1984, A.A. Mikolajczak 1980) |

3 Please note that, at the request of some participants, a few symbols and standard configurations in the present report do not correspond to those in Ref. 4. Refer to the section entitled "Updating of Nomenclature" for these changes.

performed and comparisons between experimental data and theoretical results were presented at the Third Symposium (1984) [7]. The conclusion drawn from the work was promising and it was decided to continue the comparative efforts, while encouraging new experimental and theoretical investigations, until the Fourth Symposium (1987).

Special emphasis should now be put on defining a small set of aeroelastic test cases for detailed comparison between experiments and theories, to coordinate new investigations and to discuss the physical phenomena of aeroelasticity.

The objective of the present report is to conclude the workshop initiated in 1980, and look ahead to the Aachen Symposium, by which time the methods so validated may be used for detailed and systematic calculations, in order to obtain a better understanding of the aeroelastic phenomena.

This exercise should serve as a guideline for the improving the numerical modeling that will be required to achieve the goal of providing an efficient and reliable unsteady aerodynamic analyses, which can be used in turbomachinery aeroelastic design investigations [5].

The Scientific Committee hopes that this report will constitute a bench-mark for the validation of both experimental and theoretical aeroelastic investigations in turbomachines.

The present report will be updated at the Aachen Symposium, so that any new experimental and/or theoretical investigations can be included.

The members of the Scientific Committee express their thanks to Mr. T. Fransson, who coordinated, compiled and evaluated all the results, and to all research colleagues who participated in the study.

For the Scientific Committee

A. Bölcs

## II. Abstract

The aeroelastician needs reliable, efficient methods for calculating unsteady blade forces in turbomachines. The validity of such theoretical or empirical prediction models can be established only if researchers apply their flutter and forced vibration predictions to a number of well documented experimental test cases.

In the present report, the geometrical and time-averaged flow conditions of nine two-dimensional and quasi-three-dimensional experimental (mainly) standard configurations for aeroelasticity in turbomachine-cascades are given. Some aeroelastic test cases are defined for each configuration, comprising different incidence angles, Mach numbers, interblade phase angle, reduced frequencies, etc.

Furthermore, a proposal for uniform nomenclature and reporting formats is included, in order to facilitate the comparison of different experimental data and theoretical results.

In total, results from 15 theoretical prediction methods have been compared with each other, and with experimental data.

The comparative investigation has shown that present theoretical models can predict accurately the aeroelastic behavior of certain cascade configurations in two-dimensional flow. Other configurations, on the other hand, cannot be predicted as well.

It is concluded that, although present methods can predict stability limits in some cases, the physical reasons for flutter in cascades are not yet fully understood. Further investigations, both experimental and theoretical, are thus urgently required.

## IV. Nomenclature

Note:

**a)** At the request of some participants, the nomenclature of the first report [4] has been slightly modified. A complete list of the changes is given in section V.

**b)** Throughout this report, "standard configuration" will designate a cascade geometry and "aeroelastic case" or "aeroelastic test case" will indicate the different time-dependent (and, in some cases time-averaged) conditions within a standard configuration.

**c)** The tables and figures will be numbered as the sections. For example, Figure 3.7-2 denotes the second figure in section 3.7.

**d)** In order to be consistent with Appendix A5 in which all results obtained in the project are presented (in format A4), an identification is given in each figure as a plotnumber.
These plots are numbered according to the sections, with separation for the type of result presented such as plot K.L-M.N where

- K indicates the section (for example 7)
- L " " standard configuration number (for example, 7.4 indicates results on the fourth standard configuration, given in section 7.)
- M indicates the type of result:
  - M=1 : time-averaged pressure coefficient ($=\bar{c}_p$)
    and/or Mach number ($M_{is}$)
  - M=2 : time-dependent pressure coefficient ($=\tilde{c}_p$)
  - M=3 : " " " difference coefficient ($=\Delta\tilde{c}_p$)
  - M=4 : lift, force coefficient ($=\tilde{c}_l, \tilde{c}_h, \tilde{c}_f$)
  - M=5 : moment coefficient ($=\tilde{c}_m$)
  - M=6 : aerodynamic damping coefficient ($=\Xi$)
- N : indicates the plot number of type K.L-M

(for example, Plot 7.1-6.2 indicates the second plot of type 6 of the 1st standard configuration in section 7)

**e)** The terms "controlled excitation", "forced excitation" and "flutter" tests will be extensively used throughout the report. In the present context, they are defined as follows:

- Controlled excitation test:
  When the blades are vibrated with a force (mechanical,electro magnetic,...) external to the flow.
- Forced excitation test:
  The blades are excited by the flow, but in a known way (for example blade passing frequency from upstream blades).
- Flutter test:
  Self excited vibrations, i.e. the blades vibrate even though there is no controlled or forced excitation in the experiment.

| Symbol | Explanation | Dimension |
|---|---|---|
| **Latin Alphabet** | | |
| $A$ | amplitude (A=h for pure sinusoidal bending) | - |
| | (A=$\alpha$ for pure sinusoidal pitching) | rad |
| $A$ | Fourier coefficient | - |
| $c$ | chord length | m |
| $\tilde{c}_f(t)$ | unsteady perturbation force coefficient vector per unit amplitude, positive in positive coordinate directions (Eq. 5): $\vec{c}_f(t) = \tilde{c}_f\, e^{i\{\omega t+\Phi_f\}}\, \vec{e}_f$ | - |
| $\tilde{c}_f$ | real amplitude of the unsteady perturbation force coefficient per unit amplitude (Eq. 5) | - |
| $\tilde{c}_l(t)$ | unsteady perturbation lift coefficient per unit amplitude, positive in positive y-direction (Eq. 4): $\vec{c}_l(t) = \tilde{c}_l\, e^{i\{\omega t+\Phi_l\}}\, \vec{e}_y$ Note: In the present study, the lift coefficient is defined as the force component perpendicular to the chord! | - |
| $\tilde{c}_l$ | real amplitude of the unsteady perturbation lift coefficient per unit amplitude (Eq. 4) | - |
| $\tilde{c}_m(t)$ | unsteady perturbation moment coefficient per-unit amplitude, positive in clockwise direction (Eq. 6): $\vec{c}_m(t) = \tilde{c}_m\, e^{i\{\omega t+\Phi_m\}}\, \vec{e}_z$ | - |
| $\tilde{c}_m$ | real amplitude of the unsteady perturbation moment coefficient per unit amplitude (Eq. 6) | - |
| $\tilde{c}_p(x,t)$ | unsteady perturbation blade surface pressure coefficient per unit amplitude (Eq. 3): $\vec{c}_p(x,t) = \tilde{c}_p(x)\, e^{i\{\omega t+\Phi_p(x)\}}$ | - |

| | | |
|---|---|---|
| $\tilde{c}_p(x)$ | real amplitude of the unsteady perturbation pressure coefficient per unit amplitude (Eq. 3) | - |
| $\bar{c}_p$ | time-averaged pressure coefficient = $[p-\bar{p}_{-\infty}]/[\bar{p}_{w-\infty}-\bar{p}_{-\infty}]$ | - |
| $c_w$ | coefficient of aerodynamic work done on the airfoil during the oscillation cycle (Eq. 12, 13) | - |
| d | maximum blade thickness (dimensionless with chord) | - |
| $e_f$ | unit vector in force direction | |
| $\vec{e}_h$ | unit vector in bending direction | - |
| $\vec{e}_n$ | unit vector normal to blade surface, positive inwards) | - |
| $\vec{e}_s$ | unit vector tangent to blade surface, positive in positive coordinate directions | - |
| $\vec{e}_x$ | unit vector in x-direction | - |
| $\vec{e}_y$ | unit vector in y-direction | - |
| f | vibration frequency | Hz |
| f | function | - |
| h (x,y,t) | dimensionless (with chord) bending vibration, positive in positive coordinate directions | - |
| h | dimensionless (with chord) bending amplitude | - |
| i | complex notation = $(-1)^{0.5}$ | - |
| i | incidence angle, from mean camberline at leading edge | deg |
| k | reduced frequency $k=[c\cdot\omega]/[2\cdot v_{ref}]$ | - |
| M | Mach number | - |
| p (x,y,t) | pressure (with superscript ~ :time-dependent perturbation) (with superscript ¯ :time averaged) | $N/m^2$ |
| $\vec{R}$ | dimensionless vector from mean pivot axis to an arbitrary point on the mean blade surface | - |
| Re | real part of complex value | - |
| Re | Reynolds number = $(v_{ref}\, c)/\nu$ | - |
| T | dimensionless time: $T = t/T_0$ | - |
| $T_0$ | period of a cycle | s |
| t | time | s |
| v | velocity | m/s |
| $v_{ref}$ | reference velocity for reduced frequency $v_{ref} = v_1$ for compresor cascade $v_{ref} = v_2$ for turbine cascade | m/s |

| | | |
|---|---|---|
| $x$ | dimensionless (with chord) chordwise coordinate | - |
| $x_\alpha$ | dimensionless (with chord) chordwise position of torsion axis | - |
| $y$ | dimensionless (with chord) normal-to-chord coordinate | - |
| $y_\alpha$ | dimensionless (with chord) normal-to-chord position of torsion axis | - |
| $z$ | dimensionless (with chord) spanwise coordinate | - |

## Greek Alphabet

| | | |
|---|---|---|
| $\tilde{\alpha}(t)$ | pitching vibration, positive nose-up (Eq. 2) | rad |
| $\alpha$ | pitching amplitude | rad |
| $\beta$ | flow angle, from axial direction, positive in direction of rotation (Fig. 4.1-1) | deg |
| $\gamma$ | chordal stagger angle, from axial direction, (Fig. 4.1-1) | deg |
| $\delta$ | bending vibration direction = $\tan^{-1}(h_y/h_x)$ | deg |
| $\Delta\tilde{c}_p(x,t)$ | unsteady perturbation pressure difference coefficient (Eq. 8): | - |

$$\Delta\tilde{c}_p(x,t) = \Delta\tilde{c}_p(x)\, e^{i(\omega t+\Phi_{\Delta p}(x))} = \tilde{c}_p{}^{ls}(x,t) - \tilde{c}_p{}^{us}(x,t)$$

| | | |
|---|---|---|
| $\Delta\tilde{c}_p(x)$ | real amplitude of unsteady blade surface perturbation pressure difference coefficient (Eq. 8) | - |
| $\theta_\alpha{}^{(m)}$ | phase lead of pitching motion towards heaving motion of blade (m) | deg |
| $\nu$ | kinematic viscosity | m/s |
| $\Xi$ | aeroelastic damping coefficient, positive for stable motion | - |
| $\sigma$ | interblade phase angle between blade "m-1" and blade "m". $\sigma^m=\delta$ for constant interblade phase angle $\sigma^m$ is positive when blade "m" precedes blade "m-1" For idealized conditions (constant interblade phase angle between adjacent blades, $\sigma$, and identical blade vibration amplitude for all blades) the motion of the (m)th blade, for flexion, is given by: | deg |

$$\vec{h}^m(x,y,t) = h^0(x,y)\; e^{i(\omega t+m\sigma)}\, \vec{e}_h$$

| | | |
|---|---|---|
| $\tau$ | dimensionless (with chord) blade pitch (= gap-to-chord ratio) | - |
| $\Phi_f$ | phase lead of perturbation force coefficient towards motion | deg |
| $\Phi_l$ | phase lead of perturbation lift coefficient towards motion | deg |
| $\Phi_m$ | phase lead of perturbation moment coefficient towards motion | deg |
| $\Phi_p(x)$ | phase lead of perturbation pressure coefficient towards motion | deg |
| $\Phi_{\Delta p}(x)$ | phase lead of perturbation pressure difference coefficient towards motion | deg |
| $\varphi$ | phase angle in Fourier series | deg |
| $\omega$ | circular frequency = $2\pi f$ | rad/s |

**Subscripts**:

| | |
|---|---|
| A | A = h for bending<br>A = $\alpha$ for pitching |
| aero | aeroelastic damping |
| c | stagnation value in the absolute frame of reference |
| exp | experimental result (used only in ambiguous contexts) |
| G | center of gravity |
| global | global (= time-dependent + time-averaged) (see Eq. 7) |
| I | imaginary part |
| is | "isentropic" values, defined with total head pressure in measuring station "1" upstream of the cascade. This value is thus not the true isentropic value as it includes losses in the static pressure. |
| k | k-th harmonic in Fourier series |
| LE | leading edge |
| mech | mechanical (damping) |
| n | n-th harmonic in Fourier series |
| R | real part |
| ref | reference velocity for reduced frequency<br>$v_{ref} = v_1$ for compressor cascade<br>$v_{ref} = v_2$ for turbine cascade |
| TE | trailing edge |
| theory | theoretical results (used only in ambiguous contexts) |
| w | stagnation value in the relative frame of reference |

| | |
|---|---|
| x | component in x-direction |
| y | component in y-direction |
| z | component in z-direction |
| $\alpha$ | position of pitch axis (see Fig. 4.1-1) |
| 1 | measuring station upstream of cascade |
| 2 | measuring station downstream of cascade |
| $-\infty$ | values at "infinity" upstream |
| $+\infty$ | values at "infinity" downstream |

**Superscripts:**

| | |
|---|---|
| (B) | (B) designates lower or upper surface of profile<br>(B) = (ls) for lower surface of profile<br>(us) " upper " " " |
| c | complex value (used only in ambiguous contexts) |
| (ls) | lower surface of profile |
| (m) | blade number m =... -2, -1, 0, 1, 2, ... If the amplitude, interblade phase angle, etc. are constant for the blades under consideration, this superscript will not be used |
| (us) | upper surface of profile |
| $\bar{}$ | time-averaged (= steady) values. This superscript will be used only in ambiguous contexts |
| $\tilde{}$ | time-dependent perturbation values. This superscript will be used only in ambiguous contexts |

## V. Updating of Nomenclature

Upon the request of some participants, the nomenclature from the first report [4] has been slightly modified. The modifications are:

| Symbol | Explanation | Dimension |
|---|---|---|
| | **Greek Alphabet** | |
| $\beta$ | flow angle, from axial, positive in direction of rotation (Fig. 4.1-1) (in [4], from circumferential) | deg |
| $\gamma$ | chordal stagger angle, from axial, positive in direction of rotation (Fig. 4.1-1) ([4], from circumferential) | deg |
| | **Subscripts** | |
| c | stagnation value in the absolute frame of reference (in [4], "t" was used) | |
| w | stagnation value in the relative frame of reference (in [4], "t" was used). | |
| | **Superscripts** | |
| - | time averaged values (was time-dependent in [4]) | |
| ~ | time dependent values (was time-averaged in [4]) | |

## 1. Introduction

Considerable dynamic blade loads may occur in axial-flow turbomachines as a result of the unsteadiness of the flow. The trend towards ever greater mass flows, or smaller diameters, in the turbomachines leads to higher flow velocities and to more slender blades. It is therefore likely that aeroelastic phenomena, which concern the motion of a deformable structure in a fluid stream, will continue to increase in future turboreactors (fan stage) and industrial turbines (last stage) [6].

The considerable complications, and the high cost, involved in taking unsteady flow measurements in turbomachines make it necessary for the aeroelastician to rely on cascade experiment and theoretical prediction methods, to minimize blade failures due to aeroelastic phenomena. It is therefore of great importance to validate the accuracy of flutter and forced vibration predictions as well as experimental cascade data, and to compare theoretical results with cascade tests and trends of results obtained in turbomachines.

Various well-documented unsteady experimental cascade data exist throughout the world, as well as many separate promising calculation methods for solving the problem of unsteady flow in two-dimensional and quasi-three-dimensional cascades. However, because of the different basic assumptions used in these prediction methods, and the many individual ways of representing the results obtained , no real effort has been made to compare the different theoretical methods with each other. Furthermore, since hardly any exact solutions are known, the validity of these theoretical prediction analyses can be verified only by comparison with experiments. This is very seldom done, partly because of the reasons mentioned above, and partly because well-documented experimental data are normally of a proprietary nature.

## 2. Objectives

At the Lausanne Symposium on Aeroelasticity in 1980 [2] it was proposed that this situation could be partly remedied by selecting a number of standard configurations for aeroelastic investigations in turbomachine-cascades, and defining uniform reporting format. This would facilitate the comparison of different theoretical results with the experimental standard configurations.

It was also expected that, by defining the state-of-the-art of flutter prediction models, new experiments and theories would be initialized as a logical continuation of the workshop.

The final objective of a comparative work of the present kind is, of course, to validate theoretical prediction models with experiments performed under operating conditions in the turbomachine, i.e. considering unsteady rotor-stator interaction, flow separation, viscosity, shock-boundary layer interaction, three-dimensionality, etc. However such a far-reaching objective does not correspond to the present state-of-the-art of aeroelastic knowledge, either for prediction models or as regards well-documented experimental data to be used for validation of the theoretical methods.

The scope of the present report will thus be limited to fully aeroelastic phenomena under idealized flow conditions in two-dimensional or quasi-three-dimensional cascades. Such interesting phenomena as rotor-stator interactions, stalled flutter and fully three-dimensional effects will thus be excluded, unless as they are an extension of the idealized two-dimensional cascade flow.

In the first report on the project [4], nine standard configurations were selected, ranging from flat plates to highly cambered turbine bladings, and from incompressible to supersonic flow conditions, and a certain number of aeroelastic test cases, mostly based on existing experimental data, were defined for analysis by existing prediction methods for flutter and forced vibrations.

A number of "blind test" calculations were performed by different prediction models before the 1984 Aeroelasticity Symposium, and subsequently compared with the experimental data. A preliminary discussion on these results was presented at the Cambridge Symposium [7], where also several of the methods used for prediction were examined in detail [3].

The first objective of the present report is to sum up the work of the project, as initiated in 1980 by reporting on the comparison between the different theoretical results and the experimental data. Secondly, as it was concluded at the Cambridge Symposium that not all of the aeroelastic cases presented in the first report [4] are of interest in modern turbomachines (there were also too many for them to serve as good test cases), and as the participants decided to continue the workshop until the 1987 Symposium, some of the standard configurations and aeroelastic test cases have been updated. This is also true for the nomenclature which has been slightly changed to accommodate observations and remarks by the participants (see section V above).

The third objective is to stimulate critical discussions between experimental and theoretical research groups through the report (for example as regards the accuracy of experiments, assumptions in theories) in the hope that from these discussions new ideas will emerge.

## 3. Method of Attack

The project for establishing the mutual state-of-the-art of flutter prediction models and experimental investigations was dealt with in three parts.
First a proposal for a uniform nomenclature and representing format was defined, as presented in section 4. Secondly, a set of standard configurations was selected (see section 5) upon which, thirdly, the theoretical prediction models, as presented in section 6, are validated (see section 7).

## 4. Recommendations for Uniform Presentation of the Results

The physical reasons for self-excited blade vibrations in turbomachines are not presently understood in detail. Various representations of experimental and theoretical results are thus used by different researchers. The number of separate reporting formats employed may be very large, as a different importance is attached to the various results, depending upon the scope of the aeroelastic investigation.

However, as the main objective for both experimental and theoretical aeroelastic studies is to provide a tool for the designer of turbomachines to minimize blade failures, the important results from the different investigations should be standardized so they can be easily interpreted by non-specialists in aeroelasticity.

In order to facilitate comparisons and establish the mutual validity of both theoretical and experimental results, a certain amount of information must be unified. This is also desirable in order to avoid misinterpretation of some results.

In the present project, a minimum number of requirements have been defined. Both the nomenclature and the presentation formats are based upon references [8 - 14], especially the publication by Carta [8] ([12]). Furthermore,they have been chosen, as similar as possible to the presentation previously used for the experiments serving as standard configurations, this to avoid excessive retreatment of the data.

## 4.1 Steady Two-Dimensional Cascade Nomenclature

The profiles under investigation are arranged in a two-dimensional section of the cascade as in Fig. 4.1-1. In this figure, all the physical lengths are scaled with the chordlength "c".

It is important to note here that the chord is defined as the straight line between the intersections of the camber line and the profile surface, and that the x-coordinate is aligned with the chord.

The incidence angle, i, is defined in the way mostly used in theoretical investigations, i.e. between the inlet flow direction and the camber line. It is positive for increased static load.

Throughout this report, extensive use will be made of the time averaged blade surface pressure coefficient, which will be defined as

$$\bar{c}_p(x) = [\bar{p}-\bar{p}_{-\infty}]/[\bar{p}_{w-\infty}-\bar{p}_{-\infty}] \qquad (1)$$

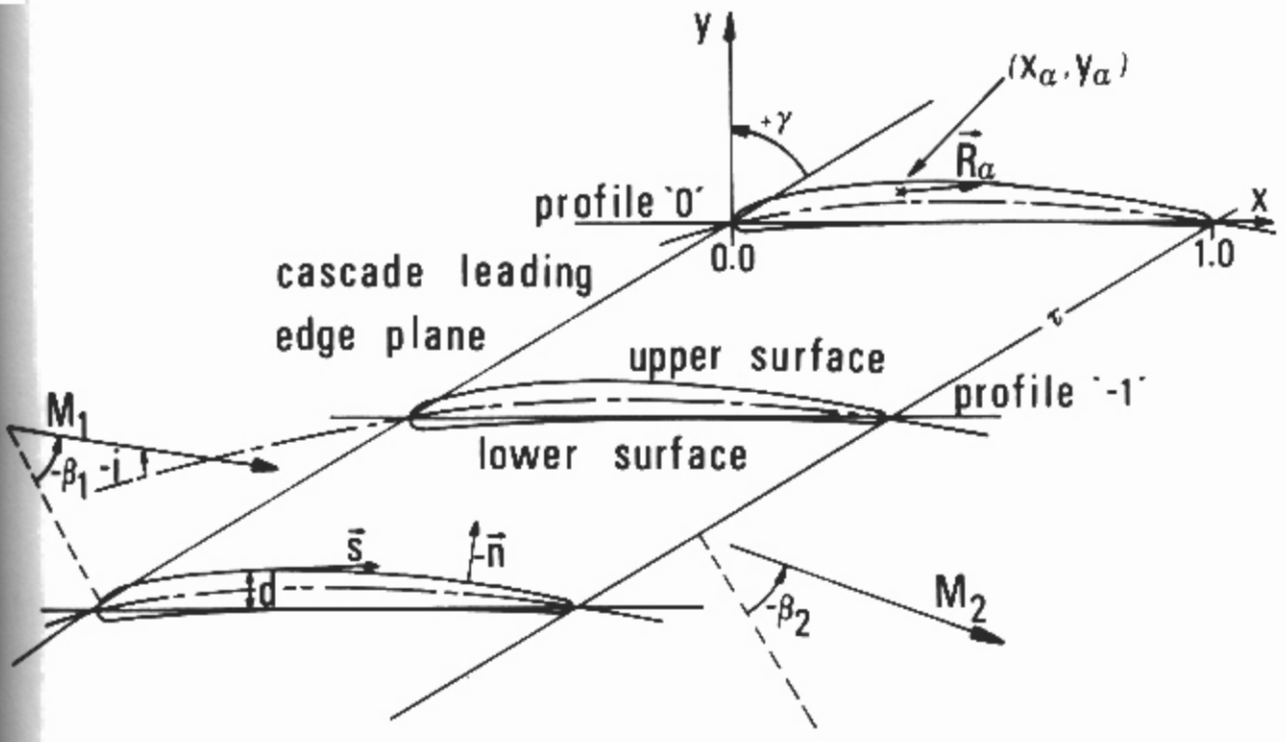


Fig. 4.1-1. Steady two-dimensional cascade geometry

## 4.2 Unsteady Two-Dimensional Cascade Nomenclature

### I: Blade Motion

Fig. 4.2-1 is a schematic representation of cascaded two-dimensional airfoils; the form of the profiles is considered to remain rigidly fixed during bending and/or pitching oscillations, $h(x,y,t)$ and $\alpha(t)$ resp., in which the components $h_x$, $h_y$ and $\alpha$ of the motion vectors $\vec{h}$ and $\vec{\alpha}$ are noted in real form and $\theta_\alpha^{(m)}$ accounts for phase differences between translation and rotation.
We will therefore define

$$\vec{h}_m(x,y,t) = h^m(x,y)e^{i\{\omega(m)t\}}\vec{e}_h \quad \text{(for bending motion)} \tag{2}$$

$$\vec{\alpha}_m(t) = \alpha^m(x,y)e^{i\{\omega(m)t\}} \quad \text{(for pitching motion)}$$

where $h^{(m)}$, $\alpha^{(m)}$ are the dimensionless amplitudes, and $\omega^{(m)}$ the circular frequency, of the vibration of the blade (m).
It is also assumed that the torsional motion, for the (m)th blade, preceeds the bending motion by a phase angle $\theta_\alpha^{(m)}$. Furthermore, if the amplitude, circular frequency or phase lead is identical for all blades, the superscript $^{(m)}$ will be omitted on the corresponding symbol.

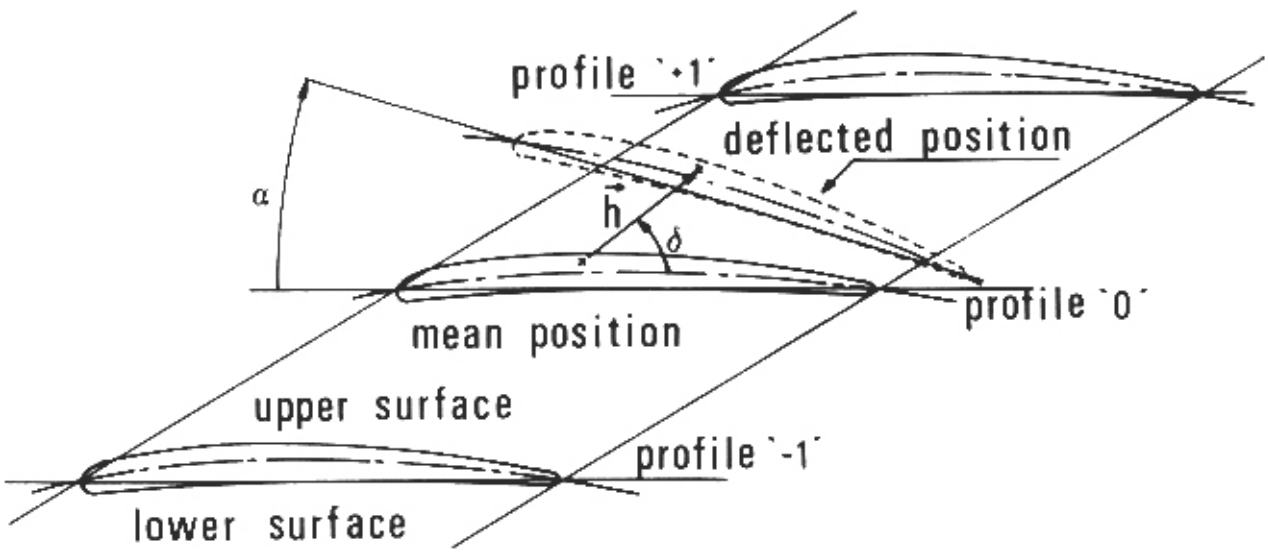


Fig. 4.2-1. Unsteady two-dimensional cascade nomenclature

## II: Two-Dimensional Aerodynamic Coefficients

The unsteady (complex) blade surface pressure coefficient $\tilde{c}_p(x, t)$, as well as the lift $\tilde{c}_l(t)$, force $\tilde{c}_f(t)$ ($\tilde{c}_h(t)$, $\tilde{c}_d(t)$) and moment $\tilde{c}_m(t)$ coefficients (per unit span), are scaled with the amplitude of the corresponding motion (amplitude ="A", where $A=h^{(m)}$ or $\alpha^{(m)}$). According to the conventional definitions of these parameters, we thus have:

$$\tilde{c}_{pA}{}^{B}(x,t) = [\tilde{p}^{B}(x,t)] \,/\, \{A\cdot[\bar{p}_{w-\infty}-\bar{p}_{-\infty}]\} \tag{3}$$

$$\tilde{c}_{lA}(t) = \{\int p(x,t)\cdot[\vec{e}_n\cdot\vec{e}_y]\cdot ds\} \,/\, \{A\cdot[\bar{p}_{w-\infty}-\bar{p}_{-\infty}]\} = \int_{le}^{te}\{\tilde{c}_{pA}{}^{ls}(x,t)-\tilde{c}_{pA}{}^{us}(x,t)\}\cdot dx \tag{4}$$

$$\tilde{c}_{fA}(t) = \{\int \tilde{p}(x,t)\cdot[\vec{e}_n\cdot\vec{e}_f]\cdot ds\} \,/\, \{A\cdot[\bar{p}_{w-\infty}-\bar{p}_{-\infty}]\} \tag{5}$$

$$\tilde{c}_{mA}(t) = \{\int[\vec{R}_\alpha \times [\tilde{p}(x,t)\cdot ds\cdot\vec{e}_n]\} \,/\, \{A\cdot[\bar{p}_{w-\infty}-\bar{p}_{-\infty}]\}\cdot\vec{e}_z \tag{6}$$

where

- $\tilde{p}(x,t)$ is the unsteady perturbation pressure
- the force $\tilde{c}_h$ is defined in the direction of bending vibration $\vec{e}_h$ (see Fig. 4.2-1)
- "lift" coefficient is defined normal to chord
- force components are positive when acting in positive coordinate directions
- moment coefficient ($\tilde{c}_m$) is positive when acting in the clockwise direction
- superscript (B) denotes the lower blade surface (ls) or upper blade surface (us).

Furthermore, the overall (=time-averaged + time-dependent) blade surface pressure coefficient is defined as

$$c_{p,global} = \bar{c}_p + A\cdot\tilde{c}_p = \{(\bar{p}+\tilde{p})-\bar{p}_{-\infty}\} \,/\, [\bar{p}_{w-\infty}-\bar{p}_{-\infty}] \tag{7}$$

A further important quantity, for slender blades, is the normalized unsteady pressure difference along the blade chord, $\Delta\tilde{c}_p(x, t)$.

This is defined as the difference of the time dependent pressures on the lower and upper blade surfaces:

$$\Delta\tilde{c}_p(x,t) = \tilde{c}_p^{ls}(x,t) - \tilde{c}_p^{us}(x,t) \qquad (8)$$

Obviously, this definition is justified only for very thin blades.
All of the above mentioned variables can be expressed either in complex exponential form or in component form as, if a harmonic response is assumed:

$$\begin{aligned} \tilde{c}_p(x,t) &= \tilde{c}_p(x)e^{i\{\omega t+\Phi_p(x)} = \{\tilde{c}_p(x)e^{i\Phi_p(x)}\} \cdot e^{i\omega t} \\ &= \tilde{c}_p{}^C(x)e^{i\omega t} = \{\tilde{c}_{pR}{}^C(x) - \tilde{c}_{pI}{}^C(x)\} \cdot e^{i\omega t} \end{aligned} \qquad (9)$$

Here, the subscripts "R" and "I" denote the real and imaginary parts of the complex pressure coefficient $\tilde{c}_p{}^C(x)$. Physically, these two parts can be interpreted as the components of the pressure coefficient which are in-phase (real part) and out-of-phase (imaginary part) with the blade motion. Furthermore, the phase angles $\Phi_p(x)$, $\Phi_{\Delta p}(x)$, $\Phi_l$, $\Phi_f$, $\Phi_m$ are all defined as positive when the pressure (pressure difference, lift, force or moment, resp.) leads the motion.
The amplitude and phase relationships in Eq. (9) are defined in the usual way, i.e.:

$$\begin{aligned} c_p(x) &= \{\tilde{c}_{pR}{}^C(x)^2+\tilde{c}_{pI}{}^C(x)^2\}^{0.5} \\ \Phi_p(x) &= \tan^{-1}\{\tilde{c}_{pI}{}^C(x)/\tilde{c}_{pR}{}^C(x)\} \end{aligned} \qquad (10)$$

$$\begin{aligned} \tilde{c}_{pR}{}^C(x) &= \tilde{c}_p(x)\cdot\cos\{\Phi_p(x)\} \\ \tilde{c}_{pI}{}^C(x) &= \tilde{c}_p(x)\cdot\sin\{\Phi_p(x)\} \end{aligned}$$

It should be noted here that, in computing the blade surface pressure distribution, only components, and not amplitudes or phase angles may be differentiated [8]. Therefore

$$\begin{aligned} \Delta\tilde{c}_{pR}{}^C(x) &= \tilde{c}_{pR}{}^{C(ls)}(x)-\tilde{c}_{pR}{}^{C(us)}(x) \\ \Delta\tilde{c}_{pI}{}^C(x) &= \tilde{c}_{pI}{}^{C(ls)}(x)-\tilde{c}_{pI}{}^{C(us)}(x) \end{aligned} \qquad (11)$$

$$\begin{aligned} \Delta\tilde{c}_p(x) &\neq \tilde{c}_p{}^{(ls)}(x)-\tilde{c}_p{}^{(us)}(x) \\ \Phi_{\Delta p}(x) &\neq \Phi_p{}^{(ls)}(x)-\Phi_p{}^{(us)}(x) \end{aligned}$$

### III: Two-Dimensional Aerodynamic Work

The two-dimensional differential work, per unit span, done on a rigid system by the aerodynamic forces and moments is conventionally expressed by the product of the real parts (in phase with motion components) of force and differential translation, as well as moment and differential torsion. Thus, the total aerodynamic work coefficient, per period of oscillation, done on the system is obtained by computing

$$\tilde{c}_w = c_{wh}+\tilde{c}_{w\alpha}+\tilde{c}_{wh\alpha}+\tilde{c}_{w\alpha h} \qquad (12)$$

Expressed in this way, the aerodynamic work coefficients $c_w$, $c_{wh}$, $c_{w\alpha}$, $c_{w\alpha h}$, $c_{wh\alpha}$ are all in nondimensionalized form, with the product of the pressure difference $(p_{w-\infty} - p_{-\infty})$ and chord$^3$ as a normalizing factor.

From the definition (Eq. 12 and 13) it is seen that these coefficients become negative for a stable motion.

As the force and moment coefficients each have time-dependent parts from both the bending and pitching oscillations, $c_{wh}$ is defined as the work done on the profile during a pure bending cycle (no torsion). Similarly, $c_{w\alpha}$ is the work done on the blade during a pure pitching cycle (no bending); $c_{w\alpha h}$ and $c_{wh\alpha}$ is the work done by the pitching force due to bending and by the bending moment due to pitching, respectively.

Thus, the work coefficients can be expressed in conventional form as

$$\begin{aligned}
\tilde{c}_{wh} &= \int \mathrm{Re}\{h\cdot\tilde{c}_h(t)\}\cdot\mathrm{Re}\{dh(x,y,t)\} \\
\tilde{c}_{w\alpha} &= \int \mathrm{Re}\{\alpha\cdot\tilde{c}_{m\alpha}(t)\}\cdot\mathrm{Re}\{d\alpha(t)\} \\
\tilde{c}_{wh\alpha} &= \int \mathrm{Re}\{h\cdot\tilde{c}_{mh}(t)\}\cdot\mathrm{Re}\{d\alpha(t)\} \\
\tilde{c}_{w\alpha h} &= \int \mathrm{Re}\{\alpha\cdot\tilde{c}_{h\alpha}(t)\}\cdot\mathrm{Re}\{dh(x,y,t)\}
\end{aligned} \qquad (13)$$

In the case of pure sinusoidal normal-to-chord bending, or pure sinusoidal torsional vibration, as well as sinusoidal lift and moment responses, respectively, the expressions (13) can be integrated to give the following simple formulas[4] (Appendix A1):

---

[4] More generally, for pure bending vibration in the $\vec{e}_h$ direction, the aerodynamic work coefficient becomes: $c_{wh}=\pi h^2\tilde{c}_{hl}=\pi h^2\tilde{c}_h\sin\Phi_h$

$$
\begin{aligned}
\tilde{C}_{wh} &= \pi h^2 \cdot \mathrm{Im}\{\tilde{C}_h\} = \pi h^2 \cdot \tilde{C}_h \cdot \sin\{\Phi_h\} \\
\tilde{C}_{w\alpha} &= \pi \alpha^2 \cdot \mathrm{Im}\{\tilde{C}_m\} = \pi \alpha^2 \cdot \tilde{C}_m \cdot \sin\{\Phi_m\} \\
C_{wh\alpha} &= 0. \\
\tilde{C}_{w\alpha h} &= 0.
\end{aligned}
\tag{14}
$$

It can thus be seen that the aerodynamic work depends only on the value of the out-of-phase component of the lift and moment coefficients, and that the airfoil damps the motion when the imaginary part of the lift or moment coefficient, resp. is negative.

The aerodynamic work can be expressed in normalized form as the aerodynamic damping parameter ≡ [8]. With the same assumptions as in Eq. (14), this parameter is defined as

$$
\begin{aligned}
\equiv_h &= -\tilde{C}_{wh}/\pi h^2 = -\mathrm{Im}\{\tilde{C}_h\} \\
\equiv_\alpha &= -\tilde{C}_{w\alpha}/\pi \alpha^2 = -\mathrm{Im}\{\tilde{C}_m\}
\end{aligned}
\tag{15}
$$

The normalized parameter ≡ is thus positive for a stable motion.

## 4.3 Precise Reporting Formats

One of the main problems which arose in comparing experimental and theoretical aeroelastic investigations at the 1980 "Symposium on Aeroelasticity in Turbomachines" was the lack of coherency in the reporting formats; the researchers participating in the present project were therefore invited to follow certain guidelines for a standardized reporting format, given in this section.

Two main groups of representation are employed:

I: The first is for the detailed comparison of measured and calculated blade pressure distributions.

II. The second is directed towards the physical mechanism of the flutter phenomena and its important parameters and towards the establishment of flutter boundaries for the different cascades.

It is evident that all participants are encouraged to use any further reporting formats to establish other comparisons, or to emphasize any special point of interest in their investigations.

### I: Detailed comparison of experimental results and theoretical approaches

The validity of theoretical results can be established only by mutual agreement between the measured and calculated unsteady pressure distributions on both blade surfaces. This detailed comparison is made on the basis of Figure 4.3-1 which is presented for different combinations of

- interblade phase angle
- reduced frequency
- inlet conditions
- cascade geometry

depending upon the existing experimental data for the configuration being investigated.

Quite a few prediction models for flutter or forced vibrations are based upon small perturbation theories, where the steady pressure distribution on the blade is an input data. The experimentally determined time-averaged blade surface pressure distributions are therefore specified for such studies, either as a pressure coefficient (Fig. 4.3-2a) or an isentropic Mach number (Fig. 4.3-2b).

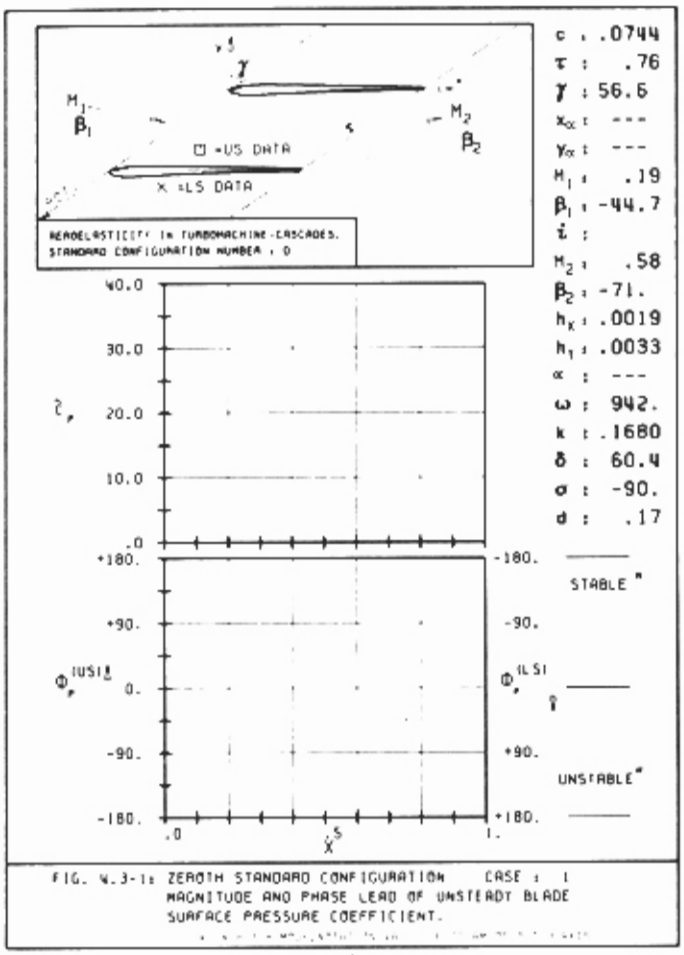


FIG. 4.3-1: ZEROTH STANDARD CONFIGURATION CASE : 1
MAGNITUDE AND PHASE LEAD OF UNSTEADY BLADE SURFACE PRESSURE COEFFICIENT.

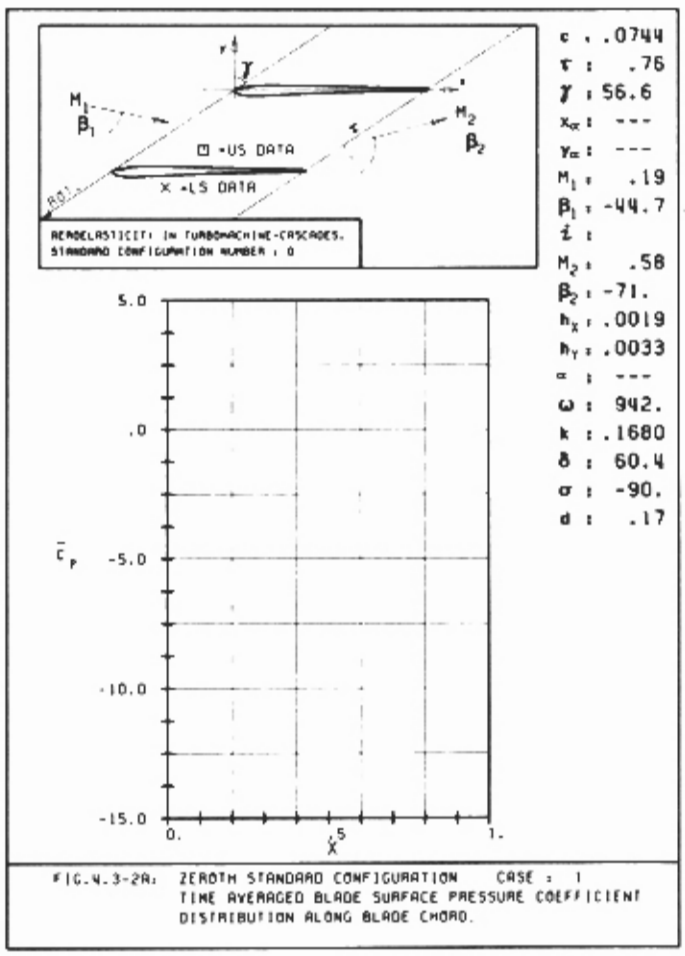


FIG.4.3-2A: ZEROTH STANDARD CONFIGURATION CASE : 1
TIME AVERAGED BLADE SURFACE PRESSURE COEFFICIENT DISTRIBUTION ALONG BLADE CHORD.

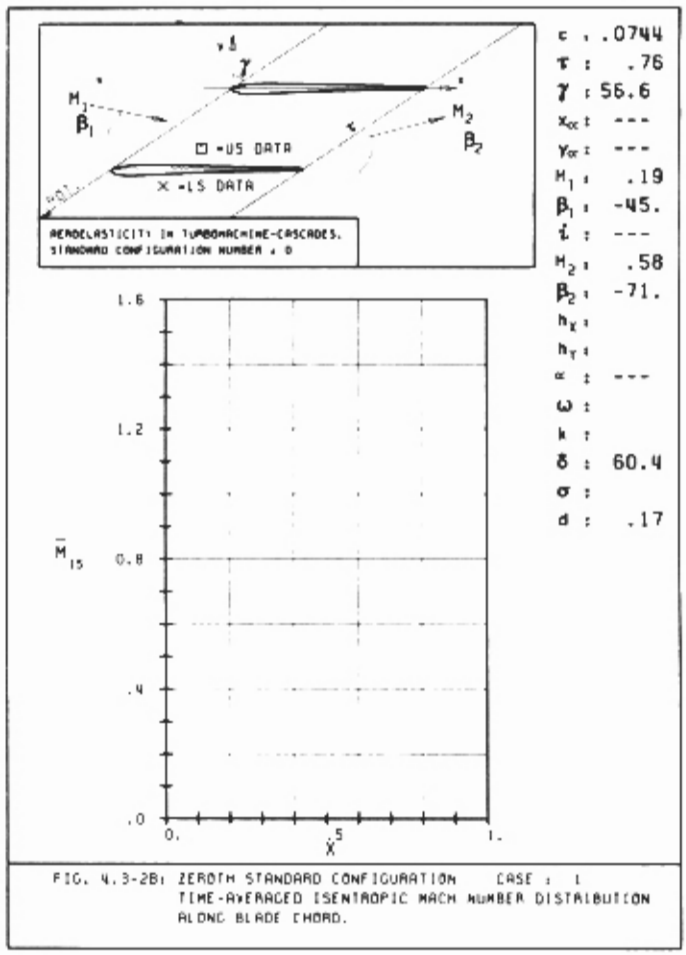


FIG. 4.3-2B: ZEROTH STANDARD CONFIGURATION CASE : 1
TIME-AVERAGED ISENTROPIC MACH NUMBER DISTRIBUTION ALONG BLADE CHORD.

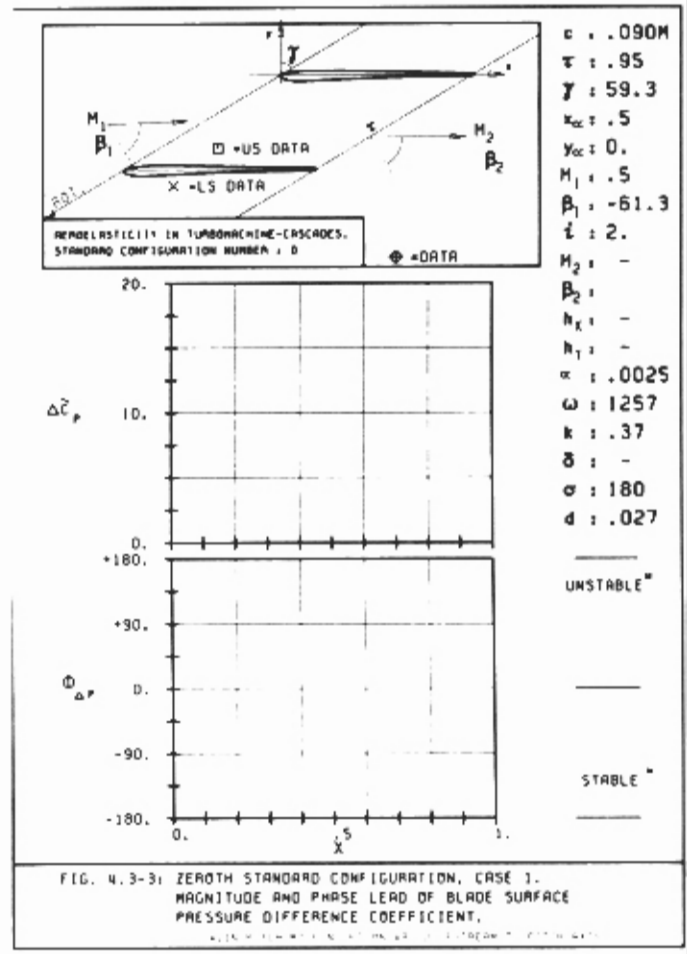


FIG. 4.3-3: ZEROTH STANDARD CONFIGURATION, CASE 1.
MAGNITUDE AND PHASE LEAD OF BLADE SURFACE PRESSURE DIFFERENCE COEFFICIENT.

**Fig. 4.3-1 to 4.3-3.** Proposed presentation format of the results from the standard configurations.

The comparison between the experimental and calculated time-averaged results also gives the first indications of eventual discrepancies in the boundary conditions between the experimental and theoretical set-up.
Moreover the comparison between the steady (Fig 4.3-2) and unsteady (Fig 4.3-1) blade pressure distributions may in some cases give a quantitative notion of the aeroelastic phenomena under investigation (instabilities due to stall, choke, shockwaves, coupling effects between the steady and unsteady flow fields...).
The distribution of the blade surface pressure difference coefficient along the blade, $\Delta\tilde{c}_p(x)$, indicates the presence of stable and unstable zones. This information is thus also of interest for slender blades, and is represented as in Figure 4.3-3.

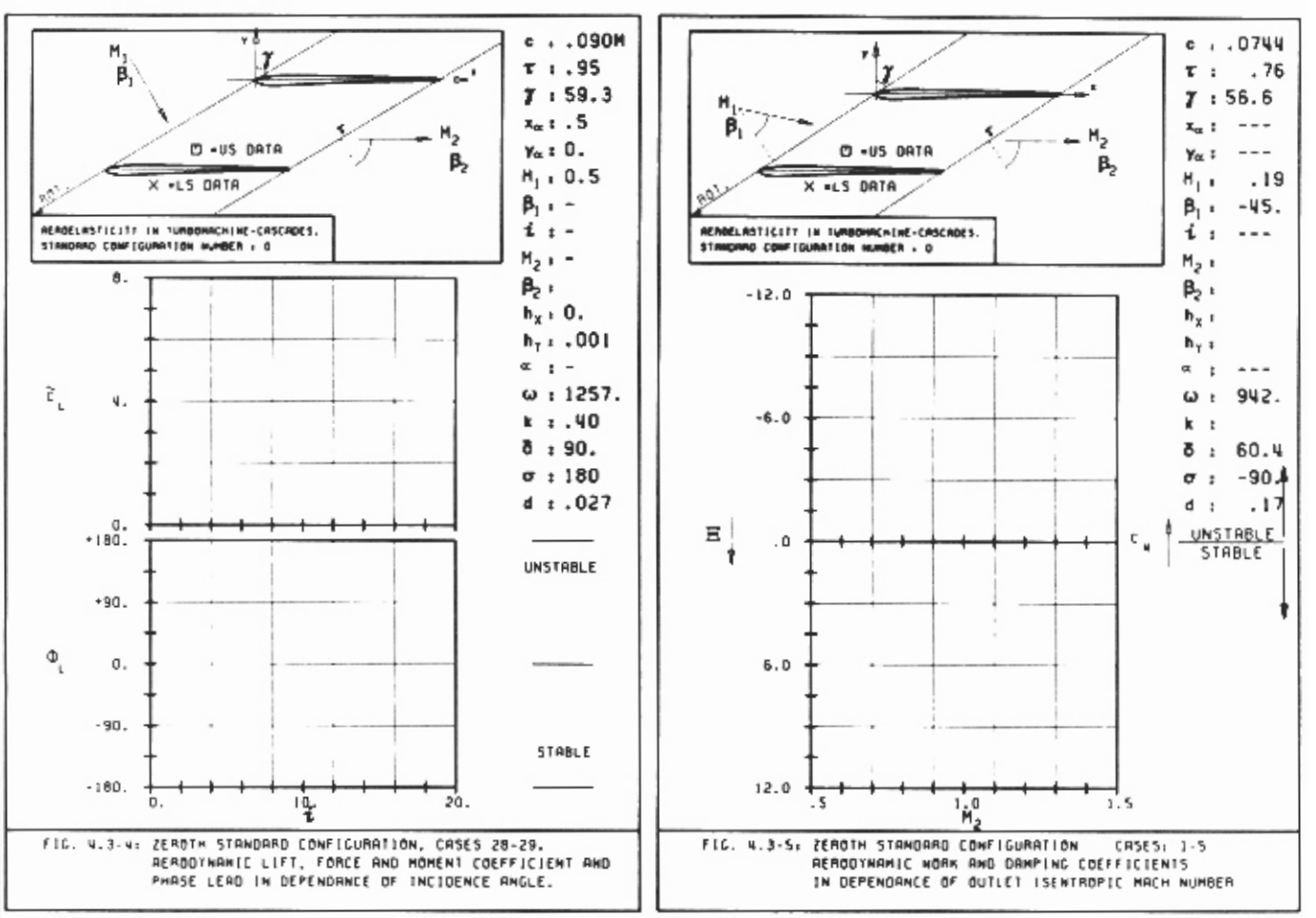


FIG. 4.3-4: ZEROTH STANDARD CONFIGURATION, CASES 28-29. AERODYNAMIC LIFT, FORCE AND MOMENT COEFFICIENT AND PHASE LEAD IN DEPENDANCE OF INCIDENCE ANGLE.

FIG. 4.3-5: ZEROTH STANDARD CONFIGURATION CASES: 1-5 AERODYNAMIC WORK AND DAMPING COEFFICIENTS IN DEPENDANCE OF OUTLET ISENTROPIC MACH NUMBER

**Fig. 4.3-4 to 4.3-5.** Proposed presentation format of the results from the standard configurations.

## II. Flutter boundaries

The second form of representation concerns the values of the resultant aerodynamic blade forces and moments, as well as the aerodynamic work and damping coefficients.

Two different presentations (see Figures 4.3-4 and 4.3-5) are used to elaborate the influence of several important parameters on the flutter boundaries

- reduced frequency
- interblade phase angle
- inlet flow velocity
- inlet flow angle
- outlet flow velocity
- cascade geometry

Firstly, the unsteady blade pressure coefficients should be integrated to yield the aerodynamic force, or lift, and moment coefficients as in Figure 4.3-4. The phase angles $\Phi_f$ and $\Phi_m$ resp., in this representation give immediate information about the aeroelastic stability of the system (see section 4.2).

Secondly, the aerodynamic work and damping coefficients per cycle of oscillation may be calculated if the mode-shape of the motion is well-defined. Most of the problems dealt with in the present work will concern motion of nondeformed profiles (at least for the theoretical predictions), so the aerodynamic damping coefficient can easily be computed and plotted. This information is useful to the turbomachine designer for judging the aeroelastic behavior of a specific cascade (Figure 4.3-5).

## 4.4 Guidelines for Validation of Experimental and Theoretical Results

It is often found that experimentalists and theoreticians do not always recognize each other's major difficulties in obtaining aeroelastic results. Under some circumstances this may lead to wrong conclusions, for example if an attempt is made to approximate a theoretical result to experimental data by artificial means, without first carefully investigate the experimental accuracy.

This section aims to give a few indications about some of the important aspects of experiments and theories, and thus to eleiminate some inaccuracies in the evaluation and comparison of results.

### I: Experiments

In the case of

- sinusoidal blade vibrations
- sinusoidal pressure response (i.e. no flow turbulence)
- identical vibration frequencies for all blades
- constant interblade phase angles
- in bending mode, normal-to-chord vibration

the experimental data are expected to have small inaccuracies from measurements and data reduction. The formulas for lift, moment, etc. coefficients, as given in section 4.2 can then be integrated to produce equations which can be evaluated in a straightforward manner.

However, these assumptions cannot be fulfilled in all experiments, especially in the transonic flow region at realistic reduced frequencies.

The large energy input needed to drive a cascade with prescribed frequencies, amplitudes and phase angles makes it difficult (or virtually impossible, depending on how the excitation mechanism is constructed) to keep these constant for all blades, apart from tests with low frequencies and/or small amplitudes. Even in this case, the pressure response on the profiles in general will not be sinusoidal, due to unsteadiness in the flow from sources other than the vibrating blades (upstream, downstream, turbulence, boundary layer, shock interactions, separations, perturbations, etc.). Furthermore, the smaller the amplitude, the lower the signal/noise ratio, which reduces the accuracy of the results.

For a detailed comparison between the experimental data and the prediction model, it is therefore important to know to what extent the theoretical assumptions approximate the experiment.

Blade Vibration Difficulties

The amplitude of the blade vibrations during experiments with controlled excitation cannot always (depending whether mechanical or electromagnetic excitation is performed) be kept constant, either in time or between the different blades. The interblade phase angle is even more difficult to control accurately.
During flutter, indications exist that the mean blade vibration frequency, both in rotating machines and in cascades [18, 28], is fairly constant in time and between the separate blades. However, the blade vibrations do show a certain amplitude and phase modulation, which indicates the simultaneous presence of different cascade eigenmodes.
During experiments with controlled excitation in the bending mode, the experimental set-up is usually performed so as to simulate the bending direction of a turbomachine blade. This direction is mostly not normal-to-chord or in the circumferential direction, as often assumed in the calculations.
Although most experiments should simulate single-degree-of-freedom vibrations, the modes of the cascade may sometimes be coupled. The blades in experiments can usually be considered as rigid bodies but, if the blades are suspended on springs and vibrated with electromagnetic excitation, the instrumented blades may have eigenfrequencies slightly separate from the others. The mode shapes of the cascade are thus somewhat modified due to the mistuning introduced by the instrumented blades [28].

Instrumentation and Data Reduction

For a flutter prediction model to be used as part of a design method for a turbomachine it should accurately predict the stability margins of the machine. Furthermore, some models also predict local flow phenomena, and so a validation of the pressure fluctuation amplitudes and phase angles is of interest. If possible, this evaluation should be the final test, as in some cases the stability limits (if zero mechanical is assumed) can be predicted accurately, despite disagreement in the local pressure values.

For experimental determination of the detailed unsteady blade surface pressure distributions, and the aerodynamic coefficients, high frequency response pressure transducers are usually mounted on one blade (or two adjacent ones). As it is not always possible to mount these transducers in the high pressure gradient regions, care should be taken to report how the time-dependent aeroelastic forces and moments are integrated from the finite number of transducers[5] .

This is all the more important for cascade tests in the transonic flow region as two other problems usually arise here. First of all, the blades are often thin and can thus accommodate only a fairly limited number of transducers.

Secondly, shock waves departing from or impinging upon the blade surfaces may significantly influence the accuracy of the local pressure response on the blade, for example as a lower signal/noise ratio.

If these shock waves are correlated with the blade motion they are part of the aeroelastic flow phenomenon and should be taken into account in the data reduction procedure. If they are not correlated, they are independent of the blade vibration and contribute marginally to the aerodynamic work (Appendix A1). They should thus be eliminated during the data reduction procedure [28].

Several data reduction methods exist for aeroelastic cascade tests. Among these the three most widely used are:

a: Averaging over a certain number of vibration cycles (e.g. [36])

b: Fourier analyses (e.g. [8])

c: Spectral analyses (e.g. [27])

The fundamental consideration of these methods is that, although the pressure response on the vibrating blades may be highly non-harmonic, it is only the frequency (or frequencies in the case of higher harmonics) of the pressure response spectra corresponding to the blade vibration that contributes to the aerodynamic work (see Appendix A1).

a: If the blade vibration frequency is known (controlled excitation) the first method mentioned above is often used.

Here the signals are sampled at a multiple of the blade vibration frequency. The data for each period are averaged, thus eliminating random fluctuations for a sufficiently large number of periods averaged. The number of samples

---

5 In contrast to this indirect method, it is also possible to measure the forces directly on the suspension [34, 35]. If both the indirect and direct methods are used simultaneously, information about the data accuracy can be obtained [35].

per vibration cycle determines the number of harmonics that can be resolved. The main advantage of the procedure is the short computing time needed.
This method therefore gives directly, and in most cases on-line, information about the amplitude and phase lead of the unsteady blade pressure response. Details about this testing procedure can be found for example in [36].

b: If it is also of interest to retain some information about eventual higher harmonics in the pressure spectra, a Fourier analysis is often used. This has the advantage of giving detailed information about the accuracy of the independent pressure signals. Thus can be helpful in analyzing the data since, for example under some operating conditions, the amplitudes of a higher harmonic may approach the fundamental. It can also give valuable information about how far disturbances propagate away from one specific blade.

c: If the blade vibration frequency is not controlled, and thus not known a priori (as for example during flutter experiments), it is not possible to use the averaging procedure as above. In such a case, either a "auto-or cross-correlation approach"or a Fourier analyses is often used.
If the correlation model is used the amplitude of the physical quantities can be defined as the root-mean-square value (RMS) times a factor $2^{0.5}$ (for example: $h = \{2 \cdot \int_0^T h^2(t)dt/T\}^{0.5} = \{2\}^{0.5} \cdot RMS$
This RMS-value may take the form e.g. of the output of a narrow-band filter applied to the unsteady pressure signal, centered at the blade oscillation frequency; the factor $2^{0.5}$ is introduced to equalize the RMS-amplitude with the full amplitude for a purely sinusoidal fluctuation, to compare the data with theoretical results.

Information about the quality of the signal (i.e. signal/noise ratio) should be given if possible. This can be achieved for example by indicating a confidence interval for the signals.
This confidence interval should not be given only for the amplitudes of the time-dependent data, but also for the phase angles. This is especially important as the value of the phase angle determines the stability limits of the bladings, and since it has been found in the present study that some disagreement between the analyses and the experiments can be found in the absolute value of the phase angles.

Error Analyses

Aeroelastic experiments mainly include two kinds of error sources [28]:

- Measuring equipment, reliability of calibration
- Nature of the signals: The data reduction procedure cannot entirely eliminate the effects of noise, and there is an a priori uncertainty independent of the data acquisition system. This uncertainty may be different for separate transducers, depending on the local signal/noise ratio.

In this context it is also important to mention that such phenomena as wind tunnel disturbances may introduce higher harmonics in the local unsteady pressures [15].

As already mentioned, indications about the accuracy of the results should be given if possible.

## II: Prediction Models

In the theoretical computations, several assumptions have to be made. These normally include, among others, harmonic blade vibrations and constant interblade phase angles (traveling wave formulation). For comparing different theoretical results, and for the mutual validation of the theories and experiments, these assumptions should be clearly stated. For the evaluation of numerical results, it is also of great interest to have information about the treatment of the far field boundaries (reflective or radiative boundary conditions) and grid generation, especially in the leading edge and shock regions.

## III: Conclusions

From the above it is evident that the data reduction procedure used should be clearly stated, and that a detailed error analyses should, if possible, accompany the experimental data. This is especially important when the prediction models, as is presently the case for certain configurations (see section 7), can accurately predict the aeroelastic response of a cascade, as eventual discrepancies between experimental and theoretical results may then be explained.

A detailed description of major assumptions should accompany theoretical results.

It is also important to perform experimental and theoretical investigations simultaneously. This may help to put into evidence, in the early stages of a project, eventual inaccuracies in the experimental or theoretical procedure.

## 5. Standard Configurations

On the basis of existing test facilities in the participating laboratories, and with relation to the state-of-the-art of theoretical methods, nine standard configurations[6] for establishing the mutual validity of two-dimensional and quasi three-dimensional aeroelastic cascade experiments and prediction models have been selected. The configurations should approximate idealized flows, therefore stall effects have been excluded, except as extensions of unstalled experiments.

In order to guarantee a correct validation of the theoretical models, the quality of the experimental results must also be verified. If possible, two similar experimental cascade geometries have therefore been identified as standard configurations for each of the following flow regimes:

- low subsonic (= incompressible)
- subsonic
- transonic
- supersonic

Of the nine standard configurations, which are summarized in Table 5-1, seven are based on experimental cascade results; the eighth is directed towards the establishment of validity for prediction models in the limiting case of flat plates and for comparison of the large number of existing flat plate theories. The final configuration (ninth) is defined so as to investigate blade thickness effects on the aeroelastic behaviour of the cascade, and on the theoretical results, especially at high subsonic flow velocities.

Each of the standard configurations selected allows for a systematic variation of one or several aerodynamic and/or aeroelastic parameters. However, too large a number of aeroelastic cases in each standard configuration would limit the usefulness in this report in providing comparisons for experimentalists and analysts working independently of each other.

For this reason, a restricted number of aeroelastic configurations for each test case, based upon available experimental data, has been chosen

---

[6] Throughout this report, "standard configuration" will designate a cascade geometry and "aeroelastic case" or "aeroelastic test case" will indicate the different time dependent (and, in some cases, time averaged) conditions within a standard configuration.

| Stand Config No | Insti-tution | Lin-Ann./ Thickness/ Camber | Compr / Turbine Config | Mach/ Stall | Excitation/ Motion/ Mode | Results | Instru-mentation | Parameters varied |
|---|---|---|---|---|---|---|---|---|
| 1 | United Technol. Research Center | • L (Air)<br>• 6%<br>• 10° | • C | • Incomp<br>• None | • Controlled<br>• Harmonic<br>• Torsion | • $\bar{c}_p$ + $\tilde{c}_p$ + $\Delta\tilde{c}_p$ + $\tilde{c}_m$ + ≡ | • 20 transducers<br>• Strain gauges | • i + $\tilde{\alpha}$ + σ + k |
| 2 | University of Tokyo | • L (Water)<br>• 5%<br>• 16° | • C+T | • Incomp.<br>• None+ Partial+ Fully | • Controlled<br>• Harmonic<br>• Torsion | • $\bar{c}_p$ + $\tilde{c}_l$ + $\tilde{c}_m$ | • Strain gauges | • i + σ + γ + k |
| 3 | Tokyo National Aerospace Lab | • A (Freon)<br>• 12%<br>• 60° | • T | • Sub + Sub→Super<br>• None+ Partial | • Controlled<br>• Harmonic<br>• Torsion | • $\bar{c}_p$ + $\tilde{c}_p$ + $\tilde{c}_m$ | • 10 transducers<br>• Strain gauges | • $M_2$ + σ + k |
| 4 | Ecole Polytech. Fédérale Lausanne | • A (Air)<br>• 17%<br>• 45° | • T | • Sub + Sub→Super<br>• None+ Partial | • Controlled<br>• Harmonic<br>• Bending + Torsion | • $\bar{c}_p$ + $\tilde{c}_l$ + ≡ | • 12 transducers<br>• Strain gauges | • $\beta_1$ + $M_2$ + σ |
| 5 | ONERA | • L (Air)/<br>• 3%/<br>• 0° | • C | • Subsonic<br>• None + Partial + Fully | • Controlled<br>• Harmonic<br>• Torsion | • $\bar{c}_p$ + $\tilde{c}_p$ + $\Delta\tilde{c}_p$ + $\tilde{c}_m$ + ≡ | • 26 transducers<br>• Strain gauges | • i + $M_1$ + $x_\alpha$ + k |
| 6 | Ecole Polytech Fédérale-Lausanne | • A (Air)<br>• 5%<br>• 14° | • T | • Sub + Sub→Super<br>• None + Partial | • Controlled<br>• Harmonic<br>• Bending + Torsion | • $\bar{c}_p$ + $\tilde{c}_l$ + ≡ | • 10 transducers<br>• Strain gauges | • $\beta_1$ + $M_2$ + σ |
| 7 | NASA Lewis Research Center | • L (Air)<br>• 3%<br>• -1.3° | • C | • Supersonic+ Super→Sub<br>• None+ Partial | • Controlled<br>• Harmonic<br>• Torsion | • $\bar{c}_p$ + $\tilde{c}_p$ + $\Delta\tilde{c}_p$ + $\tilde{c}_m$ | • 12 transducers<br>• Strain gauges | • $M_2$ + σ |
| 8 | - | • 2-D<br>• 0%<br>• 0° | • - | • Incomp. + Sub. + Super. + Super.→Sub<br>• None | • Controlled<br>• Harmonic<br>• Torsion | • $\bar{c}_p$ + $\Delta\bar{c}_p$ + $\tilde{c}_m$ + ≡ | •- | •- |
| 9 | - | • 2-D<br>• varied<br>• varied | • C | • Incomp. + Sub + Super. + Super.→Sub<br>• None | • Controlled<br>• Harmonic<br>• Torsion | • $\bar{c}_p$ + $\Delta\bar{c}_p$ + $\tilde{c}_m$ + ≡ | •- | •- |

Table 5.0-1. Brief Summary of nine standard configurations

for priority analyses, giving a total of 131 test cases (a larger number was defined in the first report [4, 7]). This number still seems to be rather large, but it concerns configurations over the whole velocity domain from incompressible to supersonic flow velocities. It is therefore not likely that any participant will calculate more than a limited number of these cases.
Furthermore, some of the standard configurations, especially those with fairly thick blades and large deviations, probably do not correspond with the present state-of-the-art of aeroelasticity. If this is so, they may instead serve as a base for future developments.
Configurations 1 and 2 (see Table 5-1) treat thin cascaded airfoils of rather low camber in the low subsonic velocity domain. The blades oscillate in the torsion mode with a relatively low frequency.
Standard configurations 3 and 4 concern modern high turning turbine rotor hub sections; they have therefore relatively thick blades, with subsonic inlet and subsonic or supersonic outlet conditions. In both configurations, the blade vibration frequencies correspond to the ones found in the actual turbomachine-blade.
Configuration 6 concerns low turning transonic turbine rotor tip sections with relatively thin blades with high stagger angle. The inlet condition is subsonic, with subsonic, transonic or supersonic outlet conditions.
Configurations 5 and 7 treat tip sections of fan stages in modern jet-engines and thus have rather thin profiles. The inlet flow conditions in configuration 5 are subsonic, with incidence ranging from attached to stalled flow conditions on the blades. In configuration 7, the inlet conditions are supersonic followed, in most cases, by strong in-passage shock waves.
The profiles in configurations 3-7 correspond to sections of actual turbomachine-bladings. Both linear (configurations 1, 2, 5 and 7) and annular (configurations 3, 4 and 6) cascade test facilities are used.
The last two standard configurations (8 and 9) are of theoretical nature mainly. They are included to validate numerical methods against each other, especially in the high subsonic velocity domain, and to look into some physical aspects of the flutter phenomena. However, experimental results for symmetric Double Circular Arc cascades have recently become available and should, in the future, included herein as a base for discussion.

## 6. Introduction to the Prediction Models

Several prediction models were applied to the standard configurations. In the beginning of the project, 19 methods were offered as a basis for comparison. Finally, 15 methodologies have been employed up till now.
Table 6.1 identifies the separate models in relationship with the predictions performed on the different standard configurations.

| Method N° | Name/Affiliation | Standard Configurations Computed |
|---|---|---|
| 1 | D. S. Whitehead/ Cambridge University, Cambridge, UK | 1, 2, 5, 8 |
| 2 | D. S. Whitehead/ Cambridge University, Cambridge, UK | 5, 8, 9 |
| 3 | J. M. Verdon/ United Technologies Research Center, East Hartford, USA | 1, 5, 8, 9 |
| 4 | M Atassi/ University of Notre Dame, USA | 1 |
| 5 | P. Salaün/ Office National d'Etudes et de la Recherche Aérospatiale, Paris, France | 1, 7, 8 |
| 6 | S Zhou/ Beijing Institute of Aeronautics and Astronautics, China | 1, 2, 5 |
| 7 | S. G. Newton, R. D. Cedar/ Rolls Royce Ltd, Derby, UK | 1, 4, 7, 8 |

**Table 6.1** Continued on next page

| | | |
|---|---|---|
| 8 | V. Carstens/ DFVLR-AVA, Göttingen, Germany | 1 |
| 9 | F. Molls/ NASA Lewis Research Center, Cleveland, USA | 8 |
| 10 | S. Kaji/ University of Tokyo, Japan | 4, 6 |
| 11 | O. O. Bendiksen/ Princeton University, USA | 8 |
| 12 | T. Araki/ Toshiba Corporation, Japan | - |
| 13 | K. Vogeler/ Technische Hochschule Aachen, Germany | - |
| 14 | J. M. R. Graham/ Imperial College, London, UK | 1 |
| 15 | S. Stecco/ University of Florence, Italy | 6 (Presently, steady state) |
| 16 | D. Nixon/ Nielsen Engineering and Research, Inc., Californa, USA | - |
| 17 | P. Niskode/ General Electric, Cincinatti, USA | - |
| 18 | H. Joubert/ SNECMA, Moisy Cramayel, France | 7 |
| 19 | M. Namba/ Kushuy University, Japan | 6, 8 |

**Table 6.1:** Aeroelastic Prediction Models

**Method 1**: LINSUB (Courtesy of D S Whitehead)

The program calculates the unsteady two-dimensional linearized subsonic flow in cascades in travelling wave formulation, using the theory published in [50]. The blades are assumed to be flat plates operating at zero incidence.
Both the pressure jump and lift and moment coefficients are computed for different options:

- Translational vibration of the blades normal to their chord.
- Torsional vibration of the blades about the origin at the leading edge.
- Sinusoidal wakes shed from some obstructions upstream, which move relative to the cascade in question.
- Incoming acoustic waves, coming from downstream.
- Incoming acoustic waves, coming from upstream.

Furthermore, the condition of acoustic resonance is calculated.

**Method 2**: Finite Element Method (FINSUP) (Courtesy of D. S. Whitehead)

As an example of a numerical field method, a computer program called FINSUP will be briefly described. The program has three sections: mesh generation, analysis of steady flow, and analysis of unsteady flow. The mesh generation and analysis of steady flow have been described by Whitehead and Newton (1985) [43]. The analysis of unsteady flow has been described by Whitehead (1982) [44].
A typical mesh is composed of triangular finite elements covering a strip, one blade spacing high, with the blade in the middle. The fluid is assumed to be a perfect gas with no viscosity or thermal conductivity, and the flow is assumed to be adiabatic, reversible and irrotational, so the equations are those for a velocity potential. The potential is continuous, except for a jump across the wake. In order to calculate in regions of supersonic flow it is necessary to use "upwind" densities; that means that instead of taking the density at the element under consideration, the density is taken from the neighbouring element in the most nearly upwind direction. This device stabilizes the compution in supersonic flow, but is unnecessary in subsonic flow. Weak shock waves are well simulated, but are "potential" since there is no entropy increase across the shock, and they are smeared over a few elements. The flow is matched to a linearized solution at the inlet and outlet faces of the computational domain, and is arranged to repeat between corresponding points on the top and bottom faces. The conditions specified to

the program are effectively the inlet circumferential velocity and the jump in potential between the bottom left and the bottom right corners of the domain. This choice of input conditions uniquely specifies the location of a shock in a cascade of flat plates at zero incidence, which no specification of flow conditions at either inlet or outlet can achieve. The non-linear equations are then solved by the Newton-Raphson technique. Convergence is usually achieved in three or four iterations, although up to about twelve may be necessary in difficult cases with supersonic inlet velocities. The nodes are numbered in such a way as to minimize the bandwidth of the dividing matrix at each iteration, so the method is fast. Good agreement with other methods of calculating steady transonic cascade flow in cascades has been demonstrated.
The program then goes on to the third stage in which small unsteady perturbations of the steady flow due to vibration of the blades is analysed.
Solid body motion of the blades is assumed, either in bending or torsion. The unsteady calculation is therefore similar to one more iteration of the steady calculation, except that the potential perturbation is complex, and the boundary conditions are different. Again the flow at the inlet and exit faces is matched to a linearized solution, which includes propagating or decaying acoustic waves and in the downstream flow the effect of the unsteady wake shed from the trailing edge. The repeat condition between corresponding points on the top and bottom surfaces is arranged to give the required phase difference between neighbouring blades. It is again necesary to use upwind densities in regions of supersonic flow in order to stabilize the calculation. A difficulty arises due to the term

$$(\vec{r}\cdot\Delta\vec{v})\cdot\vec{n} \qquad \text{(M2.1)}$$

for the boundary condition at the blade surface. A modified perturbation potential is defined by

$$\theta'' = \theta+\vec{r}\cdot\nabla\Phi \qquad \text{(M2.2)}$$

where r is given by

$$\vec{r} = \vec{n}+\vec{\alpha}\times\vec{R} \qquad \text{(M2.3)}$$

and this equation is now extended over the whole domain of calculation, and not just at the blade surface. This device gets rid of the awkward term in the boundary condition at the blade surface, and also eliminates a similar

awkward term in the calculation of the pressure perturbation at the surface. The unsteady pressure perturbations at the surface are then integrated to give the axial and circumferential blade forces and the moment.

**Method 3**: Linearized Unsteady Aerodynamic Analydes (Courtesy of J. M. Verdon)

The isentropic and irrotational flow of a perfect gas through a two-dimensional cascade of vibrating airfoils is considered. The blades are undergoing identical harmonic motions at frequency $\omega$, but with a constant phase angle $\sigma$ between the motions of adjacent blades. It is assumed that the flow remains attached to the blade surfaces and that the blade motion is the only source of unsteady excitation.
The flow through the cascade is thus governed by the field equations, written in form of the time-dependent velocity potential [5]. In addition to the field equations, the flow must be tangential to the moving blade surfaces and acoustic waves must either attenuate or propagate away from or parallel to the blade row in the far field. Finally, we also require that the mass and tangential momentum be conserved across shocks and that pressure and the normal component of the fluid velocity be continuous across the vortex-sheet unsteady wakes which eminate from the blade trailing edges and extend downstream.
In order to limit the computing resources required to solve the equation system, a small-unsteady-disturbance assumption is involved. Thus, the blades are assumed to undergo small-amplitude unsteady motions around an otherwise steady flow. The resulting first-order or linearized unsteady flow equation is solved subject to both boundary conditions at the mean positions of the blade, shock and wake surfaces and requirements on the behavior of the unsteady disturbances far upstream and downstream from the blade row.
Moreover, because of the cascade geometry and the assumed form of the blade motion, the steady and linearized unsteady flows must exhibit blade-to-blade periodicity. Thus, the numerical resolution of the steady and the linearized unsteady flow equations can be restricted to a single extended blade-passage region of the cascade.

**Method 4**: Aerodynamic Theory for Two-Dimensional Unsteady Cascades of Oscillating Airfoils in Incompressible Flows (Courtesy of H. Atassi)

A complete first order theory is developed for the analysis of oscillating airfoils in cascade in a uniform upstream flow. The flow is assumed to be incompressible and irrotational. The geometry of the airfoil is arbitrary. The angle of attack of the mean flow and the stagger and solidity of the cascade can assume any prescribed set of values. The airfoils have a small harmonic oscillation about their mean position with a constant interblade phase angle. Both translational and rotational oscillations are considered.
The boundary-value problem for the unsteady component of the velocity is formulated in terms of sectionally analytic functions which must satisfy the impermeability condition along the airfoils surfaces, the Kutta condition at the trailing edges of the airfoils, and the jump condition along the airfoils wakes. The expression for the velocity jump in the wakes is derived to a multiplicative constant from the condition of pressure continuity across the wakes. The velocity field is split into two components: one satisfying the oscillating motion along the airfoils surfaces and the other accounts for a normalized jump conditions along the wakes. This leads to two singular integral equations in the complex plane. The two equations are coupled by Kelvin's theorem of conservation of the circulation around the airfoils and their wakes. The integral equations are solved by a collocation technique.
The results obtained from this theory show that the airfoil geometry and loading and the cascade stagger and solidity strongly affect the aerodynamic forces and moments acting upon oscillating cascades. As a result stability and flutter boundaries are significantly modified for highly loaded cascades.

**Method 5**: (Courtesy of P. Salaün)

The two-dimensional cascade is an infinite array of thin blades.
The fluid is an inviscid perfect gas and the flow is assumed to be irrotational and isentropic.
The blades are performing harmonic motions of so small amplitude that the theory can be linearized about the undisturbed, uniform flow.
The supersonic theory is restricted to the case of subsonic leading edge locus.

The pressure difference between the two sides of the blades are taken into account when they are replaced by sheets of pressure dipoles in both subsonic and supersonic flow.
Then, the perturbation velocity potential is expressed and the boundary conditions on the blades give an integral equation where the unknown is the pressure difference on the reference blade, and the right hand side the angle of attack.
This integral equation is solved numerically.

**Method 6**: Zhou Sheng

A finite difference method is used to solve the unsteady velocity potential equation. The velocity potential is split into one steady and one unsteady part, and the unsteady small perturbation is solved with a relaxation procedure.

**Method 7**: Extended FINSUP (Courtesy of R. D. Cedar)

The flutter calculation used at Rolls Royce is an extension of the finite element method developed by D. S. Whitehead (Method 2). Since the programs introduction to Rolls Royce in 1981 it has been continually developed and evaluated [43]. The finite element mesh generator has been fully automated to the extent that it now contains "rules" about how good a mesh is. Using these "rules" the mesh construction parameters are automatically changed until a satisfactory mesh is obtained.
The steady flow calculation has been extended from being purely two-dimensional to include the quasi-three-dimensional effects of blade rotation and variations of streamtube height and streamline radius [51]. This has allowed the program to be included in the quasi-three-dimensional design system used at Rolls Royce [52]. Improvements to the upwinding scheme has been made that produce sharp shocks. A coupled boundary layer calculation (using both direct and semi-inverse coupling) has been developped [53] as well as a design or inverse calculation [54]. This allows transonic blades to be designed, including the removal of shocks, to give a controlled diffusions.
The unsteady flow calculation has been extended to include the quasi-three-dimensional effects. It has been found that it is essential to include the

effect of variation in streamtube height if test data is to be predicted correctly.

**Method 8**: Theoretical Flutter Investigation on a Cascade in Incompressible Flow (Courtesy of V. Carstens)

1. Calculation of unsteady aerodynamic coefficients

The calculation of the unsteady aerodynamic coefficients due to harmonic bending and torsion of the cascade's blades is based on an integral equation technique. The main idea of this technique is to replace each blade's surface and its wake by a distribution of vorticity. The kinematic boundary condition and the law of vorticity transport allow the formulation of the flow problem as an integral equation, the solution of which yields the correct value of the unknown unsteady blade vorticity.
Two important items in the formulation of the problem should be mentioned:
1) The prescribed harmonic motion of the entire cascade unit is a fundamental mode, in which all blades perform oscillations with the same amplitude but with a constant phase lag from blade to blade (interblade phase angle).
2) The influence of the steady flow on the unsteady quantities is obtained by a special linearizing procedure.
The unsteady pressure distribution and the aerodynamic lift and moment coefficients are calculated as a function of the blade vorticity by means of Bernoulli's equation.

2. Flutter analysis

The flutter analysis is done on the basis of a two-degree-of freedom model, which allows for bending perpendicular to the chord and torsion around a given elastic axis. The rearrangement of the two linearized equations of motion for a blade section in nondimensional matrix form yields the formulation of the flutter problem as a nonlinear eigenvalue problem. Stability boundaries are found by determining the real eigenvalues of the matrix equation in an iterative procedure if a set of elastomechanical and aerodynamic parameters is prescribed. The result of each flutter calculation is a stability curve in a reduced frequency - interblade phase angle diagram,

the maximum of which yields the absolute stability boundary and hence the nondimensional flutter speed for the given configuration.

**Method 9**: (Courtesy of F. Molls)

The model allows for two shock waves to occur in a tip blade passage in which the inlet Mach number is supersonic. A weak oblique shock from the leading edge lies off the pressure surface of the upper blade and its angle is great enough that the shock intersects the lower blade. Off the suction surface of the lower blade there is a normal wave at the trailing edge which intersects the upper blade. The oblique shock angle corresponds to the pressure ratio but not to the metal angle at the leading. The model blade, however, has a wedge angle in agreement with the pressure ratio and inlet Mach number. Where the oblique shock strikes the adjacent blade, the flow turns from the inlet direction through the wedge angle to become parallel to the pressure surface; thus, as observed in actual flow, there is no reflection.

There are two options in the model. Either the pressure and suction surfaces continue uniformly to a blunt trailing edge, or the trailing surfaces are tapered to a specified thickness at the trailing edge. In the former case the differential equations for the unsteady component of the flow have constant coefficients and may be solved analytically. In the latter option, the mean flow in one portion of the blade passage is a slowly varying flow and numerical integration of the disturbance equations is required. A more detailled description with a diagram and references to experimental examples of the modelled flow is given in [37].

**Method 10**: Semi-Actuator Disk Method (Courtesy of S. Kaji)

The semi-actuator disk model converts an actual blade row to a continuous cascade by inserting many fictious blades in between and parallel to the original blades. Aerodynamic loading and inter-blade phase change are all shared by inserted blades. Thus the change of physical quantity in the cascade direction is given by crossing each blade stepwise, and we can treat the flow inside a blade channel one-dimensionally.

The first part of the analyses is to solve the linearized governing equations of mass, momentum and energy for the upstream, inside and downstream field

of the cascade separately. We have a pressure wave in the upstream field, two pressure waves going back and forth (and an entropy wave if the total pressure loss is present) inside the cascade and also we have a pressure wave, (an entropy wave) and a vorticity wave due to blade oscillation in the downstream field. The unknown amplitude of each wave is related to the known amplitude of blade oscillation through boundary conditions at the leading edge plane and the trailing edge plane of the cascade.

At the leading edge plane we use

- mass flow continuation,
- relative total enthalpy continuation, and
- the condition of total pressure loss change in accordance with flow incidence.

At the trailing edge plane we can assume a smooth continuation of all physical quantities, i.e., two components of velocity, pressure and density.

The aerodynamic forces acting on blades can be evaluated by use of the momemtum principle applied to the control volume taken for a blade channel.

The merits and demerits of the method are:

- Aerodynamic loading
- Total-pressure-loss
- Arbitrary direction of oscillation
- No large inter-blade phase angles

**Method 11:**

**Method 12:**

**Method 13:**

The code is based on the nonlinear transonic small perturbation equation. The disturbances are assumed to be small. Hence the principle of superposition is applied and the problem is split into a steady and an unsteady part. A method of characteristics was developed for both the steady and the unsteady solutions to handle the supersonic flow past a finite cascade of oscillating parabolic - not necessarily symmetric - blades.

Considerable progress was achieved with the extended treatment of the unsteady shocks including a shock equation for the unsteady perturbation

potential. Furthermore the application of the method of characteristics to unsteady sliplines, shock intersections and the crossing of a shock with a slipline was developed.
The results are steady and unsteady pressure distributions, the integrated lift- and moment-coefficients and the shock geometry in the cascade. At the moment the code is for research purposes only. It is planned to rewrite it for industrial application.

**Method 14:** Discrete Vortex (Cloud-in-Cell) Method for Unsteady Cascade Flows (Courtesy of J. M. R. Graham and J. Basuki)

This method represents shed vortex wakes in two-dimensional incompressible flow by large numbers of discrete point vortices which are convected by the local velocity field. In the cloud-in-cell method the vorticity associated with the moving point vorices is transfered to a fixed Eulerian mesh [32]. The streamfunction and hence velocity distribution is calculated from the vorticity on this mesh using a standard fast Poisson solver.
The present version of this method used to calculate unsteady flow through a cascade represents the individual aerofoils in the cascade by a boundary integral method [33] which uses piecewise constant vorticity panels. The appropriate streamfunction boundary condition is satisfied on the surface of each aerofoil by summing the contributions of the surface vorticity panels (including implied periodicity) and the mesh streamfunction. The boundary condition on the mesh also assumes periodicity along the cascade with the interblade phase angle limited to a small integral number of aerofoils within the mesh flow field. The computation follows the evolution of an unsteady flow by forward time marching, tracking the positions of the vortices.
The program has been used to compute cases with superimposed unsteady flow, upstream wakes, and blade vibration. In the latter case when the interblade phase angle is non-zero, exact application of the boundary integral method requires the influence functions to be recalculated at each time-step to account for changes in the relative blade to blade displacement. This has not been done in the present program for reasons of computational cost. The present boundary condition includes the relative motion but is evaluated on the mean surface of each blade and is therefore limited to small displacement amplitudes compared to the blade spacing.
The program evaluates time histories of surface pressures and forces induced on the aerofoils by the unsteady flows. Since the method involves time

marching from an impulsive start fairly long computations are required to reach a final state free of initial transients.

**Method 15**: (Courtesy of S. Stecco)

The inviscid planar compressible flow is governed by the continuity, Crocco's and energy equation:

$$\nabla(\varrho C) = 0 \qquad \text{(M15.1)}$$

$$C\times(\nabla\times C)+\nabla H-T\nabla S = 0 \qquad \text{(M15.2)}$$

$$dS/dT = 0 \qquad \text{(M15.3)}$$

In the case of practical interest it can be assumed that the total enthalpy is constant, and that the flow is homoentropic; this leads to the statement of "irrotational flow".
The assumption of homoentropic flow is not correct in transonic flow where the shock waves can introduce entropy gradients, but such gradients can be neglected, in first approximation, if the shocks are weak as it usually happens in the passage of blades cascades.
In order to get a pseudo-unsteady formulation, after Viviand, it is possible to write Crocco's equation in the streamwise direction:

$$\partial\theta/\partial t = -(\partial v/\partial x - \partial u/\partial y) \qquad \text{(M15.4)}$$

and the continuity equation:

$$\partial Z(\varrho)/\partial t = -(\partial[\varrho u]/\partial x + \partial[\varrho v]/\partial y) \qquad \text{(M15.5)}$$

where Z is a suitable function of density as it will be seen later. The closure equation comes from the conditions:

$$\nabla S = \nabla H = 0 \qquad \text{(M15.6)}$$

After Viviand the function Z has been choosen in order to achieve good stability all over the working Mach number range.

$$Z(\varrho) = -k\varrho^{*}M^{*} \qquad \text{(M15.7)}$$

where k is an integer number and *refer to critical conditions.
In order to increase the convergence rate of equations (M15.4) and (M15.5) two functions and have now been introduced to multiply the RHS and new stability analysis has been performed.
The choice of these functions is not straight forward because of the presence of high non linear instability; any way a final expression have been found which leads to good results.
The equations (M15.4) and (M15.5) can be written as:

$$\partial f/\partial t+\partial F/\partial x+\partial G/\partial y = 0 \qquad \text{(M15.8)}$$

where now:

$$f = \begin{vmatrix} Z(\varrho)/\xi \\ \theta/\eta \end{vmatrix}$$

$$F = \begin{vmatrix} \varrho u \\ v \end{vmatrix}$$

$$\begin{vmatrix} \varrho v \\ -u \end{vmatrix} \qquad \text{(M15.9)}$$

$$G = \begin{vmatrix} -u \end{vmatrix}$$

$$\xi = M^2 dZ(\varrho)/d\varrho$$

$$\eta = \left|1-M^2\right|$$

The numerical solution of these equations will be carried out by an explicit scheme, then the stability condition on the time step has been derived from the CFL criterion that states that the physical dependence domain must be included in the numerical one.
The boundary conditions are:

- upstream the total thermodynamic conditions and the flow angle (if the axial flow is supersonic, also the only Mach number) are fixed.
- downstream the Mach number is fixed, i.e. the preassure ratio across the cascade (if the axial flow is supersonic not any condition is fixed).
- the solid wall require the tangent condition of velocity that substitutes the 2nd equation and impose conditions on the flux terms of first equation.
- the ideal periodic boundaries require the velocity vector to be equal in correspondent point at one pitch distance. When choosing such lines the

normal velocity component must be subsonic. Their treatment results easy in the numerical scheme.
Finally the trailing edge condition is the really delicate one.
In fact there it has to be simulated the base region, from where the shock waves system starts in turbine cascades.
We consider a truncated trailing edge and the velocity vector free on the two points on each side of the trailing edge.
The choice of the truncation must be done carefully owing to its significant influence on the results. It represents roughly the separation points at the trailing edge.
Results are obtained with a coarse grid of 10x57 and a fine mesh of 19x57 points, and by using a finer convergence limit.
Now we test the convergence on the inlet-outlet mass flow difference after the local time variations of the unknowns are within a fixed limit.
Execution time on Honeywell DPS 6:

| $M_{2is}$ | CPU time | n. of iteration |
|---|---|---|
| 1.2 | 348 s | 120 |
| .98 | 383 s | 130 |
| .95 | 514 s | 170 |

**Method 16**: Computer Code "Cascade" (Courtesy of D. Nixon )

The code will compute the unsteady transonic flow through a nonstaggered cascade. Thin airfoil boundary conditions are used and the code is an extension of the XTRAN2L code for isolated airfoils. The algorithm is the Rizzetta-Chin algorithm for arbitrary frequencies. The code is used for research purposes and is not a production code.

**Method 17**:

**Method 18**: (Courtesy of H. Joubert)

A model has been developed at SNECMA for calculating the unsteady aerodynamic flow through vibrating cascades in view of studying supersonic flutter in axial flow compressors.

The calculation deals with an ideal fluid, in unsteady transonic flow, including shocks, through a quasi three-dimensional cascade.
The explicit Mac Cormack scheme was used to numerically solve the unsteady Euler's equations on a blade to blade surface. An 80 x 15 grid points mesh was used which was displaced to follow the blade motion. For further details, see ref. [47].
This model has been applied to the seventh standard configuration of the workshop on aeroelasticity in turbomachine-cascades. Two cases were studied, the first one corresponding to an exit Mach number of 1.25 and the second one to an exit Mach a number of 0.99. The unsteady aerodynamic damping coefficients for both cases are represented (see section 7.7) and the magnitude and phase lead of blade surface pressure coefficient for two interblade angles are plotted.

**Method 19**: Method of Calculating Unsteady Aerodynamic Forces on Two-Dimensional Cascades. (Courtesy of M. Namba.)

The basic assumptions of the method are that the flow should be inviscid and isentropic. The gas should be perfect and the blade oscillations small.
The blades are represented by pressure dipoles of fluctuating strength

$$\Delta p(x_0) e^{i\omega t + im\sigma} \qquad (m = 0, \pm 1, \ldots) \tag{M19.1}$$

and the problem is reduced to an integral equation for $\Delta p(x_0)$:

$$\int_0^c \Delta p(x_0) K(x - x_0) dx_0 = i\omega\alpha(x) + U\alpha'(x) \tag{M19.2}$$

The Kernel function $K(x-x_0)$ is resolved into:

- a singular part $K(S)(x-x_0)$ in a closed form
- a regular part $K(R)(x-x_0)$ in an infinite series form of uniform convergence (A sufficient convergence with truncation at the 30th term is confirmed.)

The dipole distribution function $\Delta p(x_0)$ is then expanded into a mode function series.

The flow can be either sub- or supersonic:

- Subsonic Cascade:

$$\Delta p(x_0) = \sum_{K=0}^{K-1} P_k Y_k(\varphi) \qquad \text{(M19.3)}$$

where

- $x_0 = 0.5c(1-\cos\varphi)$
- $Y_0(\varphi) = \cot(0.5\varphi)$
- $Y_k(\varphi) = \sin(k\varphi)$ $(k \geq 1)$ (Glauert series)

- Supersonic Cascade:

$$\Delta p(x_0) = g(x_0) + \sum_r Fr \quad \begin{cases} g(x_0+xr) & : x_{\ell-} \leq x_0 \leq x_{\ell+} \\ 0 & : \text{otherwise} \end{cases} \qquad \text{(M19.4)}$$

where

- r=reflection number (this technique corresponds to the Nagashima & Whitehead' technique)

$$g(x_0) = \sum_{K=0}^{K-1} P_k Y_k(\varphi) \text{ , with } x_0 = 0.5c(1-\cos\varphi) \qquad \text{(M19.5)}$$

- $Yk(\varphi) = \cos k\varphi$ ( equivalent to shifted Chebyshev polynomials)

The integral equation is converted into algebraic equations for Pk ( k = 0,1,2,...,K-1 ).

$$\sum_{k=0}^{K-1} P_k YK_k(x_j) = i\omega\alpha(xj) + U\alpha'(xj) \text{ , } j = 1,2,\ldots,K \qquad \text{(M19.6)}$$

where

$$- YK_k(x) = \int_0^c Y_k(\varphi)K^{(S)}(x-x_0)dx_0 + \int_0^c Y_k(\varphi)K^{(R)}(x-x_0)dx_0 \qquad \text{(M19.7)}$$

with the first term calculated analytically and the second numerically integrated with about 240 integration points from $x_0$ = 0 to c ). In the present cases, calculations were conducted with six control points (K=6).

## 7.1 First Standard Configuration (Compressor Cascade in Low Subsonic Flow)

### Definition

This configuration is compiled from two-dimensional cascade experiments in the low subsonic flow region. It is therefore mainly directed towards the validation of incompressible predictions.

The experiments were performed in air, in the linear low subsonic oscillating cascade wind tunnel at the United Technologies Research Center and are included in the present study by courtesy of F.O. Carta ([8, 15, 16]).

The cascade configuration consists of eleven vibrating NACA 65-series blades, each having a chord c=0.1524 m and a span of 0.254 m, with a 10° circular arc camber and a thickness-to-chord ratio of 0.06. The pitch-to-chord ratio is 0.750 and the stagger angle for the experiments presented here is 55°.

The cascade geometry and profile coordinates are given in Figure and Table 7.1-1, resp.

The airfoils oscillate, in pitching mode, around a pivot axis at (0.5, 0.0115).

Experiments have been performed with vibration frequencies between 6 and 26 Hz and with two pitching amplitudes (0.5° and 2°).

Both the time-averaged and time-dependent instrumentation on this cascade is very complete, and a large number of well documented data have been obtained during the tests. The time-dependent instrumentation consists of 10 high frequency response pressure transducers on each side of the center blade, arranged in a Gaussian array, to obtain maximum accuracy in the numerical integration of the moment and damping coefficients of the resulting pressure distributions [15, 17].

Further to the center blade, 5 others and the tunnel sidewall were partially instrumented to validate the time-dependent periodicity of the flow through several blade passages.

All the blades in the cascade are vibrated with a cambar system to produce a highly accurate harmonic motion.

## Low Subsonic Compressor Profiles.

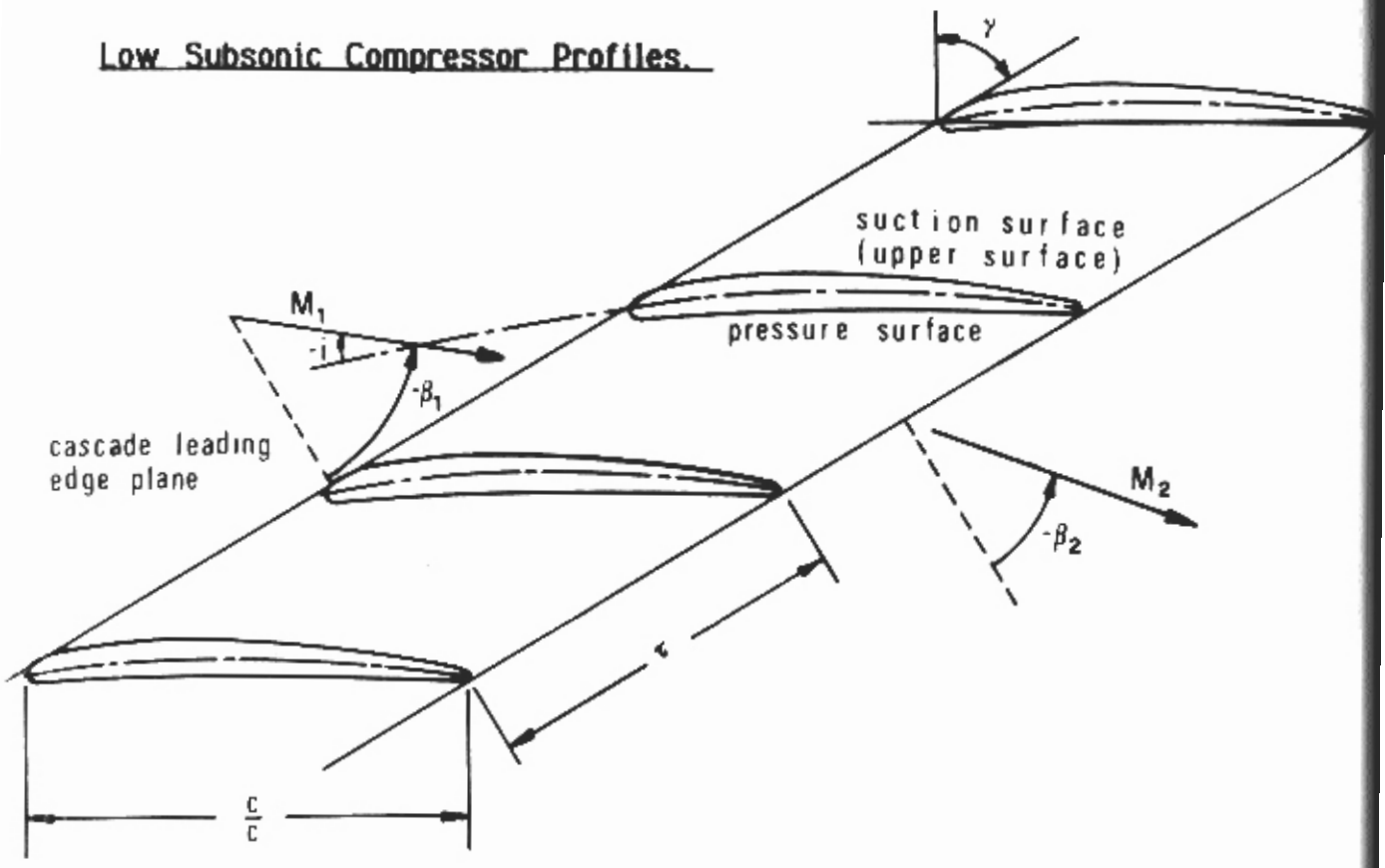


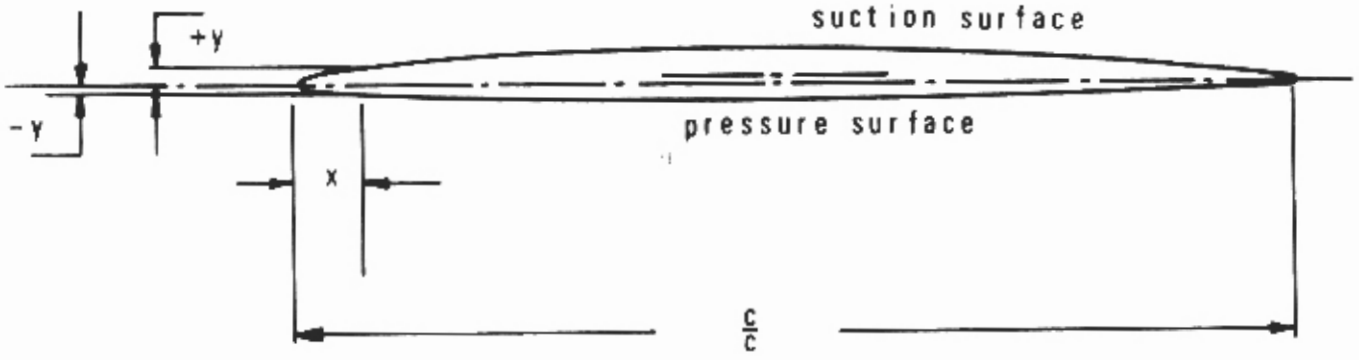


Maximum thickness at x = 0.5
Vibration in pitch around $(x_\alpha, y_\alpha)$ = (0.5,0.0115)
d = (thickness/chord) = 0.06
α = 0.5°, 2.0° (= 0.0087, 0.0349 rad)

| | | | |
|---|---|---|---|
| c | = | 0.1524 m | i = variable (2°, 6°) |
| τ | = | 0.75 | camber = 10° |
| k | = | variable | γ = 55° |

span = 0.254 m
Working fluid: Air

Fig. 7.1-1. First standard configuration: Cascade geometry

| c = 15.24 cm (6 in.) | | | |
|---|---|---|---|
| SUCTION SURFACE | | PRESSURE SURFACE | |
| X | Y | X | Y |
| 0.0008 | 0.0020 | 0.0012 | -0.0019 |
| 0.0046 | 0.0053 | 0.0054 | -0.0042 |
| 0.0070 | 0.0064 | 0.0080 | -0.0050 |
| 0.0120 | 0.0083 | 0.0130 | -0.0061 |
| 0.0244 | 0.0116 | 0.0256 | -0.0077 |
| 0.0494 | 0.0164 | 0.0507 | -0.0098 |
| 0.0743 | 0.0204 | 0.0757 | -0.0115 |
| 0.0993 | 0.0237 | 0.1007 | -0.0129 |
| 0.1494 | 0.0290 | 0.1506 | -0.0150 |
| 0.1994 | 0.0331 | 0.2006 | -0.0165 |
| 0.2495 | 0.0364 | 0.2505 | -0.0177 |
| 0.2996 | 0.0387 | 0.3004 | -0.0185 |
| 0.3998 | 0.0411 | 0.4002 | -0.0188 |
| 0.5000 | 0.0406 | 0.5000 | -0.0176 |
| 0.6002 | 0.0370 | 0.5998 | -0.0146 |
| 0.7003 | 0.0306 | 0.6997 | -0.0104 |
| 0.8003 | 0.0223 | 0.7997 | -0.0069 |
| 0.8503 | 0.0176 | 0.8497 | -0.0053 |
| 0.9003 | 0.0127 | 0.8997 | -0.0040 |
| 0.9502 | 0.0078 | 0.9497 | -0.0032 |
| 0.9975 | 0.0030 | 0.9973 | -0.0025 |

| | RADIUS CENTER COORDINATES |
|---|---|
| L.E. RADIUS/c = 0.0024 | X = 0.0024, Y = 0.0002 |
| T.E. RADIUS/c = 0.0028 | X = 0.9972, Y = 0.0003 |

**Table 7.1-1. First standard configuration: Dimensionless airfoil coordinates.**

The time-dependent data were recorded in digit form at sampling rates of 1000 samples/sec. Data for each channel were then Fourier anlysed to provide the first, second and third harmonic results.
Details of the experimental procedure and all the data acquired are given in [15]. Furthermore, for convenience, the section on data acquisition and initial reduction from [15] (pages 15-16) appears in Appendix A4.

## Aeroelastic Test Cases

From the tests presented in [15], 15 aeroelastic cases have been retained as recommendations for off-design calculations. These cases are given in Table 7.1-2 They correspond to two different mean settings of the cascade, variable vibration amplitudes, reduced frequencies and interblade phase angles.

| | Time averaged | | | | Time Dependent Parameters | | | | |
|---|---|---|---|---|---|---|---|---|---|
| Aeroelastic Test Case No | $M_1$ (-) | i (°) | $p_1/p_{w1}$ (-) | $p_2/p_{w1}$ (-) | $\beta_2$ (°) | k (-) | $\alpha$ (°) | $\sigma$ (°) | f (Hz) |
| 1 | 0.18 | 2 | 0.9774 | 0.9818 | 62.0 | 0.122 | 0.5 | - 45° | 15.5 |
| 2 | " | " | " | " | " | " | " | + 45° | " |
| 3 | 0.17 | 6 | 0.9790 | 0.9852 | 62.5 | " | " | - 45° | " |
| 4 | " | " | " | " | " | " | 2.0 | + 45° | " |
| 5 | " | " | " | " | " | " | " | - 45° | " |
| 6 | " | " | " | " | " | " | " | -180° | " |
| 7 | " | " | " | " | " | " | " | -135° | " |
| 8 | " | " | " | " | " | " | " | - 90° | " |
| 9 | " | " | " | " | " | " | " | - 0° | " |
| 10 | " | " | " | " | " | " | " | + 90° | " |
| 11 | " | " | " | " | " | " | " | +135° | " |
| 12 | " | " | " | " | " | 0.072 | " | - 90° | 9.2 |
| 13 | " | " | " | " | " | 0.151 | " | - 90° | 19.2 |
| 14 | " | " | " | " | " | 0.301 | " | - 90° | 38.4 |
| 15 | " | " | " | " | " | 0.603 | " | - 90° | 76.8 |

**Table 7.1-2** First standard configuration.
Experimental values for 15 recommended test cases

All the test cases were extensively treated by several prediction models (see Table 6.1), wherefore a detailed comparison between experimental data and theoretical results is possible.

## Discussion of Time Averaged Results

The 15 proposed aeroelastic test cases comprise two separate stationary flow conditions: 2° (cases 1-2) and 6° (cases 3-15) incidence respectively. These time-averaged results are given in Fig. 7.1-2. It is concluded that the data agree well with theoretical results from Method 3.

However, some ambiguity seems to exist in the determination of the incidence angle. It should be noted here that both in the present work and in the study by Carta [15], the incidence angle, i, is defined towards the mean camberline angle at the leading edge (Fig. 4.1-1). The experimentally determined values are $i_{exp}$= 2° and 6°, respectively. It was found by several persons, independent of each other, that the data for the local time-averaged blade surface pressure distribution and the analyses agree better if the incidence angle is slightly modified for the theoretical calculations.

Several possible explanations for this discrepancy can be put forward:

- The experimental cascade consists of 11 blades while the analyses consider infinite cascades [15].
- The axial velocity density ratio was not measured in the experiment [15].
- The possibility of separate definitions of the incidence angle between different researchers must also be considered. In fact, it has been pointed out by H. Atassi and F.O. Carta [38] that the incidence angle sometimes used by analysts is the angle between the uniform upstream flow and the airfoil chord (defined on this page as $i_{chord}$). For the first standard configuration, the relationship between the mean camber line (at the leading edge) incidence and the chordal incidence angle is [38]

$$i = i_{chord} - 2.5°$$

However, as this last remark concerns only the definition of the incidence angle and as there is still disagreement about the values given for the inlet flow angle, it cannot be the sole reason for the differences.

The two most likely explanations for the need to correct the incidence angle to make the theoretical and experimental results agree well are thus the first ones, referenced by Carta in [15].

It can be pointed out that, for the two methods with which a detailed investigation of the steady-state incidence was performed (Methods 3 and 7), both give best agreement for the same corrected incidence angle ($i_{exp}$=2°, $i_{theory}$=-0.27°; $i_{exp}$=6°, $i_{theory}$=2.23°, see [5, 40]).

Apart from the discrepancies in incidence angle, agreement with the data is good (see Figures 7.1-2 for examples), which mutually validates both the experimental and theoretical time-averaged results.

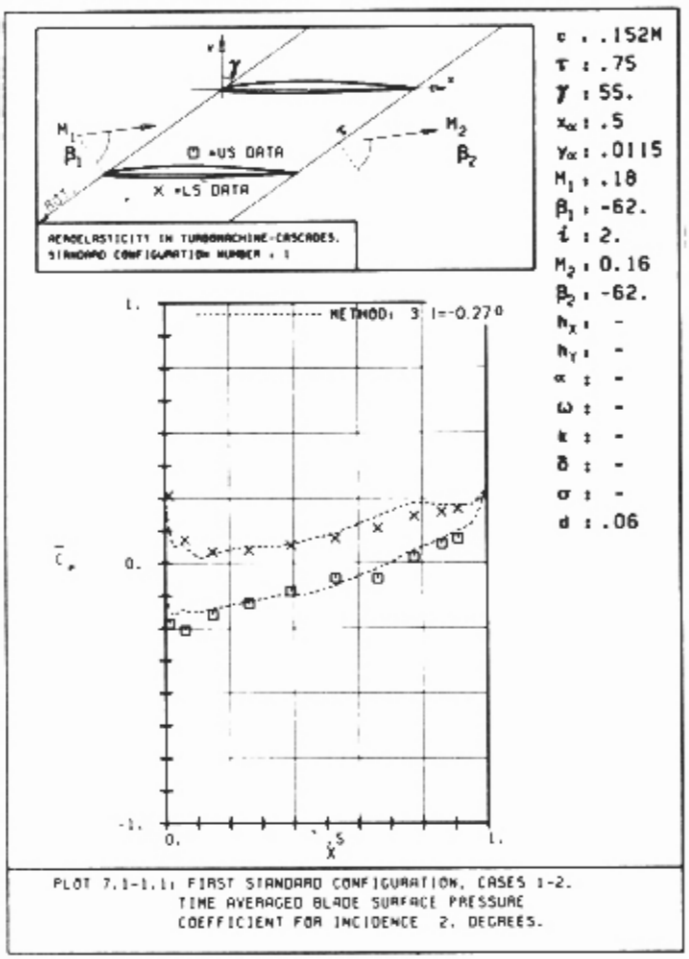


PLOT 7.1-1.1: FIRST STANDARD CONFIGURATION, CASES 1-2.
TIME AVERAGED BLADE SURFACE PRESSURE
COEFFICIENT FOR INCIDENCE 2. DEGREES.

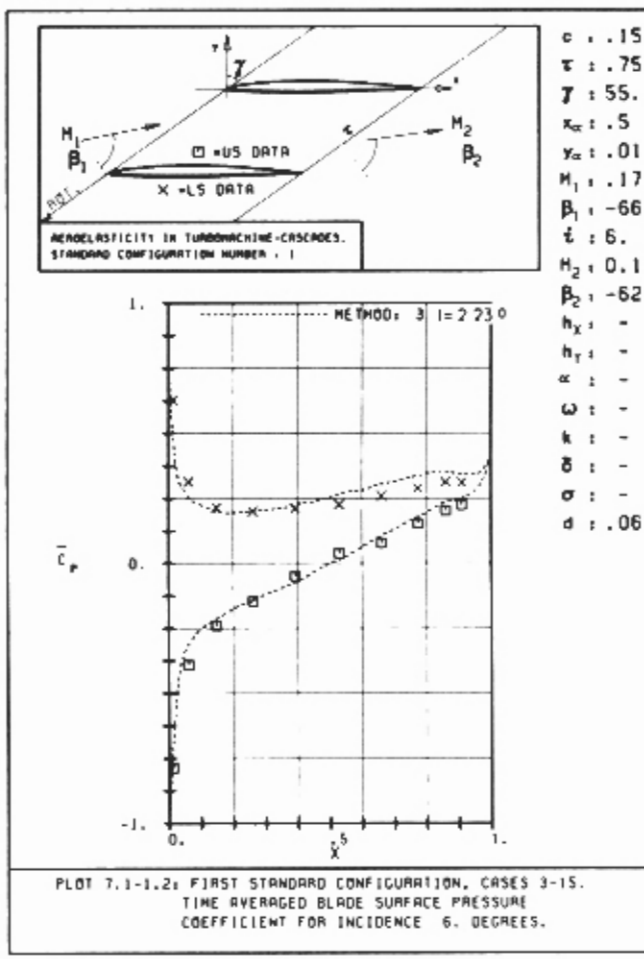


PLOT 7.1-1.2: FIRST STANDARD CONFIGURATION, CASES 3-15.
TIME AVERAGED BLADE SURFACE PRESSURE
COEFFICIENT FOR INCIDENCE 6. DEGREES.

a) $i_{exp} = 2°$ b) $i_{exp} = 6°$

Fig. 7.1-2. First Standard Configuration, Cases 1-2. Time Averaged Blade Surface Pressure Coefficient for $i_{exp} = 2°$ and $i_{exp} = 6°$

## Discussion of Time-Dependent Results

In total eight methods have presently been applied to the first standard configuration (Table 6-1). All of these calculate the time-dependent blade surface pressures, wherefore it is possible to evaluate both these and the stability limit of the cascade.
Full details of all the results obtained for the 15 aeroelastic cases are given in section 1 in Appendix A5.

### Integrated Parameters

Evaluation of the results shows that the stability limits ($\Xi$=0) of the cascade are well predicted by all analyses for a reduced frequency of k=0.122 (Fig. 7.1-3a,b). However, some scatter appears in the magnitude of the aerodynamic damping coefficient around its maximum and minimum values. It is interesting to note that the dissimilarity in damping magnitude between the data and the separate analyses at, ±90° interblade phase angles, appears for some methods mainly because of disagreement in the magnitude of the moment coefficient, and for some mainly because of disagreement in its phase lead (Fig. 7.1-3c).
This certainly also indicates some scatter in the unsteady surface pressures.
The analytically determined acoustic resonances ([15, 39], see also Appendix A3), lie for this specific cascade close to a 0° interblade phase angle for the flow conditions presented in Figures 7.1-3. It is concluded that the theoretical and experimental results agree well, especially for the damping coefficient, also in the surroundings of this interblade phase angle, although the disagreement of Method 4 with the others around a 0° interblade phase angle is certainly due to the resonance conditions. (If slightly different interblade phase angles had been used for the calculation in Method 4, the curve would probably concur with the others.)
An information which does not influence the flutter behavior of a cascade in the pitching mode, namely the aerodynamic lift coefficient, is given in Fig. 7.1-4. Here some larger disagreement than in the moment coefficient is found, especially in the magnitude.

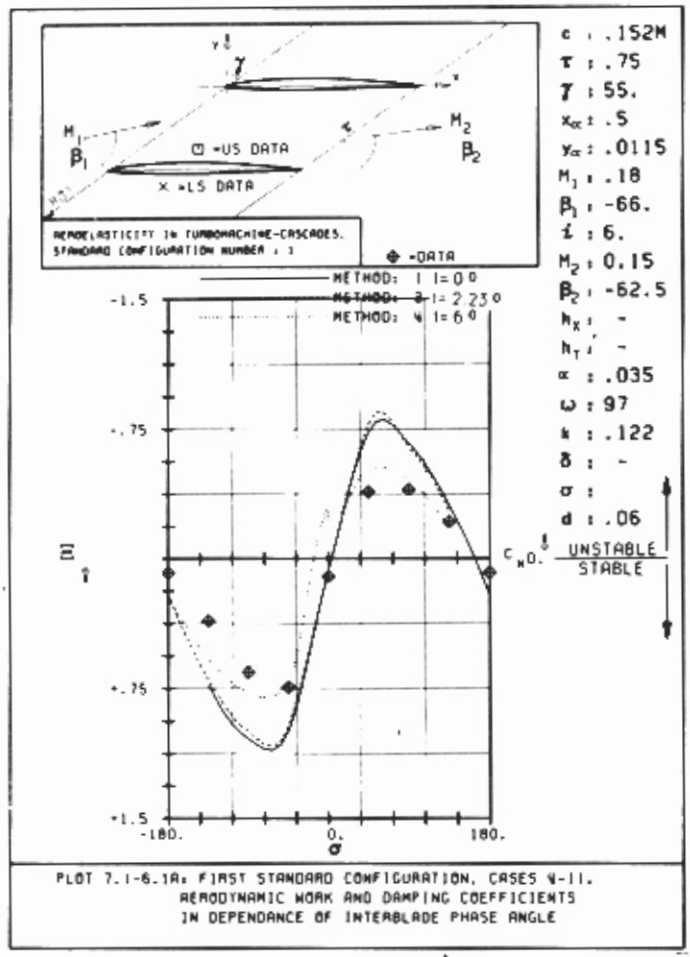


PLOT 7.1-6.1A: FIRST STANDARD CONFIGURATION, CASES 4-11.
AERODYNAMIC WORK AND DAMPING COEFFICIENTS
IN DEPENDANCE OF INTERBLADE PHASE ANGLE

a)

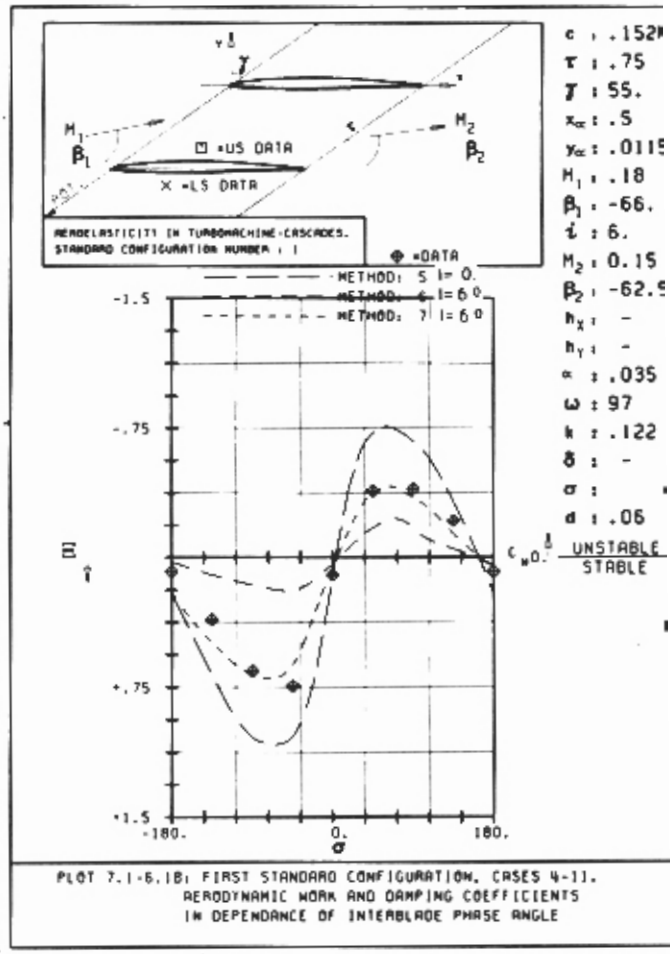


PLOT 7.1-6.1B: FIRST STANDARD CONFIGURATION, CASES 4-11.
AERODYNAMIC WORK AND DAMPING COEFFICIENTS
IN DEPENDANCE OF INTERBLADE PHASE ANGLE

b)

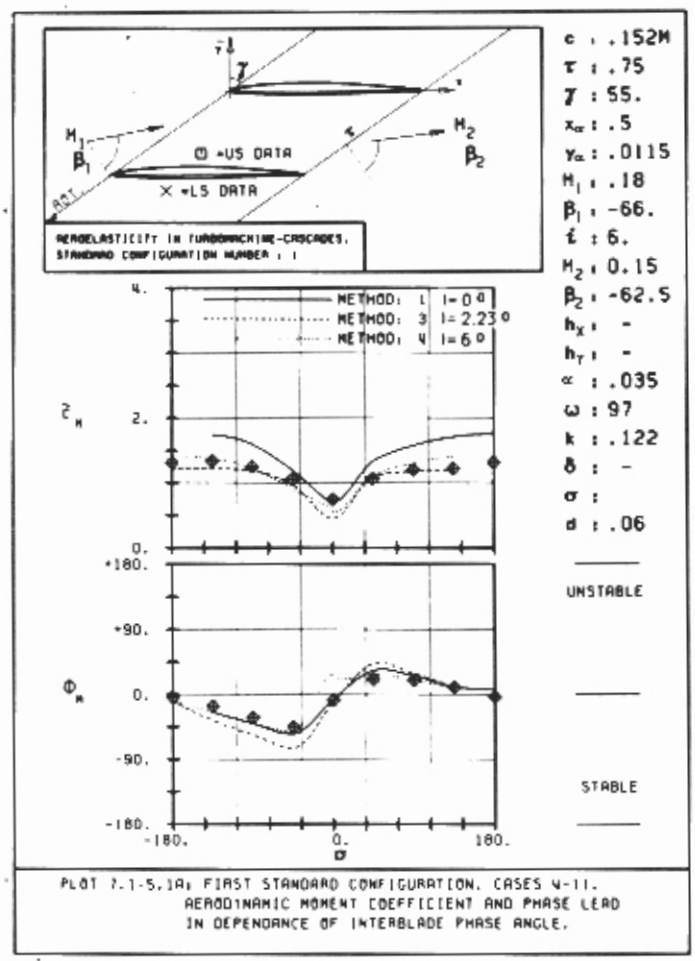


PLOT 7.1-5.1A: FIRST STANDARD CONFIGURATION, CASES 4-11.
AERODYNAMIC MOMENT COEFFICIENT AND PHASE LEAD
IN DEPENDANCE OF INTERBLADE PHASE ANGLE.

c)

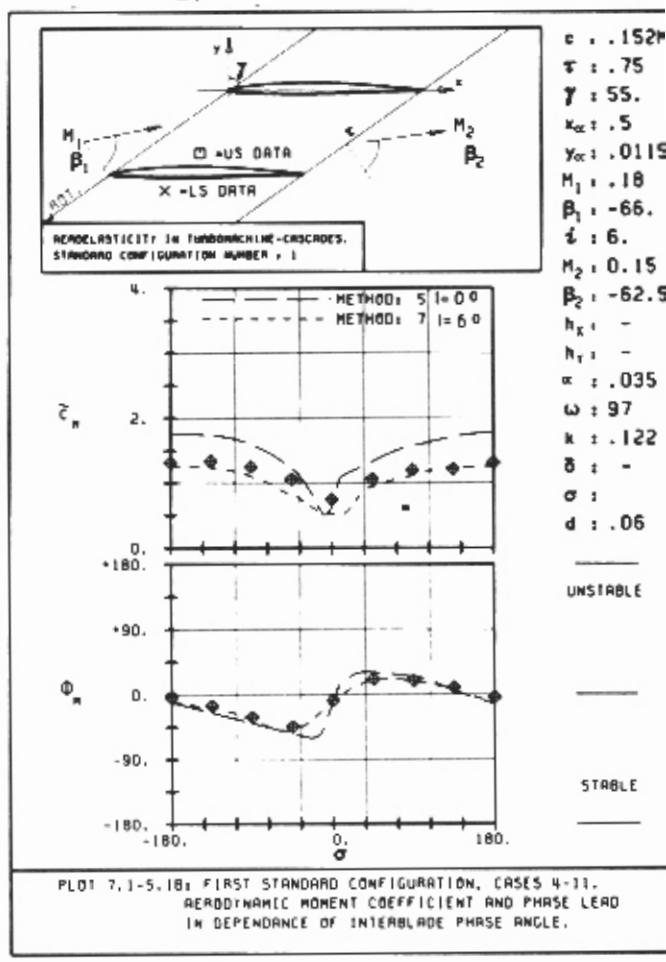


PLOT 7.1-5.1B: FIRST STANDARD CONFIGURATION, CASES 4-11.
AERODYNAMIC MOMENT COEFFICIENT AND PHASE LEAD
IN DEPENDANCE OF INTERBLADE PHASE ANGLE.

d)

Fig. 7.1-3. Aerodynamic damping and moment coefficients versus interblade phase angle

An interesting investigation was performed in [40], where the unsteady behavior of the cascade was calculated with Method 7 to investigate the effect of geometry and incidence on the aerodynamic damping for $i_{exp}=6°$. The trends found in Fig. 7.1-3 were confirmed, and it was noted that, although the best time-averaged agreement with the data was for $i_{theory}=2.23°$, the best unsteady agreement was for $i_{theory}=i_{exp}=6°$ (Fig. 7.1-5).

No explanation for this apparent contradiction can presently be given.

It can also be seen (Fig. 7.1-3) that the two methods which give the best approximation to the magnitude of the experimental data both use $i_{theory}=i_{exp}=6°$ (Methods 4 and 7).

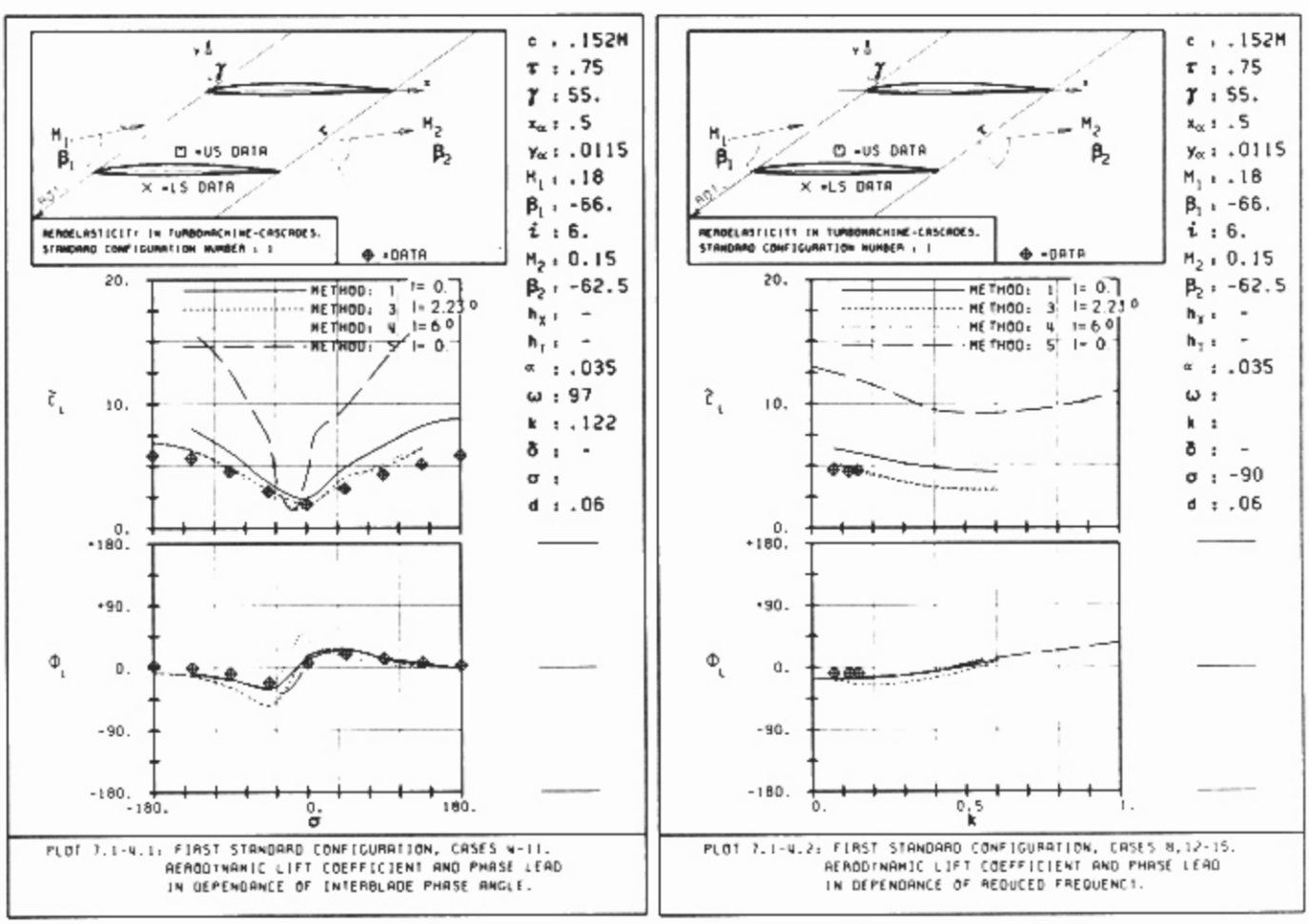


a) b)

Fig. 7.1-4. Aerodynamic lift coefficient versus interblade phase angle and reduced frequency, resp.

This indicates that the ambiguity in the steady-state incidence angle, as discussed earlier, also remains for the unsteady results. From Figures 7.1-3 and 7.1-5 it is concluded that the flat plate calculations (Methods 1 and 5 in Fig. 7.1-3 and Method 7 in Fig. 7.1-5) give a good qualitative approximation of the damping coefficient shape. The magnitude is however exaggerated.
This disagreement in magnitude is not dangerous from the flutter point of view as long as the blades are assumed to have zero mechanical damping. However, if a certain mechanical damping is admitted in the flutter design process, the results can be disastrous. Indeed, if a mechanical damping of $\Xi_{mech}=0.6$ is assumed in Fig. 7.1-3, the experiments and prediction models 4, 5 and 7 indicate a stable system (i.e. $\Xi_{aer} + \Xi_{mech}>0$) for all interblade phase angles, while the other models still predict flutter between $40°<\sigma<100°$.

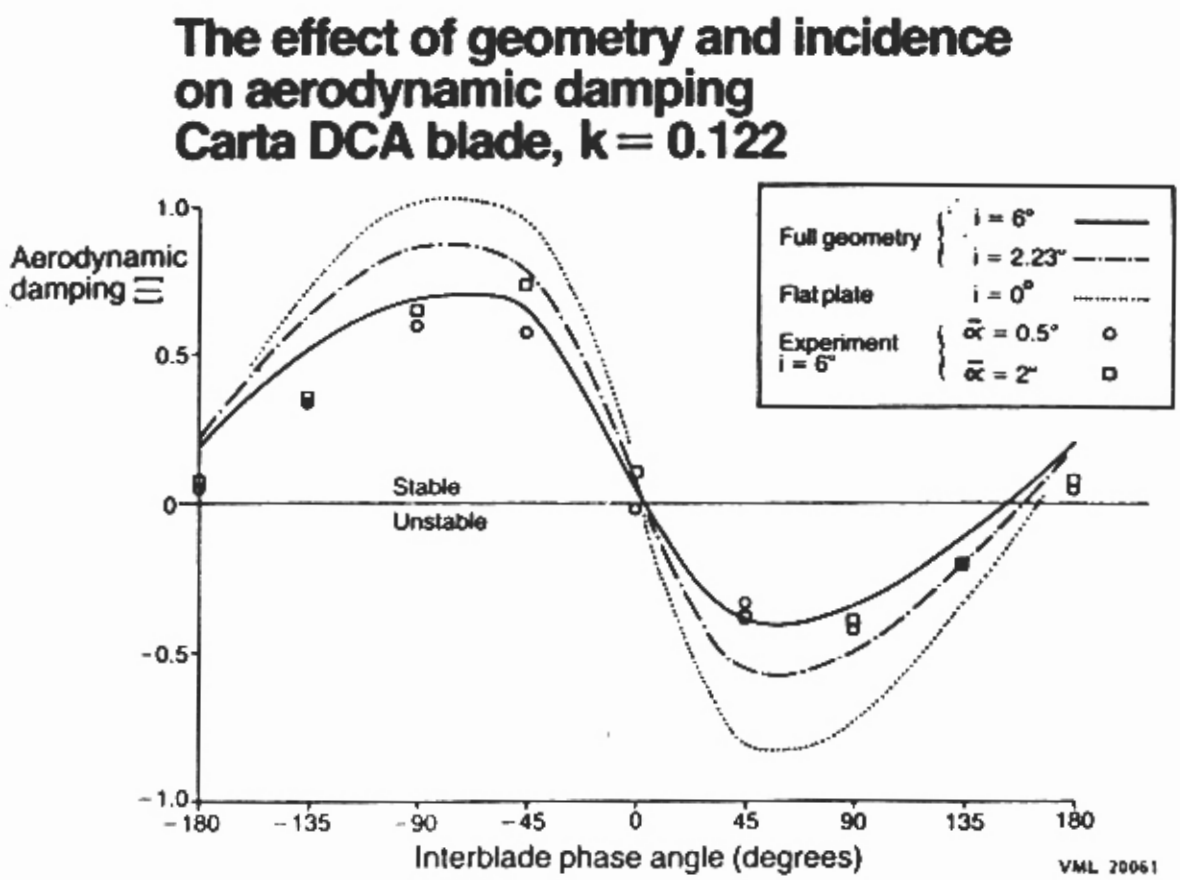


Fig. 7.1-5. Aerodynamic damping coefficient versus interblade phase angle (from / 40/, Fig. 8)

Blade Surface Pressure Differences

As the largest scatter in the aerodynamic damping coefficient was found at approximatively ± (45°-90°) interblade phase angles, the largest disagreement between the predicted and the experimental blade surface pressure distributions could be expected to exist in this region.
In general, the agreement in blade surface pressure difference coefficient is good (Fig. 7.1-6), with some exceptions. First of all, the good agreement in aerodynamic damping coefficient between the data and, for example, Method 3 which was found at ±180° interblade phase angle ($i_{exp}$=6°, Fig. 7.1-3) is confirmed by the pressure difference coefficient (Fig. 7.1-6a). Here, both the amplitude and phase lead are predicted very accurately. This is also the case for a flat plate theory, Method 1, for the phase angle, but some small disagreement is found in the amplitude.
At a -90° interblade phase angle, the agreement of Methods 1 (Flat Plate) and 3 with the data is still good as far as the amplitude is concerned (Fig.7.1-6b) This indicates that the disagreement in aerodynamic damping at this interblade phase angle (Fig. 7.1-3) probably comes from the differences in the pressure difference phase angle. However, this is not the case for the +45° interblade phase angle (Fig. 7.1-6c), although here the phase angle differences between the analyses and the data close to the trailing edge are very large (which does not influence the aerodynamic damping to a large extent as the pressure difference amplitudes are small here)[7]. It seems instead that disagreements in the amplitude of the pressure difference coefficient are mainly responsible for differences in the magnitude of the damping.
At a 0° interblade phase angle (which is close to the analytically determined acoustic resonance) discrepancies between the different analyses and the data are fairly large in the phase angle, although the trend is correctly predicted by most methods (Fig. 7.1-6d). The aerodynamic nevertheless damping has an identical value for most methods and the data (Fig. 7.1-3), which is clearly the case, as the amplitude of the pressure difference coefficent is smaller than at other interblade phase angles (compare for example Fig. 7.1-6c,d). Furthermore, in the part of the blade where the amplitude is large, i.e. close to the leading edge, the phase angle is almost zero for a 0° interblade phase angle, wherefore this part of the blade makes only a small contribution to the total aerodynamic damping.

7 This apperently large discrepancy is explained in next section

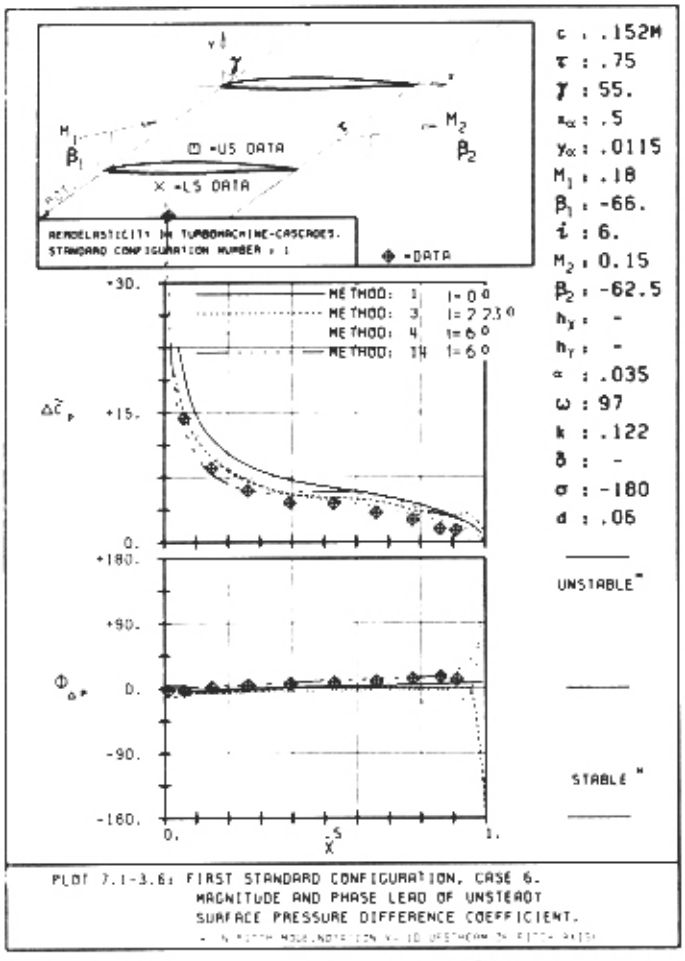


PLOT 7.1-3.6: FIRST STANDARD CONFIGURATION, CASE 6.
MAGNITUDE AND PHASE LEAD OF UNSTEADY
SURFACE PRESSURE DIFFERENCE COEFFICIENT.

a)

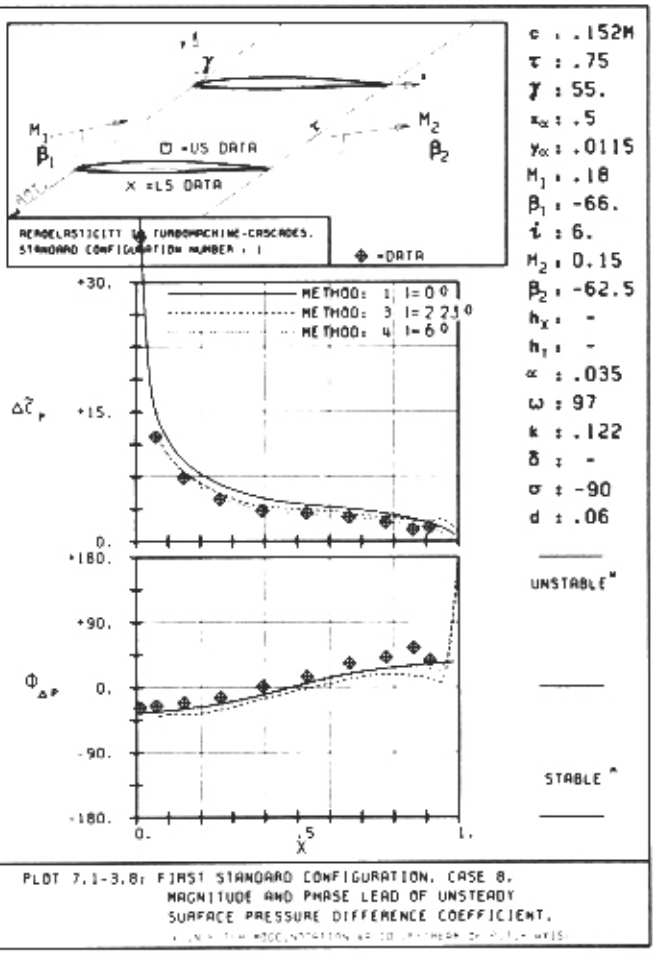


PLOT 7.1-3.8: FIRST STANDARD CONFIGURATION, CASE 8.
MAGNITUDE AND PHASE LEAD OF UNSTEADY
SURFACE PRESSURE DIFFERENCE COEFFICIENT.

b)

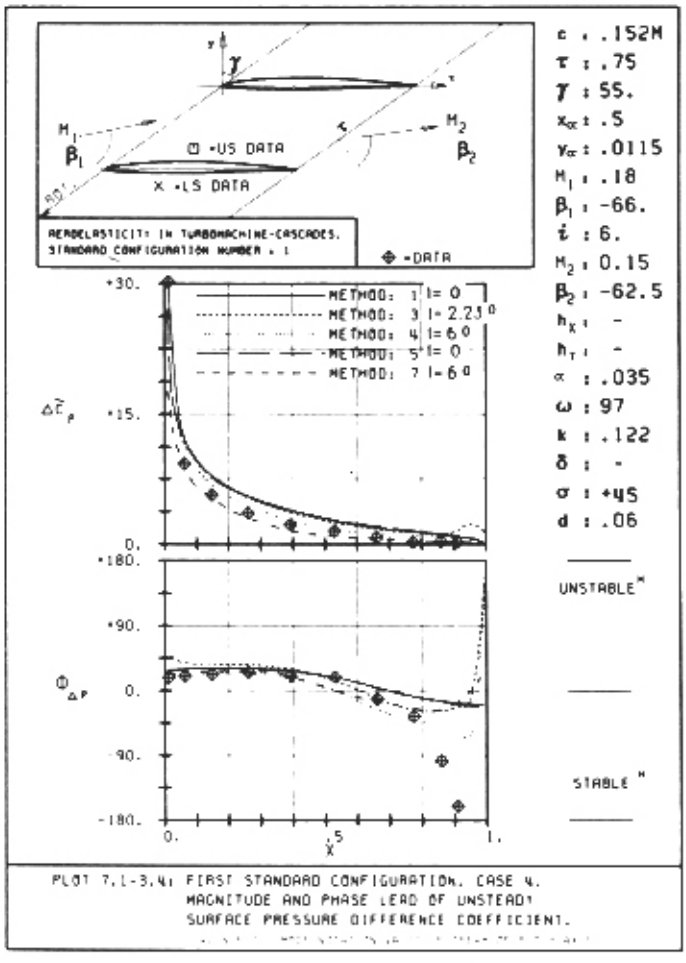


PLOT 7.1-3.4: FIRST STANDARD CONFIGURATION, CASE 4.
MAGNITUDE AND PHASE LEAD OF UNSTEADY
SURFACE PRESSURE DIFFERENCE COEFFICIENT.

c)

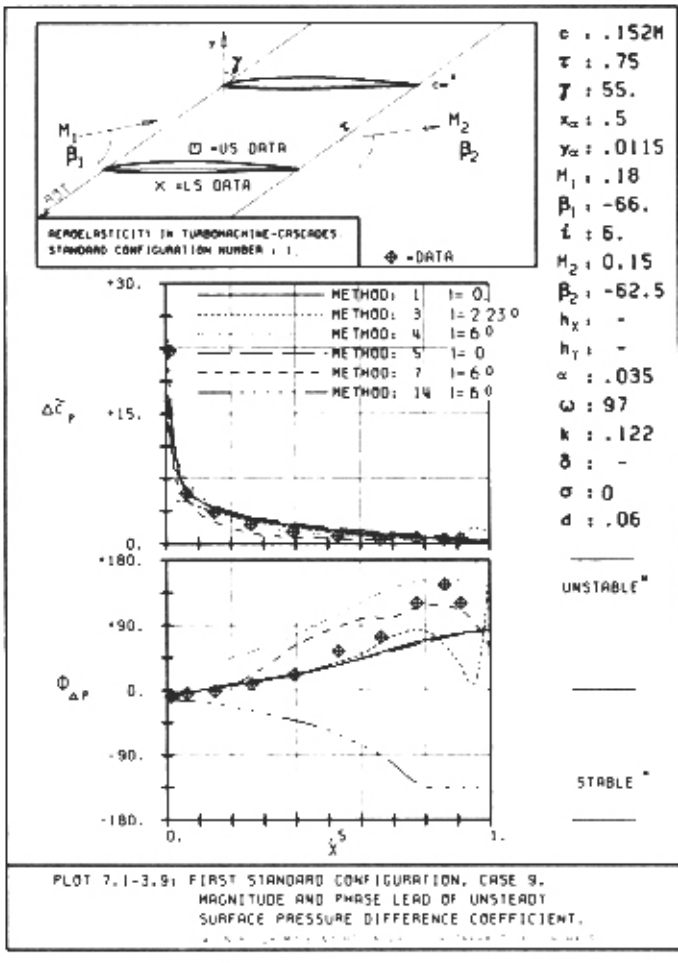


PLOT 7.1-3.9: FIRST STANDARD CONFIGURATION, CASE 9.
MAGNITUDE AND PHASE LEAD OF UNSTEADY
SURFACE PRESSURE DIFFERENCE COEFFICIENT.

d)

Fig. 7.1-6. Continued on next page

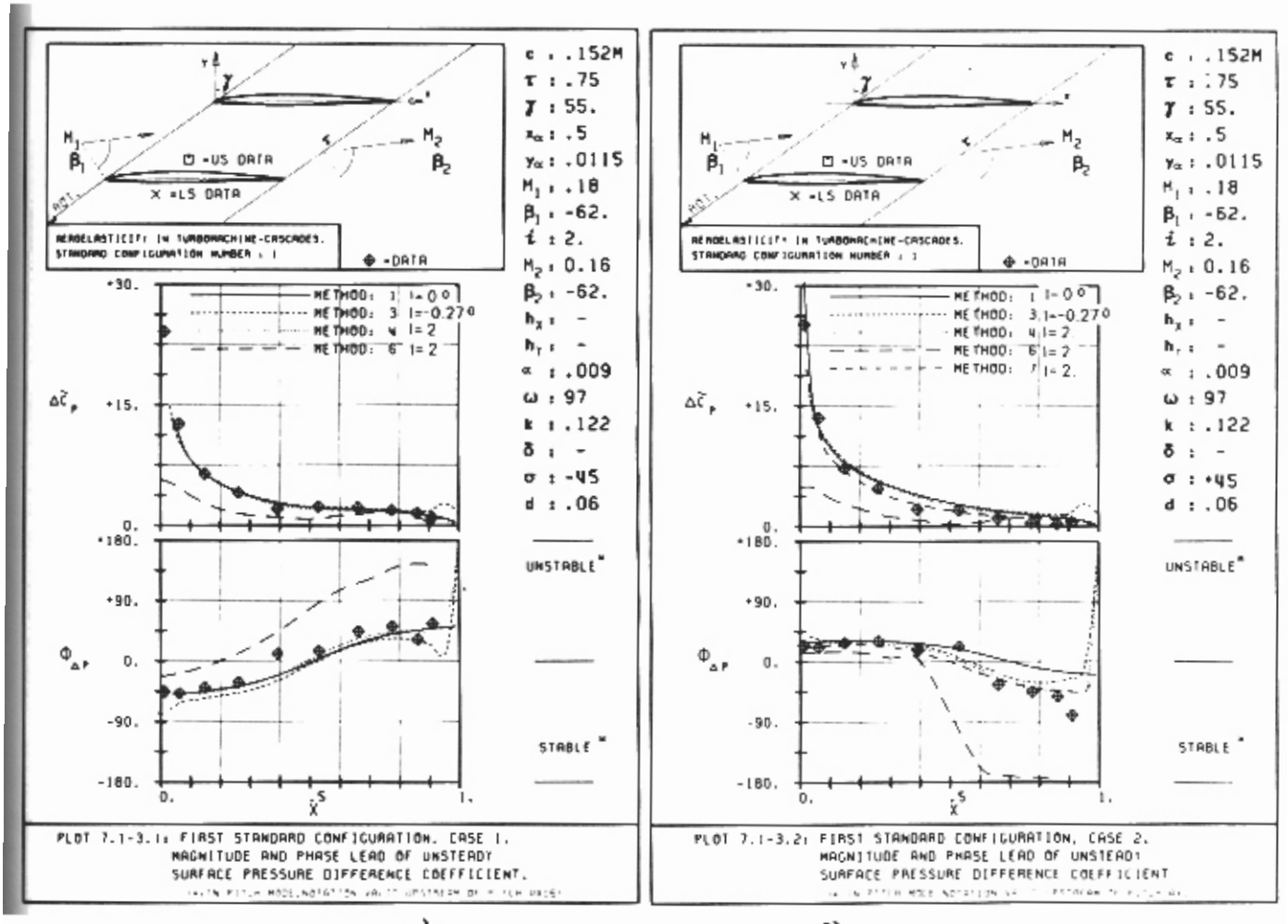


e) f)

**Fig. 7.1-6.** Unsteady blade surface pressure difference coefficient versus chord at different interblade phase angles

However, methods 6 and 14 show some larger discrepencies in the phase angle (Fig.7.1-6d,e,f).

Method 6 still predicts the correct trend, while method 14 shows a different distribution. The authors [55] give as a possible explanation for this phenomenon the time-dependent aspect of their method. It is not certain that the periodic solution has been obtained.

It is thus concluded that, in most cases, the theoretical and experimental results for the time-dependent blade surface pressure difference coefficient agree well, both in trend and magnitude.

Blade Surface Pressures on Upper and Lower Surfaces

If instead the time-dependent blade surface pressures on the pressure (lower) and suction (upper) surfaces are considered, some disagreement is noted.
In Figure 7.1-7 this information is plotted for the same aeroelastic test cases as in Fig. 7.1-6 (interblade phase angles = -180°, -90°, 0°, +45°).
From all diagrams it is concluded that the amplitudes of the lower and upper blade surface pressures are better predicted than the phase angles. It is interesting to note that the largest disagreements in the phase angle seem to be on the lower (= pressure) surface in the second half of the blade[8] . Presently, no explanation for this phenomenon has been put forward, apart from noting that on this part of the blade the pressure fluctuations are small (and thus the signal/noise-ratio), which automatically gives a larger inaccuracy in phase angle. Again, there are some discrepancies between Method 14 and the experimental data (Fig. 7.1-7b,h).
As for the pressure difference coefficient, the surface pressures show large disagreements, both between the different analyses and with the data, for a 0° interblade phase angle (Fig. 7.1-7f,g,h). Again, the good agreement for the aerodynamic damping in this range of interblade phase angles (Fig. 7.1-3) can be attributed only to the fact that the amplitudes are so small that discrepancies in phase angles are not noted.
The large disagreement (between the analyses and the experiment) in the phase angle of the pressure difference coefficient close to the trailing edge, for a +45° interblade phase angle (Fig. 7.1-6c) can now be explained on the basis of the pressure difference coefficient calculation. This can be seen by investigating the upper and lower blade surface pressures. Indeed, by comparing Figures 7.1-6c and 7.1-7d it is concluded that the disagreement is larger in the pressure difference coefficient than in the upper and lower pressures. The reason for this is probably to be found in the data reduction method. The pressure difference coefficient is calculated by passing via the real and imaginary parts of the complex pressure coefficients (section 4). In the specific case shown in Fig. 7.1-7d, the real parts of the complex pressure coefficient on the upper and lower surfaces are almost identical, which gives a small value of the real part of $\Delta\tilde{c}_p$, while the imaginary part has a larger value. Therefore the value of the phase angle, as calculated by eq. (10a), becomes uncertain.

8 This is confirmed also for other elastic test cases, see Appendix A5

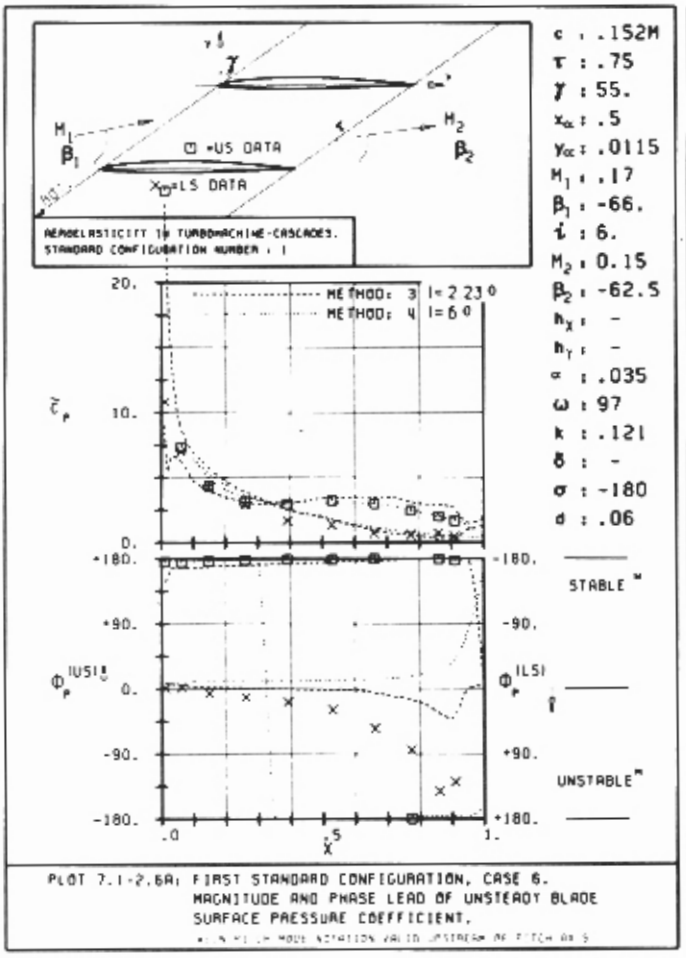


PLOT 7.1-2.6A: FIRST STANDARD CONFIGURATION, CASE 6.
MAGNITUDE AND PHASE LEAD OF UNSTEADY BLADE SURFACE PRESSURE COEFFICIENT.

a)

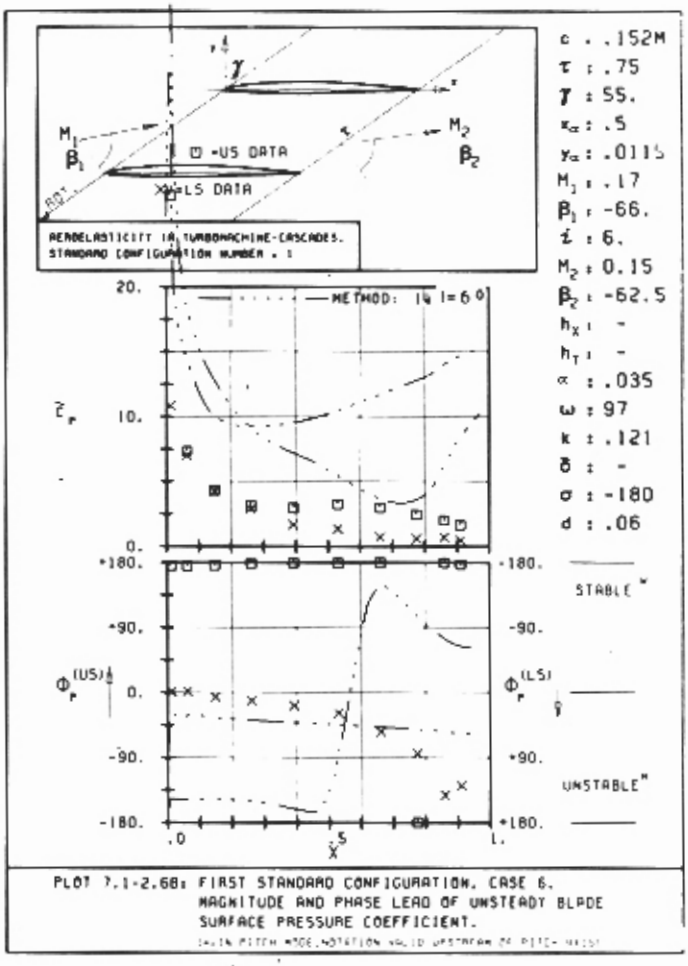


PLOT 7.1-2.6B: FIRST STANDARD CONFIGURATION, CASE 6.
MAGNITUDE AND PHASE LEAD OF UNSTEADY BLADE SURFACE PRESSURE COEFFICIENT.

b)

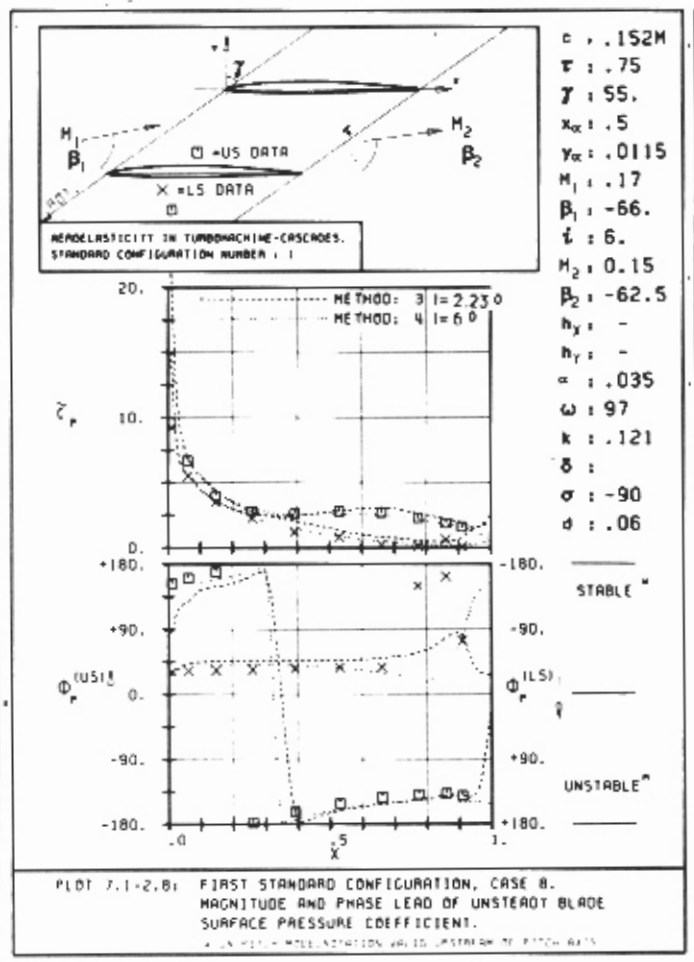


PLOT 7.1-2.8: FIRST STANDARD CONFIGURATION, CASE 8.
MAGNITUDE AND PHASE LEAD OF UNSTEADY BLADE SURFACE PRESSURE COEFFICIENT.

c)

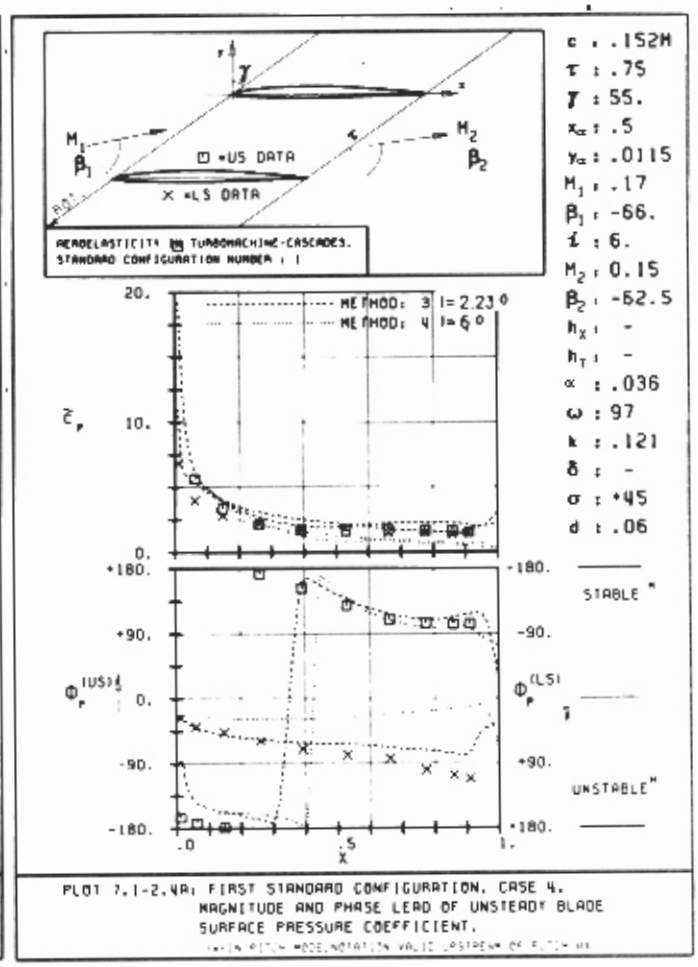


PLOT 7.1-2.4A: FIRST STANDARD CONFIGURATION, CASE 4.
MAGNITUDE AND PHASE LEAD OF UNSTEADY BLADE SURFACE PRESSURE COEFFICIENT.

d)

Fig. 7.1-7. Continued on next page

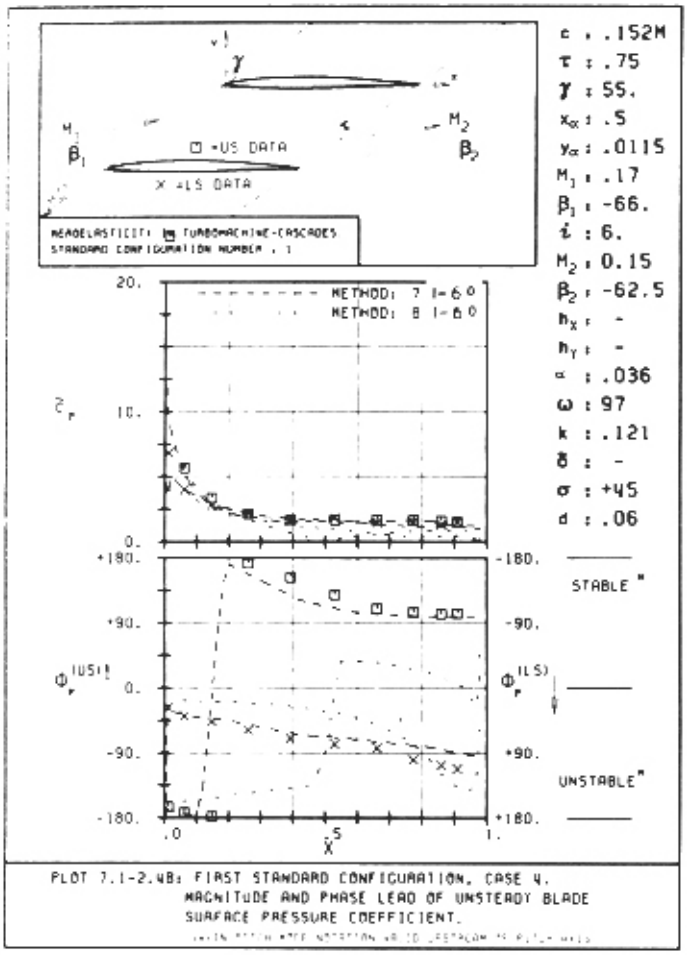


PLOT 7.1-2.9B: FIRST STANDARD CONFIGURATION, CASE 4. MAGNITUDE AND PHASE LEAD OF UNSTEADY BLADE SURFACE PRESSURE COEFFICIENT.

e)

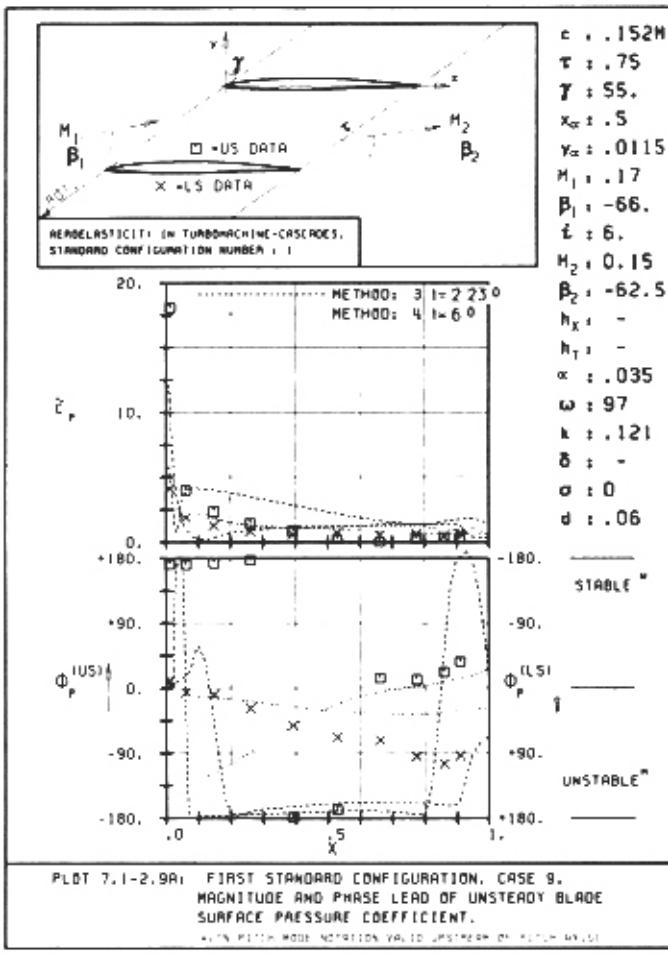


PLOT 7.1-2.9A: FIRST STANDARD CONFIGURATION, CASE 8. MAGNITUDE AND PHASE LEAD OF UNSTEADY BLADE SURFACE PRESSURE COEFFICIENT.

f)

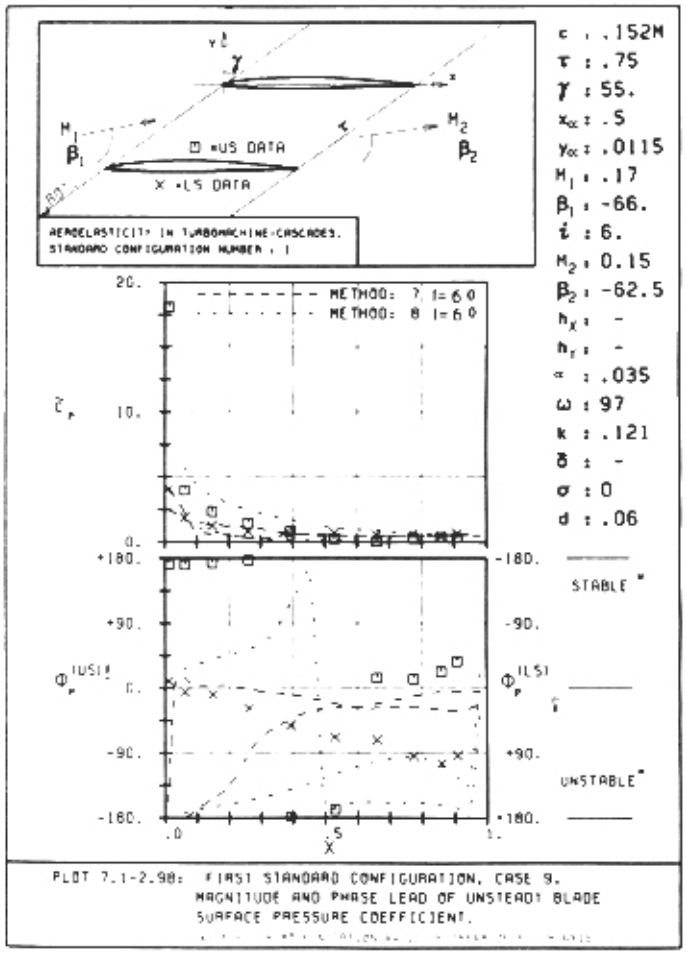


PLOT 7.1-2.9B: FIRST STANDARD CONFIGURATION, CASE 8. MAGNITUDE AND PHASE LEAD OF UNSTEADY BLADE SURFACE PRESSURE COEFFICIENT.

g)

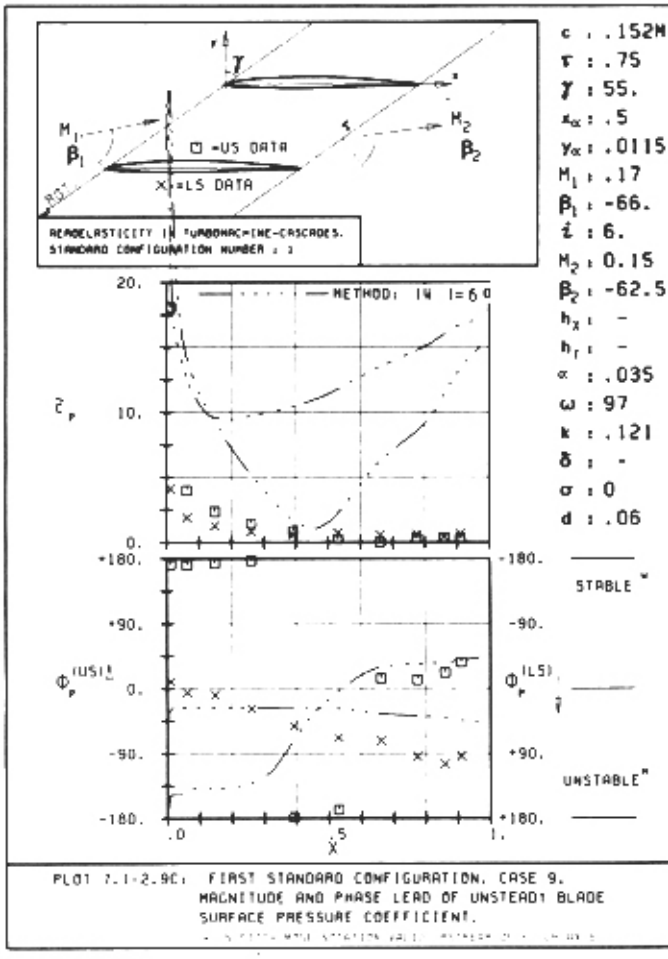


PLOT 7.1-2.9C: FIRST STANDARD CONFIGURATION, CASE 8. MAGNITUDE AND PHASE LEAD OF UNSTEADY BLADE SURFACE PRESSURE COEFFICIENT.

h)

**Fig. 7.1-7.** Continued on next page.

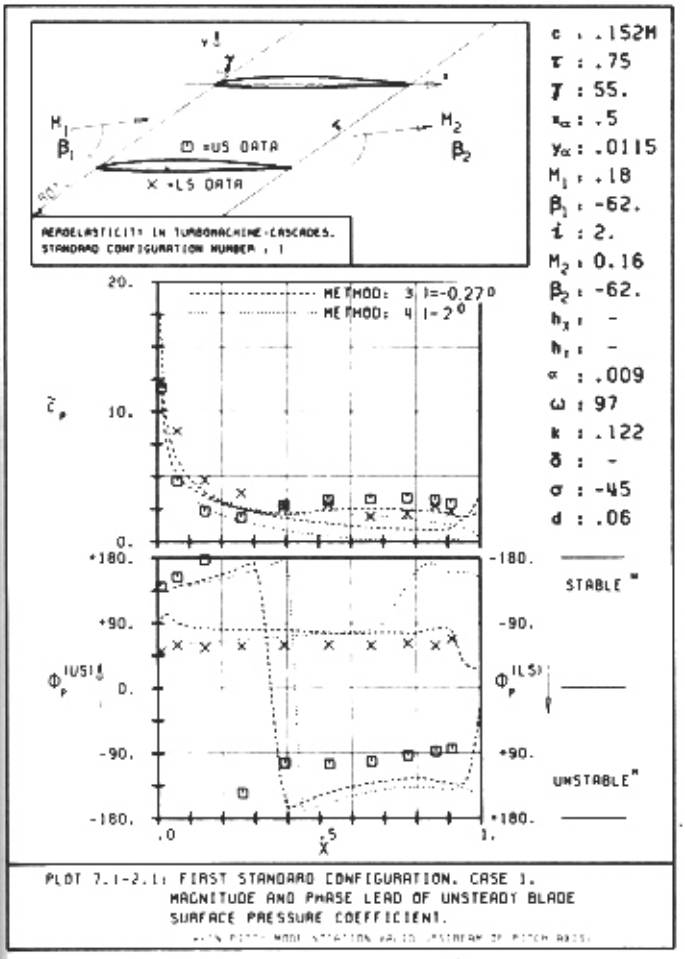


PLOT 7.1-2.1: FIRST STANDARD CONFIGURATION, CASE 1.
MAGNITUDE AND PHASE LEAD OF UNSTEADY BLADE SURFACE PRESSURE COEFFICIENT.

j)

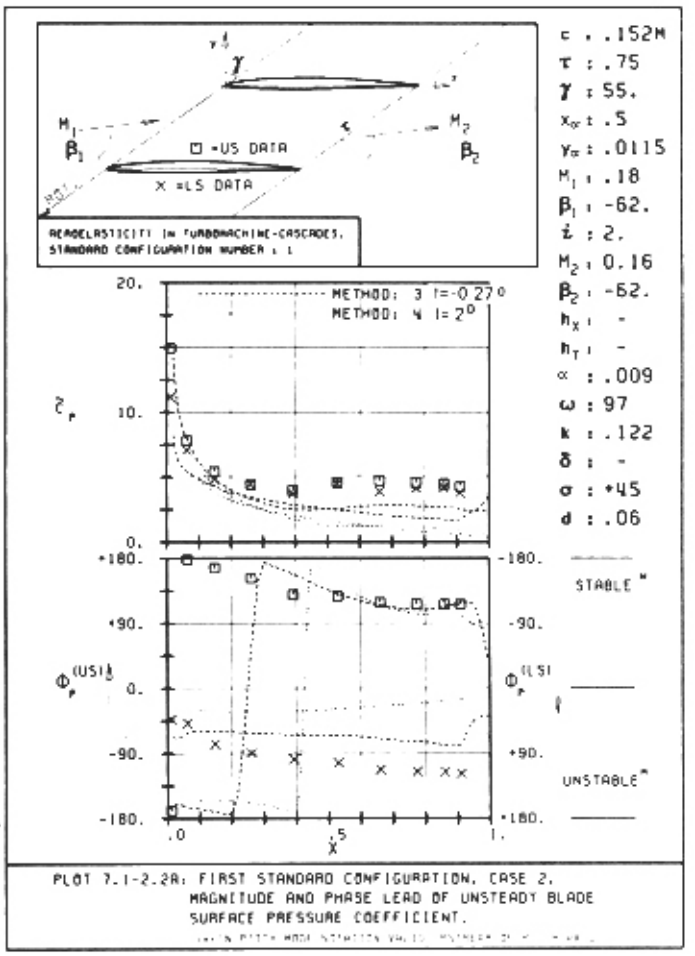


PLOT 7.1-2.2A: FIRST STANDARD CONFIGURATION, CASE 2.
MAGNITUDE AND PHASE LEAD OF UNSTEADY BLADE SURFACE PRESSURE COEFFICIENT.

k)

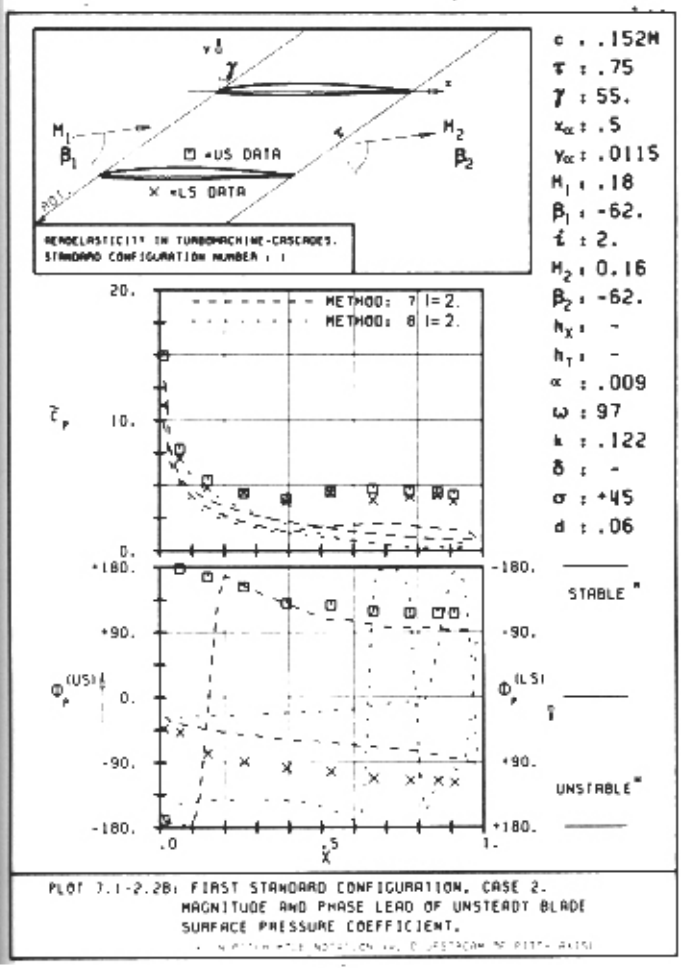


PLOT 7.1-2.2B: FIRST STANDARD CONFIGURATION, CASE 2.
MAGNITUDE AND PHASE LEAD OF UNSTEADY BLADE SURFACE PRESSURE COEFFICIENT.

**Fig. 7.1-7.** Unsteady blade surface pressure difference coefficient versus chord for different interblade phase angles

However, the same argument cannot be used to explain the differences in phase angle in Fig. 7.1-6b (which in any case is much smaller than the ones in Fig. 7.1-6d), as in this case the values of the real parts of the pressures on the lower and upper surfaces are further apart. (The difference in the imaginary part betweeen the lower and upper surfaces of the blade is of the same order of magnitude as the difference in the real part.)

In this context, the interesting investigation of different vibration amplitudes performed by Carta in [15] can also be discussed. In Fig. 7.1-5 (copied from ref. [40]), the experimentally determined aerodynamic damping coefficient is represented for 0.5° and 2° vibration amplitudes. A slight difference is found at a -45° interblade phase angle which, by investigating the surface pressures (Fig. 7.1-8a,b), can be attributed mainly to differences in the first 10% of the blade. Again some slight disagreement, this time between the two experiments, is found in the lower surface phase angles in the second half of the blade, where the amplitudes are small. However, the trend for both vibration amplitudes is identical.

For other cases, presented in [15], the pressure amplitudes in the leading edge region show smaller differences between 0.5° and 2° vibration amplitude than in Fig. 7.1-8. This is confirmed also in Fig. 7.1-5, as the experimental aerodynamic damping coefficient has almost the same value for both vibration amplitudes. But also for these interblade phase angles, differences appear in the phase angle of the lower surface pressure in the second half of the blade (see Appendix A5). A detailed investigation of the data in [15] indicates that these differences are probably due to run-to-run variations in the unsteady data, and not to nonlinear effects. This can be concluded from Fig. 7.1-9 and 7.1-10, where the values

$$\delta\tilde{c}_p = \tilde{c}_p{}^{\alpha=2} - \tilde{c}_p{}^{\alpha=0.5}$$

$$\delta\Phi_p = \Phi_p{}^{\alpha=2} - \Phi_p{}^{\alpha=0.5}$$

are shown for two incidence angles, i=2° and 6°, at 77% and 6% chordwise position respectively, for both the upper and lower surfaces, as a function of the interblade phase angle.

In these diagrams, it is seen that:

- The scatter in $\delta\Phi_p$ is larger on the lower than on the upper surface of the blade in the 77% chordwise position (Fig. 7.1-9a, b). A possible explanation for this is that the pressure amplitudes are smaller on the lower than on the upper surface of the blade. The accompaning smaller signal/noise ratio may influence the accuracy of the phase angles.

- The differences in $\delta\Phi_p$ are much smaller in the leading edge region (x=0.06, Fig. 7.1-10a,b) than in the trailing edge region (x=0.77, Fig. 7.1-9a,b). Again this can be explained by difficulties in determining accurately the phase angle by small pressure fluctuations.
- The scatter in $\delta\Phi_p$, both at the 6 and 77% chordwise position, is approximately the same for both incidence angles (i=2° and 6°), which indicates that the unsteady flow and the experimental accuracy are similar in both cases (Fig. 7.1-9a,b and 7.1-10a,b).
- The scatter in the absolute value of $\delta\tilde{c}_p$ is approximately the same for the lower and upper surfaces and for both incidence angles in the 77% chordwise position although, as mentioned earlier, the pressure amplitudes are in general smaller on the lower surface (Fig.7.1-9c,d).

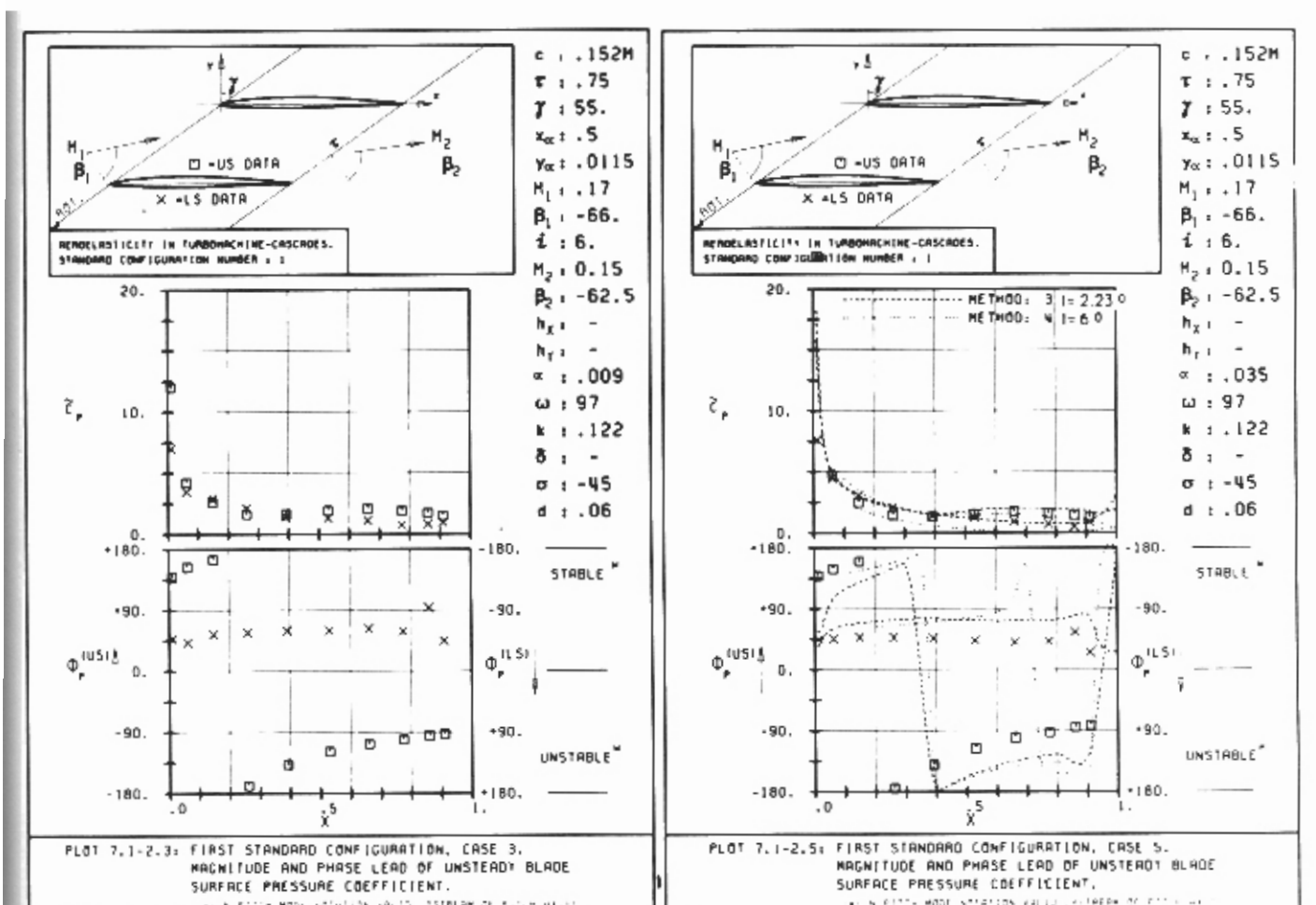


PLOT 7.1-2.3: FIRST STANDARD CONFIGURATION, CASE 3. MAGNITUDE AND PHASE LEAD OF UNSTEADY BLADE SURFACE PRESSURE COEFFICIENT.

PLOT 7.1-2.5: FIRST STANDARD CONFIGURATION, CASE 5. MAGNITUDE AND PHASE LEAD OF UNSTEADY BLADE SURFACE PRESSURE COEFFICIENT.

Fig. 7.1-8. Experimentally determined unsteady blade surface pressure distributions for two vibration amplitudes (α = 0.009 and 0.035 rad.)

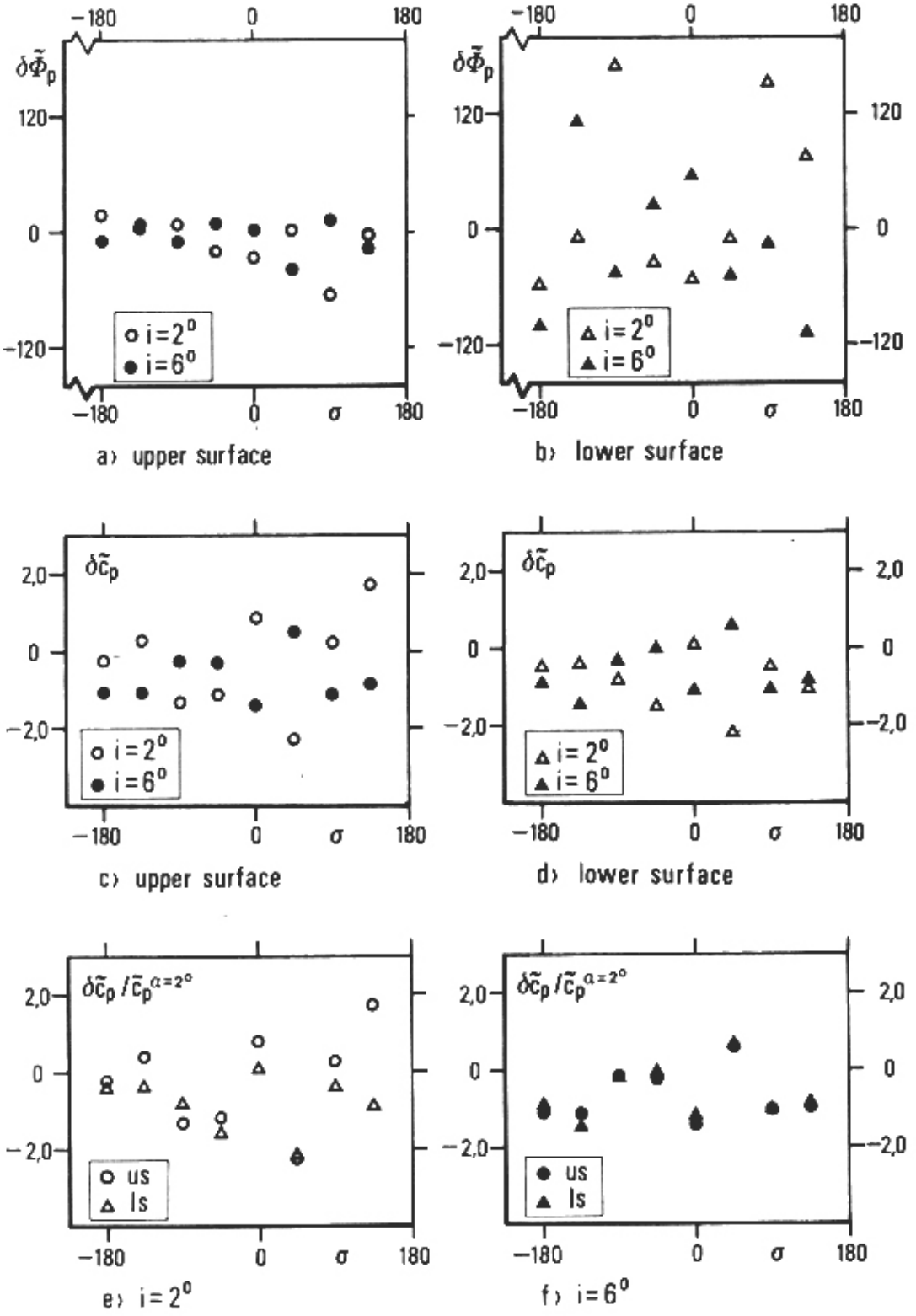


Fig. 7.1-9. Pressure coefficient and phase angle differences between 2° and 0.5° vibration amplitude on the lower and upper blade surfaces at 77.4 % chordwise location (i = 2°, 6° ; k = 0.12).

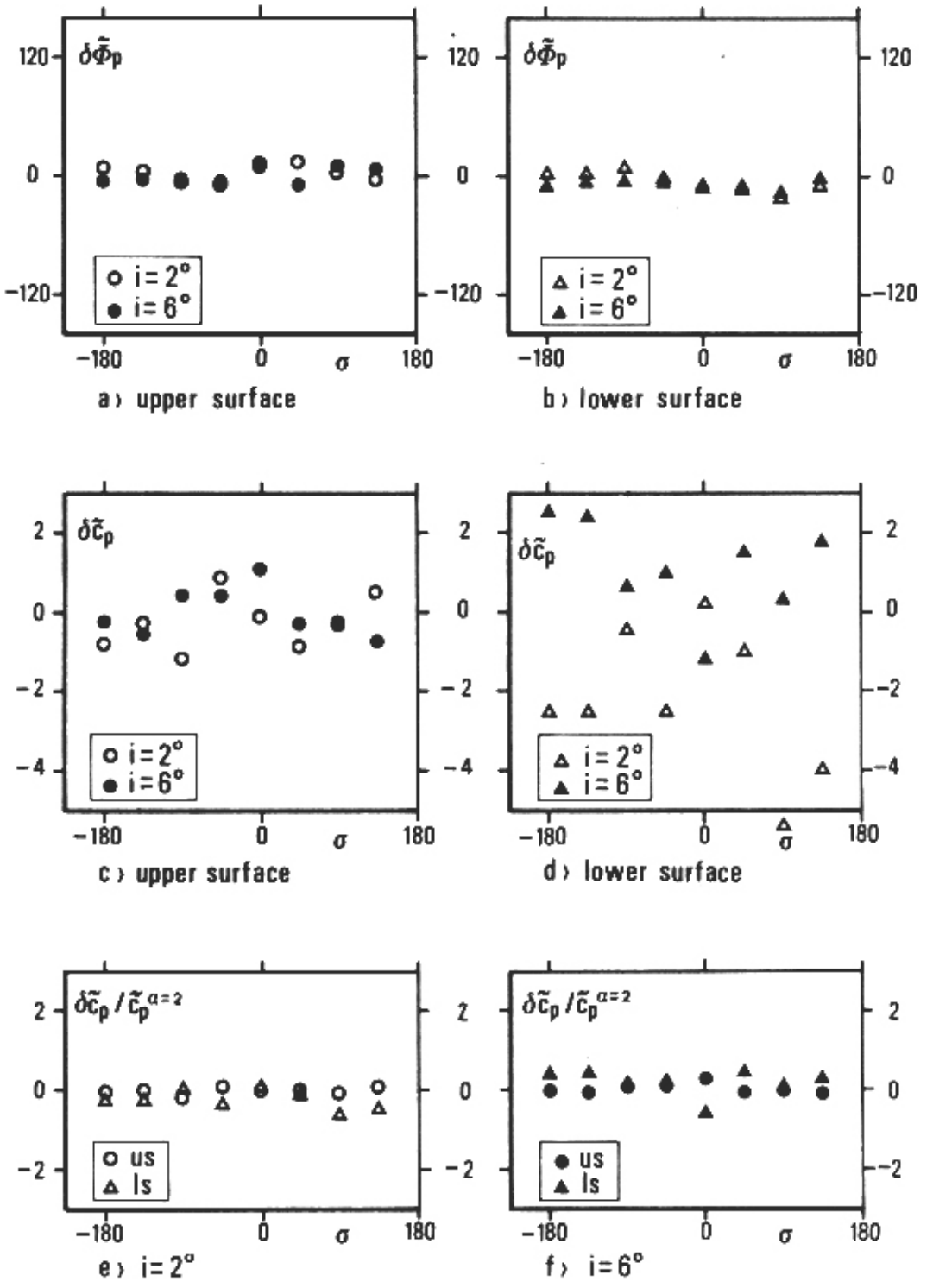


Fig. 7.1-10. Pressure coefficient and phase angle differences between 2° and 0.5° vibration amplitude on the lower and upper blade surfaces at 6 % chordwise location (i = 2°, 6° ; k = 0.12).

- In absolute values, the scatter in $\delta\tilde{c}_p$ is larger for the 6% than the 77% chordwise position (Fig. 7.1-9c,d and 7.1-10c,d). However, in relative values ($\delta\tilde{c}_p/\tilde{c}_p^{\alpha=2°}$) there is much less scatter close to the leading edge, as here the pressure amplitudes are higher (Fig. 7.1-9e, 7.1-10e).
- The differences in $\delta\tilde{c}_p$ seem to be independent of the steady incidence angle.

From Figures 7.1-9 and 7.1-10 it can thus be concluded that a possible explanation for the disagreement between the predicted and experimental phase angles in the after part of the lower surface of the blade is run-to-run variations in the data.

## Conclusions for the First Standard Configuration

From the controlled excitation work in traveling wave mode (i.e. constant interblade phase angle between all blades) on a 6% thick compressor cascade, with 10° camber in the low subsonic flow region, it can be concluded that:

- It is today possible to predict accurately the aeroelastic behavior of a thin, low cambered compressor cascade oscillating in traveling wave mode in low subsonic two-dimensional flow.
- The good agreement between the unsteady experimental data and predicted results mutually validates both approaches. Where disagreements are found, it is not possible a priori to exclude either theoretical or experimental inaccuracies.
- For this specific cascade, the predicted time-averaged results agree better with the data if the theoretical incidence is slightly modified (Fig. 7.1-2). However, the agreement between the time-dependent predictions and data is better if the experimentally determined incidence angle is used for the analyses. No explanation for this apparent contradiction has yet been found (Fig.7.1-5).

Conclusions for aerodynamic damping:

- The theoretical models accurately predict the stability limits for the cascade, using the assumption of zero mechanical damping (Fig. 7.1-3). The shape of both the theoretical and experimental damping curves is identical, but the magnitude shows disagreement. This would be dangerous if a non-zero mechanical damping is assumed in a design phase, as the different prediction models would then give different stability limits.
- The stability limits of the cascade (with zero mechanical damping assumed) is predicted just as well with flat plate theories as with other models (Fig. 7.1-3). Discrepancies are however present in the magnitude of the aerodynamic damping coefficient. For conservative stability analyses (zero mechanical damping), flat plate theories thus seems to be sufficient for cascades of the kind used here.
- Neglecting the blade geometry (i.e. using a flat plate model) apparently has an effect of the same order of magnitude on the aerodynamic damping as that of neglecting the incidence angle (using 0° incidence).

Conclusions for the unsteady blade surface pressure difference coefficient:

- Both the flat plate models and the ones with the true geometry agree well with the experimental data, as far as the unsteady blade surface pressure difference coefficient is concerned.
- The $\Delta\tilde{C}_p$ amplitude trend is correctly predicted with all methods. The magnitude is slightly exaggerated with some of them (especially the flat plate models).
- In most cases the phase angle $\Phi_{\Delta p}$ of the unsteady blade surface pressure difference coefficient is predicted well. Some disagreements can probably be explained by run-to-run variations in the data and by the data reduction procedure for calculating $\Delta\tilde{C}_p$ and $\Phi_{\Delta p}$.
- The small disagreements in aerodynamic damping between theories and experiment (Fig. 7.1-3, 5) can sometimes be traced to dissimilarities in the amplitude of the blade surface pressure difference coefficients, and sometimes to the phase angles (Fig. 7.1-6), both for the experiments and the analyses.
- A large part of the aerodynamic damping comes from the leading edge region. For an accurate experimental evaluation of this parameter it is important to measure the unsteady response close to the leading edge (which was done in the experimental work serving as base for this standard configuration [15]).

Conclusions for the unsteady blade surface pressures:

- The local unsteady blade surface pressure coefficient on the upper and lower surfaces is also predicted well. The amplitude shows a particularly good agreement between the experiment and the separate analyses.
- The local phase angle ($\Phi_p^{(us)}$, $\Phi_p^{(ls)}$) trend is captured well. In some cases the magnitude, especially for small pressure amplitudes (i.e. low signal/noise ratio which might indicate data inaccuracies), shows some slight disagreement between the experiment and the analyses (Fig. 7.1-7).
- The largest disagreement between the experiment and the separate analyses is found at a 0° interblade phase angle (Fig. 7.1-7f,g,h). This behavior can perhaps be explained by the small pressure amplitudes in the experiments for this interblade phase angle. The analytically determined acoustic resonances are also close to a 0° interblade phase angle, which might influence the theoretical results.

## 7.2 Second Standard Configuration

### Definition

This incompressible two-dimensional cascade configuration has been measured in a water cascade tunnel at the University of Tokyo. The results have been submitted by kind permission of H. Tanaka [19-20].
The cascade consists of eleven vibrating and six stationary double circular arc profiles. Each of the blades has a chord of c=0.050 m and a span of 0.100 m, with a camber angle of 16° and a gap-to-chord ratio of 1.00. The water velocity during the tests was $v_1$=2.4 m/s, with the Reynolds number at Re=1.2* $10^5$. The eleven vibrating blades oscillate in pitch, with an amplitude of 0.059 rad (3.4°) and a frequency between 1.3 and 13Hz. Thus, the reduced frequency lies in the range 0.1 to1.0.
The cascade geometry is given in Figure 7.2-1 and the profile coordinates in Table 7.2-1.
Experiments have been performed with incidence ranging from attached to partly-separated and fully-separated flow. Further, the stagger angle as well as the interblade phase angle and pivot axis have been varied systematically.
The experimental data indicate the unsteady lift and moment coefficients (amplitudes together with the corresponding phase lead angles). These coefficients are computed from strain gauge measurements and no time-dependent or time-averaged pressures are measured on the blade surfaces.

Aeroelastic Test Cases

From the large amount of data obtained during the experiments, and from the sample presented in [4, 20] 8 aeroelastic test cases have been proposed (Table 7.2-2).
All 8 correspond to the same steady-state configuration (stagger angle = 30°, inlet flow angle $\beta_1$=-30°, $M_1$=0.), and the interblade phase angle is varied.

## Low Subsonic Compressor Profiles.

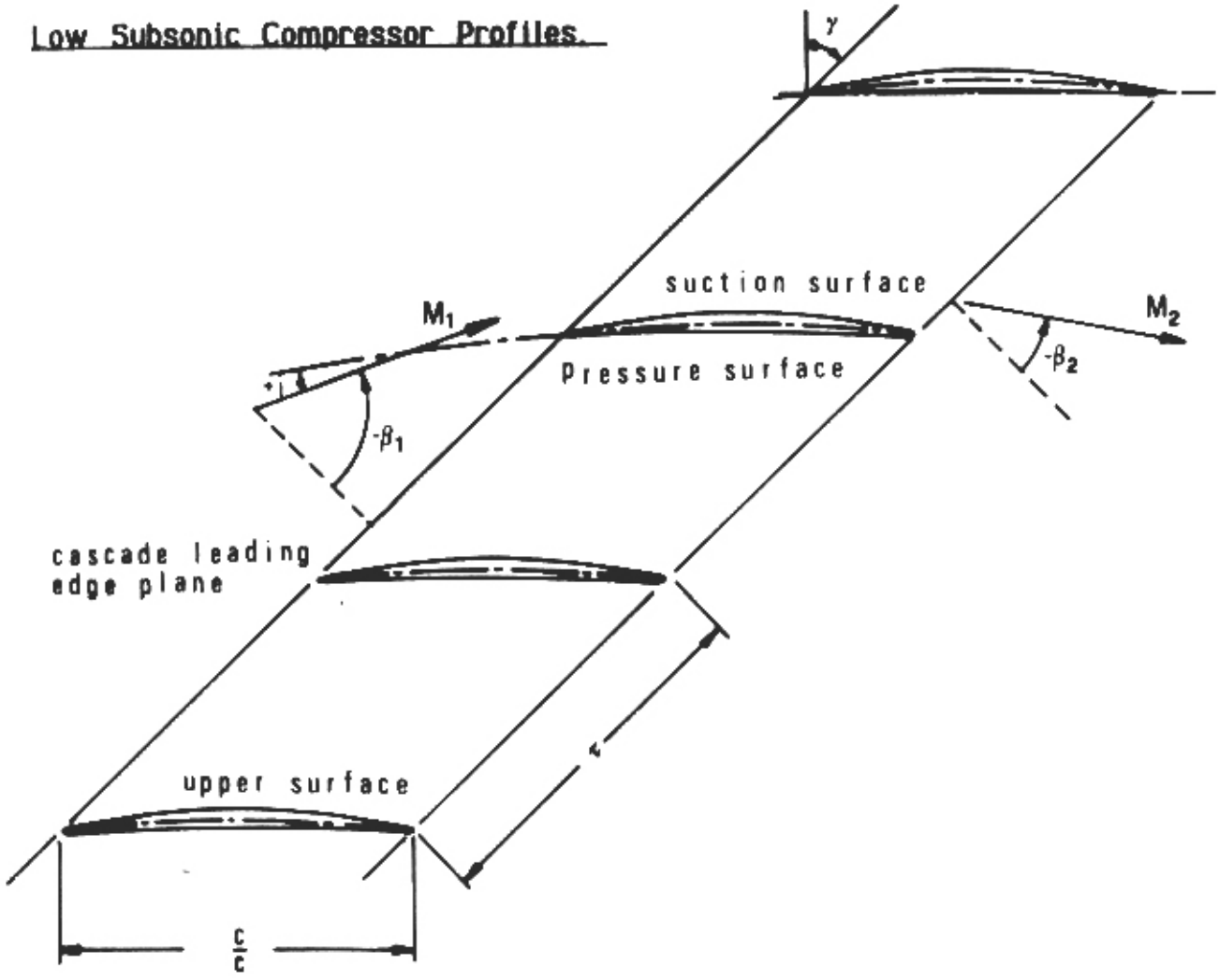


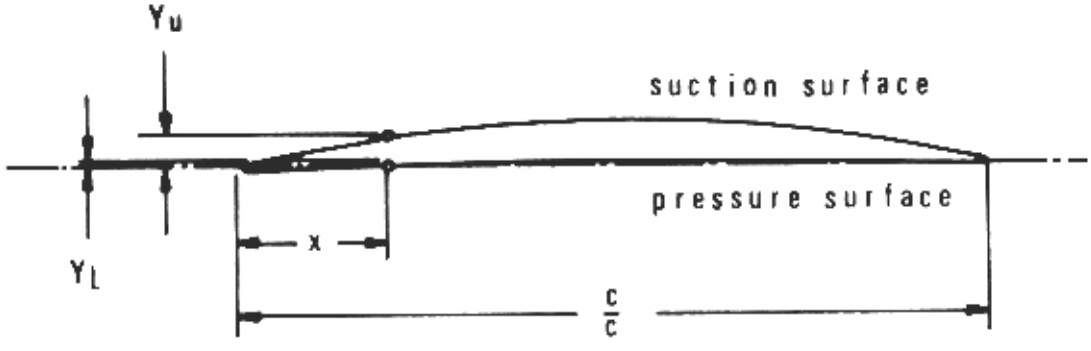


Maximum thickness at x = 0.5
Vibration in pitch around $(x_\alpha, y_\alpha)$ = (0.5,0.0362)
d = (thickness/chord) = 0.0524
α = 3.4° (=0.06 rad)
c = 0.050 m
τ = 1.00
k = 0.4
span = 0.100 m
Working fluid: Air

| | |
|---|---|
| $\beta_1$ | = -30° |
| camber | = 16.8° |
| $\gamma$ | = 30° |
| $\sigma$ | = variable |

Fig. 7.2-1. Second standard configuration: Cascade geometry

| Double Circular Arc Blade<br>c=0.050 m (1.968 in.) | | |
|---|---|---|
| | Suction surface<br>(upper surface) | Pressure surface<br>(lower surface) |
| x (%) | y (%) | y (%) |
| 0 | 0 | 0 |
| 5 | 1.644 | -0.404 |
| 10 | 2.637 | -0.127 |
| 15 | 3.509 | 0.115 |
| 20 | 4.262 | 0.326 |
| 25 | 4.897 | 0.505 |
| 30 | 5.416 | 0.650 |
| 35 | 5.818 | 0.764 |
| 40 | 6.105 | 0.845 |
| 45 | 6.272 | 0.893 |
| 50 | 6.334 | 0.910 |
| 55 | 6.272 | 0.893 |
| 60 | 6.105 | 0.845 |
| 65 | 5.818 | 0.764 |
| 70 | 5.416 | 0.650 |
| 75 | 4.897 | 0.505 |
| 80 | 4.262 | 0.326 |
| 85 | 3.509 | 0.115 |
| 90 | 2.637 | -0.127 |
| 95 | 1.644 | -0.404 |
| 100 | 0 | 0 |

| L.E. and T.E. RADIUS | | RADIUS CENTER COORDINATES |
|---|---|---|
| L.E. | RADIUS/c = 0.666 (%) | x = 0.666 (%), y = 0 (%) |
| T.E. | RADIUS/c = 0.666 (%) | x = 0.993 (%), y = 0 (%) |

**Table 7.2-1. Second standard configuration: Dimensionless airfoil coordinates.**

Discussion of Time-Dependent Results

For the moment only one method (Method 1) has been applied to this standard configuration. The reason is the resemblance to the first standard configuration, in which the time-averaged and time-dependent pressures were also measured on the blades.

No detailed comparison between the experimental data and the theoretical results can therefore be made presently. However, Fig. 7.2-2 gives an indication of the expected results.

Here, the predicted blade surface pressure difference coefficient ($\Delta\tilde{c}_p$) is presented for two phase angles ($\sigma$=-135°, 0°, Fif. 7.2-2a,b) together with the aerodynamic moment ($\tilde{c}_m$) and damping coefficient ($\Xi$) versus the interblade phase angle (Fig. 7.2-2c,d).

It is concluded (Fig. 7.2-2c,d) that the same trend exists for the experimental data and the results predicted with the flat plate analyses (Method 1).

| Aeroelastic Test Case No | Time-Averaged Parameters $v_1$ (m/s) | $\gamma$ (°) | $\beta_1$ (°) | Time-Dependent Parameters f (Hz) | k (-) | $\alpha$ (rad) | $\sigma$ (°) |
|---|---|---|---|---|---|---|---|
| 1 | 2.4 | 30.0 | - 30 | 6.1 | 0.4 | 0.059 | - 135 |
| 2 | " | " | " | " | " | " | - 90 |
| 3 | " | " | " | " | " | " | - 45 |
| 4 | " | " | " | " | " | " | 0 |
| 5 | " | " | " | " | " | " | + 45 |
| 6 | " | " | " | " | " | " | + 90 |
| 7 | " | " | " | " | " | " | + 135 |
| 8 | " | " | " | " | " | " | + 180 |

**Table 7.2-2** Second standard configuration.
8 recommended aerolastic test cases

However, judging from the theory, some scatter seems to be present in the experimentally determined phase angle $\Phi_m$, which can most clearly be seen in the aerodynamic damping coefficient (Fig. 7.2-2d). The trend for the amplitude of the moment coefficient shows a better agreement (Fig. 7.2-2c) although the flat plate theory predicts slightly higher values than the measured ones. This agrees with the results from the first standard configuration (compare Fig. 7.1-3b and Fig. 7.2-2c).

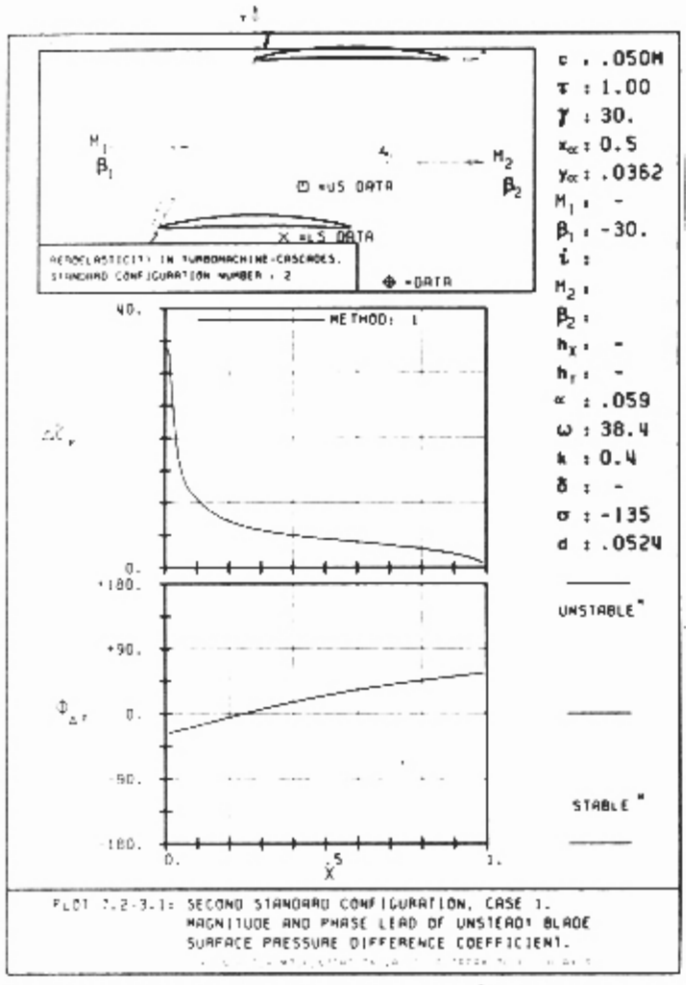


PLOT 7.2-3.1: SECOND STANDARD CONFIGURATION, CASE 1.
MAGNITUDE AND PHASE LEAD OF UNSTEADY BLADE
SURFACE PRESSURE DIFFERENCE COEFFICIENT.

a)

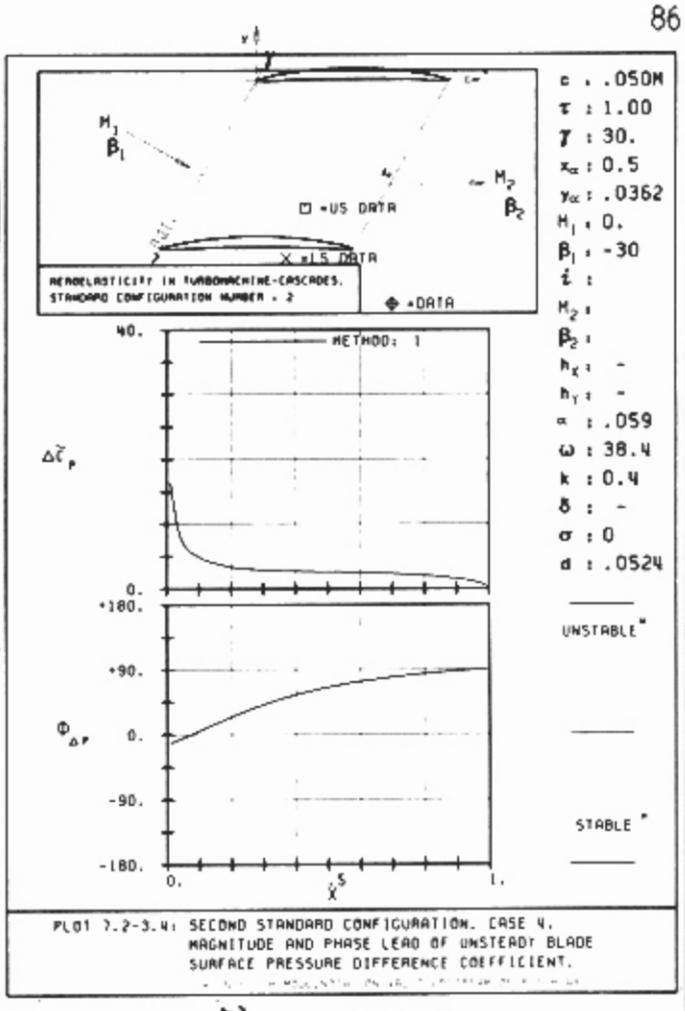


PLOT 7.2-3.4: SECOND STANDARD CONFIGURATION, CASE 4.
MAGNITUDE AND PHASE LEAD OF UNSTEADY BLADE
SURFACE PRESSURE DIFFERENCE COEFFICIENT.

b)

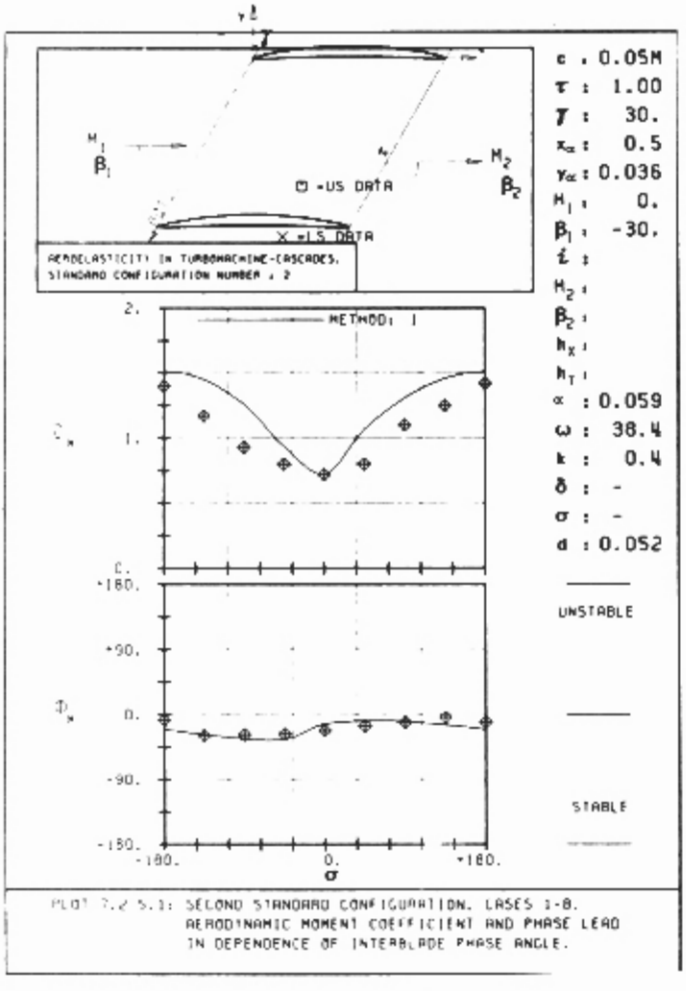


PLOT 7.2-5.1: SECOND STANDARD CONFIGURATION, CASES 1-8.
AERODYNAMIC MOMENT COEFFICIENT AND PHASE LEAD
IN DEPENDENCE OF INTERBLADE PHASE ANGLE.

c)

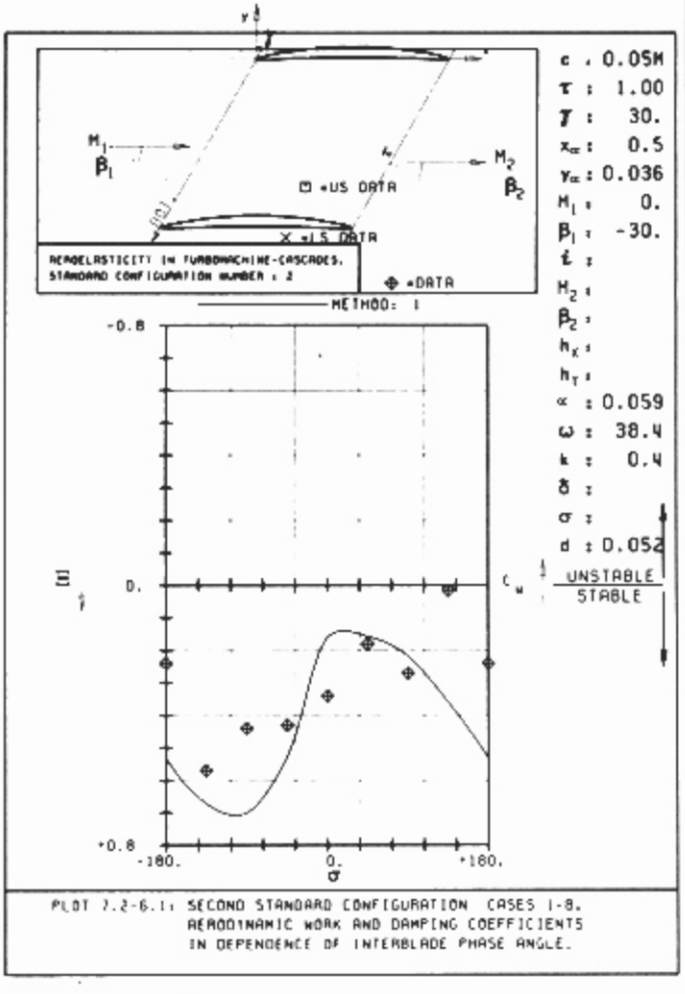


PLOT 7.2-6.1: SECOND STANDARD CONFIGURATION CASES 1-8.
AERODYNAMIC WORK AND DAMPING COEFFICIENTS
IN DEPENDENCE OF INTERBLADE PHASE ANGLE.

d)

Fig. 7.2-2. Second standard configuration. Blade surface pressure difference, moment and damping coefficients

## 7.3 Third Standard Configuration

### Definition

This quasi three-dimensional transonic turbine configuration is being tested, in freon, in the annular test facility at the Tokyo National Aerospace Laboratory. The experiments are included here by kind permission of H. Kobayashi.

This configuration, standard configuration N°3, is used with outlet conditions ranging from subsonic to supersonic flow velocities.

The cascade configuration consists of 16 vibrating cambered (60.8°) prismatic turbine blades. Each profile has a chord of c=0.072 m, with a span of 0.025 m and a maximum thickness-to-chord ratio of 0.124. The stagger angle for the results presented here is 45.7° and the pitch-to-chord ratio is

0.763 (hub)
0.804 (mid-span)
0.873 (tip)

The hub-tip ratio in the test facility is 0.844.

The profiles are oscillated in pitching mode, around the pivot axis at (0.195, -0.1097).

The cascade geometry is given in Figure 7.3-1 and the profile coordinates in Table 7.3-1.

The working fluid is freon gas, with the specific heat ratio = 1.137 (Freon-11, $CFCl_3$).

Experiments are performed with a variable expansion ratio ($p_2/p_{w1}$, $M_2$), oscillation frequency and interblade phase angle. All experiments are performed with constant spanwise upstream flow angle and flow velocity.

The time-dependent instrumentation includes pressure tappings on a blade (midspan) and strain gauges. The unsteady moment coefficient is determined with torsional cross spring bars.

## High Subsonic/Transonic Turbine Profiles.

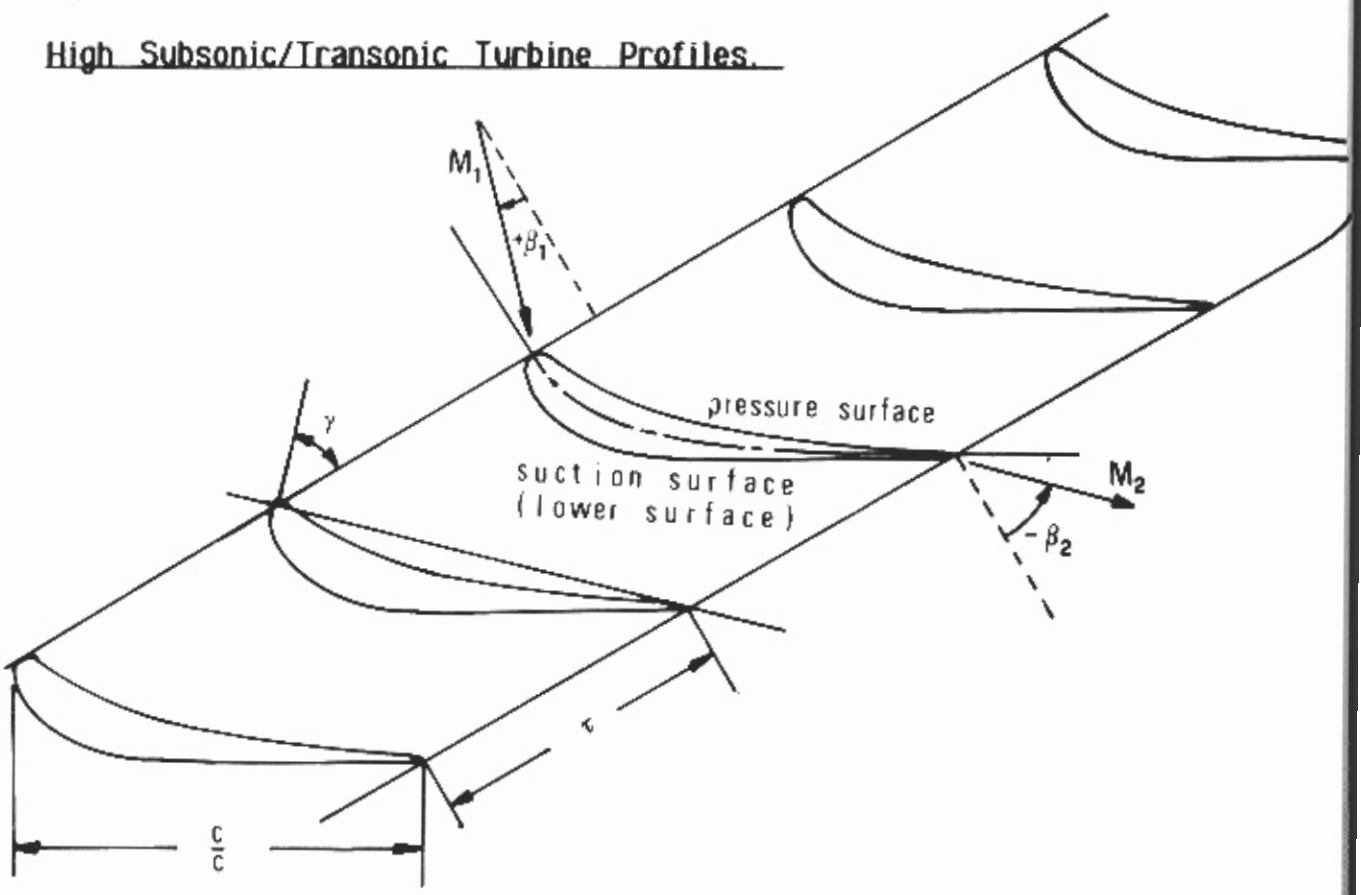


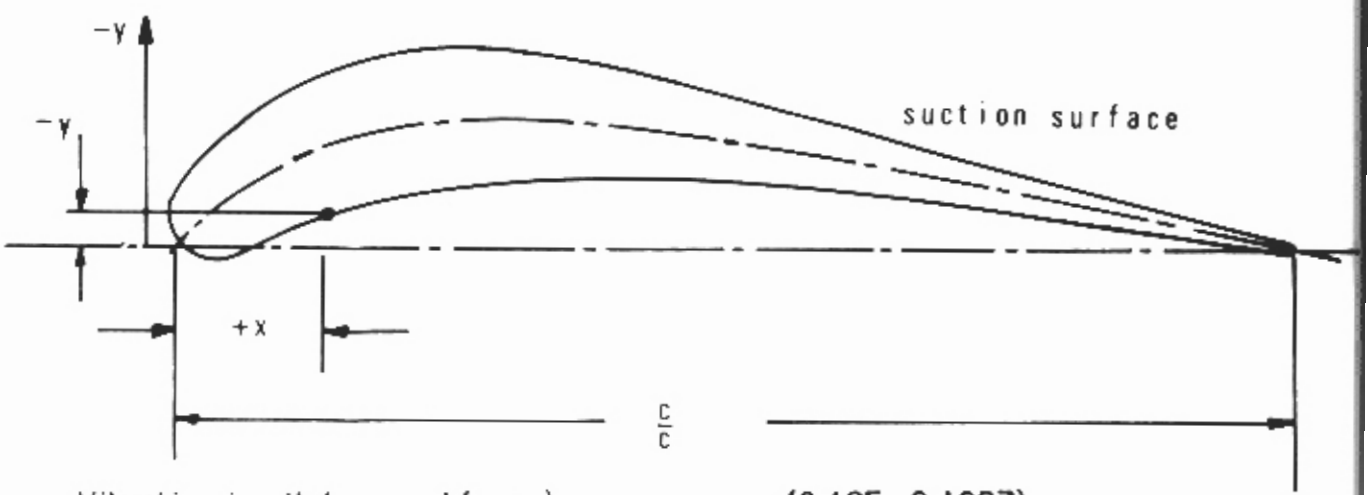


| | | | |
|---|---|---|---|
| Vibration in pitch around $(x_\alpha, y_\alpha)$ | | | = (0.195,-0.1097) |
| d = (thickness/chord) | | | = 0.124 |
| $\alpha$ = 0.0172 rad (nominal) | | k | = variable |
| c = 0.072 m | | span | = 0.025 m |
| $\tau$ = 0.763 (hub) | | camber | = 60.83° |
| 0.804 (midspan) | | $\gamma$ | = 45.7° |
| 0.873 (tip) | | hub/tip | = 0.844 |
| $M_2$ = variable | | $\sigma$ | = 67.5° (nominal) |

Working fluid: Freon-11 ($CFCl_3$) with specific heat ratio = 1.137

Fig. 7.3-1. Third standard configuration: Cascade geometry

| C = 0.072 m | | | |
|---|---|---|---|
| SUCTION SURFACE (Lower surface) | | PRESSURE SURFACE (Upper surface) | |
| X | $Y_s$ | X | $Y_p$ |
| 0.0 | 0.0 | 0.0 | 0.0 |
| -0.073 | -0.0096 | 0.0247 | +0.0108 |
| -0.0115 | -0.0290 | 0.0439 | +0.0066 |
| -0.0051 | -0.0487 | 0.0718 | -0.0073 |
| 0.0102 | -0.0698 | 0.0932 | -0.0144 |
| 0.0296 | -0.0918 | 0.1213 | -0.0265 |
| 0.0462 | -0.1080 | 0.1478 | -0.0356 |
| 0.0668 | -0.1240 | 0.1742 | -0.0434 |
| 0.0887 | -0.1384 | 0.2014 | -0.0502 |
| 0.1117 | -0.1508 | 0.2289 | -0.0538 |
| 0.1358 | -0.1610 | 0.2563 | -0.0601 |
| 0.1606 | -0.1693 | 0.2840 | -0.0637 |
| 0.1864 | -0.1749 | 0.3119 | -0.0660 |
| 0.2122 | -0.1781 | 0.3395 | -0.0674 |
| 0.2354 | -0.1797 | 0.3676 | -0.0676 |
| 0.2584 | -0.1800 | 0.3891 | -0.0669 |
| 0.2814 | -0.1793 | 0.4113 | -0.0662 |
| 0.3046 | -0.1772 | 0.4329 | -0.0657 |
| 0.3274 | -0.1745 | 0.4547 | -0.0646 |
| 0.3432 | -0.1719 | 0.4765 | -0.0639 |
| 0.3591 | -0.1692 | 0.4982 | -0.0623 |
| 0.3748 | -0.1657 | 0.5201 | -0.0613 |
| 0.3904 | -0.1621 | 0.5419 | -0.0596 |
| 0.4058 | -0.1580 | 0.5633 | -0.0579 |
| 0.4806 | -0.1396 | 0.5850 | -0.0562 |
| 0.5552 | -0.1208 | 0.6069 | -0.0540 |
| 0.6291 | -0.1018 | 0.6285 | -0.0519 |
| 0.7038 | -0.0829 | 0.6502 | -0.0497 |
| 0.7780 | -0.0640 | 0.6721 | -0.0470 |
| 0.8525 | -0.0452 | 0.6939 | -0.0446 |
| 0.9270 | -0.0264 | 0.7152 | -0.0419 |
| 1.0 | -0.0075 | 0.7368 | -0.0388 |
| | | 0.7583 | -0.0359 |
| | | 0.7986 | -0.0295 |
| | | 0.8387 | -0.0237 |
| | | 0.8792 | -0.0176 |
| | | 0.9195 | -0.0118 |
| | | 0.9597 | -0.0060 |
| | | 1.0 | 0.0 |

**Table 7.3-1.** Third standard configuration: Dimensionless airfoil coordinates (spanwise identical).

The unsteady pressures are measured with a high-response pressure transducer located outside the test-rig, and a calibration for losses, change of frequency and amplitude in the pneumatic tubes[9] is performed.

Aeroelastic Test Cases

From the results obtained from these experiments, 9 aeroelastic test cases have been proposed by H. Kobayashi for off-design calculation [46]. These were defined after the Cambridge Symposium and therefore do not correspond with those presented in [4]. The data were also received late in the project, and for the present no attempt has been made to calculate the aeroelastic behavior of this standard configuration. Therefore, only the experimental data are included here, without theoretical results. It has thus not been possible to validate either the time-averaged, or the time-dependent data[10] .
The aeroelastic test cases proposed by H. Kobayashi are given in Table 7.3-2. The corresponding time-averaged and time-dependent data are presented in Figs. 7.3-2 and 7.3-3 respectively, and in Fig. 7.3-4 the measured aerodynamic damping coefficient is given in dependence of the reduced frequency.

9 Details about the cascade, instrumentation and data reduction was presented by H. Kobayashi at the 1984 Cambridge Symposium on Aeroelasticity [45].

10 The comparison with theoretical results will be especially interesting as the idea to use pneumatic tubes for the unsteady pressure responses significantly reduces the experimental costs (see [45] for details).

| Aeroelastic Test Case No | Time - Averaged Parameters | | | | | |
|---|---|---|---|---|---|---|
| | $M_1$ | $\beta_1$ | $Pw_2/Pw_1$ | $P_1/P_2$ | $M_2$ | $\beta_2$ |
| 1 - 3 | 0.303 | - 1.2 | 0.984 | 0.778 | 0.682 | - 58.3 |
| 4 - 6 | 0.334 | - 1.1 | 0.946 | 0.432 | 1.242 | - 56.1 |
| 7 - 9 | 0.319 | - 1.2 | 0.864 | 0.345 | 1.390 | - 55.5 |

| Aeroelastic Test Case No | Time-Dependent Parameters | | | | | | | | | | |
|---|---|---|---|---|---|---|---|---|---|---|---|
| | Amplitude (Nominal = 0.01745rad) | | | | | Frequency | Reduced Frequency | Interblade phase angle measured (Nominal = 67.5°) | | | |
| | $\alpha_L^{(-2)}/\alpha_L^{(0)}$ | $\alpha_L^{(-1)}/\alpha_L^{(0)}$ | $\alpha_L^{(0)}$ (rad) | $\alpha_L^{(+1)}/\alpha_L^{(0)}$ | $\alpha_L^{(+2)}/\alpha_L^{(0)}$ | (Hz)f | K | $\sigma^{(-2)}$ (°) | $\sigma^{(-1)}$ (°) | $\sigma^{(0)}$ (°) | $\sigma^{(+1)}$ (°) | $\sigma^{(+2)}$ (°) |
| 1 | 0.965 | 0.952 | 0.0172 | 0.996 | 1.028 | 25 | 0.057 | 65.5 | 73.6 | 66.6 | 67.9 | 70.2 |
| 2 | 1.008 | 0.973 | 0.0172 | 1.026 | 1.032 | 100 | 0.229 | 76.4 | 67.4 | 67.6 | 64.6 | 70.5 |
| 3 | 1.087 | 1.024 | 0.0171 | 0.966 | 1.075 | 200 | 0.457 | 71.2 | 68.7 | 71.8 | 68.5 | 70.3 |
| 4 | 0.965 | 0.952 | 0.0172 | 0.996 | 1.028 | 25 | 0.031 | 65.5 | 73.6 | 66.6 | 67.9 | 70.2 |
| 5 | 1.008 | 0.973 | 0.0172 | 1.026 | 1.032 | 100 | 0.126 | 76.4 | 67.4 | 67.6 | 64.6 | 70.5 |
| 6 | 1.087 | 1.024 | 0.0171 | 0.966 | 1.075 | 200 | 0.251 | 71.2 | 68.7 | 71.8 | 68.5 | 70.3 |
| 7 | 0.965 | 0.952 | 0.0172 | 0.996 | 1.028 | 25 | 0.028 | 65.5 | 73.6 | 66.6 | 67.9 | 70.2 |
| 8 | 1.008 | 0.973 | 0.0172 | 1.026 | 1.032 | 100 | 0.112 | 76.4 | 67.4 | 67.6 | 64.6 | 70.5 |
| 9 | 1.087 | 1.024 | 0.0171 | 0.966 | 1.075 | 200 | 0.223 | 71.2 | 68.7 | 71.8 | 68.5 | 70.3 |

**Table 7.3-2.** Third standard configuration: 9 recommended aeroelastic test cases (Fluid used is Freon-11; all values are at midspan)

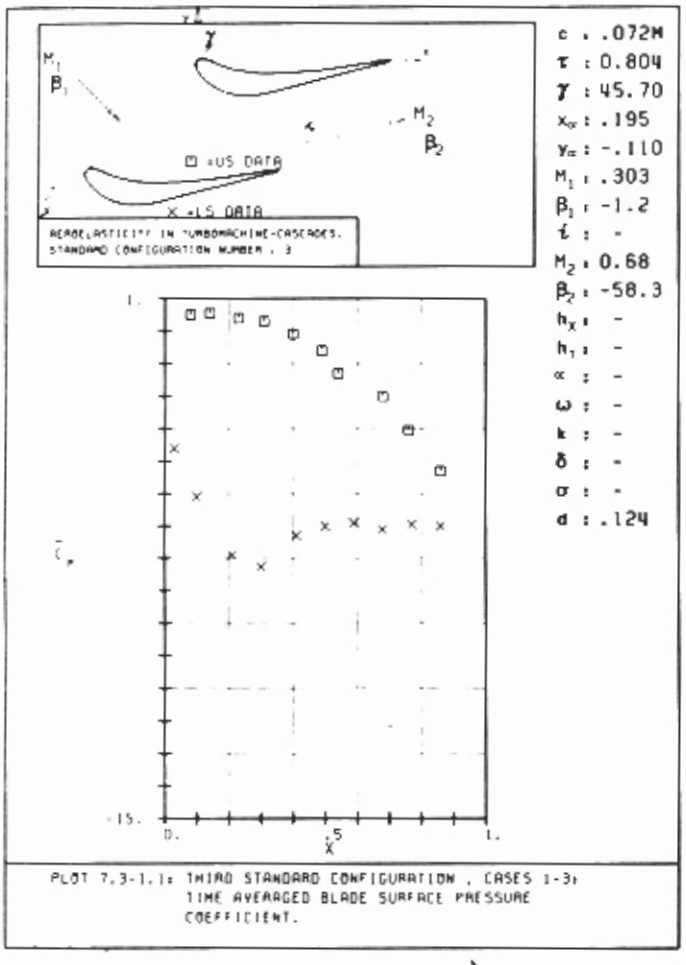


PLOT 7.3-1.1: THIRD STANDARD CONFIGURATION , CASES 1-3: TIME AVERAGED BLADE SURFACE PRESSURE COEFFICIENT.

a)

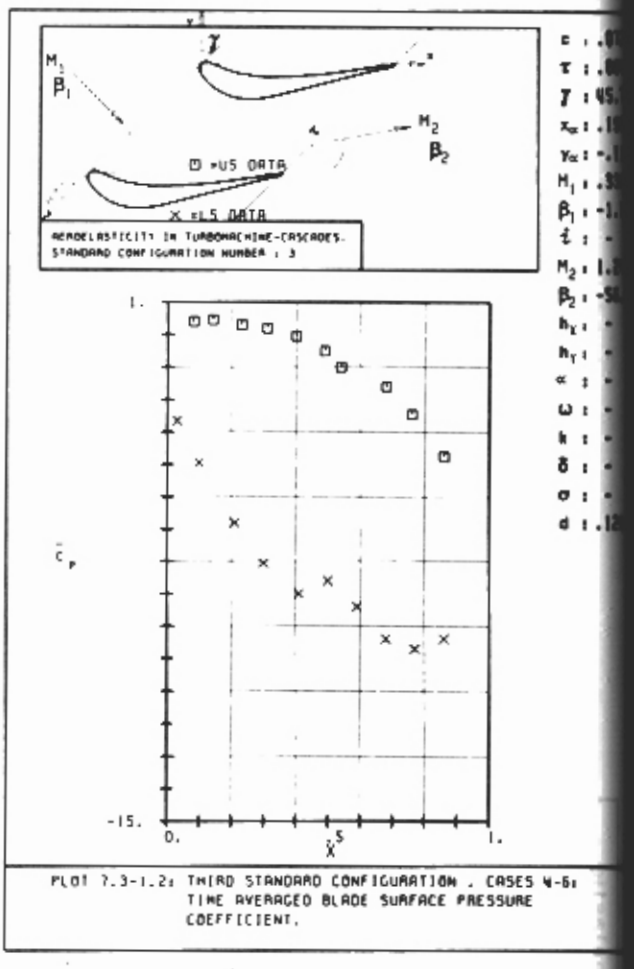


PLOT 7.3-1.2: THIRD STANDARD CONFIGURATION , CASES 4-6: TIME AVERAGED BLADE SURFACE PRESSURE COEFFICIENT.

b)

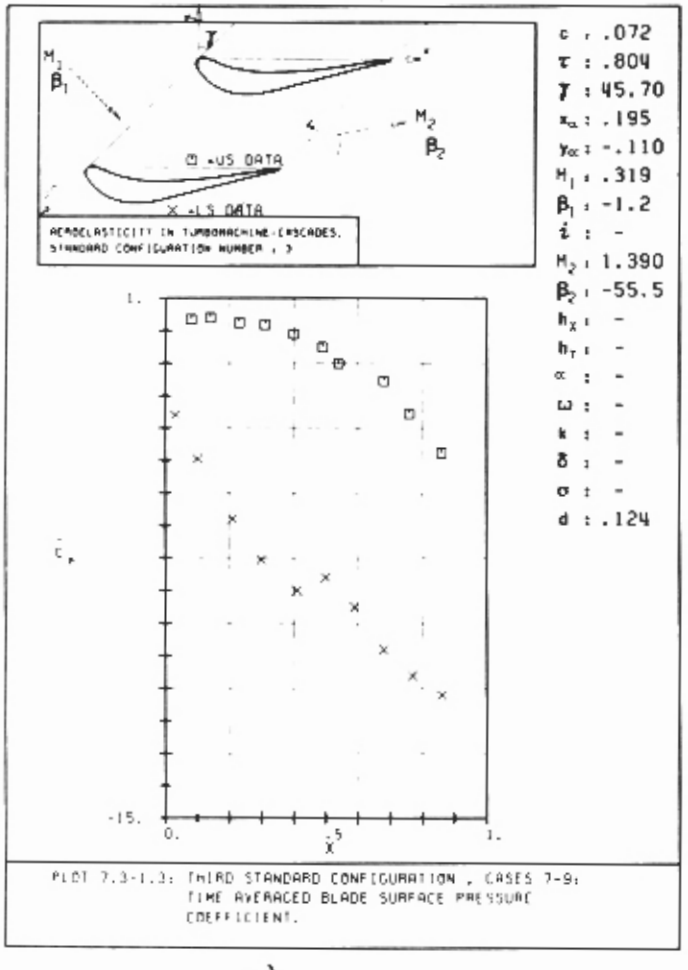


PLOT 7.3-1.3: THIRD STANDARD CONFIGURATION , CASES 7-9: TIME AVERAGED BLADE SURFACE PRESSURE COEFFICIENT.

c)

Fig. 7.3-2. Third standard configuration. Time averaged blade surface pressure distribution for $M_2$ = 0.68, 1.24 and 1.39 resp.

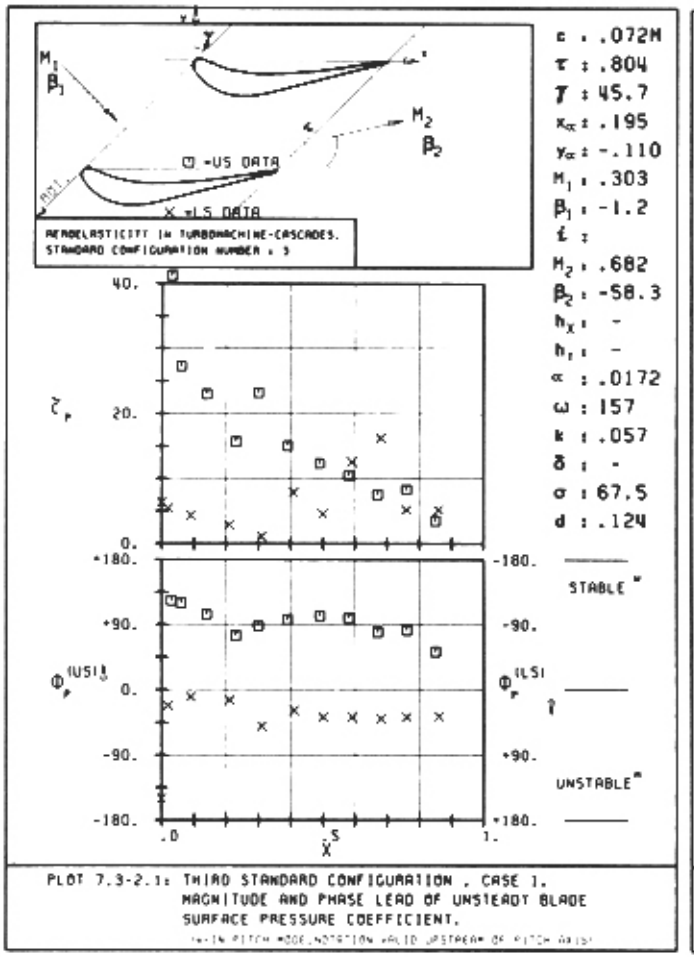


a)

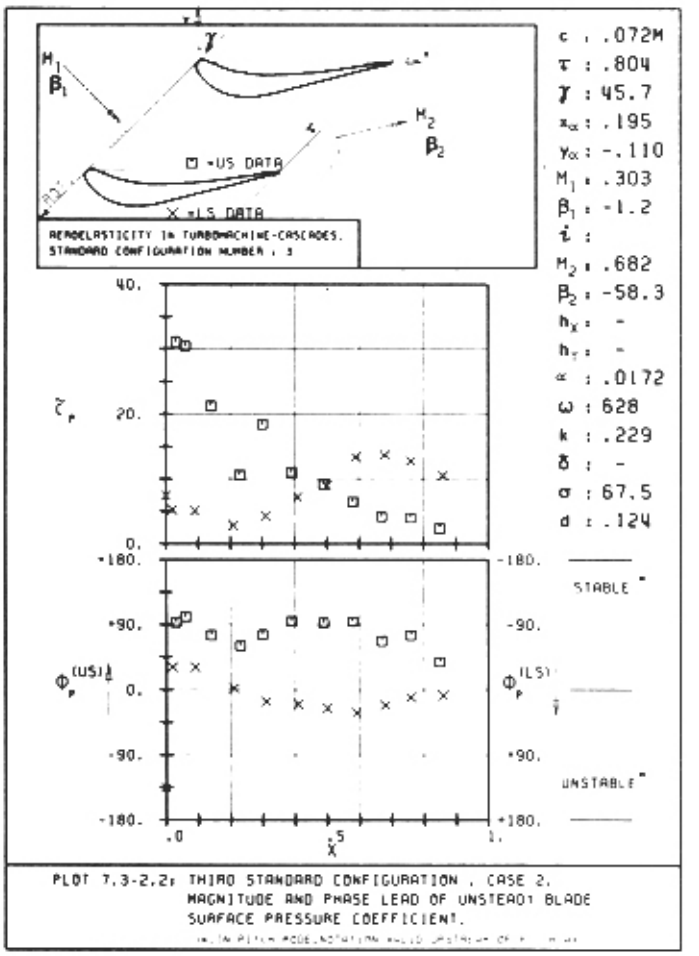


b)

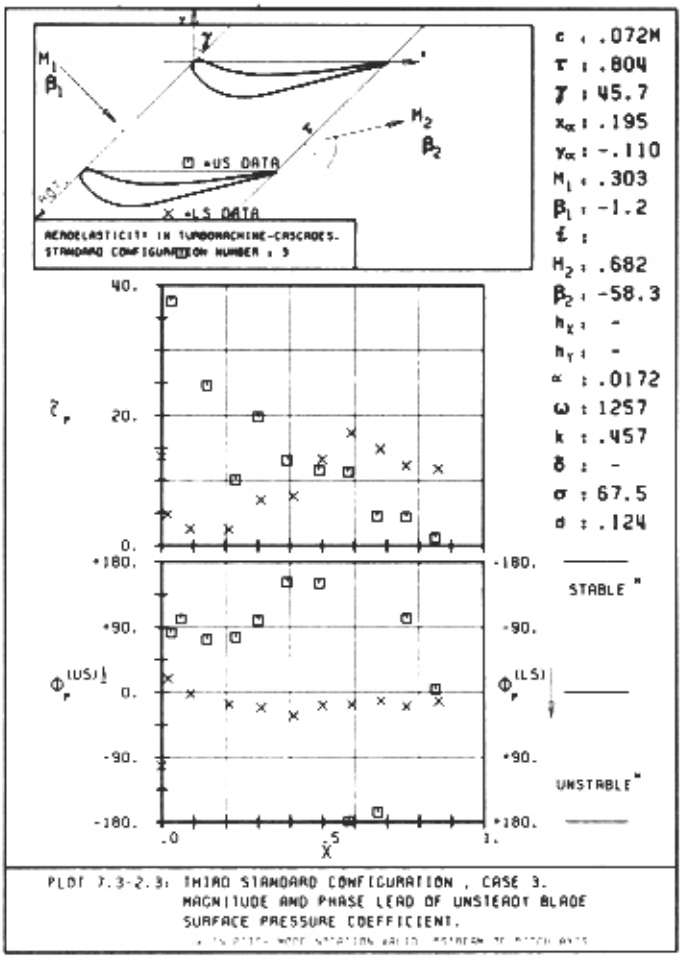


c)

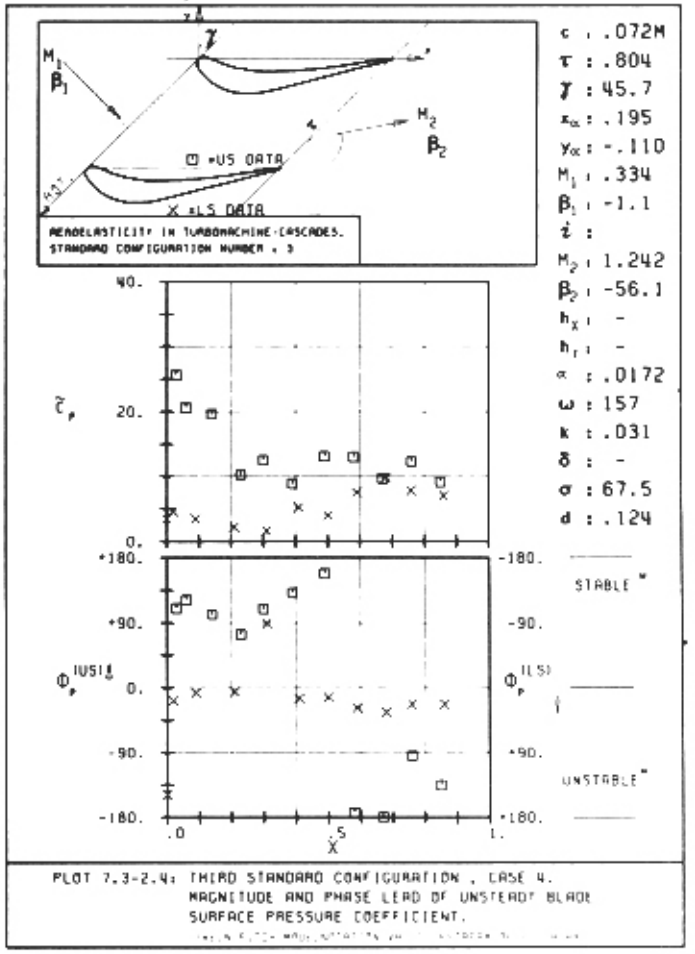


d)

Fig. 7.3-3. Continued on next page

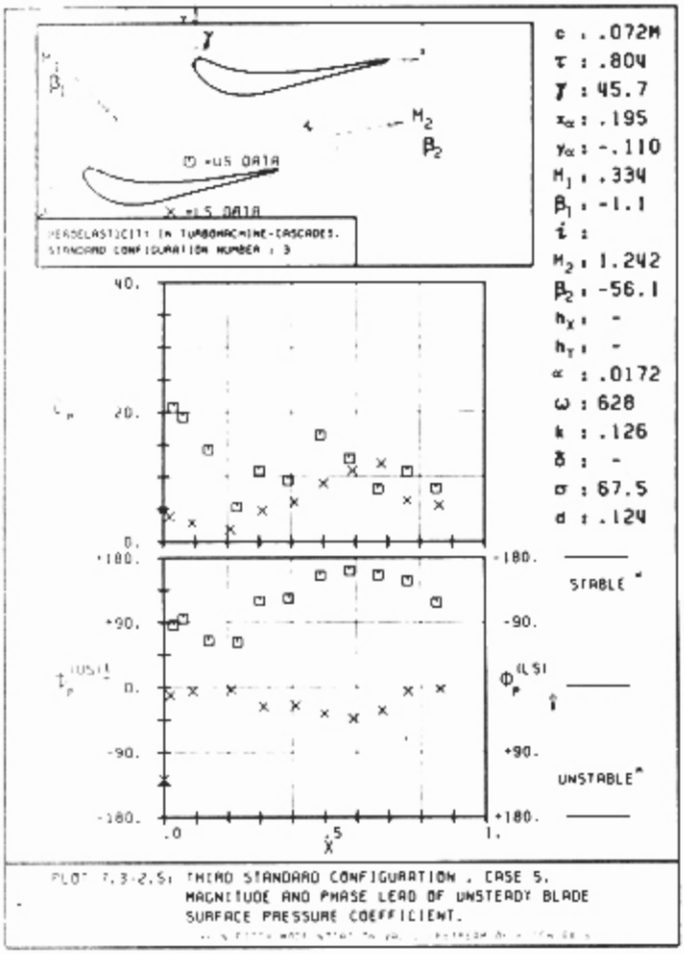


PLOT 7.3-2.5: THIRD STANDARD CONFIGURATION , CASE 5.
MAGNITUDE AND PHASE LEAD OF UNSTEADY BLADE SURFACE PRESSURE COEFFICIENT.

e)

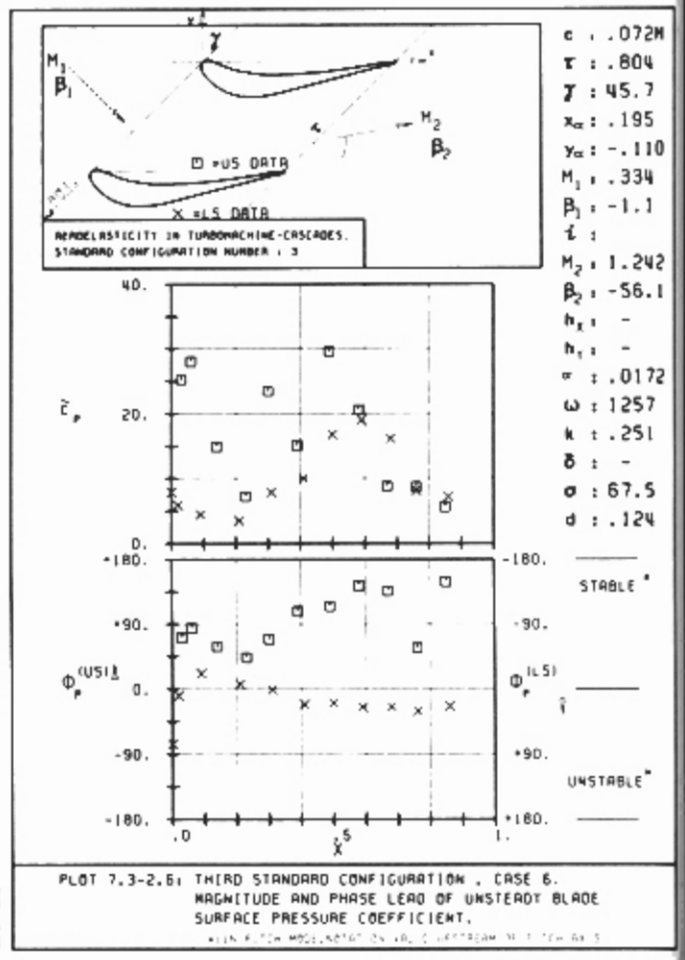


PLOT 7.3-2.6: THIRD STANDARD CONFIGURATION , CASE 6.
MAGNITUDE AND PHASE LEAD OF UNSTEADY BLADE SURFACE PRESSURE COEFFICIENT.

f)

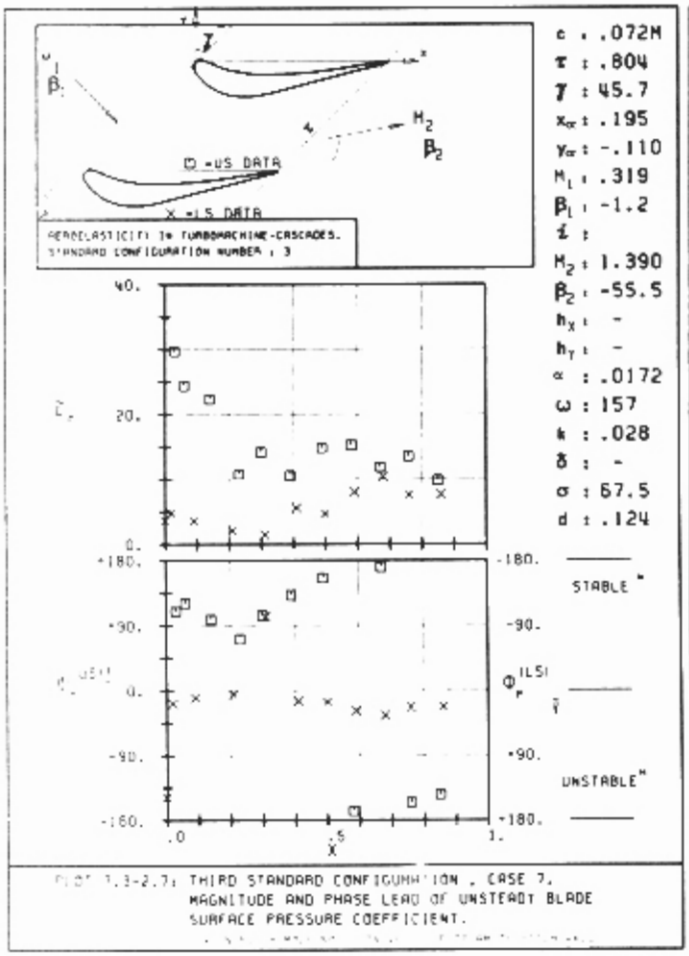


PLOT 7.3-2.7: THIRD STANDARD CONFIGURATION , CASE 7.
MAGNITUDE AND PHASE LEAD OF UNSTEADY BLADE SURFACE PRESSURE COEFFICIENT.

g)

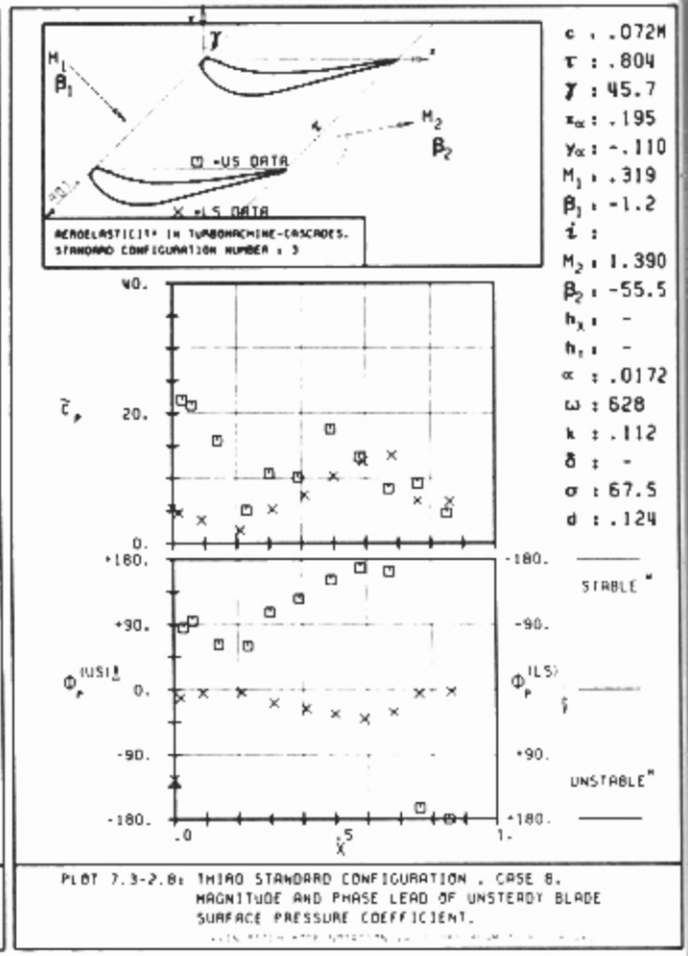


PLOT 7.3-2.8: THIRD STANDARD CONFIGURATION , CASE 8.
MAGNITUDE AND PHASE LEAD OF UNSTEADY BLADE SURFACE PRESSURE COEFFICIENT.

h)

**Fig. 7.3-3.** Continued on next page.

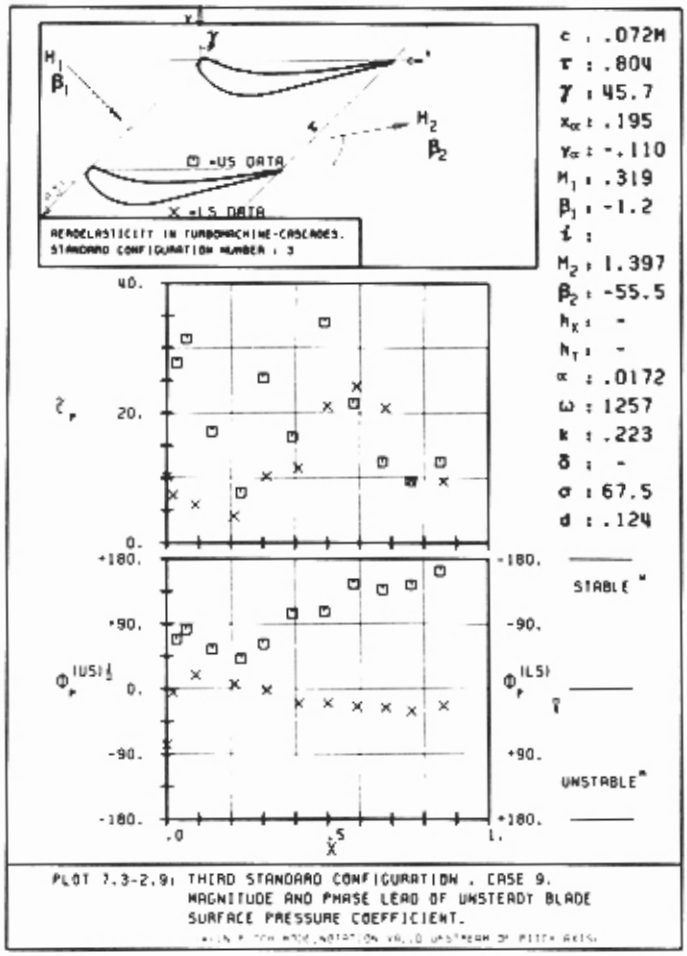


i)

Fig. 7.3-3. Third standard configuration. Time-dependent blade surface pressure distribution for the nine aeroelastic test cases

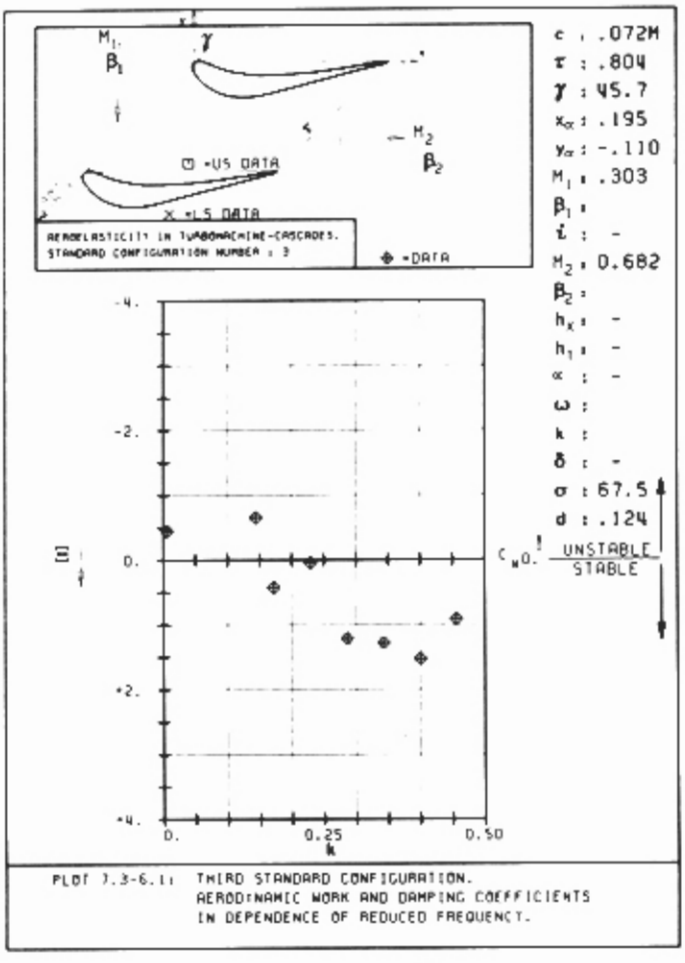


PLOT 7.3-6.1: THIRD STANDARD CONFIGURATION.
AERODYNAMIC WORK AND DAMPING COEFFICIENTS
IN DEPENDENCE OF REDUCED FREQUENCY.

a)

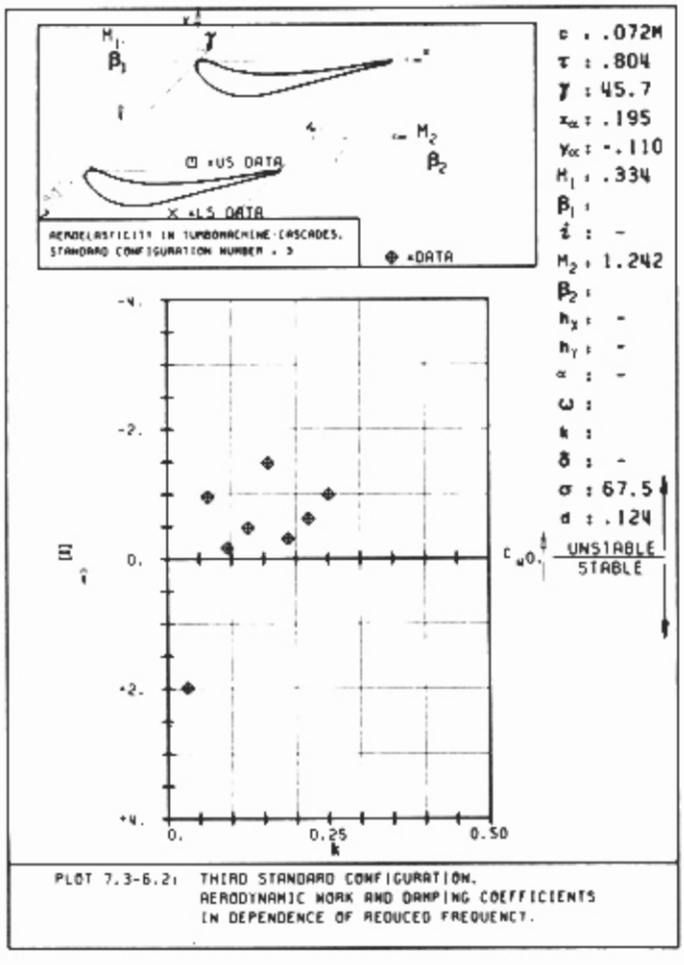


PLOT 7.3-6.2: THIRD STANDARD CONFIGURATION.
AERODYNAMIC WORK AND DAMPING COEFFICIENTS
IN DEPENDENCE OF REDUCED FREQUENCY.

b)

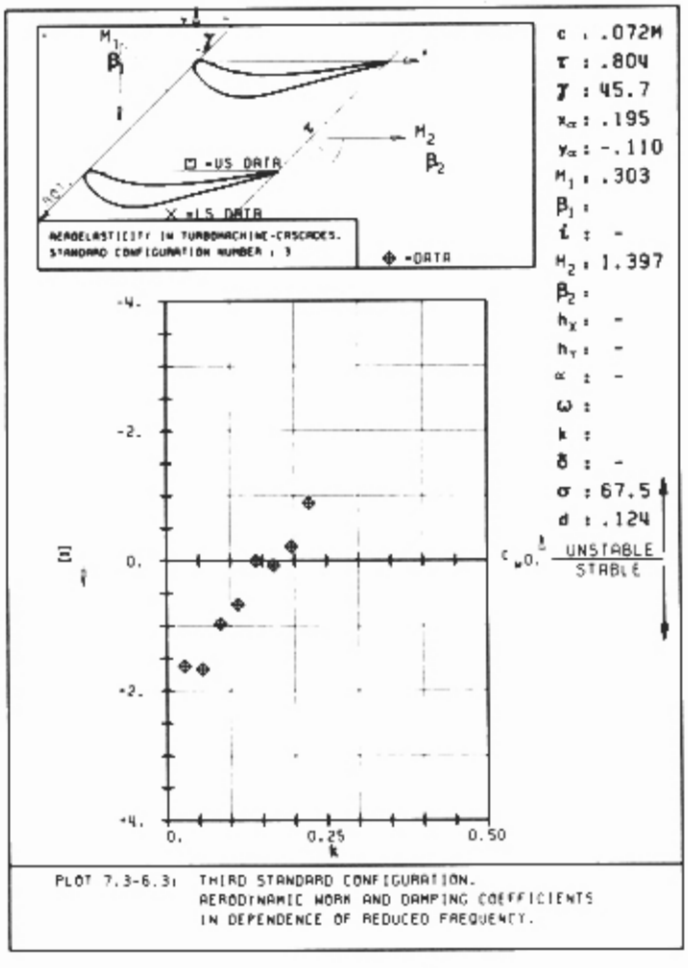


PLOT 7.3-6.3: THIRD STANDARD CONFIGURATION.
AERODYNAMIC WORK AND DAMPING COEFFICIENTS
IN DEPENDENCE OF REDUCED FREQUENCY.

c)

Fig. 7.3-4. Third standard configuration
Aerodynamic damping coefficient
versus reduced frequency for
$M_2$ = 0.68, 1.24 and 1.40 resp.

## 7.4 Fourth Standard Configuration (Cambered Turbine Cascade in Transonic Flow)

### Definition

Quasi three-dimensional cascade experiments on high load turbine rotor sections are being performed in the annular cascade facility at the Lausanne Institute of Technology [22]. The experimental data have been made available by Brown Boveri & Co and are included in the present report by kind permission of A. Bölcs [21-25].

The fourth standard configuration is of interest mainly because it represents a typical section of modern free standing turbine blades. This type of airfoil has relatively high blade thickness and camber and operates under high subsonic flow conditions. It normally exhibits flutter instabilities in the first bending mode.

The cascade configuration consists of 20 vibrating prismatic blades, each with a chord of c=0.0744 m and a span of 0.040 m, with 45° turning and a maximum thickness-to-chord ratio of 0.17.

The stagger angle is 56.6°, with the pitch-to-chord ratio of the cascade:

0.67 (hub)
0.76 (midspan)
0.84 (tip)

The hub-tip ratio in the test facility is 0.8.

The cascade geometry is given in Figure 7.4-1 and the profile coordinates are tabulated in Table 7.4-1.

Experiments are performed with variable inlet flow velocity and angle ($M_1$, i), expansion ratio ($p_2/p_{w1}$, $M_2$), vibration mode, oscillation frequency and interblade phase angle. All the experiments presently being performed have constant spanwise flow conditions upstream.

The time-averaged instrumentation consists of static pressure tappings on the outer and inner tunnel walls, as well as blade surface pressure tappings (14 on pressure surface, 15 on suction surface, Table 7.4-2) on two adjacent blades. The inlet flow conditions are determined by wedge probe traverses 0.09 chord

lengths upstream, in the axial direction, of the midspan leading edge plane. The outlet flow angle is determined using cone probe traverses and the outlet

"isentropic" Mach number, in the present test cases, was calculated from a linear interpolation in the static pressures measured on the outer (tip) and inner (hub) walls, together with upstream stagnation pressure.
The outlet conditions are measured 1.14 chordlengths downstream of the trailing edge plane (in the axial direction, at midspan).
Boundary layer suction is performed at three different locations, both on the inner and outer walls. The first is located just downstream of the inlet guide vanes, the second 1.3 chordlengths upstream (in the axial direction) of the blade leading edge plane, and the third 1.2 chordlengths downstream of the blade trailing edge plane (in the axial direction). This last suction is applied only at the outer wall.
The experimental accuracy of the steady-state data presented herein are estimated to be approximately ±1° in the flow angles[11] and approximately ±0.01 in the Mach numbers. It is also possible that the inlet flow angle may not correspond exactly to the one at infinity upstream, as it is measured less than 0.1 chordlengths upstream of the leading edge plane.
The stationary three-dimensional shock structure in the cascade has been visualized with laser holography [24], and the same profiles have been tested (in steady state conditions) in a linear test facility [25]. In the latter investigation high-speed Schlieren visualization was performed.
The time-dependent instrumentation consists of 11 high frequency response pressure transducers, 6 on the suction surface and 5 on the pressure surface on two neighboring blades (Table 7.4-2). The blade vibrations are determined with straingauges (on each blade).
All the blades in the cascade are vibrated with an electromagnetic excitation mechanism [26], which allows for variation of the blade vibration amplitude, frequency and interblade phase angle.
The time-dependent data are registered on an analog tape recorder and processed
off-line, with acceleration correction of the pressure transducer response. The data reduction follows with a cross-correlation technique [27, 28] (data reduction method "c" in section 4.4) and the experimental accuracy for all unsteady values is evaluated with a 95% confidence interval. This method is briefly reported in Appendix A4.

---

11 The probe support systems showed some drift, and the tests are scheduled to be repeated

**High Subsonic/Transonic Turbine Profiles.**

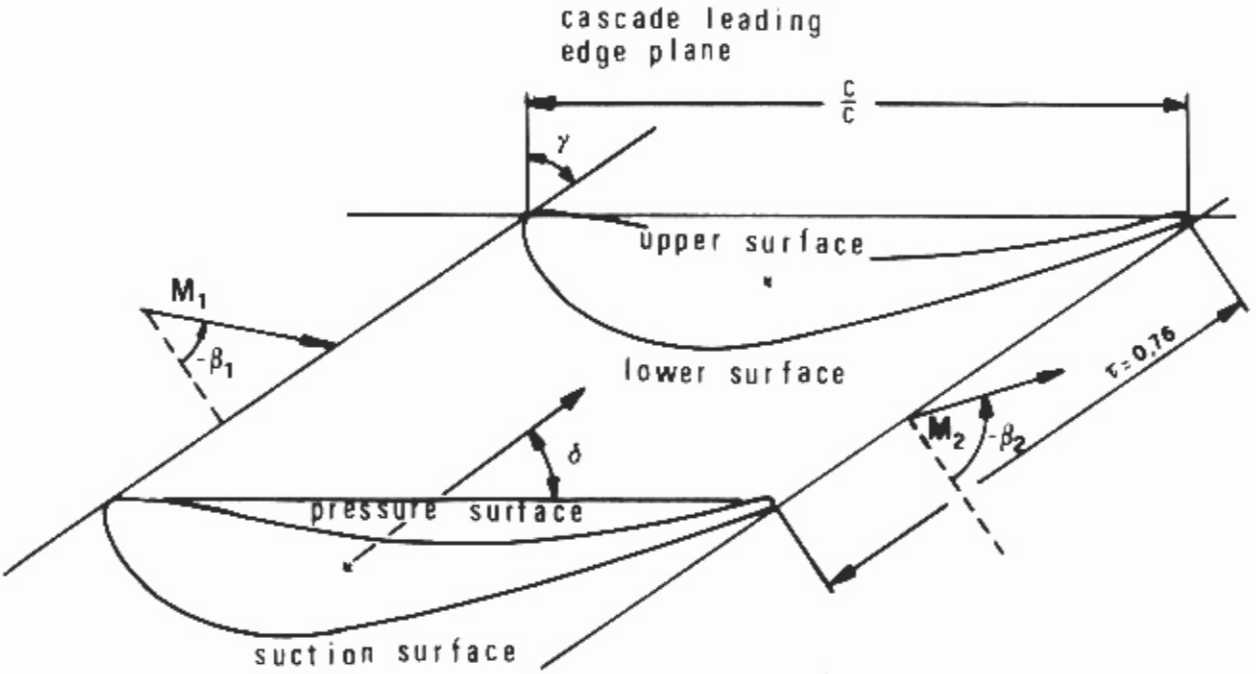


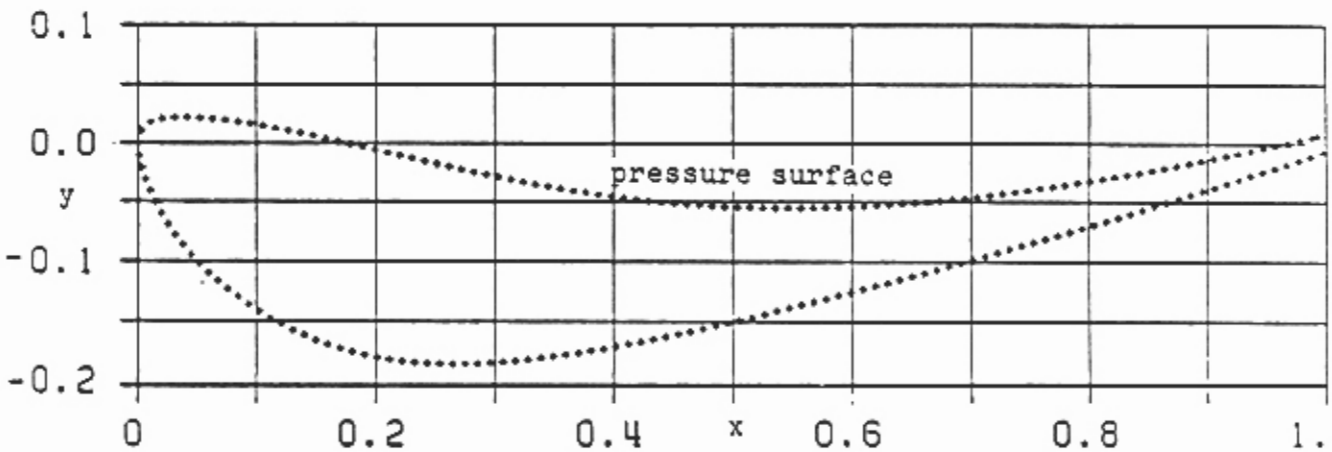


Vibration in first bending mode

d = (thickness/chord)

γ = 56.6°

c = 0.0744 m

τ = 0.67 (hub)
0.76 (midspan)
0.84 (tip)

$M_{2is}$ = variable

δ = 60.4°

= 0.17

k = variable

span = 0.040 m

camber = 45.°

hub/tip = 0.8

f = 150 Hz

σ = variable

Nominal values: $M_1$=0.31; $\beta_1$=-44.1°; $M_2$=0.90; $\beta_2$=-72.4°

Working fluid: Air

**Fig. 7.4-1a.** Fourth standard configuration: Cascade geometry

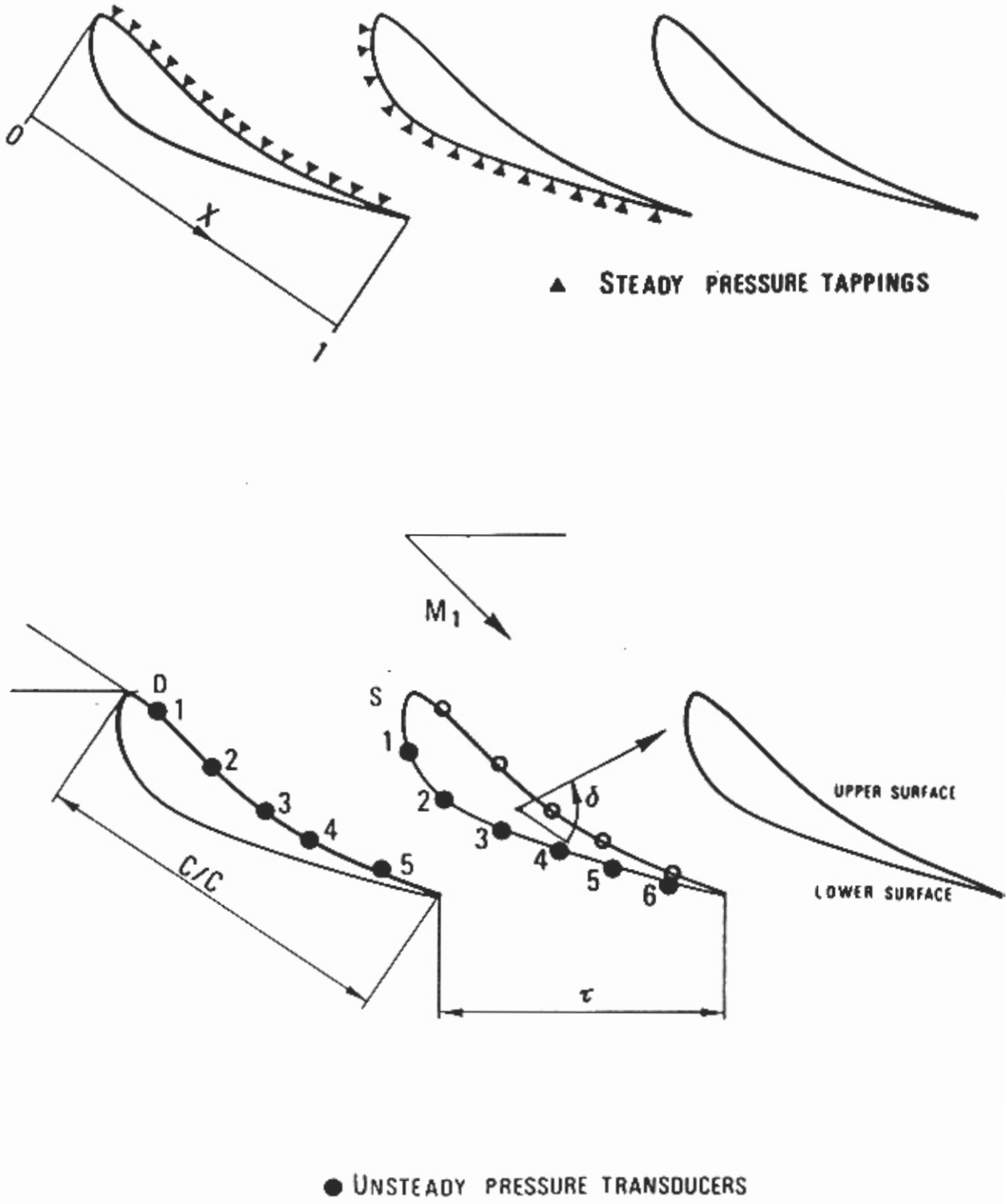


Fig. 7.4-1b. Fourth standard configuration: Location of pressure measurements on blade surfaces.

C = .0744 M

| UPPER SURFACE | | | | LOWER SURFACE | | | |
|---|---|---|---|---|---|---|---|
| X | Y | X | Y | X | Y | X | Y |
| 0.000 | 0.000 | .514 | -.055 | 0.000 | 0.000 | .443 | -.163 |
| .003 | .010 | .524 | -.055 | .001 | -.011 | .453 | -.160 |
| .010 | .018 | .535 | -.055 | .003 | -.021 | .464 | -.158 |
| .020 | .021 | .546 | -.055 | .006 | -.031 | .474 | -.156 |
| .031 | .022 | .556 | -.055 | .010 | -.041 | .485 | -.154 |
| .042 | .022 | .567 | -.055 | .014 | -.051 | .495 | -.151 |
| .052 | .021 | .578 | -.055 | .020 | -.060 | .505 | -.149 |
| .063 | .020 | .588 | -.055 | .025 | -.069 | .516 | -.146 |
| .074 | .019 | .599 | -.054 | .031 | -.078 | .526 | -.144 |
| .084 | .018 | .610 | -.054 | .038 | -.087 | .536 | -.141 |
| .095 | .016 | .620 | -.053 | .044 | -.095 | .547 | -.139 |
| .105 | .014 | .631 | -.052 | .052 | -.102 | .557 | -.136 |
| .116 | .012 | .642 | -.052 | .059 | -.110 | .568 | -.134 |
| .126 | .010 | .652 | -.051 | .067 | -.117 | .578 | -.131 |
| .136 | .008 | .663 | -.050 | .076 | -.124 | .588 | -.129 |
| .147 | .006 | .673 | -.049 | .084 | -.130 | .598 | -.126 |
| .157 | .004 | .684 | -.048 | .093 | -.136 | .609 | -.123 |
| .168 | .001 | .695 | -.047 | .102 | -.142 | .619 | -.121 |
| .178 | -.001 | .705 | -.046 | .111 | -.147 | .629 | -.118 |
| .188 | -.003 | .716 | -.044 | .120 | -.153 | .640 | -.115 |
| .199 | -.006 | .726 | -.043 | .130 | -.157 | .650 | -.113 |
| .209 | -.008 | .737 | -.042 | .139 | -.162 | .660 | -.110 |
| .220 | -.011 | .747 | -.040 | .149 | -.166 | .671 | -.107 |
| .230 | -.013 | .758 | -.039 | .159 | -.170 | .681 | -.104 |
| .240 | -.015 | .768 | -.037 | .169 | -.173 | .691 | -.101 |
| .251 | -.018 | .779 | -.036 | .179 | -.176 | .701 | -.099 |
| .261 | -.020 | .790 | -.034 | .190 | -.179 | .712 | -.096 |
| .271 | -.022 | .800 | -.032 | .200 | -.181 | .722 | -.093 |
| .282 | -.025 | .811 | -.030 | .211 | -.182 | .732 | -.090 |
| .292 | -.027 | .821 | -.029 | .221 | -.184 | .742 | -.087 |
| .303 | -.029 | .832 | -.027 | .232 | -.185 | .753 | -.084 |
| .313 | -.031 | .842 | -.025 | .243 | -.185 | .763 | -.081 |
| .324 | -.033 | .852 | -.023 | .253 | -.186 | .773 | -.078 |
| .334 | -.035 | .863 | -.021 | .264 | -.186 | .783 | -.075 |
| .345 | -.037 | .873 | -.019 | .274 | -.186 | .794 | -.072 |
| .355 | -.039 | .884 | -.017 | .285 | -.186 | .804 | -.069 |
| .365 | -.041 | .894 | -.015 | .296 | -.185 | .814 | -.066 |
| .376 | -.043 | .905 | -.013 | .306 | -.184 | .824 | -.063 |
| .387 | -.044 | .915 | -.010 | .317 | -.183 | .834 | -.060 |
| .397 | -.046 | .926 | -.008 | .328 | -.182 | .844 | -.057 |
| .408 | -.047 | .936 | -.006 | .338 | -.181 | .855 | -.054 |
| .418 | -.048 | .946 | -.004 | .349 | -.179 | .865 | -.050 |
| .429 | -.049 | .957 | -.001 | .359 | -.178 | .875 | -.047 |
| .439 | -.051 | .967 | .001 | .370 | -.176 | .885 | -.044 |
| .450 | -.051 | .978 | .003 | .380 | -.175 | .895 | -.041 |
| .461 | -.052 | .988 | .006 | .391 | -.173 | .905 | -.037 |
| .471 | -.053 | | | .401 | -.171 | .926 | -.031 |
| .482 | -.054 | | | .412 | -.169 | .936 | -.028 |
| .493 | -.054 | | | .422 | -.167 | .946 | -.024 |
| .503 | -.055 | | | .433 | -.165 | .956 | -.021 |
| | | | | | | .966 | -.017 |
| | | | | | | .976 | -.014 |
| | | | | | | .986 | -.011 |
| | | | | | | .996 | -.007 |

Table 7.4-1. Fourth standard configuration: Dimensionless airfoil coordinates (spanwise identical).

| Location x | Type of pressure measurement US/TA | US/TD | LS/TA | LS/TD |
|---|---|---|---|---|
| 0.01 | - | - | x | - |
| 0.04 | x | - | x | - |
| 0.10 | x | x | x | x |
| 0.17 | x | - | x | - |
| 0.24 | x | - | x | x |
| 0.30 | x | x | x | - |
| 0.37 | x | - | x | - |
| 0.44 | x | - | x | x |
| 0.50 | x | x | x | - |
| 0.57 | x | - | x | x |
| 0.64 | x | x | x | - |
| 0.71 | x | - | x | x |
| 0.77 | x | - | x | - |
| 0.84 | x | x | x | x |
| 0.91 | x | - | x | - |
| 1.00 | x | - | x | - |

US/TA: Upper surface, time-averaged
US/TD: Upper surface, time-dependent
LS/TA: Lower surface, time-averaged
LS/TD: Lower surface, time-dependent

**Table 7.4-2** Location of blade surface pressure measurements

## Aeroelastic Test Cases

A large amount of data (approximately 250 aeroelastic cases) has been obtained to date [22]. Of these, 8 have been selected as test cases for the fourth standard configuration [21]. These cases treat all vibration in the first bending mode, with a vibration frequency of f=150Hz and a vibration direction of 60.4° (see Fig. 7.4-1).
The 8 aeroelastic test cases are presented in Table 7.4-3. The variation over outlet Mach number for a -90° interblade phase angle was chosen as the cascade here shows a slight instability for transonic flow conditions.

| Aeroelastic Test Case | Time-Averaged Parameters $M_1$ (-) | $\beta_1$ (°) | $M_{2is}$ (-) | $\beta_2$ (°) | Time-Dependent $\sigma$ (°) | k (-) | $h^0$ (-) | $\delta$ (°) |
|---|---|---|---|---|---|---|---|---|
| 1 | 0.19 | - 45 | 0.58 | - 71 | - 90 | 0.168 | 0.0038 | 60. |
| 2 | 0.26 | " | 0.76 | " | " | 0.128 | " | " |
| 3 | 0.28 | " | 0.90 | " | " | 0.107 | " | " |
| 4 | 0.29 | " | 1.02 | " | " | 0.095 | 0.0033 | " |
| 5 | " | " | 1.19 | " | " | 0.082 | 0.0038 | " |
| 6 | 0.28 | " | 0.90 | " | +180 | 0.107 | 0.0033 | " |
| 7 | " | " | " | " | + 90 | " | | " |
| 8 | " | " | " | " | 0 | " | | " |

**Table 7.4-3.** Fourth Standard Configuration.
8 Recommended Aeroelastic Test Cases.

## Discussion of Time-Averaged Results

The 8 proposed aeroelastic test cases include 5 separate stationary flow conditions at nominal flow angle, with outlet flow Mach number varying from subsonic to supersonic conditions. These results are given in Figures 7.4-2, together with predicted results from Method 7. Furthermore, results are presented from a two-dimensional steady-state time-marching code by Denton ([41, 42], indicated as Method 99 in the figures).

The good agreement in the results presented indicates that both the calculations and the experiments are of high quality. The differences in the forward 30% of the blade may probably be explained either by inaccuracy in the experimentally determined inlet flow angle and/or by a stream tube height variation in the experiments. It should be pointed out here that the results of Method 7 have been obtained by adjusting the stream tube height so as to adapt the computed outlet conditions to the measured ones, while Method 99 is a two-dimensional model.

The mutual validation of both the experiments and the computations can also be seen from Figure 7.4-3, where an example of experimental data from the annular facility (with span/chord = 0.54) [23] are compared to data from a linear test facility (span/chord = 1.06) [25], both at midspan, and to computed results from the two-dimensional Denton-code [42].

However, there seems to be some ambiguity about the outlet flow conditions. The outlet "isentropic" Mach number is determined experimentally from the local static pressure (linear interpolation between the inner and outer channel walls), which includes losses, and the upstream stagnation pressure. As the static pressure contains losses, this value is not the true isentropic value which might be found from an inviscid flow computation. However, the computed flow angles seem to be within the experimental accuracy although some stream tube height variation (up to 15% in some cases) is introduced in Method 7.

The agreement between the different theoretical models and the experimental data for the aft portion of the blade is best for the subsonic flow conditions. In the transonic and supersonic ranges, reflections of shock waves on the blade suction surface are not predicted by the theories, although the sonic transition is captured well. This is seen especially in Fig. 7.4-2e where the sharp decrease in blade surface Mach number at 50% chord is due to such a reflection. Furthermore, the second small decrease in Mach number

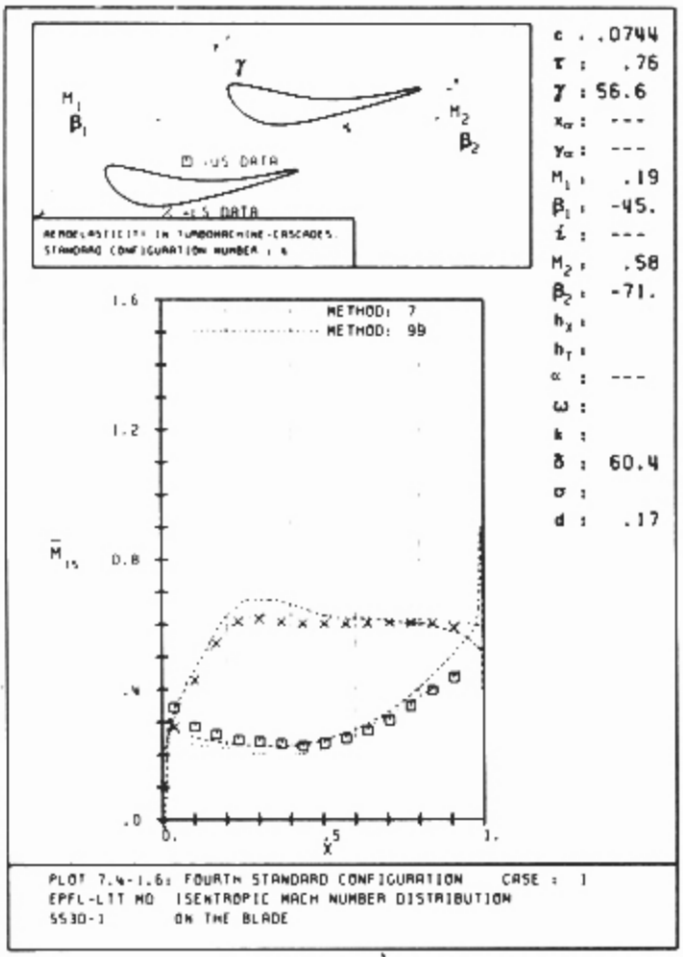


a)

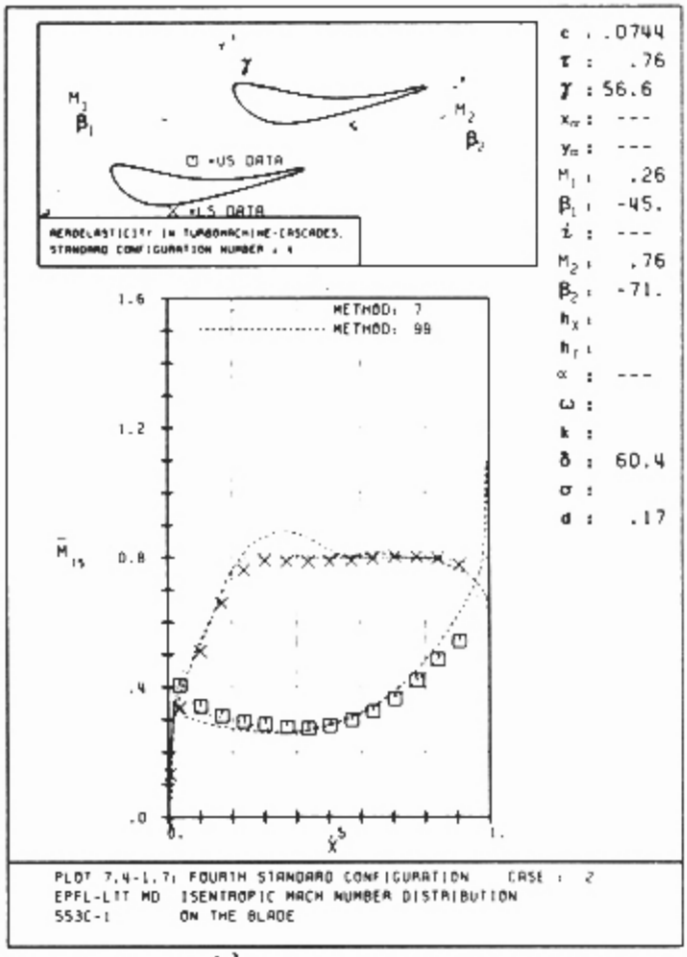


b)

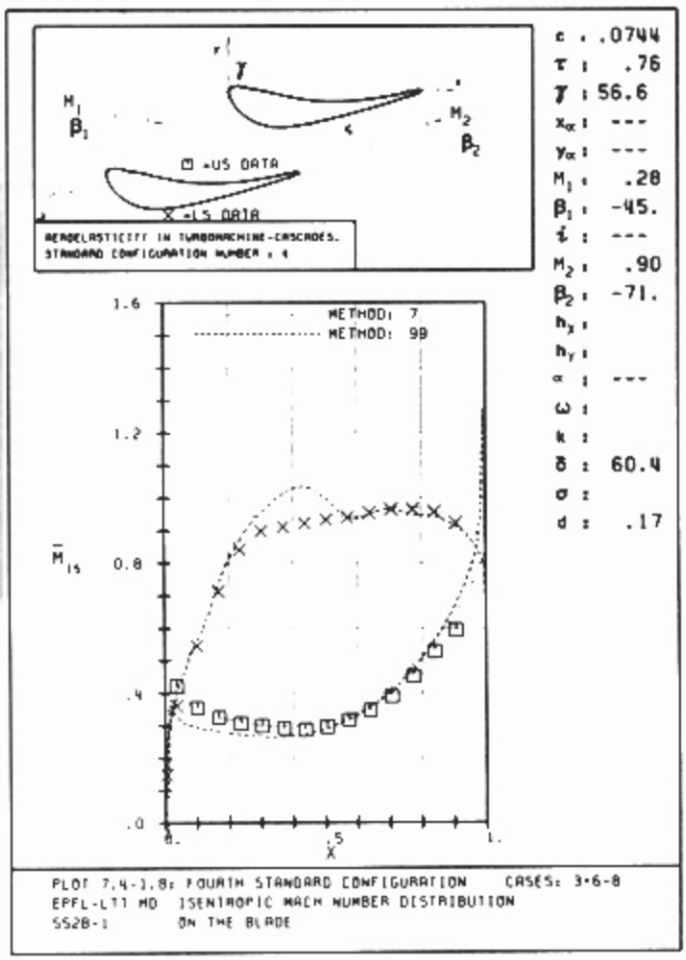


c)

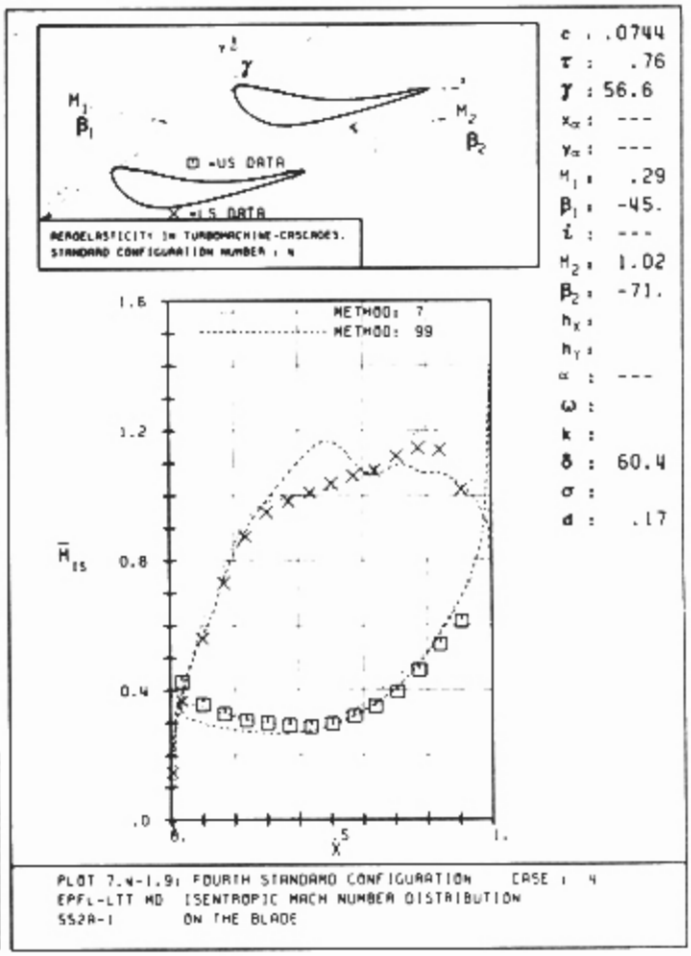


d)

Fig. 7.4-2. Continued on next page

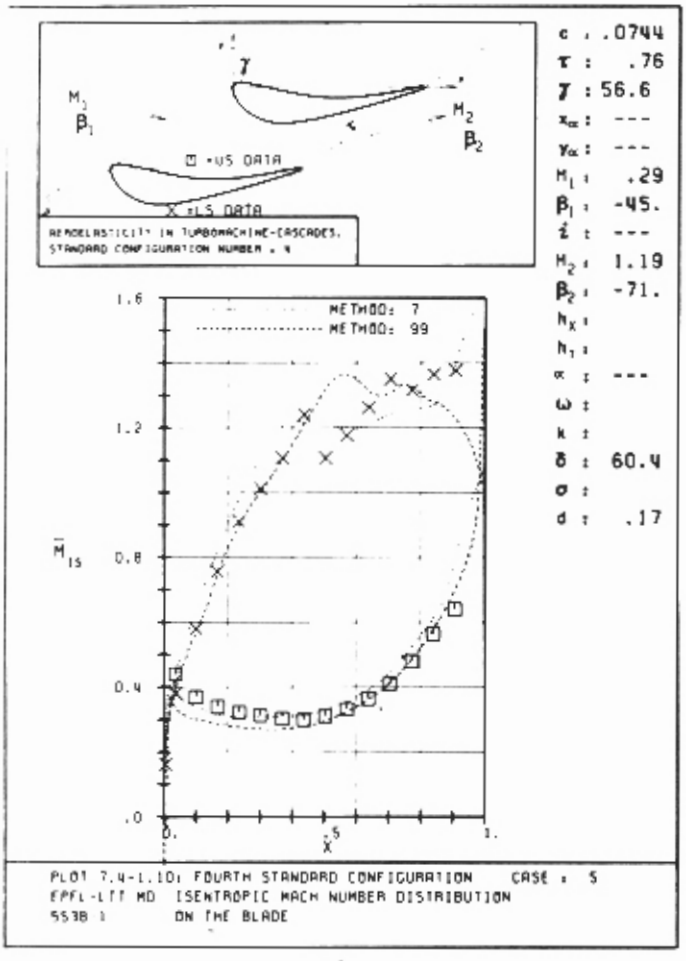


e)

Fig. 7.4-2. Fourth standard configurat
Time-averaged blade surface
isentropic Mach number distributio
for outlet Mach numbers
$M_{2is}$ = 0.58, 0.76, 0.90, 1.02, and 1

(at x≈0.75) is due to the reflection of the first shock on the wake of the neighboring blade (see Schlieren picture Fig. 7.4-6c), and can hardly be predicted by present theoretical models.

## Discussion of Time-Dependent Results

Before the comparison between the experimental data and the theoretical results is given, the influence of the ambiguity in the inlet flow angle on the time-dependent blade surface pressure responses should briefly be clarified.
It was concluded from Figures 7.4-2 and 7.4-3 that the theoretical models and the experimental steady-state data showed some discrepancies in the forward 30% of the blade, which probably appear because of an inaccuracy in the experimentally determined steady-state inlet flow angle. Such a difference may significantly influence the aeroelastic response for some cascades.

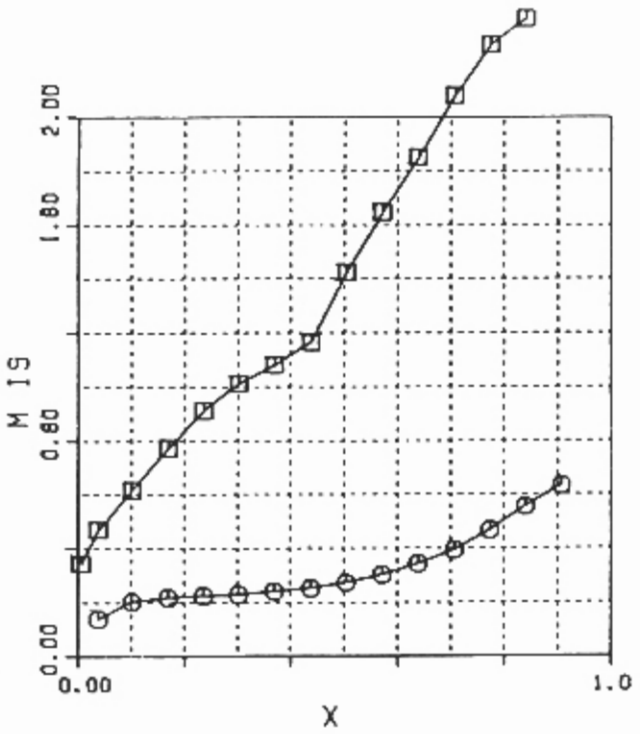


Annular test facility /23/

$M_1$=0.19 $M_1$=0.29; $\beta_1$=-23°; $M_2$=1.62

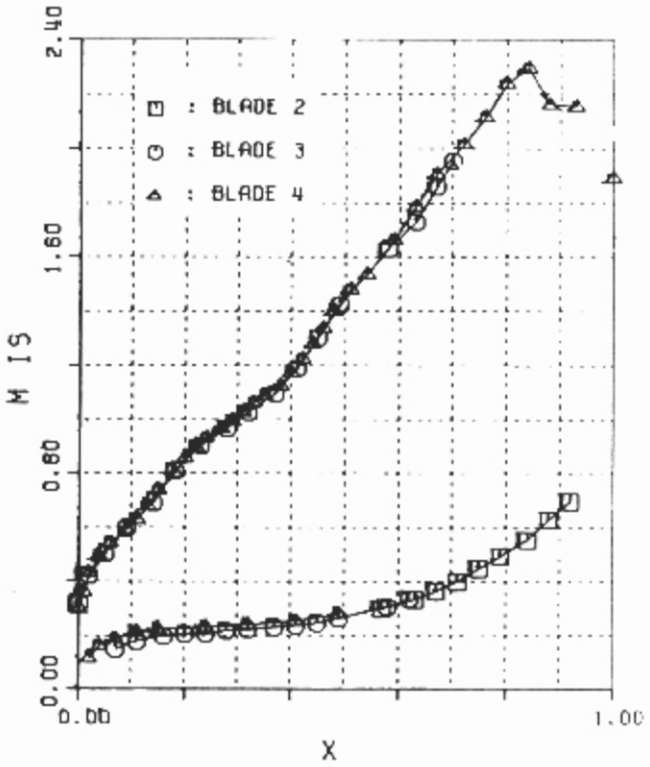


Linear test facility /25/

$M_1$=0.22; $\beta_1$=-20°; $M_2$=1.68

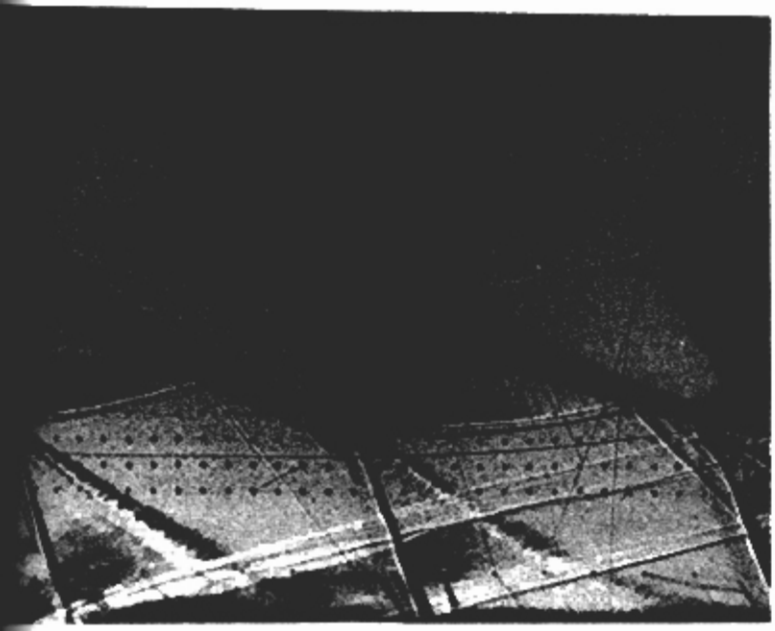

Schlieren from linear test facility /25/

$M_1$ = 0.23, $\beta_1$ = - 20°, $M_2$ = 1.68

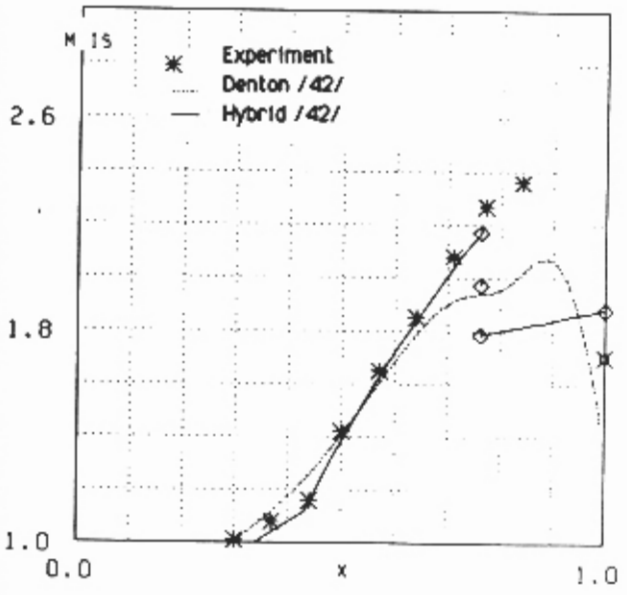


Comparison of experimental data from the annular test facility with two numerical methods

Fig. 7.4-3. Steady-state flow from tests in an annular test facility /23/, linear test facility /25/ and from two-dimensional flow calculations /42/ at an inlet flow angle of $\beta_1$=(-20° to -23°).

It can however, be concluded from Figures 7.4-4 and 7.4-5 that this is not the case around the nominal incidence angle, for the aft 90% of the turbine blade presented here (the first pressure transducer is situated at x = 0.101). In Fig 7.4-4 the measured time-dependent pressure, normalized with the upstream stagnation pressure, is represented along the chord for two inlet flow angles (-39° and -45°) for a subsonic outlet Mach number (M=0.6) It is seen here that the amplitude of the pressure fluctuation is, within the accuracy of the experiments, independent of an eventual error in the experimental inlet flow angle, both for the pressure and suction surface ($\Delta\beta_1$=6°) This is also true for the phase angle on the blade lower (suction) surface. The phase angle on the pressure side indicates instead a somewhat higher value, up to about x=0.4, for the case with the higher (negative) flow angle (inlet angle = -45°) However, the pressure amplitude is small in this part of the blade and the inaccuracy in the determination of the phase angle is thus fairly large[12] The absolute difference in the phase angles can thus vary somewhat.

In the case of a supersonic outlet velocity, the same representation (Fig. 7.4-5) indicates that the pressure amplitude on the upper (pressure) surface is fairly independent of an experimental inaccuracy in the inlet flow angle. Again, the higher (negative) flow angle (inlet flow angle = -45°) shows a higher phase value in the forward part of the blade.

On the blade suction (lower) surface, the pressure response is influenced by shock waves in the blade passage. The steady-state shock position is, as expected, the same for both inlet flow angles (Fig. 7.4-6, $x_{shock}$ = 0.45). Upstream of this position, the unsteady pressure coefficient phase angles ($\Phi_p^{us}$, $\Phi_p^{ls}$) are close to the ones at the subsonic Mach number ($M_{2is}$ = 0.6, Fig. 7.4-4), but change suddenly as response to the shockwave impinging upon the blade surface (Fig. 7.4-5, see also Schlieren picture in Fig. 7.4-6c).

However, the phase angles for both incidence angles are close to each other also in the vicinity and downstream of the shock, apart from the transducer at x=0.71 for 180° interblade phase. But here the pressure amplitudes are small, which again gives greater inaccuracy in the phase angle.

It can thus be concluded that, although a certain ambiguity exists in the absolute value of the inlet flow angle, a small variation around the nominal inlet angle (= -44°) does not seem to influence significantly the unsteady experimental blade surface pressure response, from x=0.1 onwards. Obviously,

---

[12] This phenomenon is explained in more detail in the following sections, see e.g. Fig. 7.4-8

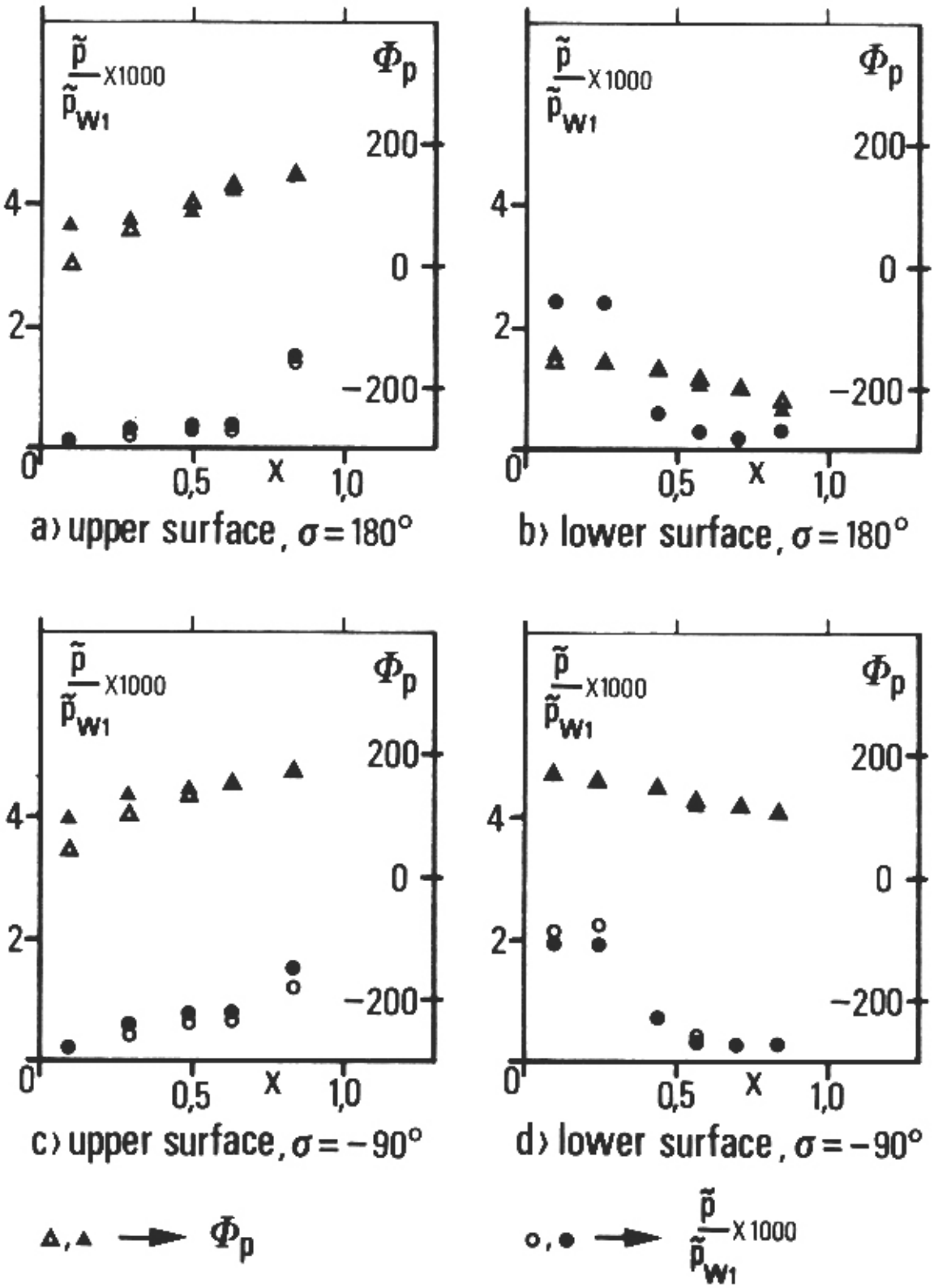


▲, ● $\beta_1 = -45°$, $M_{2is} = 0.58$

Δ, ○ $\beta_1 = -39°$, $M_{2is} = 0.59$

Fig. 7.4-4. Chordwise unsteady pressure distribution for two different inlet flow angles at $M_{2is} = 0.6$

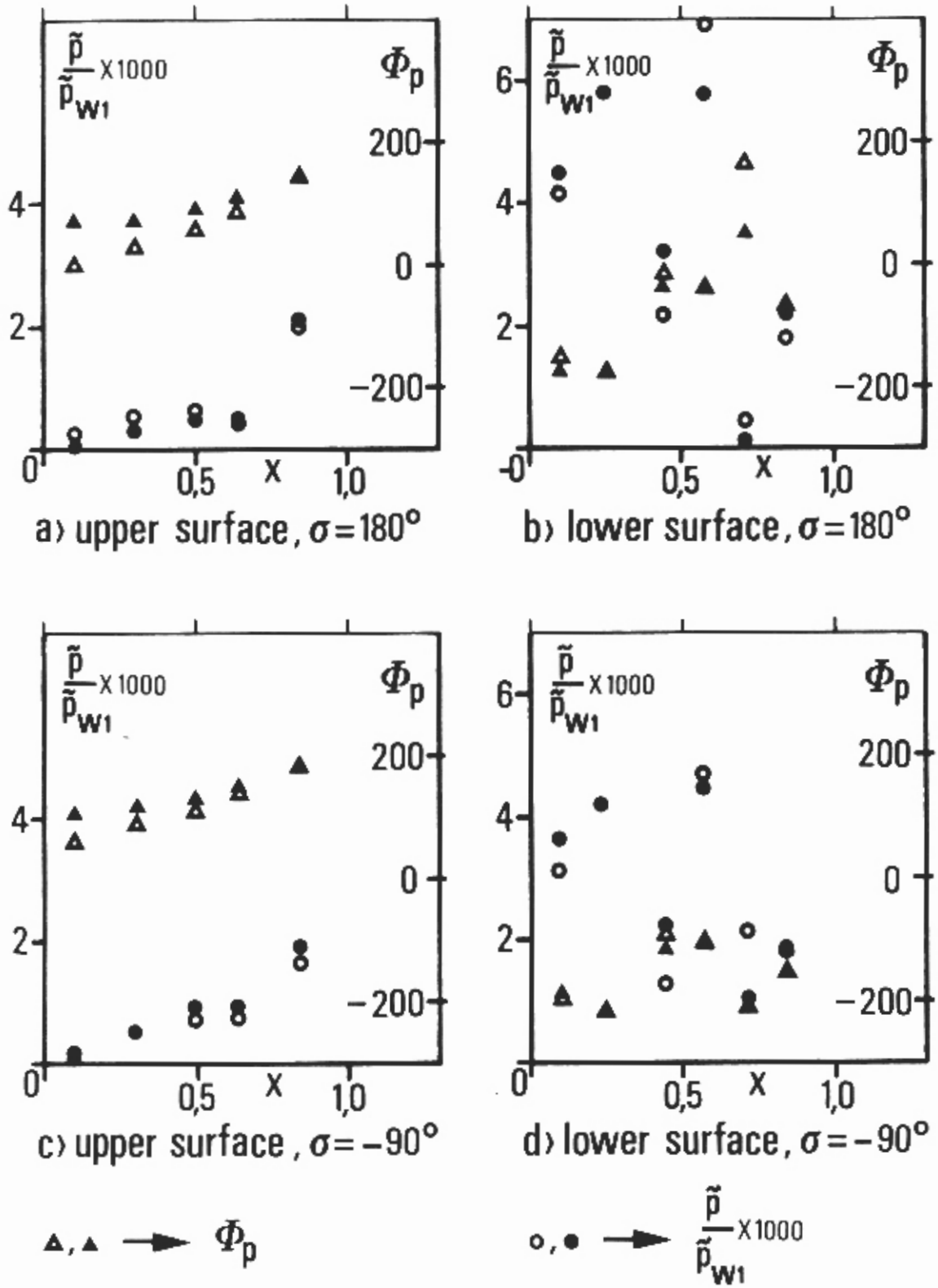


a) upper surface, $\sigma = 180°$

b) lower surface, $\sigma = 180°$

c) upper surface, $\sigma = -90°$

d) lower surface, $\sigma = -90°$

▲, ▲ → $\Phi_p$

○, ● → $\frac{\tilde{p}}{\tilde{p}_{w1}}$ X1000

▲, ● $\beta_1 = -45°$, $M_{2is} = 1.19$

Δ, ○ $\beta_1 = -36°$, $M_{2is} = 1.20$

Fig. 7.4-5. Chordwise unsteady pressure distribution for two different inlet flow angles at $M_{2is} = 1.2$

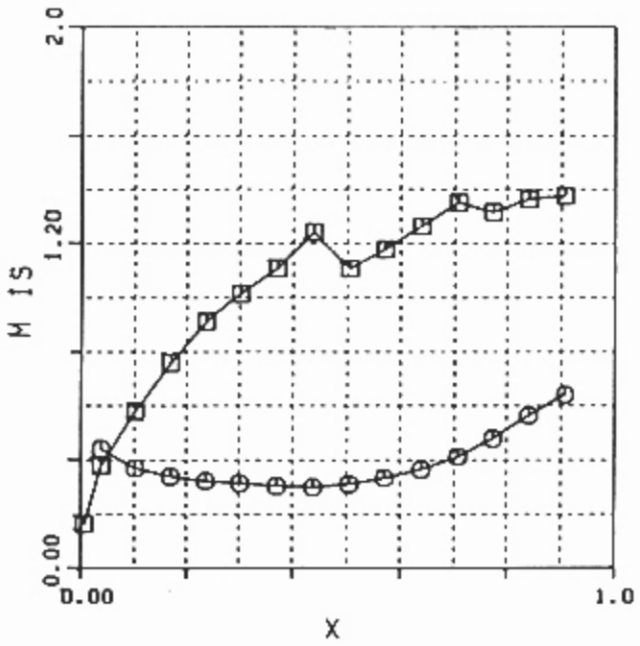


a) $\beta_1$=-45°, $M_{2is}$=1.19

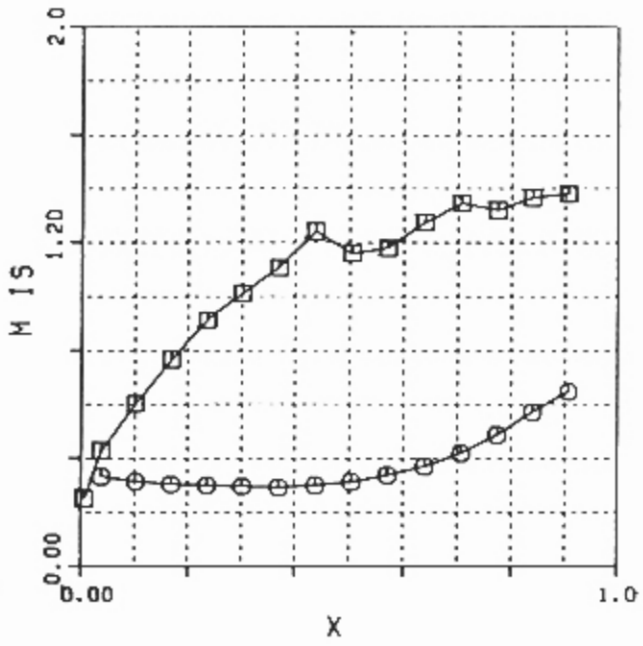


b) $\beta_1$=-37°, $M_{2is}$=1.20

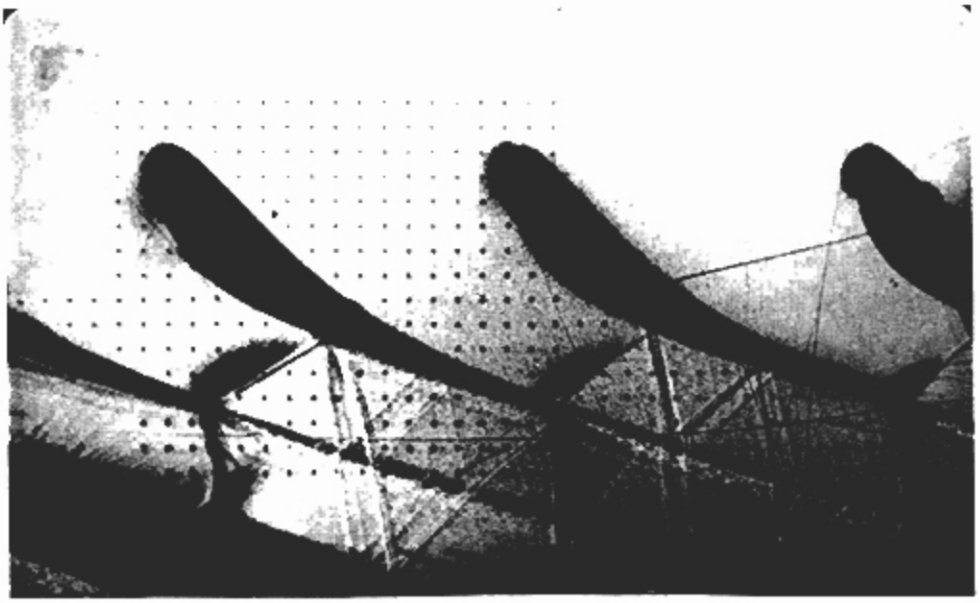

c) Schlieren picture from a linear test facility /25/. $\beta_1$=-20°; $M_{2is}$=1.16

Fig. 7.4-6. Time-averaged flow for $M_{2is}$=1.2

a change in incidence angle will influence the unsteady response closer to the leading edge.
Care should still be taken when comparing the amplitude of the unsteady pressure coefficient, $\Delta\tilde{c}_p$. This coefficient, as can be seen from eq. (3), is normalized with the steady-state dynamic pressure $(\bar{p}_{w1} - \bar{p}_1)$, which is dependent on the inlet flow angle.

Integrated values

The number of pressure transducers on the blades (6 on the suction surface, 5 on the pressure surface) is not enough to determine the blade force and aerodynamic damping coefficients accurately. However, as long as the unsteady pressure response along the blade is smooth (see for example Fig. 7.4-4) the trend of the integrated values should be correct although the magnitude will be inaccurate, depending especially on the pressure response close to the leading edge.
In Fig. 7.4-7a the aerodynamic damping coefficient is presented as a function of the interblade phase angle for two different inlet flow angles. For an inlet flow angle of -10° the tests have been performed with a variation of 18° interblade phase angle. The aerodynamic damping coefficient is represented together with the experimentally determined 95% confidence interval (see Appendix A4). The sinusoidal shape, as also seen for the first and second standard configurations, is recognized, although with some higher harmonics. It is concluded that the cascade shows instability for some interblade phase angles at an outlet Mach number of $M_{2is}$=0.9.
In the same diagram the four interblade phase angles defined as aeroelastic test cases (0°, 90°, 180°, 270°) for a -45° inlet flow angle are presented. Also at this flow angle the cascade shows instability in the region of a 270° interblade phase angle.
The same sinusoidal form is also recognized for other outlet flow velocities (Fig. 7.4-7b). Here it is also noted that, as already seen in Fig. 7.4-7a, the cascade is unstable, in subsonic flow, for interblade phase angles around 270° (=-90°). However, for a supersonic outlet Mach number of $M_{2is}$=1.19 the aerodynamic damping coefficient indicates instead a stable blade vibration at this interblade phase angle. This phenomenon which is also present for other flow angles, will be discussed at the same time as the local blade surface pressures.
Up till now, only two methods (N° 10, semi actuator disk theory, N° 7, finite element, potential flow) have been applied to calculate the aerodynamic

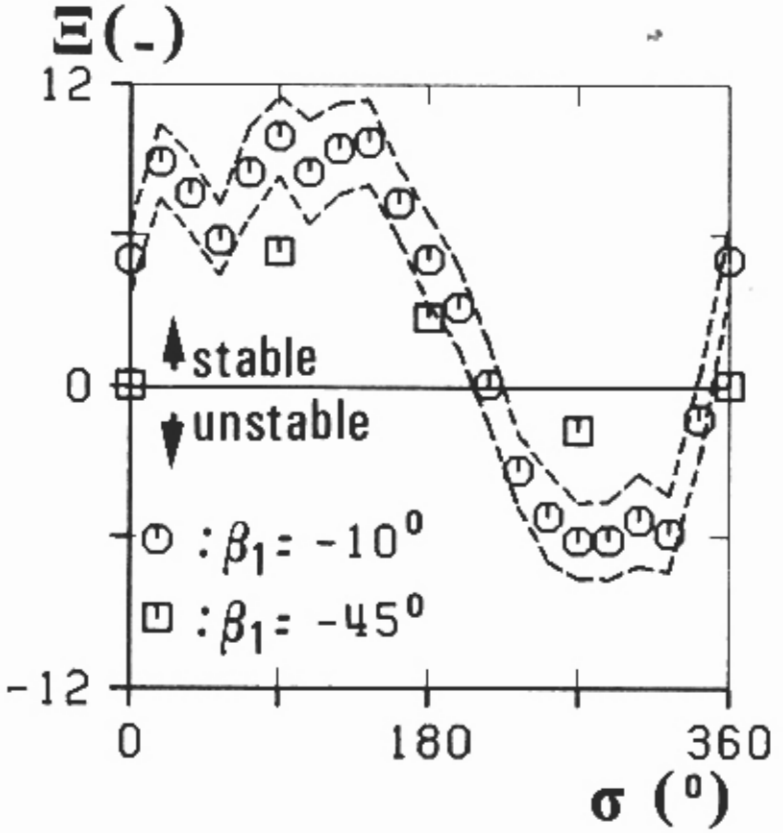


a) Aerodynamic damping coefficient for two different inlet flow angles at $M_{2is}$=0.90.

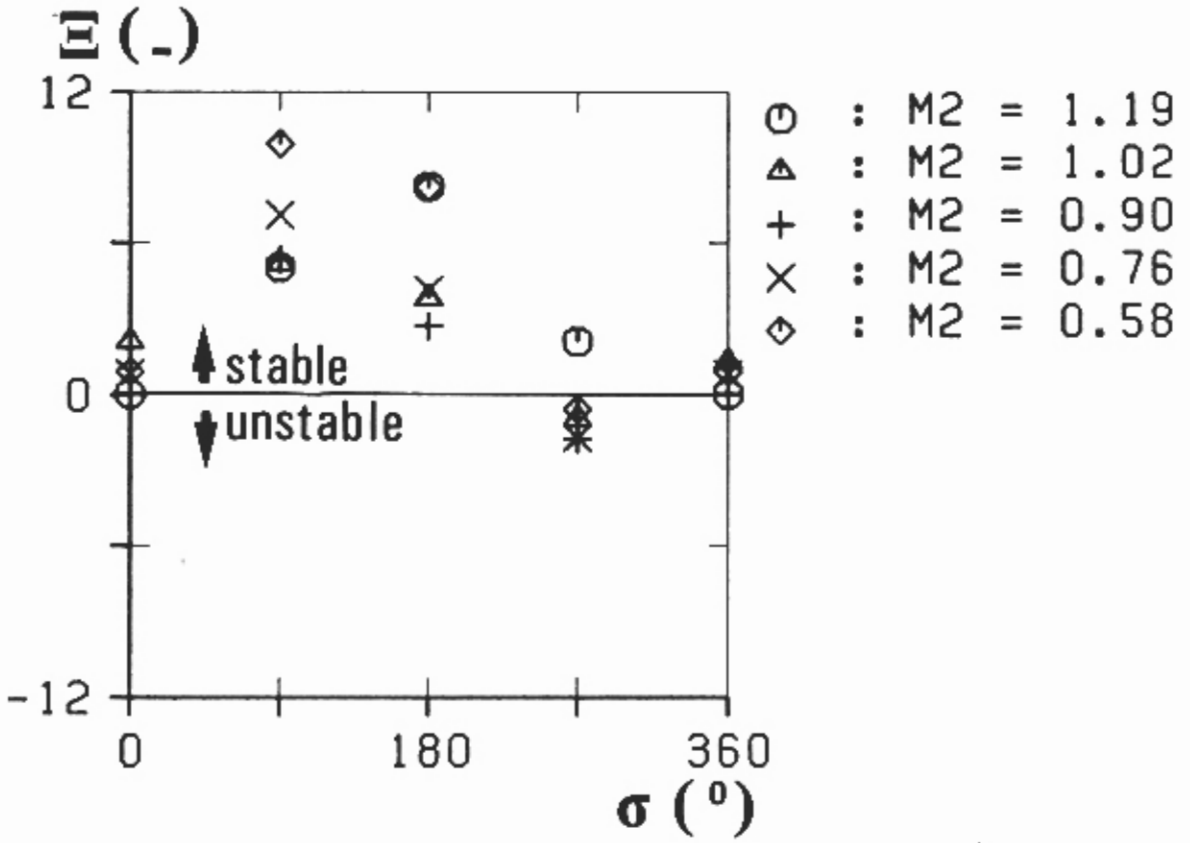


b) Aerodynamic damping coefficient for different outlet isentropic Mach numbers at an inlet flow angle of -45°

Fig. 7.4-7. Experimentally determined aerodynamic damping coefficient

damping coefficient. These results are given in Fig. 7.4-8, together with the experimental data (including 95% confidence interwals) for the 8 aeroelastic test cases selected. It can be seen that, by comparing Fig. 7.4-8a and c, the shape of the aerodynamic damping coefficient versus the interblade phase angle is similar for both theory and experiment. The results of Method 7 and the data agree well, apart from at $\sigma$=90°. However, the maximum damping value is not reached at the same interblade phase angle for Method 10, and the predicted results for this method are one order of magnitude larger than the measured ones.

The experimentally determined aerodynamic damping coefficient versus the outlet Mach number, for $\sigma$=-90°, agree well with the results predicted by Method 7 (Fig. 7.4-8b). However, the shape for Method 10 does not agree with the data (figs 7.4-8b,d).

Although the order of magnitude of the damping coefficient is the same for both the Method 10 and the experiment, the theory predicts a stable vibration for subsonic Mach numbers, whereas the experiments (and Method 7) indicate a stability for the supersonic Mach number instead. At present the reason for this discrepancy is not clear, and the author of Method 10 believes that the effect of blade camber in the semi-actuater disk theory should be validated [56]. Obviously, an inaccuracy in the experimental results cannot be excluded a priori but the experimental data agree well with results from Method 7 , so it is probable that the experiments are correct in trend and order of magnitude of the aerodynamic damping coefficient.

The reason for the discrepancy between experiment and Method 7 at 90° interblade phase angle is found by examining the local blade surface pressures, and will be discussed in that section.

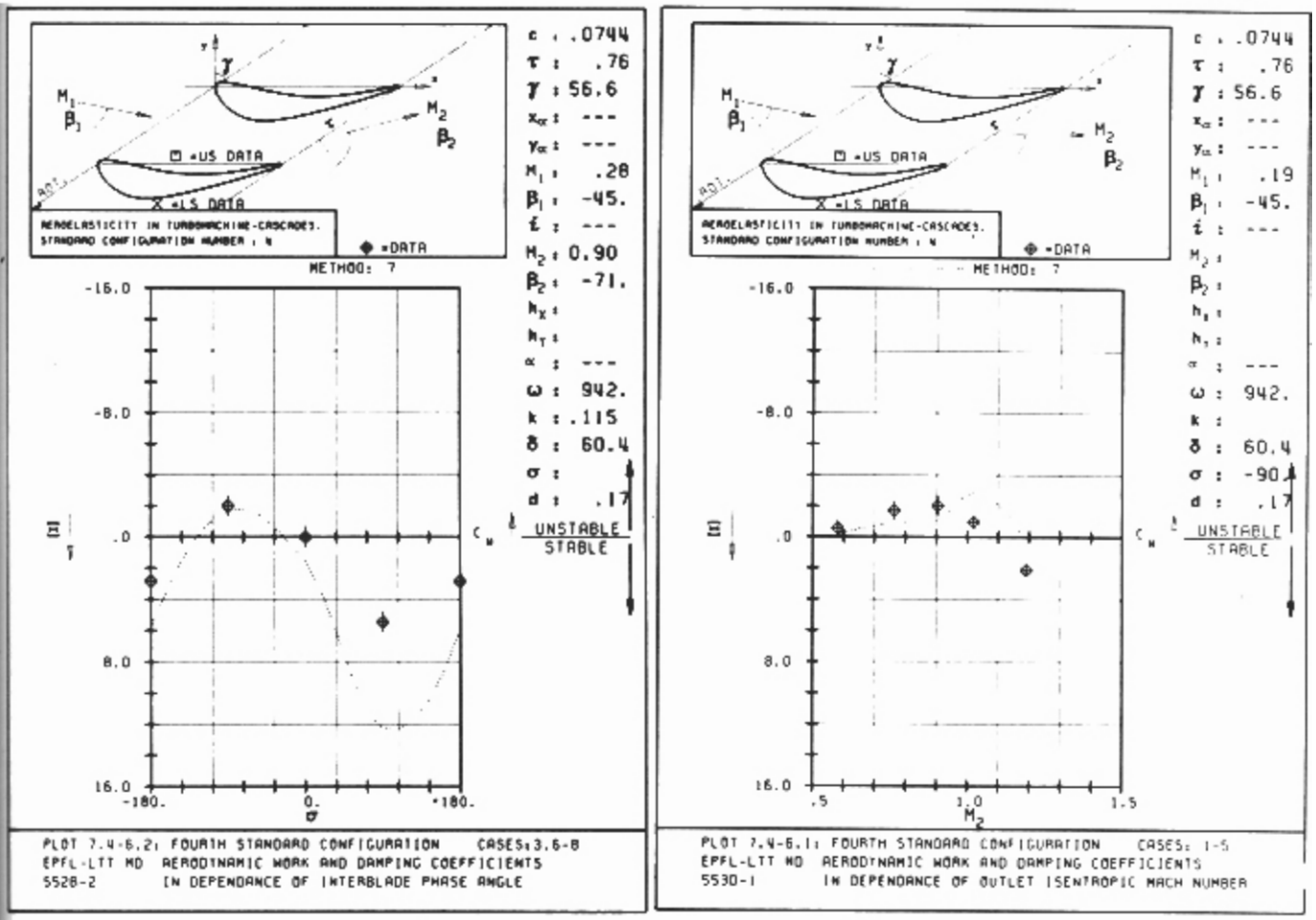


a) b)

Experimental data (with 95% confidence interval) and predicted results.

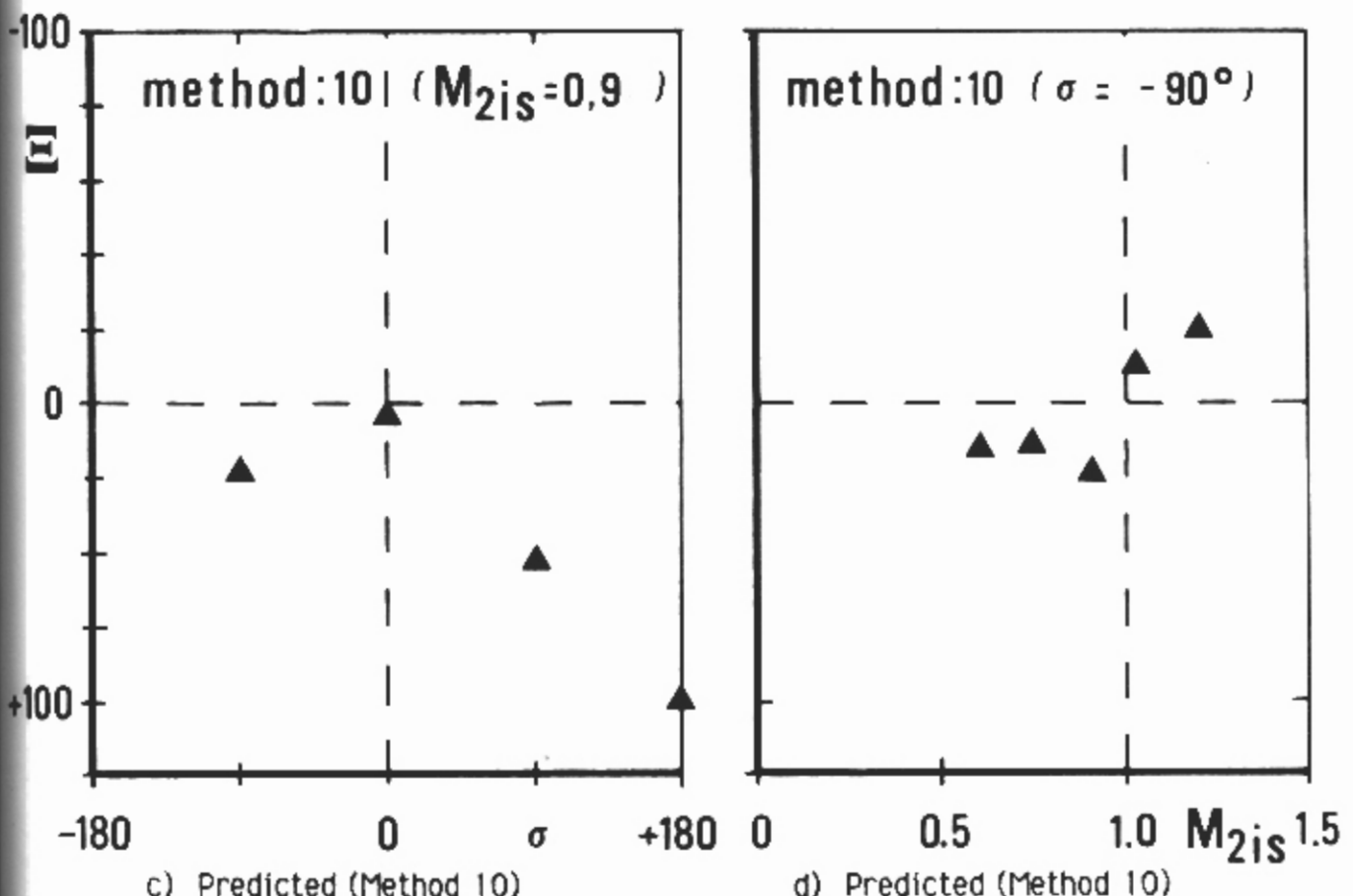


c) Predicted (Method 10) d) Predicted (Method 10)

**Fig. 7.4-8.** Experimental aerodynamic damping coefficient together with predicted results from Methods 7 and 10.

Blade Surface Pressures

Theoretical results from one method (N° 7) have been obtained for this standard configuration. In general, data and the predicted results agree well (Fig. 7.4-9), both as regards the amplitude and the phase angle of the pressure coefficient $c_p(x,t)$ along the blade chord.

The experimental accuracy, represented in Fig. 7.4-9 as a 95% confidence interval (see Appendix A4), shows as expected that the uncertainty in the measured phase angle is greater when the pressure amplitude is smaller. Considering this confidence interval, the data and the prediction agree extremely well for the subsonic cases (Fig. 7.4-9a,b,c; compare Fig. 7.4-2a,b,c for steady-state blade surface distribution) at -90° interblade phase angle. This is true for both the amplitude and the phase angle.

Especially interesting to note is that the trend is correct for all cases. On the pressure (upper) surface of the blade the only notable exception is the first pressure transducer (x=0.1) which indicates a low pressure amplitude, whereas the theory predicts a higher value here.

Towards the trailing edge (last transducer at 84% chord) both theory and experiment predict an increase in the unsteady pressure amplitude on the pressure surface. The value here approaches the magnitude of the pressure amplitude around the 20% chord on the blade suction surface. This can possibly be explained by the fact that the last transducer on the pressure surface and the second on the suction surface are both situated in the vicinity of the throat (see Fig. 7.4-1b), and that the aerodynamic coupling effects are therefore high. It can also be seen that the phase angles in these two positions are fairly close together (e.g. $\Phi_p^{us}$ (x=0.84) = +170°, $\Phi_p^{ls}$(x=0.24) = +160° in Fig. 7.4-9a).

The same conclusions can also be drawn from other phase angles, as long as the flow is subsonic (Fig. 7.4-9f,g,h for 180°, 90°, 0° respectively), apart from the phase angles with in-phase blade motion (Fig. 7.4-9h). In this last case the experimental and theoretical results show instead a discrepancy of the order of 90° or more, and the experimental data on the suction surface show some fairly large irregularities. The phase shift of 180° between the two pressure tranducers located at x=0.24 and x=0.44 is particularly interesting. The same phenomenon is found also for all other inlet flow angles and outlet flow velocities investigated [23], but no explanation for this has yet been put forward. However, it should be noted that the unsteady pressure signals at $\sigma$=0° are weak, and the confidence interval is large for almost all pressure transducers.

The reason for the difference in aerodynamic damping coefficient between experiment and Method 7 at $\sigma$=90°, as found in Fig. 7.4-8a, can now be explained on the basis of Figs.7.4-9. It is here seen (Fig. 7.4-9g) that the theory predicts a somewhat higher pressure value along the whole suction surface than the experiment for this interblade phase angle. The phase angles are predicted just as well for $\sigma$=90° as for other phase angles, wherefore the difference in $\Xi$ can be attributed to differences in the pressure amplitude. However, no explanation for why the difference in $\hat{c}_p^{(us)}$ between experiment and theory is larger for $\sigma$=90° than for other interblade phase angles is presently put forward.

As the back pressure is lowered towards transonic and supersonic outlet velocities the unsteady pressure amplitude and phase angle on the pressure surface do not significantly change from the result in the subsonic cases (Fig. 7.4-9d,e). On the other hand, larger differences are notable on the suction surface

First of all it is concluded from Fig. 7.4-2d and 7.4-9d that the transition from subsonic to supersonic flow on the blade suction surface (x=0.45) introduces a phase shift in the unsteady pressures for a transonic outlet condition ($M_{2is}$=1.02) at a -90° interblade phase angle. This shift is present both in the experimental and theoretical results, although to a larger extent in the experiment. Aft of the sonic transition the theory indicates an increase in the unsteady pressure amplitude, which is not seen in the experiment. Towards the trailing edge both the theoretical and experimental pressure amplitude increases probably due to the presence of a shock wave, although not on the same scale. It should however again be noted that the last pressure transducer is situated at 84% chord and the experiments indicate that the shock at an isentropic outlet Mach number of $M_{2is}$=1.02 is situated somewhat closer to the trailing edge (Fig. 7.4-10).

Again, as in the subsonic cases, the experimental increase in pressure amplitude towards the pressure surface trailing edge is larger than the theoretically determined one. The pressure surface phase angle ($\Phi_p^{us}$) is, however, well predicted (Fig. 7.4-9d).

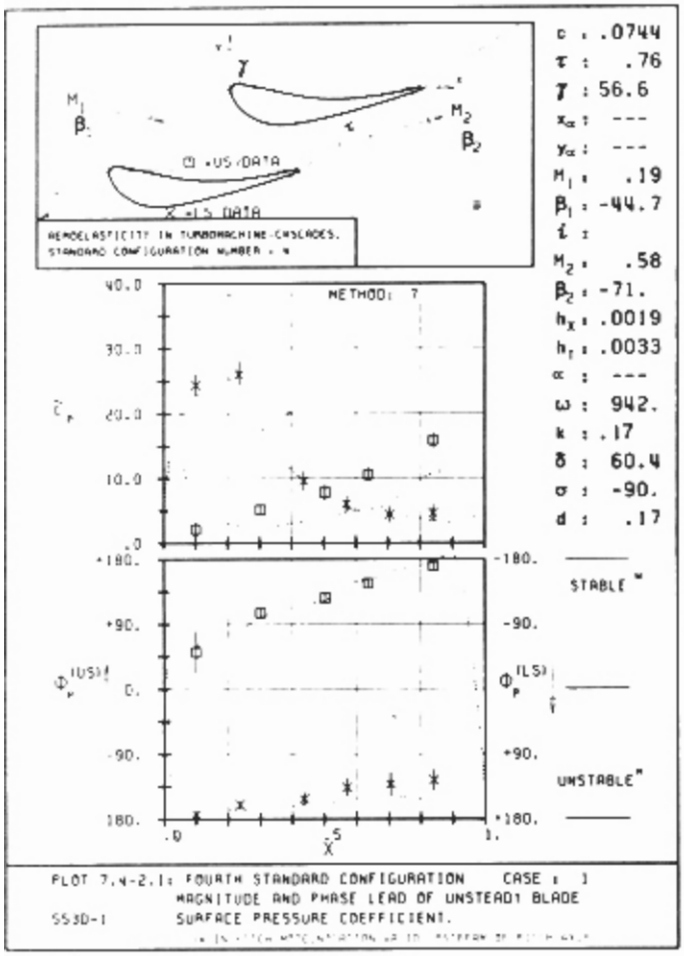


PLOT 7.4-2.1: FOURTH STANDARD CONFIGURATION CASE : 1
MAGNITUDE AND PHASE LEAD OF UNSTEADY BLADE
553D-1 SURFACE PRESSURE COEFFICIENT.

a)

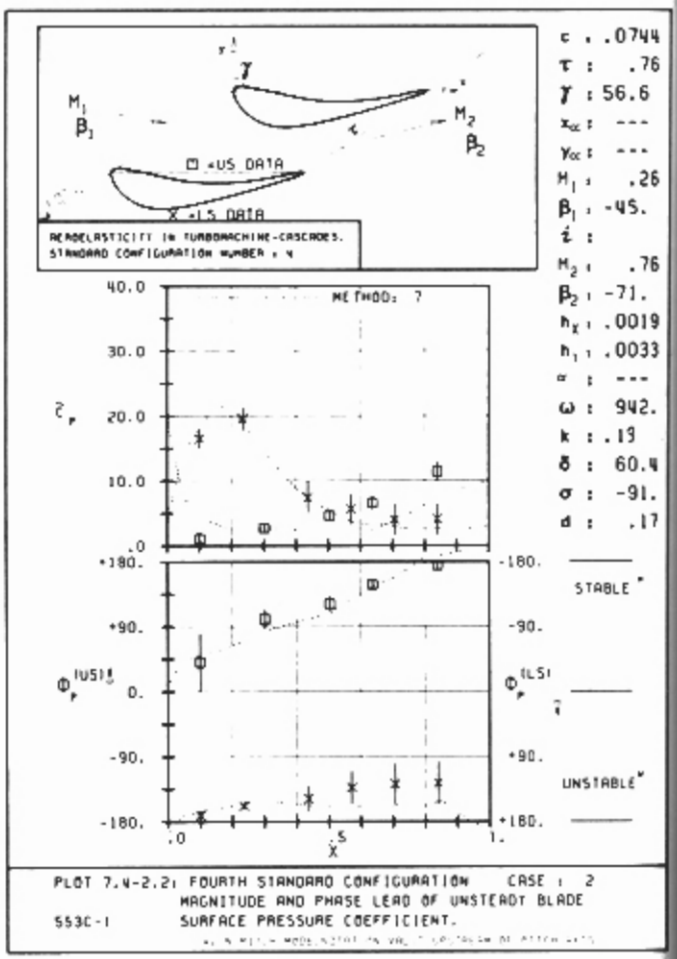


PLOT 7.4-2.2: FOURTH STANDARD CONFIGURATION CASE : 2
MAGNITUDE AND PHASE LEAD OF UNSTEADY BLADE
553C-1 SURFACE PRESSURE COEFFICIENT.

b)

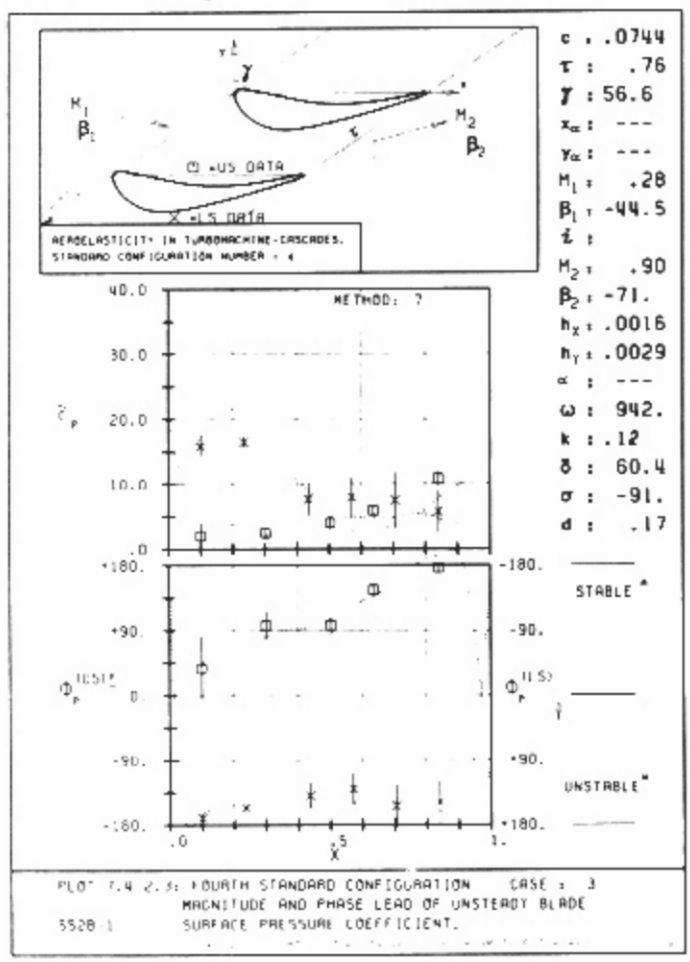


PLOT 7.4-2.3: FOURTH STANDARD CONFIGURATION CASE : 3
MAGNITUDE AND PHASE LEAD OF UNSTEADY BLADE
552B-1 SURFACE PRESSURE COEFFICIENT.

c)

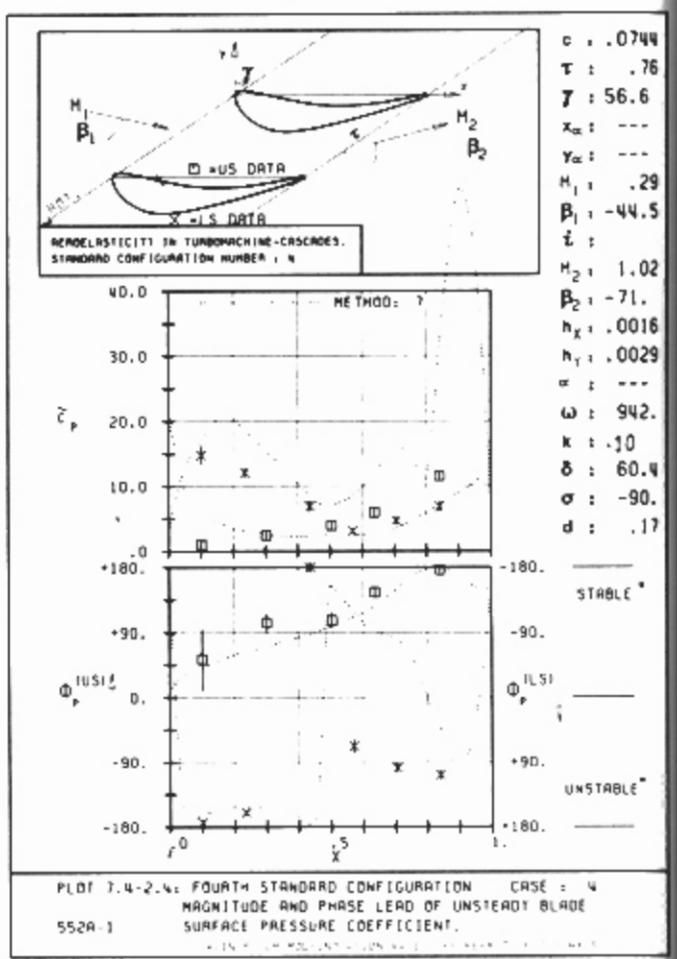


PLOT 7.4-2.4: FOURTH STANDARD CONFIGURATION CASE : 4
MAGNITUDE AND PHASE LEAD OF UNSTEADY BLADE
552A-1 SURFACE PRESSURE COEFFICIENT.

d)

Fig. 7.4-9. Continued on next page

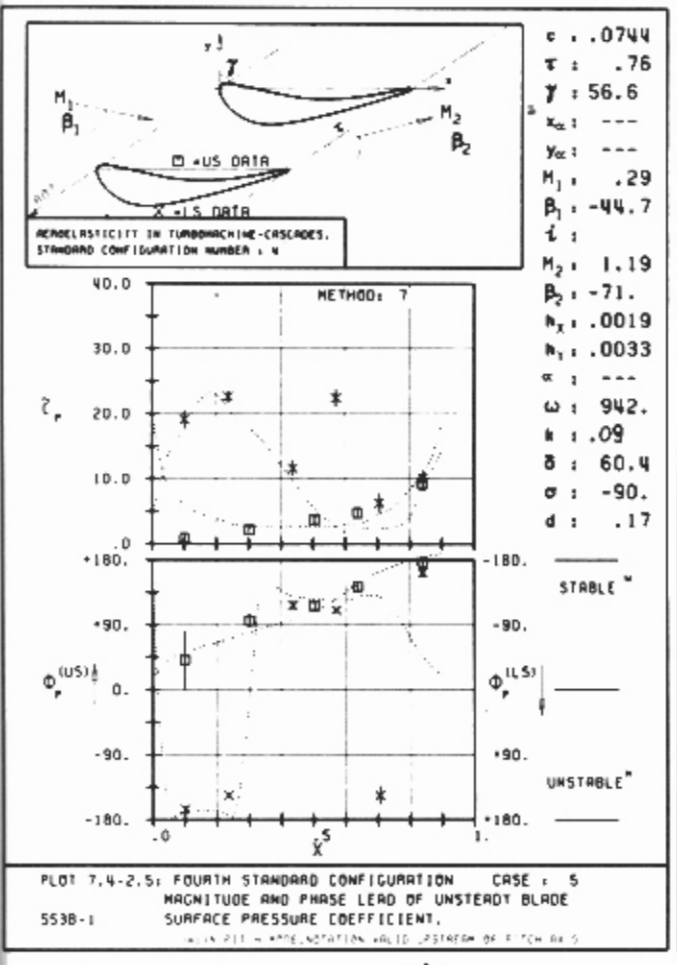


PLOT 7.4-2.5: FOURTH STANDARD CONFIGURATION CASE : 5
MAGNITUDE AND PHASE LEAD OF UNSTEADY BLADE
553B-1 SURFACE PRESSURE COEFFICIENT.

e)

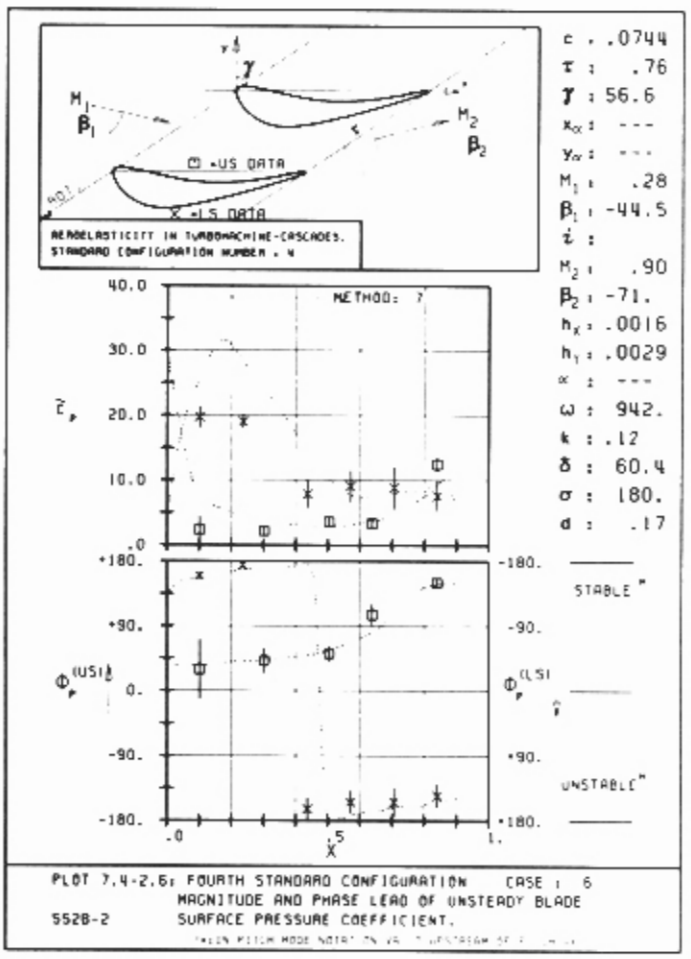


PLOT 7.4-2.6: FOURTH STANDARD CONFIGURATION CASE : 6
MAGNITUDE AND PHASE LEAD OF UNSTEADY BLADE
552B-2 SURFACE PRESSURE COEFFICIENT.

f)

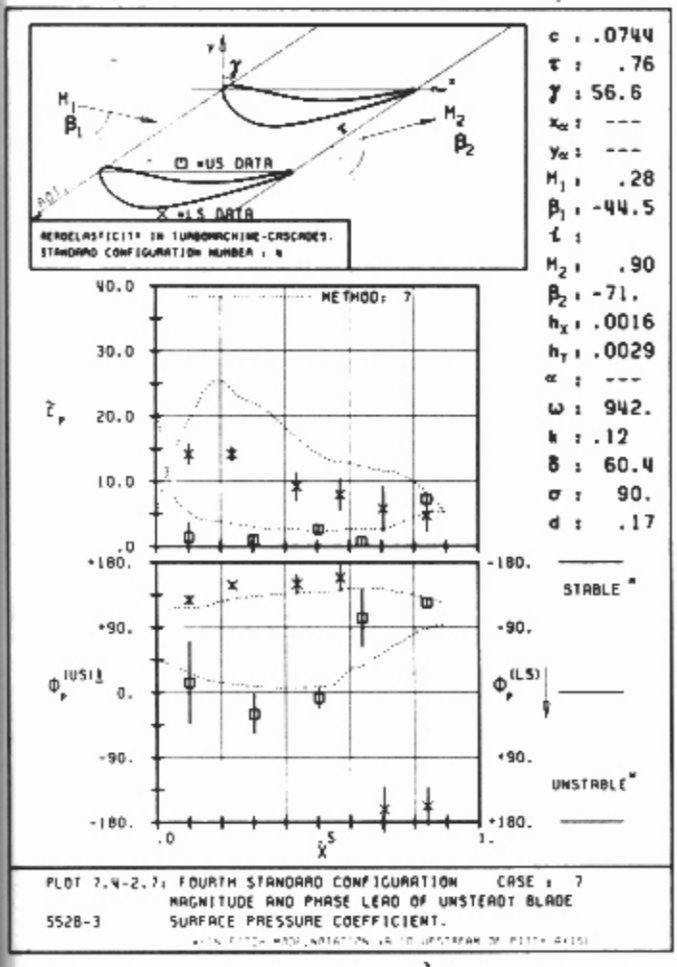


PLOT 7.4-2.7: FOURTH STANDARD CONFIGURATION CASE : 7
MAGNITUDE AND PHASE LEAD OF UNSTEADY BLADE
552B-3 SURFACE PRESSURE COEFFICIENT.

g)

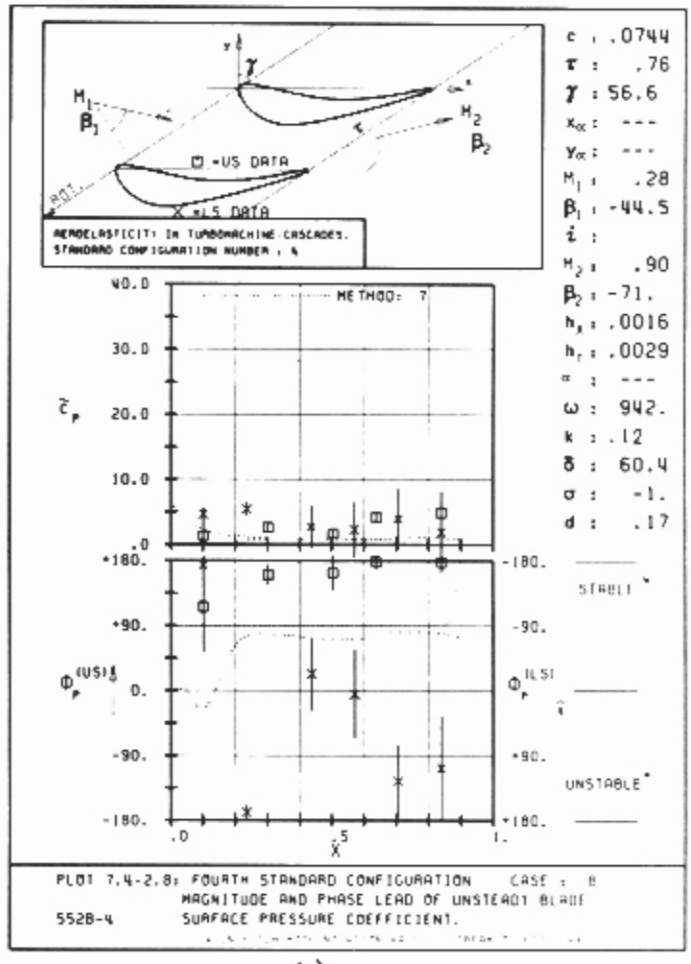


PLOT 7.4-2.8: FOURTH STANDARD CONFIGURATION CASE : 8
MAGNITUDE AND PHASE LEAD OF UNSTEADY BLADE
552B-4 SURFACE PRESSURE COEFFICIENT.

h)

Fig. 7.4-9. Unsteady blade surface pressure coefficient for the 8 aeroelastic test cases (vertical bars in the data points indicate 95 % confidence interval)

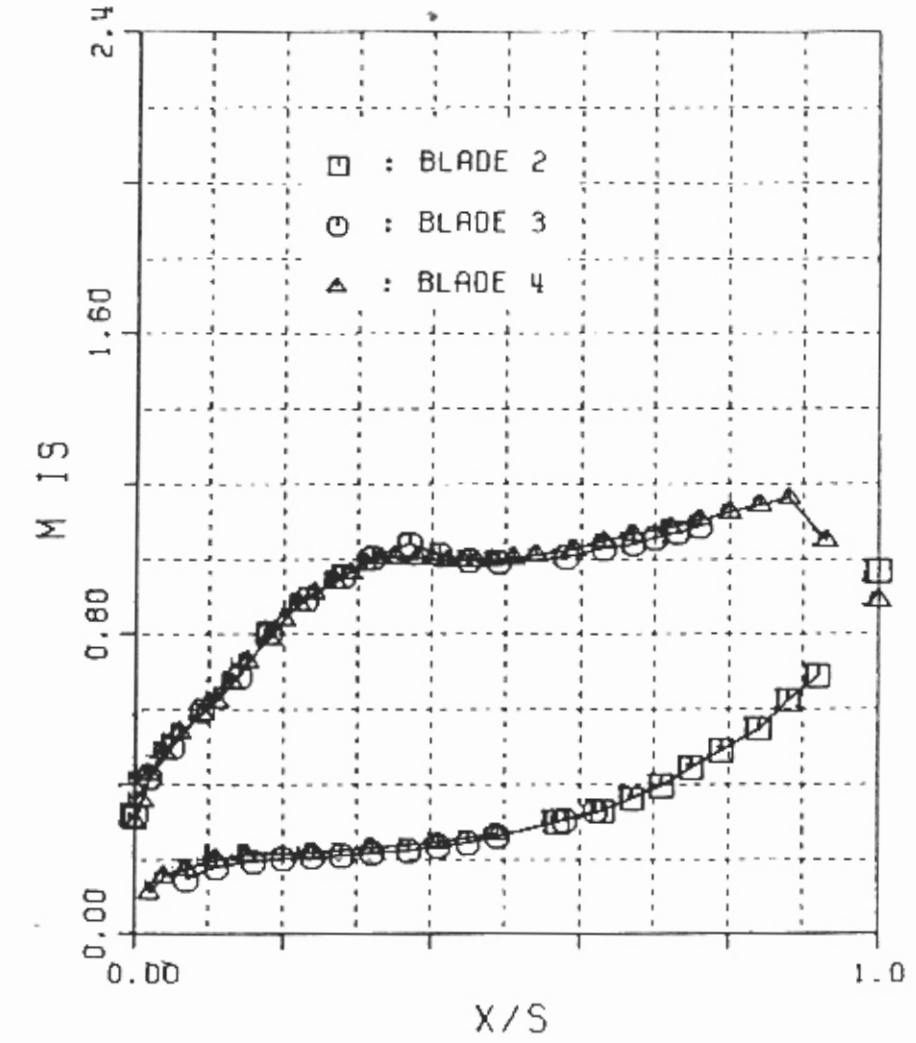


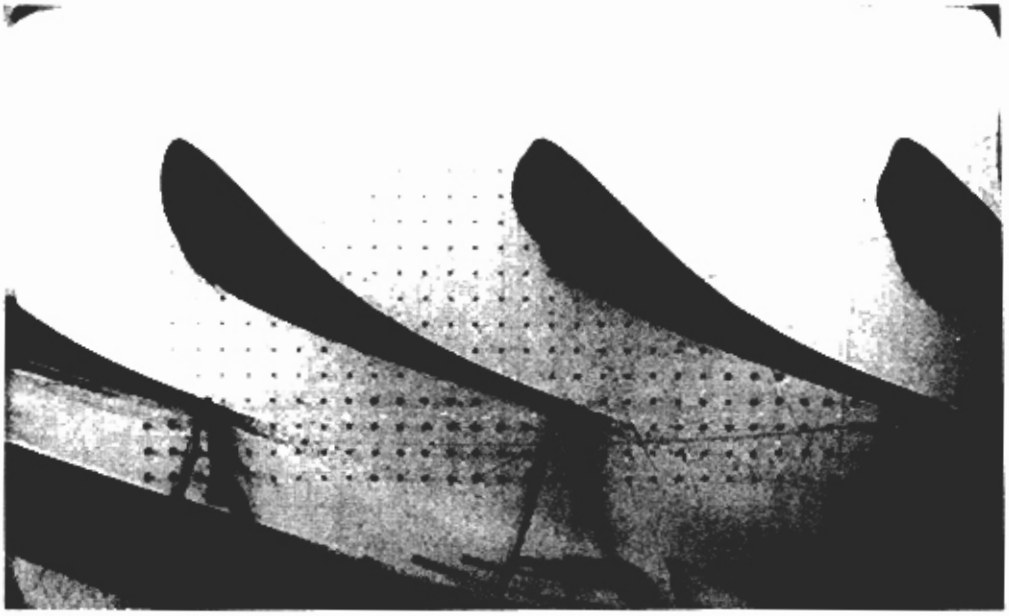

Fig. 7.4-10. Flow through the cascade at an isentropic outlet Mach number $M_{2is}$=1.02 in a linear test facility /25/.

As the back pressure is lowered ($M_{2is}$=1.2, Fig. 7.4-9e), the experimental and predicted results still agree well on the pressure surface. This is also true for the suction surface, upstream of the shockposition ($x_{shock}$=0.5, see Fig. 7.4-2e). However, for this outlet Mach number, contrary to test case 4 ($M_{2is}$=1.02), the experiment shows a larger influence of the shock on the unsteady pressure amplitude than the theory. Furthermore, the suction surface phase angle ($\Phi_p^{ls}$) shows some discrepancies between theory and prediction aft of the shock.

As seen in Fig. 7.4-8a the cascade configuration showed an instability at high subsonic Mach numbers at $\sigma$=-90°, whereas other interblade phase angles showed stability. The reason for this change of sign in the aerodynamic damping coefficient can be found by investigating the unsteady blade surface pressures for $\sigma$=-90° and $\sigma$=+90° at an outlet Mach number of $M_{2is}$=0.90 (Fig. 7.4-9c,g). It can be seen that the experimental blade surface pressure amplitudes ($\tilde{c}_p$) are similar in both cases. Case 7 ($\sigma$=+90°) is stable mainly because the forward 60% on the suction surface are stable. However, case 3 ($\sigma$=-90°) is unstable as the whole suction surface is unstable.

No physical explanation for this change of stability can presently be given.

It is also interesting to note that the two last pressure transducers on the suction surface indicate almost the same amplitudes and phase angles for $\sigma$=-90° as for $\sigma$=+90°, and that the first four suction surface tranducers change at an almost constant value with the variation in interblade phase angle. ($\delta\Phi_p^{ls}=\Phi_p^{ls}(\sigma=+90°)-\Phi_p^{ls}(\sigma=-90°)$ = 62°, 55°, 71° and 71°, resp., see Figs. 7.4-9c,g and data sheets in Appendix A5, section 4.). The same trend can be recognized from the prediction model 7 for x<0.6. Aft of this position a larger difference is found in $\Phi_p^{ls}$ between theory and experiment. A possible explanation for this phenomenon could be the hypothesis of a small separation bubble on the last 30% of the suction surface at $M_{2is}$=0.9 [28].

From Fig. 7.4-8b it was also concluded that the cascade configuration became stable with an increasing Mach number. Once again, the reason can be found by investigating the unsteady blade surface pressure distribution (Fig. 7.4-9c,e for $M_{2is}$=0.9, 1.2 resp.).

It can be seen that the pressure surface data are identical for both Mach numbers. However, the suction surface pressure amplitude and phase angle are different at x=0.5. At $M_{2is}$=0.9 the phase angles indicate instability at x=0.5, while at $M_{2is}$=1.2 the same transducers instead show a high stability ($\Phi_p^{ls}$=-90°) This change in stability can thus clearly be attributed to the presence of the shock at 50% chord, and it can be concluded that the shock has a stabilizing effect, at least for low supersonic outlet flow velocities.

## Conclusions for the Fourth Standard Configuration

From the controlled excitation study in traveling wave mode (i.e. constant interblade phase angle between all blades) on a 17% thick, 45° cambered steam turbine cascade, experimentally investigated in an annular test facility in subsonic and supersonic flow, it can be concluded that:

- The fact that the unsteady experimental data and the (by Method 7) predicted results agree well validates mutually both approaches, at least for shock-free flows.
- Prediction model 7 gives a good overall view of the unsteady blade surface pressures for subsonic outlet flow conditions. In the transonic and supersonic cases some discrepancies between the experiments and theory can be found in the vicinity of the shocks.

Conclusions for aerodynamic damping:

- The experimental data indicate a slight instability at subsonic outlet Mach numbers (for $\sigma$=-90°), and stable vibrations for supersonic outlet flow conditions. This behavior is predicted by Method 7 but not by Method 10 (semi-actuator disk theory) (see Figs. 7.4-7, 7.4-8).

Conclusions for unsteady blade surface pressures:

- The local unsteady blade surface pressure coefficient on the upper and lower surfaces is well predicted by Method 7 for subsonic flow conditions, especially by considering the experimentally determined 95% confidence interval (Fig. 7.4-9). The only noticeable exception is the first transducer on the pressure surface, located at x=0.101.
- Also for supersonic outlet flow conditions, the experimentally determined unsteady pressures on the upper (= pressure) surface are predicted well, both as regards amplitude and phase angle (Fig. 7.4-9d,e).
- Some discrepancies between the unsteady pressure data and predicted results exist on the suction surface for supersonic outlet Mach numbers (Figs 7.4-9d,e). Here, the unsteady shock impinging on the blade suction surface does not appear in the same way in the theory and the experiment
- The change in stability at approximately sonic outlet conditions can be attributed, both in the experiment and in Method 7, to a change in the local unsteady blade suction surface pressures in the vicinity of the shock.

## 7.5 Fifth Standard Configuration (Compressor Cascade in High Subsonic Flow).

### Definition

This two-dimensional subsonic/transonic cascade configuration has been tested in a rectilinear cascade air tunnel at the Office National d'Etudes et de Recherches Aérospatiales (ONERA). The configuration and experimental results are included by kind permission of E. Szechenyi ([29-31]).

The cascade configuration consists of six fan stage tip sections, each blade with a chord of c=0.090 m and a span of 0.120 m. The maximum thickness-to-chord ratio is 0.027, with no camber and a gap-to-chord ratio of 0.95. The present configuration was measured with a stagger angle of 59.3°.

The cascade geometry is given in Figure 7.5-1 and the profile coordinates in Table 7.5-1.

The two center blades can vibrate in pitch about several axes, and then the aeroelastic coefficients for different interblade phase angles can be computed by linearized summation of the unsteady pressure responses on all six blades.

Experiments have been performed with oscillation frequencies between of 75 and 550 Hz, inlet Mach numbers of between 0.5 and 1.0 and with incidence angles between attached and fully separated flow (2° to 15°).

Both the time-averaged and time-dependent instrumentation on this cascade is extensive and a large amount of well-documented data has been obtained during the experiments. The large number of flush-mounted high response pressure transducers on one blade (9 on lower blade surface and 10 on upper blade surface) allows the determination of resultant time-dependent blade forces.

The upstream and downstream steady-state flow quantities are determined 2 chord lengths upstream of the leading edge plane and 0.5 chord length downstream of the trailing edge plane, respectively.

The unsteady pressure measurements are all filtered, simultaneously sampled, multiplexed, digitized, averaged over a certain number of periods and recorded on disc after which the pressure, lift and moment coefficients are computed [29].

**High Subsonic Compressor Profiles.**

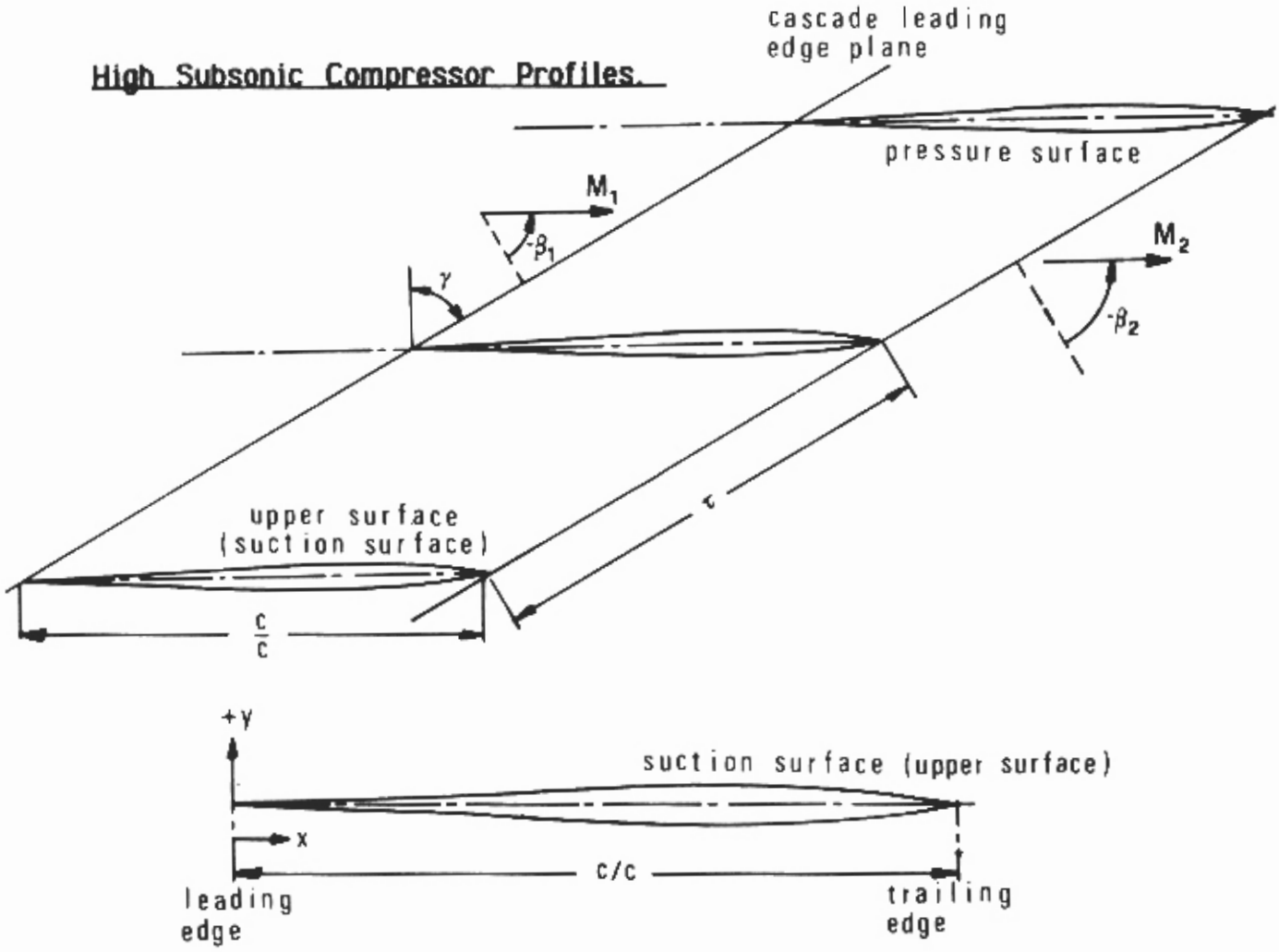


| | | | |
|---|---|---|---|
| Maximum thickness at x | | = | 0.67 |
| Vibration in pitch around $(x_\alpha, y_\alpha)$ | | = | (0.5,0.) |
| d = (thickness/chord) | | = | 0.027 |
| $\alpha$ = 0.00524 rad | f | = | variable (75-550 Hz) |
| c = 0.090 m | i | = | variable (2°-15°) |
| $\tau$ = 0.95 | camber | = | 0° |
| k = variable | $\gamma$ | = | 59.3° |
| span = 0.120 m | $\sigma$ | : | Only one blade vibrated |
| $M_1$ = variable (0.5-1.0) | | | |
| Working fluid: Air | | | |

Fig. 7.5-1. Fifth standard configuration: Cascade geometry

| c = 0.090 m | | |
|---|---|---|
| | Upper surface (Suction surface) | Lower surface (Pressure surface) |
| x | y | y |
| 0. | 0. | 0. |
| 0.0124 | 0.0016 | -0.0016 |
| 0.0250 | 0.0018 | -0.0018 |
| 0.0500 | 0.0026 | -0.0026 |
| 0.0750 | 0.0033 | -0.0033 |
| 0.1000 | 0.0041 | -0.0041 |
| 0.1500 | 0.0053 | -0.0053 |
| 0.2000 | 0.0062 | -0.0062 |
| 0.2500 | 0.0079 | -0.0079 |
| 0.3000 | 0.0101 | -0.0101 |
| 0.3500 | 0.0103 | -0.0103 |
| 0.4000 | 0.0111 | -0.0111 |
| 0.4500 | 0.0119 | -0.0119 |
| 0.5000 | 0.0124 | -0.0124 |
| 0.5500 | 0.0128 | -0.0128 |
| 0.6000 | 0.0133 | -0.0133 |
| 0.6500 | 0.0135 | -0.0135 |
| 0.7000 | 0.0135 | -0.0135 |
| 0.7500 | 0.0128 | -0.0128 |
| 0.8000 | 0.0116 | -0.0116 |
| 0.8500 | 0.0098 | -0.0098 |
| 0.9000 | 0.0076 | -0.0076 |
| 0.9500 | 0.0048 | -0.0048 |
| 1.0000 | 0. | 0. |
| $\frac{\text{LE radius}}{c} = \frac{\text{TE radius}}{c} = 0.002$ | | |

Table 7.5-1 Fifth standard configuration : Dimensionless Airfoil Coordinates

## Aeroelastic Test Cases

A large amount of data has been obtained during the tests [31]. Of this, 29 cases were recommended as test cases in [4]

Of special interest in this fifth standard configuration is the extensive variation of time-averaged parameters, such as inlet flow velocity ($M_1$) and incidence (i).

The inlet Mach number is varied from $M_1$=0.5 to $M_1$=1.0, and the range of incidence is from fully-attached (incidence less than 5°) up to fully-separated (incidence greater than 10°) flow conditions

At the Cambridge Symposium [3] it was concluded that the present state-of-the-art of prediction models does not allow for the calculation of stalled flow [7]. Therefore, the 29 recommended cases from [4] were reduced to the ones dealing with attached flow only. A total of 11 test cases were then selected. These are contained in Table 7.5-2.

| | Time Averaged | | | Time Dependent Parameters | | | | Flow |
|---|---|---|---|---|---|---|---|---|
| Aeroelastic | $M_1$ | i | $p_2/p_{w1}$ | $\alpha$ | $\sigma$ | f | k | |
| Test Case No. | (-) | (°) | (-) | (rad) | (°) | (Hz) | (-) | |
| 1 | 0.5 | 2 | 0.84 | 0.00524 | 180 | 200 | 0.37 | Attached |
| 2 | " | 4 | 0.86 | " | " | " | " | " |
| 3 | " | 6 | 0.87 | " | " | " | " | Part. sep. |
| 4 | " | 4 | 0.86 | " | " | 75 | 0.14 | Attached |
| 5 | " | " | " | " | " | 125 | 0.22 | " |
| 6 | " | " | " | " | " | 300 | 0.54 | " |
| 7 | " | " | " | " | " | 550 | 1.02 | " |
| 8 | " | 6 | 0.87 | " | " | 75 | 0.14 | Part. sep. |
| 9 | " | " | " | " | " | 125 | 0.22 | " |
| 10 | " | " | " | " | " | 300 | 0.56 | " |
| 11 | " | " | " | " | " | 550 | 1.02 | " |

Pitch axis at $(x_\alpha, y_\alpha) = (0.5, 0.)$ for all the above aeroelastic test cases

**Table 7.5-2.** Fifth standard configuration.
11 recommended aeroelastic test cases (restricted set from /4/)

Discussion of Time-Averaged Results

The 11 proposed aeroelastic test cases comprise three separate stationary flow conditions, all at the same inlet flow velocity ($M_1$=0.5), but at different incidence angles (i=2°, 4° and 6°, respectively).

These data are presented in Fig. 7.5-2, together with the theoretical results of Methods 2 and 3. The data and the theoretical results agree well, if the theoretical incidence is slightly modified. The theoretical incidence angles for Method 3 in Fig. 7.5-2b,c are $i_{theory}$=2.5° and 4.0°, compared to the experimented ones (and theoretical for Method 2) $i_{exp}$=4.0° and 6.0°, respectively. This change in steady-state incidence angle corresponds fairly well with the change introduced in the first standard configuration for similar reasons ($\Delta i$=2.3° to 4° in standard configuration 1; $\Delta i$=1.5° to 2° in standard configuration 5).

It should also be noted that the theoretical results obtained using Methods 2 and 3 agree extremly well for the same theoretical incidence angle (Figs. 7.5-2a, b for $i_{theory}$=2°; Figs. 7.5-2b,c for $i_{theory}$=4°).

It is thus likely that an experimental effect, which is not taken into account in the inviscid theoretical flow models, is responsible for the need to correct the experimental incidence angle in order to achieve a good steady-state agreement.

The largest discrepancy between the experimental and theoretical results is found on the suction (=upper) surface in the leading edge region. This effect becomes more pronounced with an increase in incidence angle. It is found that the difference in the leading edge region between Method 3 and the experimental data is somewhat larger for the present cascade than for the first standard configuration (Fig. 7.1-2). This can perhaps be attributed to the higher flow velocity and the sharper leading edge in the present case. However, calculations with other methods should be performed before any detailed conclusions regarding the reasons for this discrepancy can be drawn.

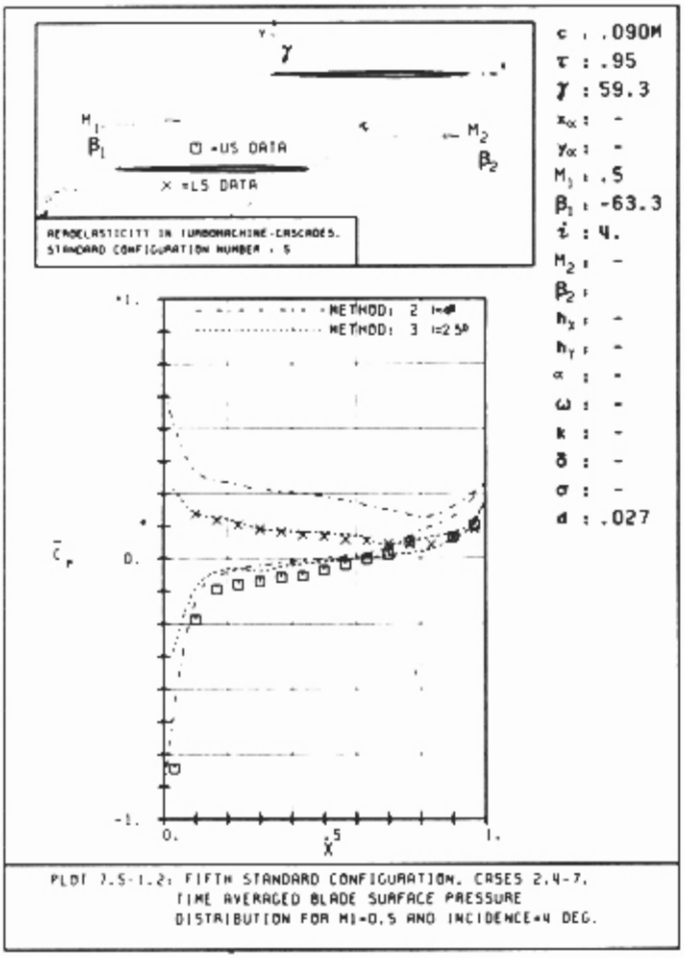


PLOT 7.5-1.2: FIFTH STANDARD CONFIGURATION. CASES 2,4-7.
TIME AVERAGED BLADE SURFACE PRESSURE
DISTRIBUTION FOR M1=0.5 AND INCIDENCE=4 DEG.

a)

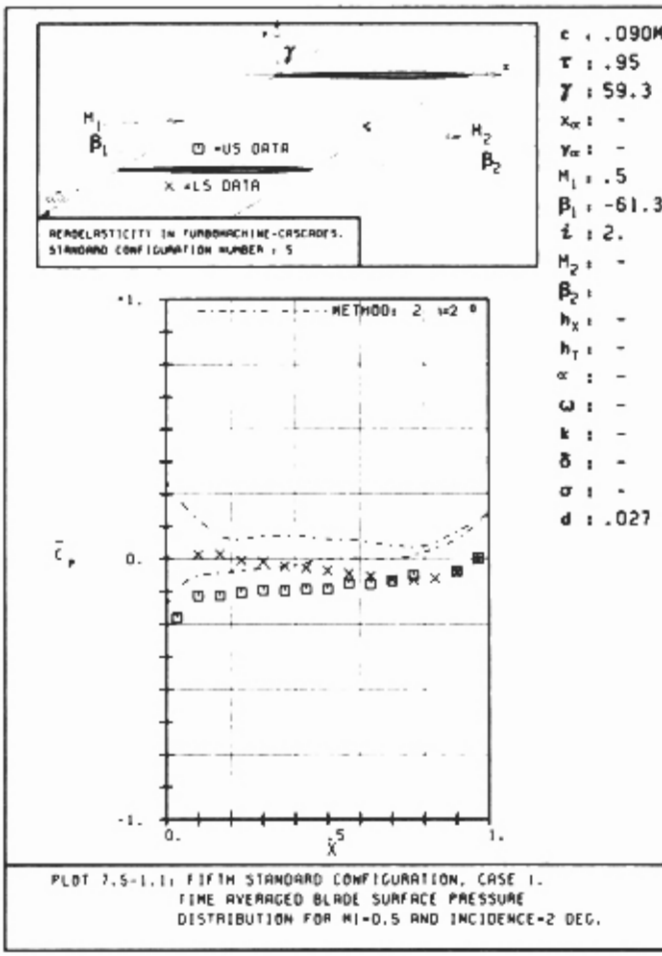


PLOT 7.5-1.1: FIFTH STANDARD CONFIGURATION, CASE 1.
TIME AVERAGED BLADE SURFACE PRESSURE
DISTRIBUTION FOR M1=0.5 AND INCIDENCE=2 DEG.

b)

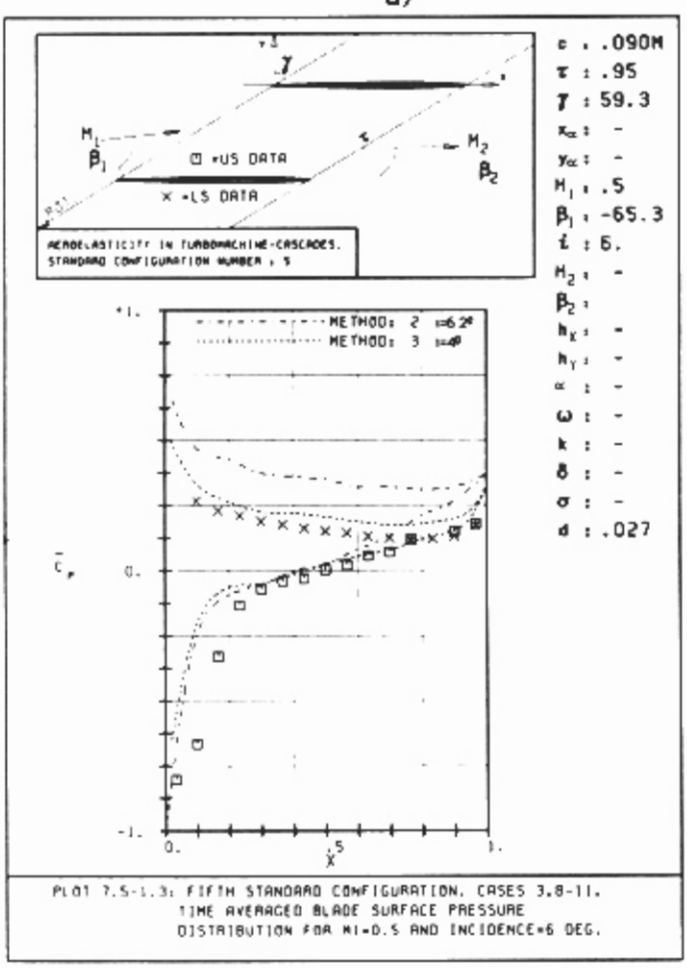


PLOT 7.5-1.3: FIFTH STANDARD CONFIGURATION. CASES 3,8-11.
TIME AVERAGED BLADE SURFACE PRESSURE
DISTRIBUTION FOR M1=0.5 AND INCIDENCE=6 DEG.

c)

**Fig. 7.5-2.** Time-averaged blade surface pressure distribution for $i_{exp}$= $2^0$, $4^0$ and $6^0$ , respectively.

Discussion of Time-Dependent Results

Up till now, four unsteady prediction models have been applied to the fifth standard configuration (Table 6.1). From the results, both the time-dependent blade surface pressures and the stability limits of the cascade can be evaluated.

When comparing the unsteady results it should be considered that the experiments were performed with only one blade vibrating (i.e. only the influence of the blade on itself was considered), and that aeroelastic coupling effects between neighboring blades has not been corrected for. This is unfortunate, but the objective of the experiments was to investigate flutter at high incidence angles, for which the aeroelastic coupling effects have been determined [31]. It was only because it was found that present prediction models cannot treat such flow conditions that the low incidence angle experiments were selected as test cases.

In order to estimate how large the aerodynamic coupling effects are, a breakdown of the theoretical results obtained from Method 1 has been done. This study shows that if only one blade is vibrated (in Method 1), the results approach the experimental values. This fact will be discussed in the following sections.

Integrated Parameters

The experimentally determined aerodynamic damping coefficient (one blade vibrated) and the predicted results (all blades vibrated) agree well for an experimental incidence angle of $i_{exp}=6°$ (Fig. 7.5-3a), over a wide range of reduced frequency ($0.22<k<1.02$). However, the agreement is not so good for $i_{exp}=4°$ (Figs. 7.5-3b,c), although the stability trend is again correct.

The same information is found by examining the moment coefficient (Figs. 7.5-3d,e,f).

It is presently not possible to explain the sudden change in the experimental curves around $i_{exp}=4°$ (Figs. 7.5-3c,f).

A certain discrepancy is found also for the different theories. The flat plate theory (Method 1, $i_{theory}$=0°) and Method 2 ($i_{theory}$=$i_{exp}$, full blade geometry taken into account) agree well, whereas Method 3 (full blade geometry, $i_{theory}$=2.5° and 4° resp. in Figs. 7.5-3a-f) is somewhat nearer to the experiments. It is found that the difference is largest for the magnitude and that all the predicted phase angles $\Phi_m$ are close to the measured ones.

The reason for the differences between the theoretical model predictions are not apparent at the present time.

The aerodynamic coupling effects can be estimated by considering the decomposition of the results of a calculation with all blades vibrated, into the separate influence coefficients of each blade [28, 30, 59]. This investigation, based on results obtained from Method 1 (flat plate, $i_{theory}$=0°), is shown in Fig. 7.5-4 for a 180° interblade phase angle. It is concluded that, for $\sigma$=180°, the amplitude and phase angle of $\tilde{c}_m(x,t)$ does not change if 2 or more blades are vibrated. However, a certain change is found if only one blade is oscillated. In the present case the amplitude and phase angle of a single-blade vibration are $\tilde{c}_m$=1.24 and $\Phi_m$=-25°, resp., whereas the corresponding

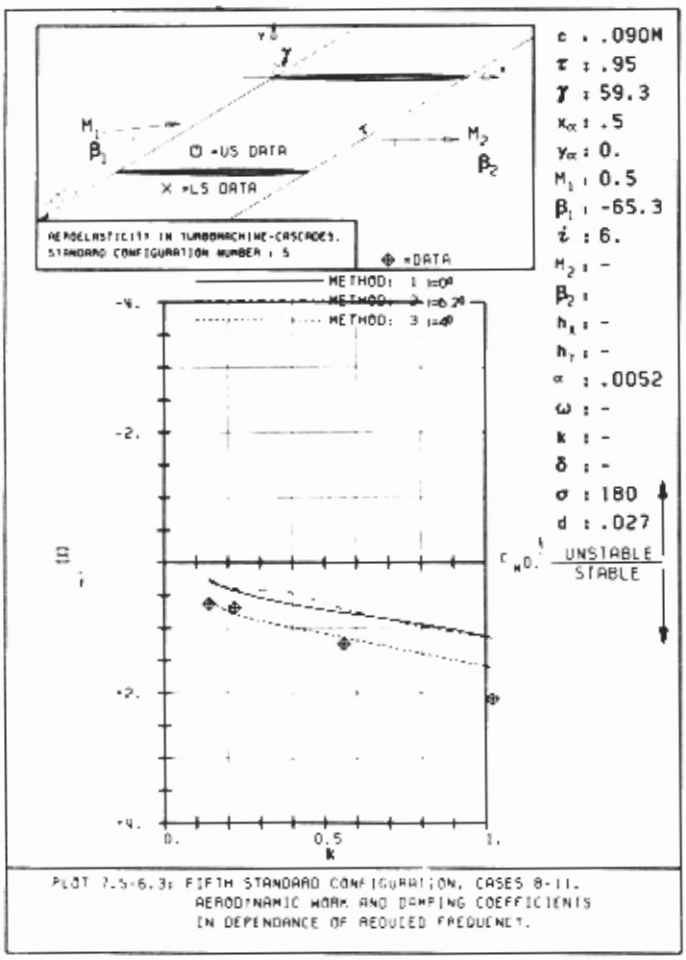


PLOT 7.5-6.3: FIFTH STANDARD CONFIGURATION, CASES 8-11.
AERODYNAMIC WORK AND DAMPING COEFFICIENTS
IN DEPENDANCE OF REDUCED FREQUENCY.

a)

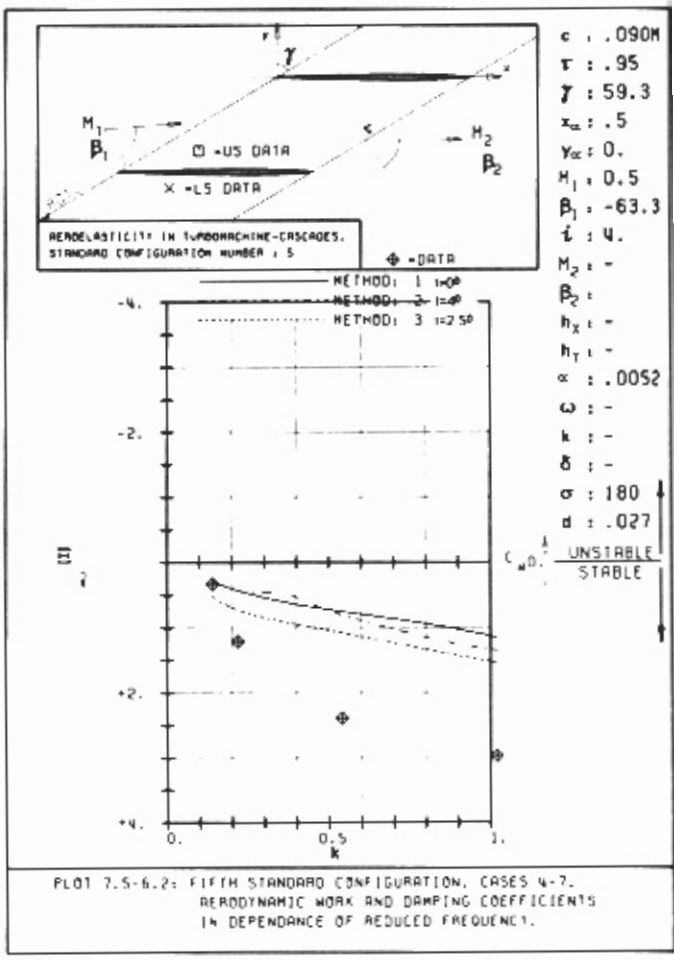


PLOT 7.5-6.2: FIFTH STANDARD CONFIGURATION, CASES 4-7.
AERODYNAMIC WORK AND DAMPING COEFFICIENTS
IN DEPENDANCE OF REDUCED FREQUENCY.

b)

**Fig. 7.5-3.** Continued on next page.

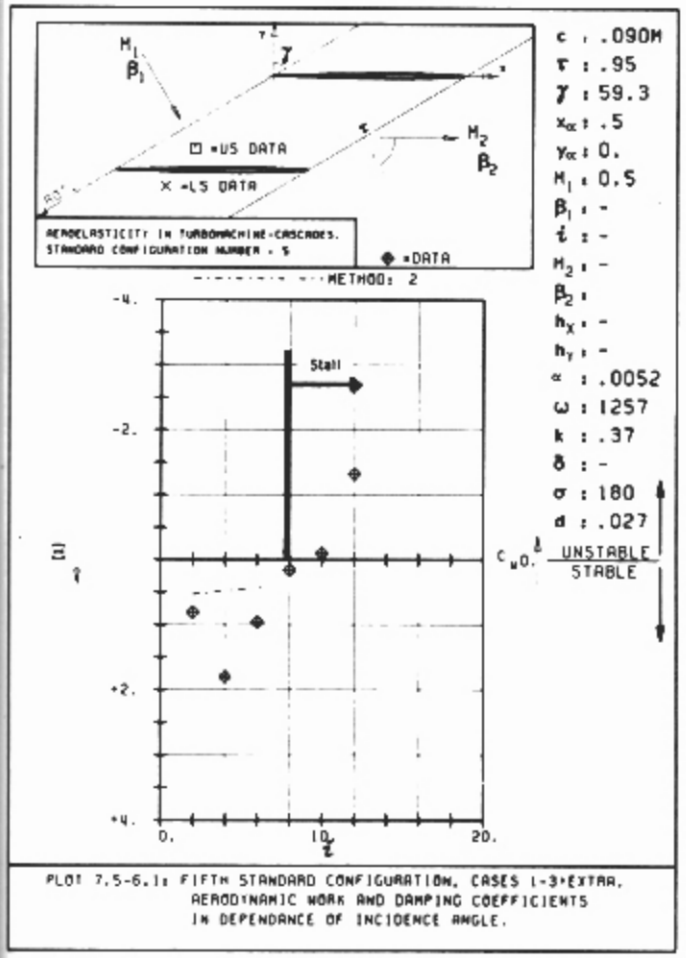


PLOT 7.5-6.1: FIFTH STANDARD CONFIGURATION, CASES 1-3+EXTRA, AERODYNAMIC WORK AND DAMPING COEFFICIENTS IN DEPENDANCE OF INCIDENCE ANGLE.

c)

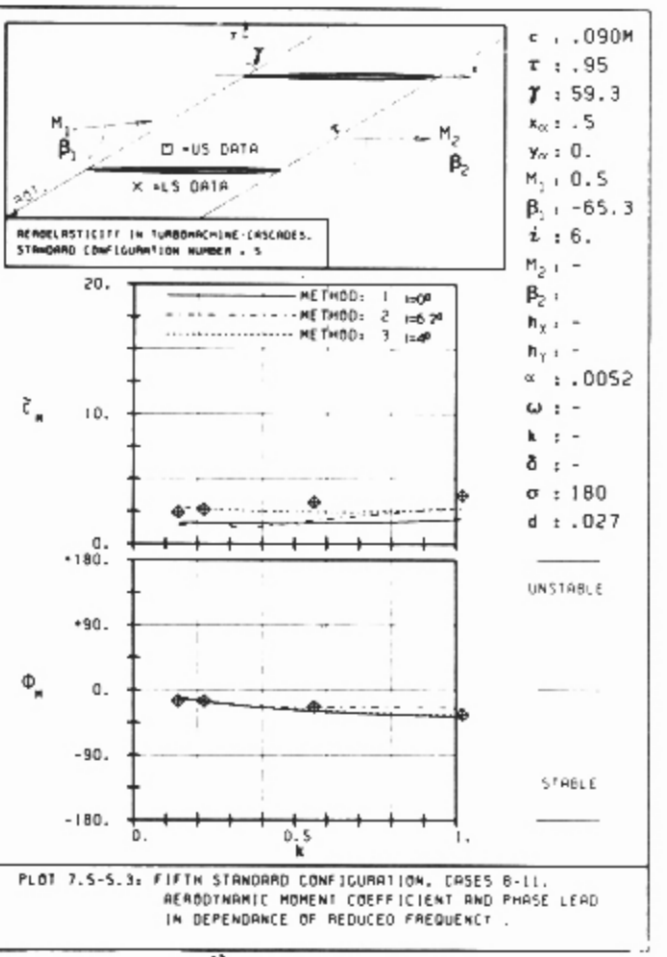


PLOT 7.5-5.3: FIFTH STANDARD CONFIGURATION, CASES 8-11, AERODYNAMIC MOMENT COEFFICIENT AND PHASE LEAD IN DEPENDANCE OF REDUCED FREQUENCY .

d)

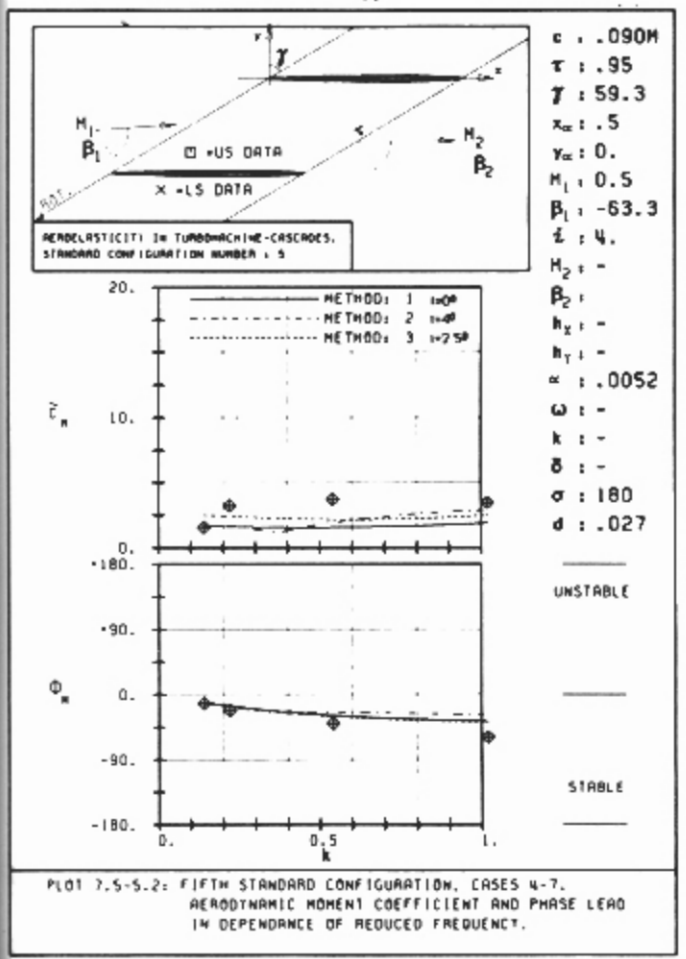


PLOT 7.5-5.2: FIFTH STANDARD CONFIGURATION, CASES 4-7, AERODYNAMIC MOMENT COEFFICIENT AND PHASE LEAD IN DEPENDANCE OF REDUCED FREQUENCY.

e)

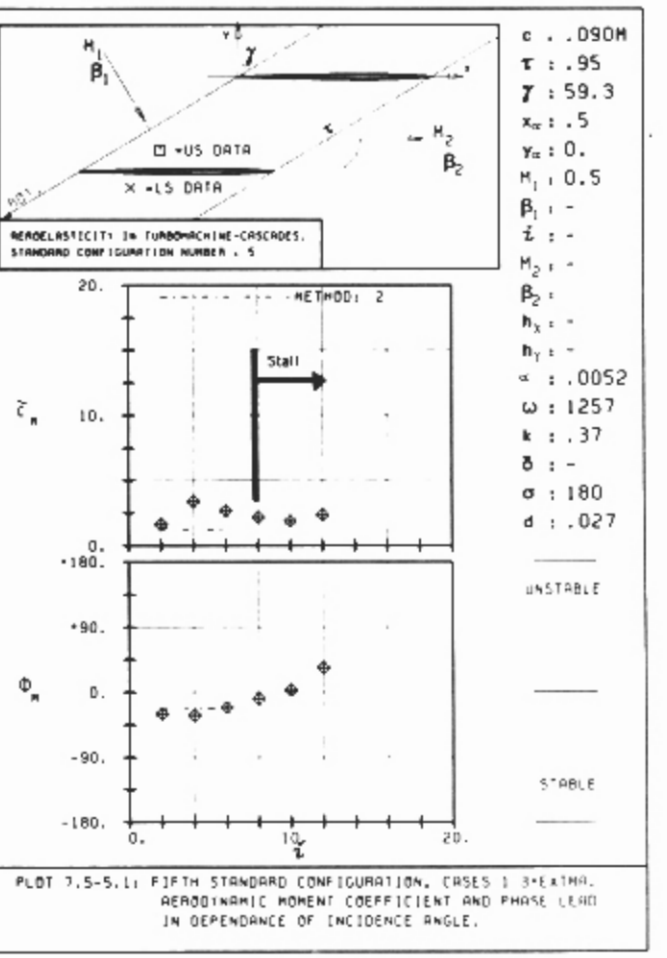


PLOT 7.5-5.1: FIFTH STANDARD CONFIGURATION, CASES 1-3+EXTRA, AERODYNAMIC MOMENT COEFFICIENT AND PHASE LEAD IN DEPENDANCE OF INCIDENCE ANGLE.

f)

**Fig. 7.5-3.** Aerodynamic damping and moment coefficients for the fifth standard configuration.

values are $\tilde{c}_m$=1.58 and $\Phi_m$=-23° for 64 blades vibrated (Fig 7.5-4). The fact that the phase angle does not vary with the number of vibrating blades is clearly the reason for the good agreement for the phase angle ($\Phi_m$) between the experiment and the theory in Figs. 7.5-3d,e,f. The study indicates also that, if all blades were vibrated in the experiment, the experimental $\tilde{c}_m$ value would probably be somewhat larger than the ones presented, and thus approach the theoretical curves in Figs 7.5-3d,e,f.

Blade Surface Pressure Differences

As the blades in the fifth standard configuration are thin (2.7%) it is of interest to evaluate and discuss the blade surface pressure difference coefficient $\Delta\tilde{c}_p(x,t)$. This parameter is given in Fig. 7.5-5, for different incidence angles ($i_{exp}$=2°, 4° and 6°) at a reduced frequency of $k_{exp}$=0.37.
It is concluded that, for $i_{exp}$=2° (Fig. 7.5-5a), the phase angles ($\Phi_{\Delta p}$) of the pressure difference coefficient in the experiment and in the different theories agree well. A certain discrepancy exists, however, in the magnitude ($\Delta\tilde{c}_p$). Methods 1 and 2 predict identical values, whereas the experiments indicate lower pressure difference amplitudes along the whole chord. This effect becomes more pronounced in the forward part of the blade for larger

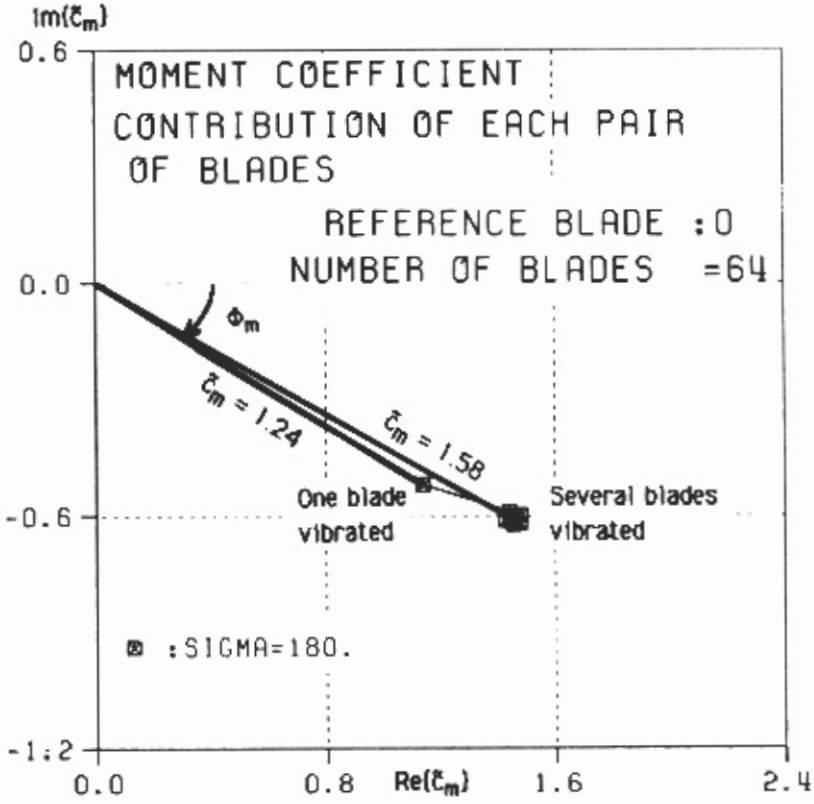


**Fig. 7.5-4.** Aerodynamic coupling effects for $\sigma$=180°, with the number of blades as parameter ( 64 blades used for the

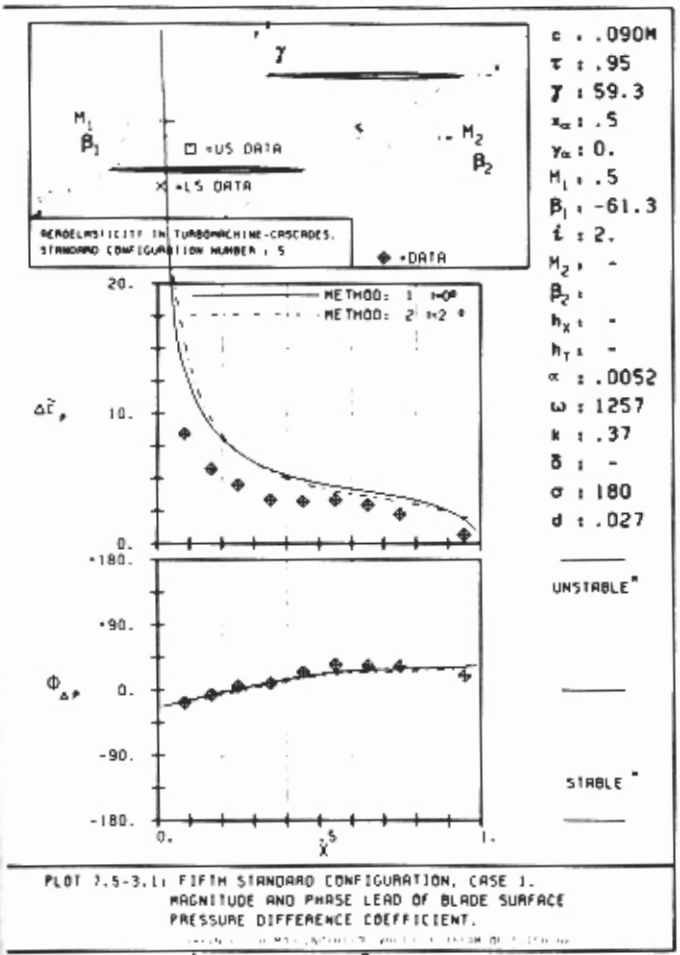


PLOT 7.5-3.1: FIFTH STANDARD CONFIGURATION, CASE 1.
MAGNITUDE AND PHASE LEAD OF BLADE SURFACE
PRESSURE DIFFERENCE COEFFICIENT.

a) $i_{exp}=2^0$; $k_{exp}=0.37$

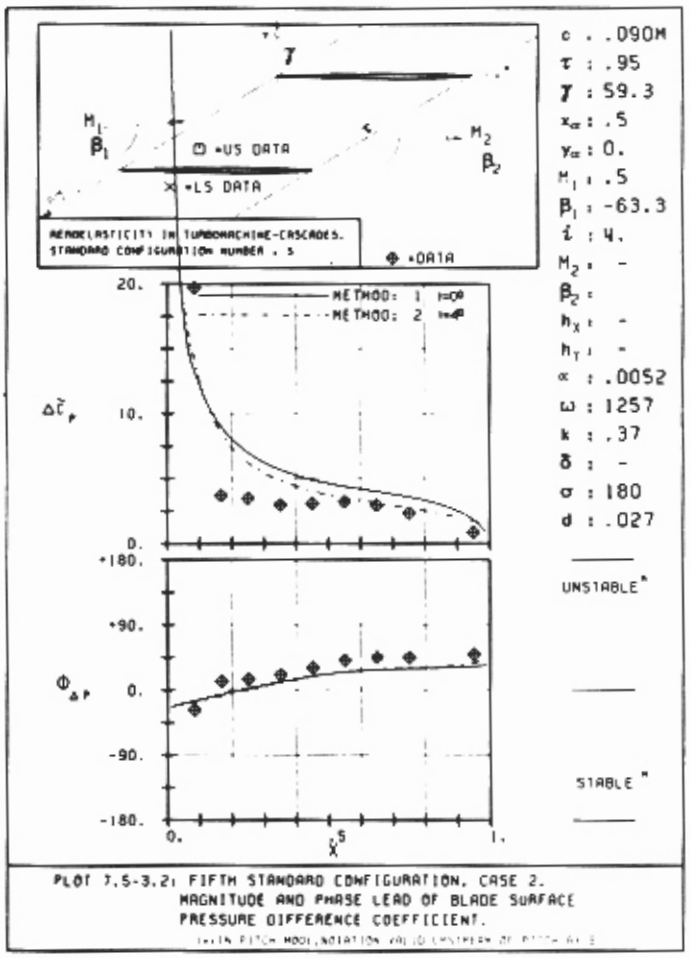


PLOT 7.5-3.2: FIFTH STANDARD CONFIGURATION, CASE 2.
MAGNITUDE AND PHASE LEAD OF BLADE SURFACE
PRESSURE DIFFERENCE COEFFICIENT.

b) $i_{exp}=4^0$; $k_{exp}=0.37$

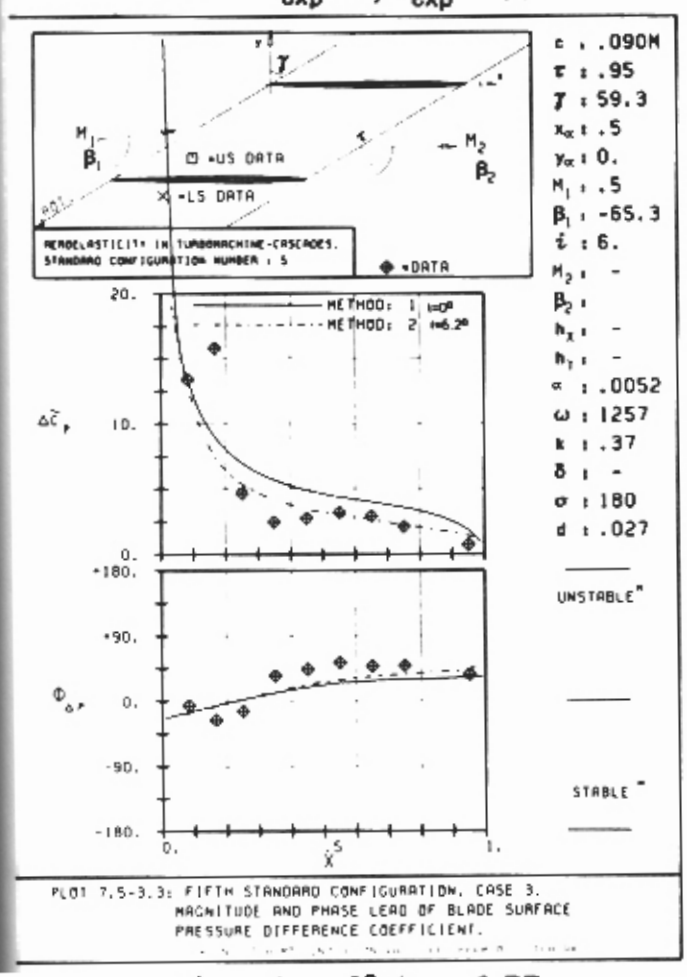


PLOT 7.5-3.3: FIFTH STANDARD CONFIGURATION, CASE 3.
MAGNITUDE AND PHASE LEAD OF BLADE SURFACE
PRESSURE DIFFERENCE COEFFICIENT.

c) $i_{exp}=6^0$; $k_{exp}=0.37$

**Fig. 7.5-5.** Blade surface pressure difference coefficient versus blade chord for $k_{exp}=0.37$, at $i_{exp}= 2^0, 4^0$ and $6^0$, respectively.

incidence angles. At $i_{exp}$=4° (Fig. 7.5-5b) the first measured pressure indicates a higher $\Delta\tilde{c}_p$-value, whereas the following ones show somewhat smaller values. Aft of about 50% of the chord, the $\Delta\tilde{c}_p$-values are identical for $i_{exp}$=2° and 4°

At $i_{exp}$=6° (Fig. 7.5-5c) the first two pressures measured indicate higher values, whereas no significant change appears for the other transducer locations.

From Fig. 7.5-5 it is also seen that no change appears in the pressure difference phase angle ($\Phi_{\Delta p}$) for the aft 70% of the blade as a result of variation in incidence angle. However, some slight variation is found in the forwad 30%. This difference of $\Delta\tilde{c}_p$ and $\Phi_{\Delta p}$ in the leading edge region for various incidence angles can probably be attributed to unsteady viscous flow effects in the experiment (possibly local unsteady separation), which are not considered in the inviscid theories being investigated.

In Fig. 7.5-5 the full line corresponds to a flat plate calculation, with a 0° incidence. It is seen that, as the incidence increases, the difference in $\Delta\tilde{c}_p$ between Method 2 and the flat plate results increases as expected, and the results obtained from Method 2 approach the experimental data. However, no significant change is found in the phase angle ($\Phi_{\Delta p}$).

As for the aerodynamic damping coefficient, on the basis of the calculations obtained from Method 1, it is possible to estimate how large the aerodynamic coupling effects can be.

Considering a breakdown of the theoretical results from Fig. 7.5-5a into separate individual influence coefficients, different results are found along the blade chord. These are given in Fig. 7.5-6. It is found that the pressure difference phase angle $\Phi_{\Delta p}$ ($=\tan^{-1}\{\mathrm{Im}[\tilde{c}_p]/\mathrm{Re}[\tilde{c}_p]\}$) is not influenced at the 9.5% chordwise location (Fig. 7.5-6a) if one or several blades are considered as oscillating. However, the magnitude decreases from $\Delta\tilde{c}_p$=12.4 to $\Delta\tilde{c}_p$=9.5 if only one blade oscillates.

At the 34% chordwise location (Fig. 7.5-6b) the change in phase angle is now noticeable, but still small (increase from $\Phi_{\Delta p}$=+11° for all blades vibrated to $\Phi_{\Delta p}$=+18° for only one blade oscillated). Similarly, the magnitude decreases from $\Delta\tilde{c}_p$=5.7 to $\Delta\tilde{c}_p$=4.8.

At 75% chordwise location (Fig. 7.5-6c) the phase angle changes somewhat more (increase from $\Phi_{\Delta p}$=29° for all blades vibrated to $\Phi_{\Delta p}$=45° for one blade vibrated). However, the variation in magnitude of $\Delta\tilde{c}_p$ is now smaller (decrease from $\Delta\tilde{c}_p$=3.5 to $\Delta\tilde{c}_p$=3.0).

The blade surface pressure difference coefficient thus obtained, with one blade vibrated, can be compared to the results for all blades vibrated (Fig. It

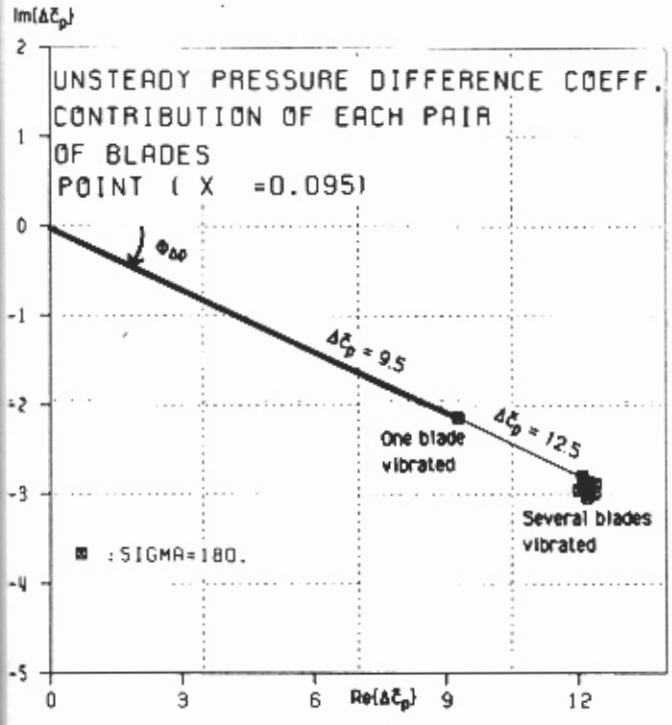


a) x=0.095

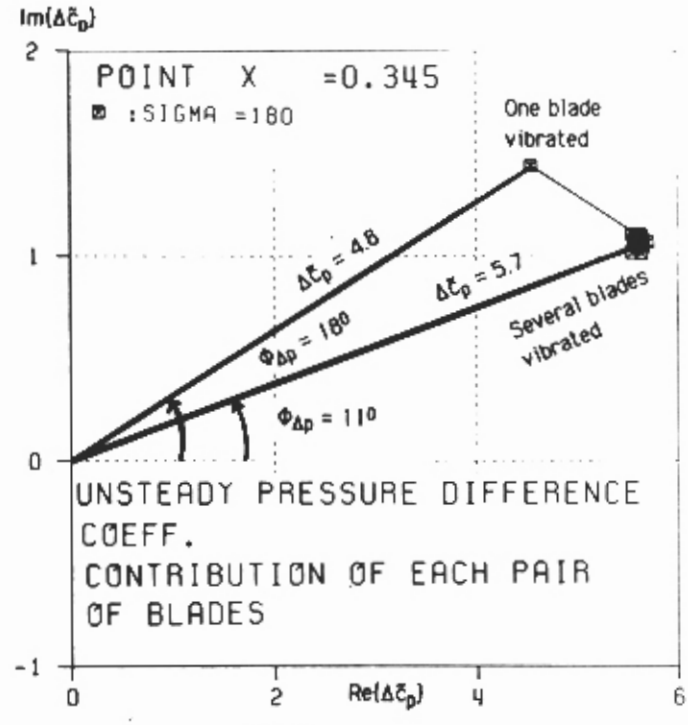


b) x=0.34

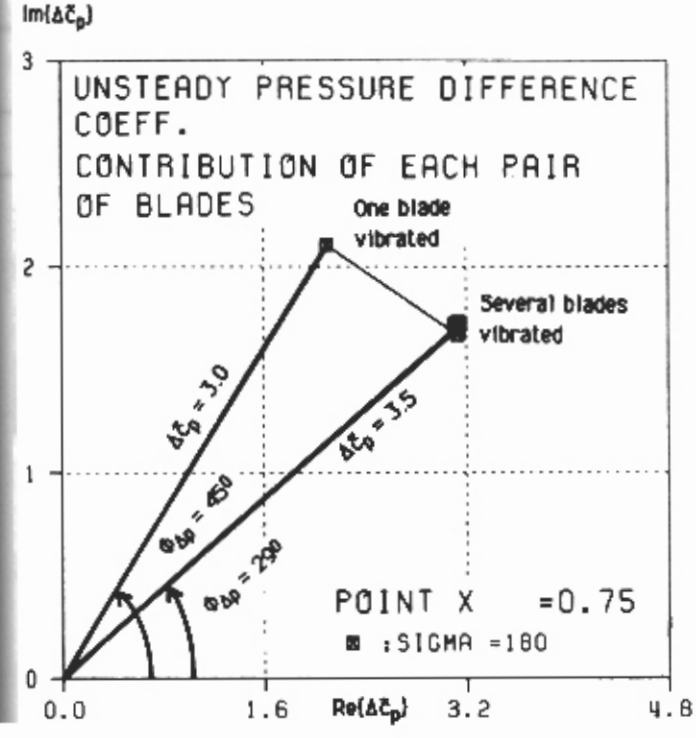


c) x=0.75

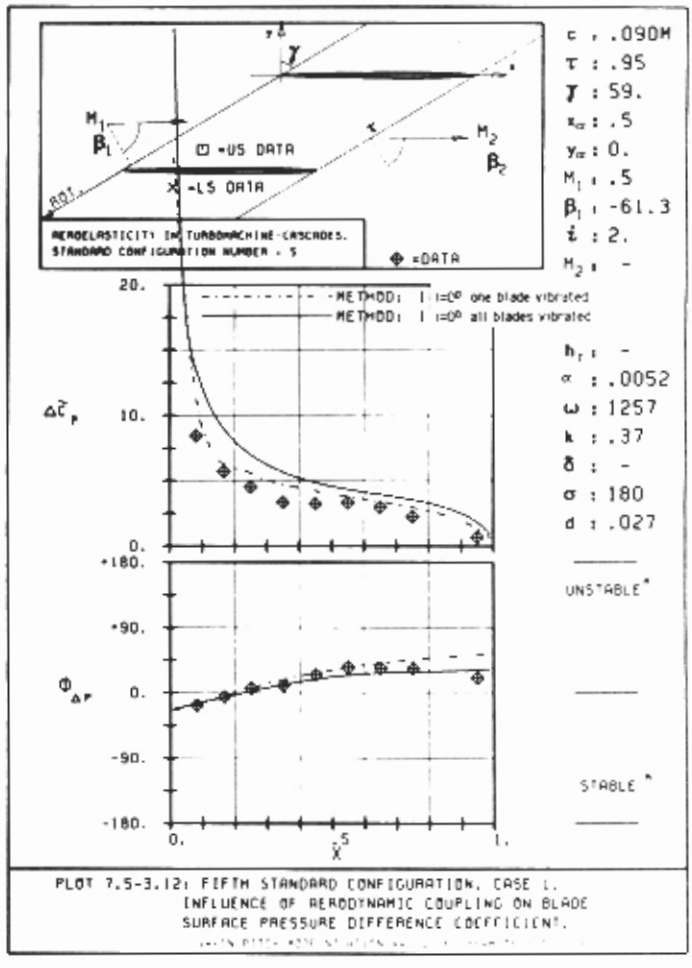


d) along chord

**Fig. 7.5-6.** Theoretical influence of vibration of one or several blades on the blade surface pressure difference coefficient ( Method I, i=0°)

7.5-6d). It is found that, if only one blade is vibrated, the magnitude of $\Delta\tilde{c}_p$ decreases along the blade (mostly for x<0.03). Simultaneously, the phase angle ($\Phi_{\Delta p}$) increases somewhat (mostly for x>0.03). A comparison between these results and the experimental data (Fig. 7.5-6d) indicates that the theoretical results with only one blade vibrated agree better with the data than if all blades are oscillated. It is thus established that a large part of the differences between the data and the theoretical results comes from the fact that only one blade was vibrated in the experiment. If the neighboring blades had also been oscillated, the agreement would have been better.

This result should be kept in mind while examining all results for the fifth standard configuration.

In Fig. 7.5-7 results are shown for $i_{exp}$=4°, at various reduced frequencies. It is concluded that the experimental pressure difference coefficient changes significantly in the leading edge region with increasing reduced frequency. The differences between the theoretical results and the experimental data are largest at the higher reduced frequency (Fig. 7.5-7d). The largest discrepancies between the different models are also found here, although a certain difference exists also for the low reduced frequencies (Fig. 7.5-7a).

The same information as in Fig. 7.5-7 is given in Fig. 7.5-8, but here for the $i_{exp}$=6° incidence angle. The same conclusions are drawn. Furthermore, it is noted that neither the experimental data, nor the theoretical results are influenced by the variation in incidence angle, except in the leading edge region (compare Figs. 7.5-7a, 7.5-8a; etc). It should again be noted that the theoretical incidence angle for Method 3 was slightly modified to obtain a better agreement with the experimental time-averaged blade surface pressure distributions. It was found (in Fig. 7.5-2b,c) that the steady-state pressure distributions for Methods 2 and 3 agree very well if the same theoretical incidence angle is used ($i_{theory}$=4° for Method 2 in Fig. 7.5-2b; $i_{theory}$=4° for Method 3 in Fig. 7.5-2c).

However, this is not the case for the time-dependent pressure difference distribution ($i_{theory}$=4° for Method 2 in Fig. 7.5-7; $i_{theory}$=4° for Method 3 in Fig. 7.5-8). Here, the differences in the unsteady pressure distributions persist.

The reasons for these differences between Method 1 and Methods 2, 3, especially at high reduced frequencies, can probably be explained by considering that Method 1 is a flat plate theory. However, the reason for the differences between the predictions of the two geometry models (2 and 3) are not apparent at the present time.

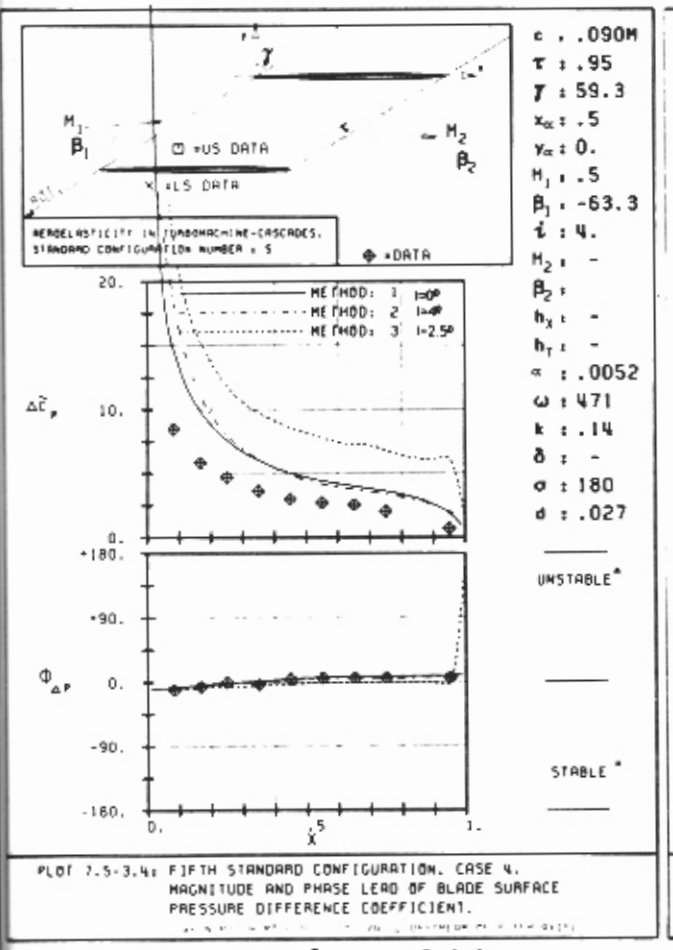


PLOT 7.5-3.4: FIFTH STANDARD CONFIGURATION. CASE 4.
MAGNITUDE AND PHASE LEAD OF BLADE SURFACE
PRESSURE DIFFERENCE COEFFICIENT.

a) $i_{exp}=4^0$; $k_{exp}=0.14$

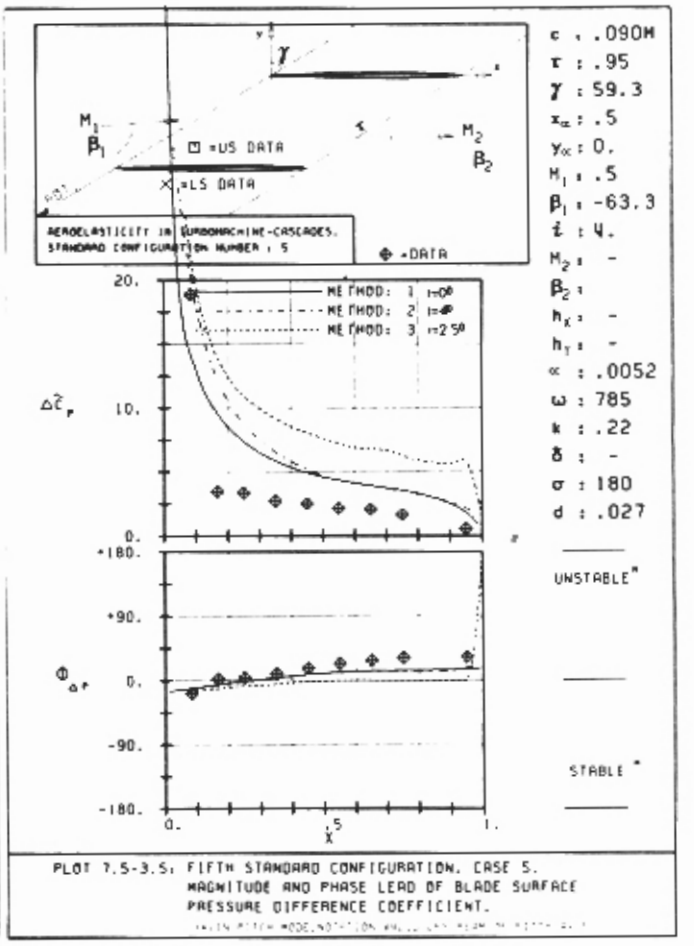


PLOT 7.5-3.5: FIFTH STANDARD CONFIGURATION. CASE 5.
MAGNITUDE AND PHASE LEAD OF BLADE SURFACE
PRESSURE DIFFERENCE COEFFICIENT.

b) $i_{exp}=4^0$; $k_{exp}=0.22$

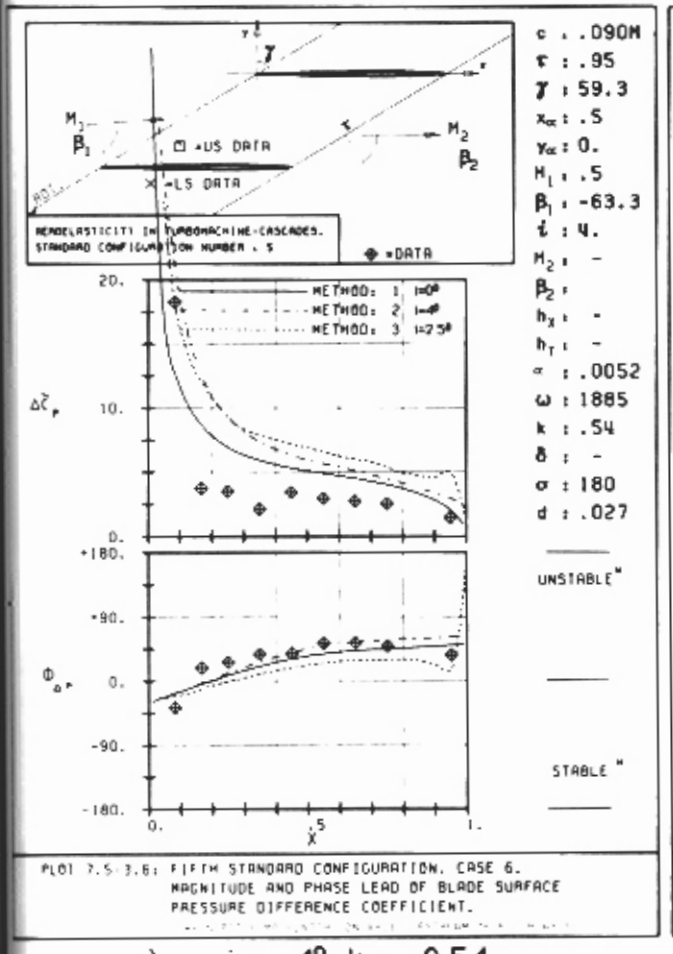


PLOT 7.5-3.6: FIFTH STANDARD CONFIGURATION. CASE 6.
MAGNITUDE AND PHASE LEAD OF BLADE SURFACE
PRESSURE DIFFERENCE COEFFICIENT.

c) $i_{exp}=4^0$; $k_{exp}=0.54$

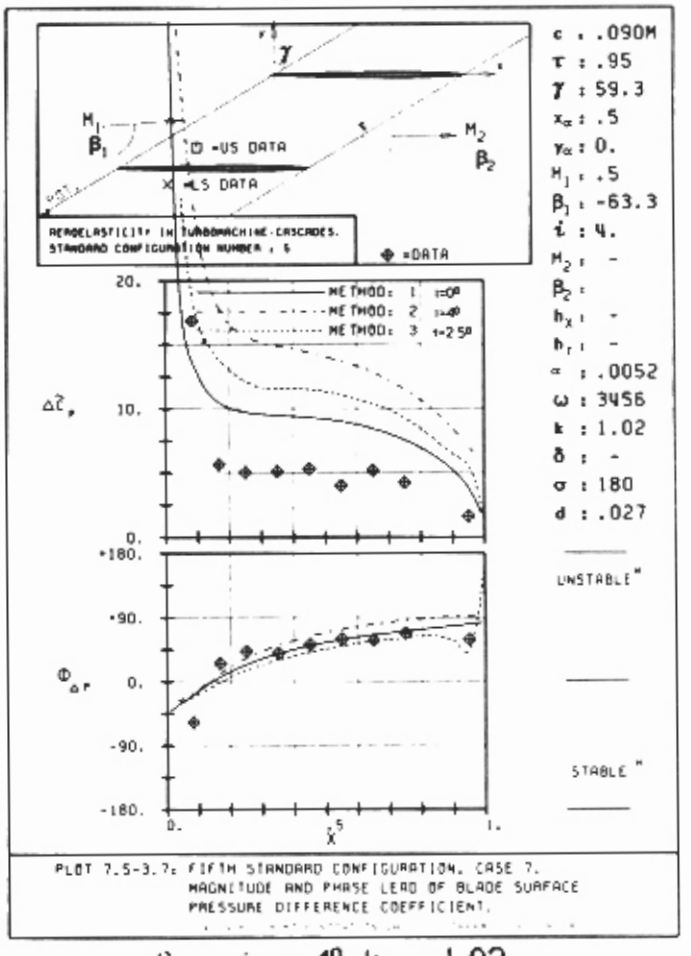


PLOT 7.5-3.7: FIFTH STANDARD CONFIGURATION. CASE 7.
MAGNITUDE AND PHASE LEAD OF BLADE SURFACE
PRESSURE DIFFERENCE COEFFICIENT.

d) $i_{exp}=4^0$; $k_{exp}=1.02$

**Fig. 7.5-7.** Blade surface pressure difference coefficient versus blade chord for $i_{exp}=4^0$, at $k_{exp}$= 0.14, 0.22, 0.56, and 1.02, resp.

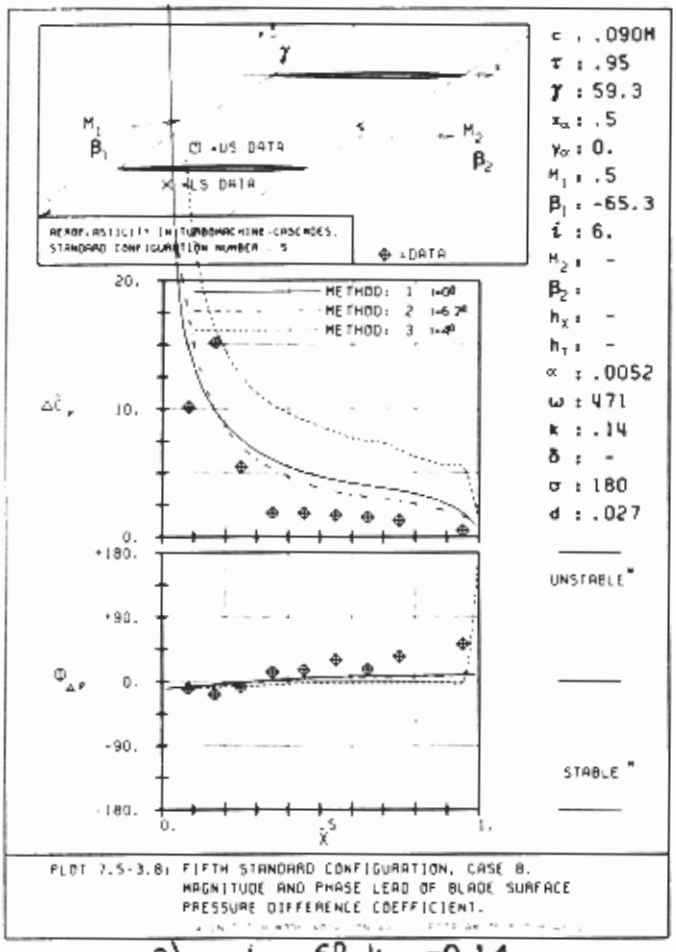


PLOT 7.5-3.8: FIFTH STANDARD CONFIGURATION, CASE 8. MAGNITUDE AND PHASE LEAD OF BLADE SURFACE PRESSURE DIFFERENCE COEFFICIENT.

a) $i_{exp}=6^0$; $k_{exp}=0.14$

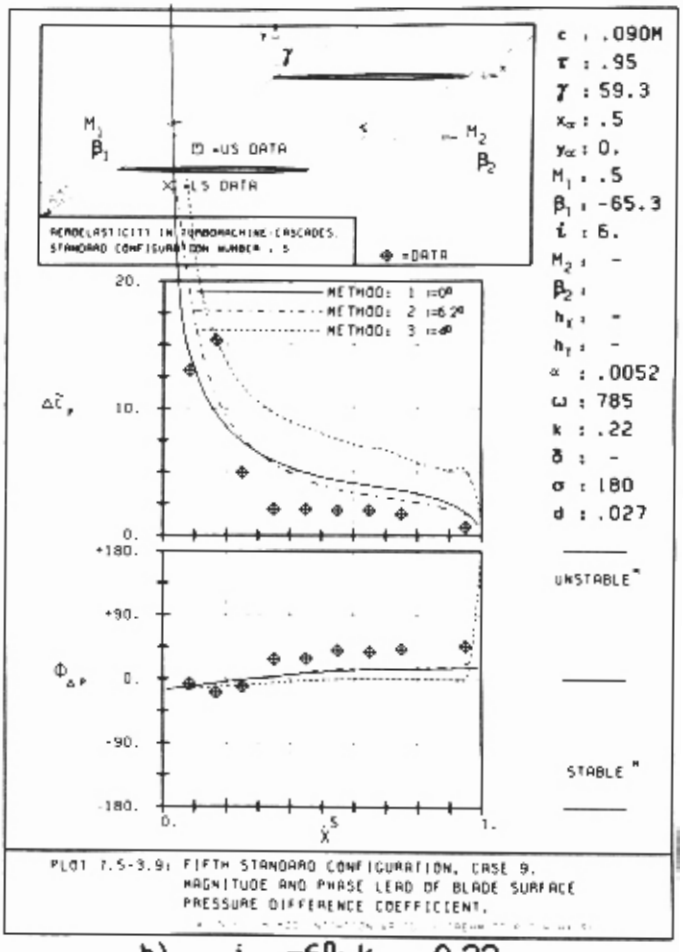


PLOT 7.5-3.9: FIFTH STANDARD CONFIGURATION, CASE 9. MAGNITUDE AND PHASE LEAD OF BLADE SURFACE PRESSURE DIFFERENCE COEFFICIENT.

b) $i_{exp}=6^0$; $k_{exp}=0.22$

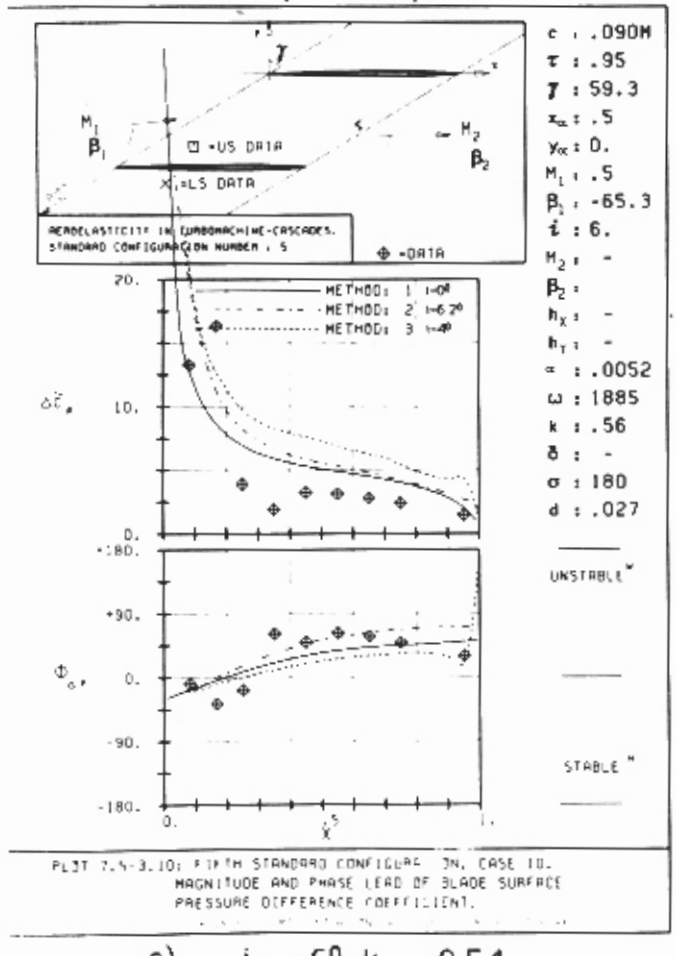


PLOT 7.5-3.10: FIFTH STANDARD CONFIGURATION, CASE 10. MAGNITUDE AND PHASE LEAD OF BLADE SURFACE PRESSURE DIFFERENCE COEFFICIENT.

c) $i_{exp}=6^0$; $k_{exp}=0.54$

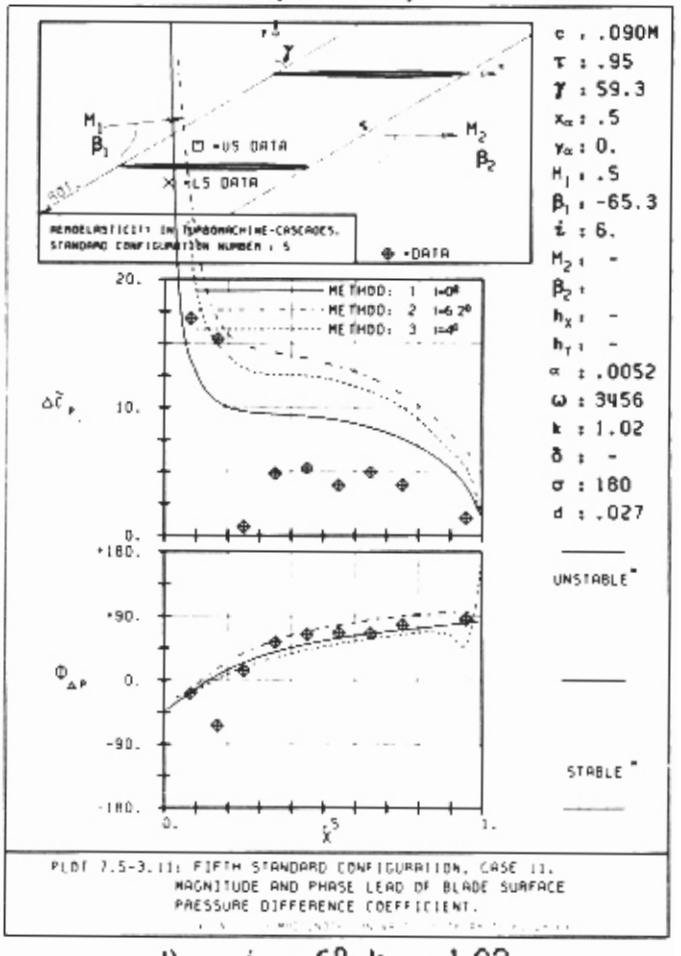


PLOT 7.5-3.11: FIFTH STANDARD CONFIGURATION, CASE 11. MAGNITUDE AND PHASE LEAD OF BLADE SURFACE PRESSURE DIFFERENCE COEFFICIENT.

d) $i_{exp}=6^0$; $k_{exp}=1.02$

**Fig. 7.5-8.** Blade surface pressure difference coefficient versus blade chord for $i_{exp}=6^0$, at $k_{exp}$= 0.14, 0.22, 0.56, and 1.02, resp.

Blade Surface Pressures on Upper and Lower Surfaces

As was also found for $\Delta\tilde{c}_p$, the experimental data and blade surface pressure distributions predicted using Method 2 ($\tilde{c}_p^{us}$, $\tilde{c}_p^{ls}$) agree well at a 2° incidence angle (Fig. 7.5-9, $k_{exp}$=0.37). The agreement is also good for $i_{exp}$=4° and 6°, although the same discrepancies as found previously in $\Delta\tilde{c}_p$ are present in the leading edge region. Especially noteworthy is the excellent agreement in the phase angles ($\Phi_p^{us}$, $\Phi_p^{ls}$). This good agreement is found also for Method 3 (Fig. 7.5-10a), although some discrepancies are found at the high reduced frequency ($k_{exp}$=1.02), and especially at $i_{exp}$=6°. But, as mentioned earlier, it is probable that the inviscid theories cannot model the viscous flow for these operating conditions.
The magnitudes of the pressure coefficients ($\tilde{c}_p^{us}$, $\tilde{c}_p^{ls}$), however, do not correspond, either to the data or between the different prediction models.

## Conclusions for the Fifth Standard Configuration

From the controlled excitation study, with one blade vibrated in the experiment, on a 2.7% thick, 0° cambered, compressor cascade, in subsonic attached (and separated) flow ($M_1$=0.5), it can be concluded that:

- No attempt was made to predict the unsteady flow in the stalled operating range.
- Two prediction models (plus one flat plate theory) predicted the unsteady flow.
- Some of the differences between the experimental data and the theoretical results may be explained by local unsteady flow separations and the fact that only one blade was vibrated in the experiment. A study of the results using a flat plate theory indicates that the data and the theories would agree better if the aeroelastic coupling effects were to be considered in the experiment (Fig. 7.5-6d).
- From the comparison between the experiments and the theories it can be judged that the results obtained are encouraging for moderate subsonic Mach numbers, around thin compressor profiles, in attached flow. No theories seem to be available for stalled or partially-stalled flow.
- More investigations are necessary to determine the reasons for some discrepancies between the theoretical models.

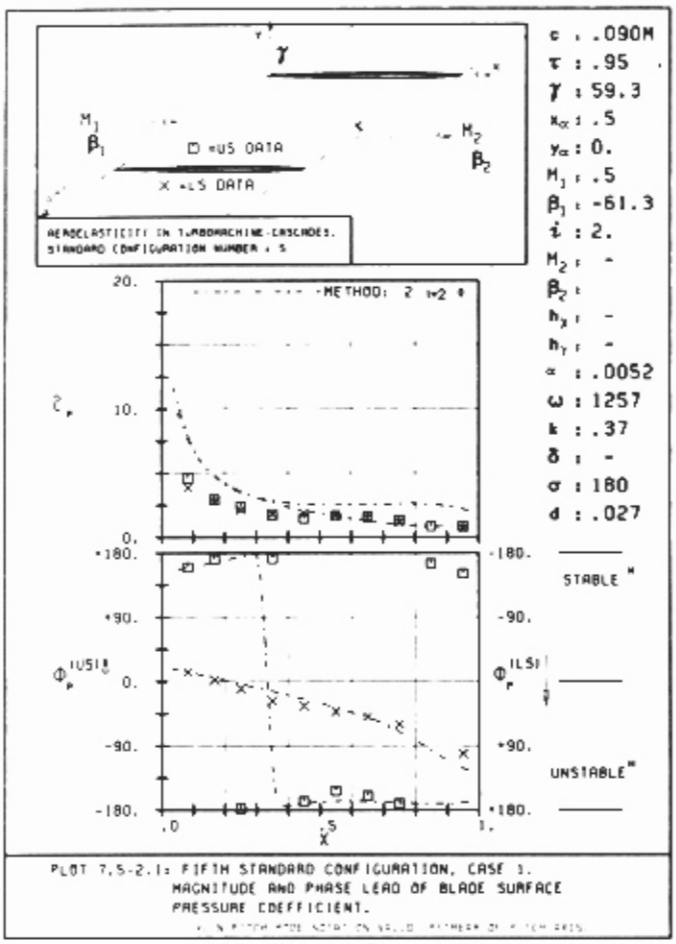


PLOT 7.5-2.1: FIFTH STANDARD CONFIGURATION, CASE 1.
MAGNITUDE AND PHASE LEAD OF BLADE SURFACE PRESSURE COEFFICIENT.

a) $i_{exp}=2^0$

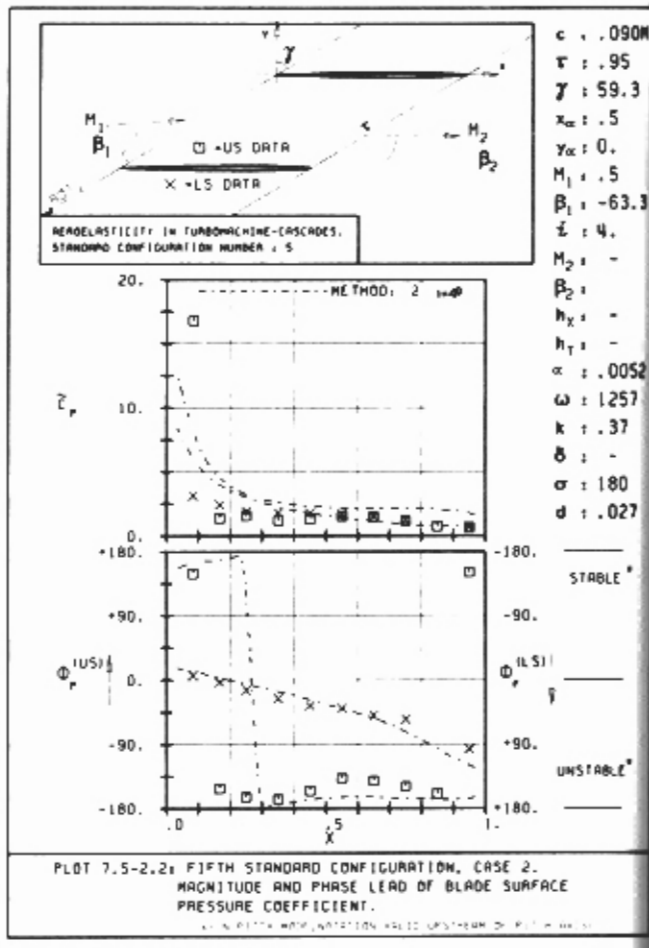


PLOT 7.5-2.2: FIFTH STANDARD CONFIGURATION, CASE 2.
MAGNITUDE AND PHASE LEAD OF BLADE SURFACE PRESSURE COEFFICIENT.

b) $i_{exp}=4^0$

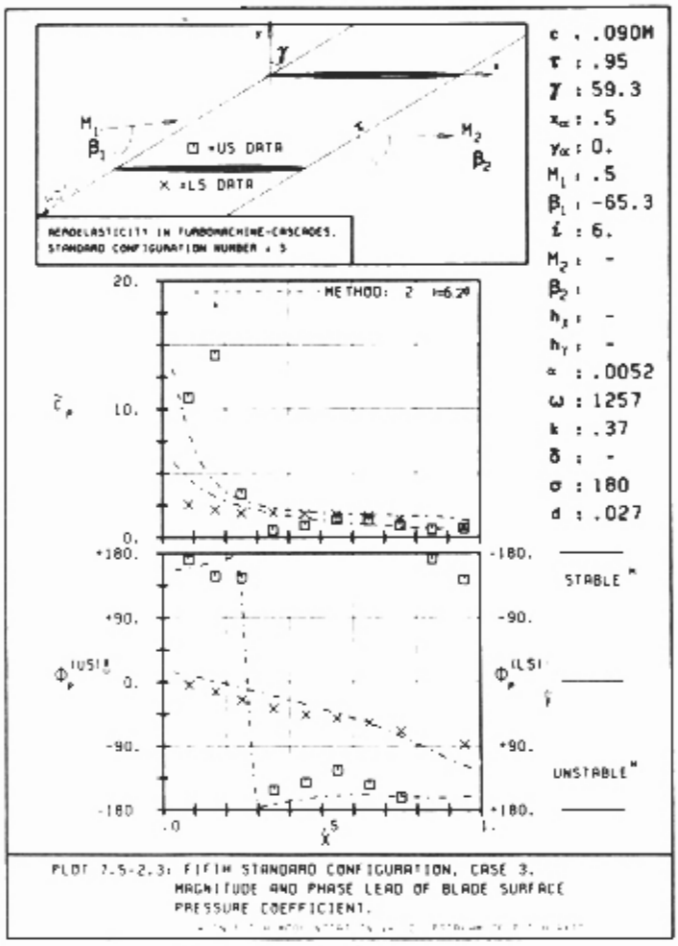


PLOT 7.5-2.3: FIFTH STANDARD CONFIGURATION, CASE 3.
MAGNITUDE AND PHASE LEAD OF BLADE SURFACE PRESSURE COEFFICIENT.

c) $i_{exp}=6^0$

**Fig. 7.5-9.** Blade surface pressure coefficient versus blade chord for $k_{exp}=0.37$, at $i_{exp}=2^0$, $4^0$ and $6^0$, resp.

Conclusions for aerodynamic damping

- The trend of stability versus reduced frequency and incidence is correctly predicted. The predicted magnitude is, however, not correct.

Conclusions for unsteady blade surface pressure difference coefficient

- The experimental data and the theoretical results agree well for a 2° incidence, at moderate reduced frequencies. At larger incidence angles, and especially at higher reduced frequencies, some larger discrepancies are found, both as regards the experiment and between the theories.
- The data and the theories agree better for the phase ($\Phi_{\Delta p}$) than for the magnitude ($\Delta \tilde{c}_p$).

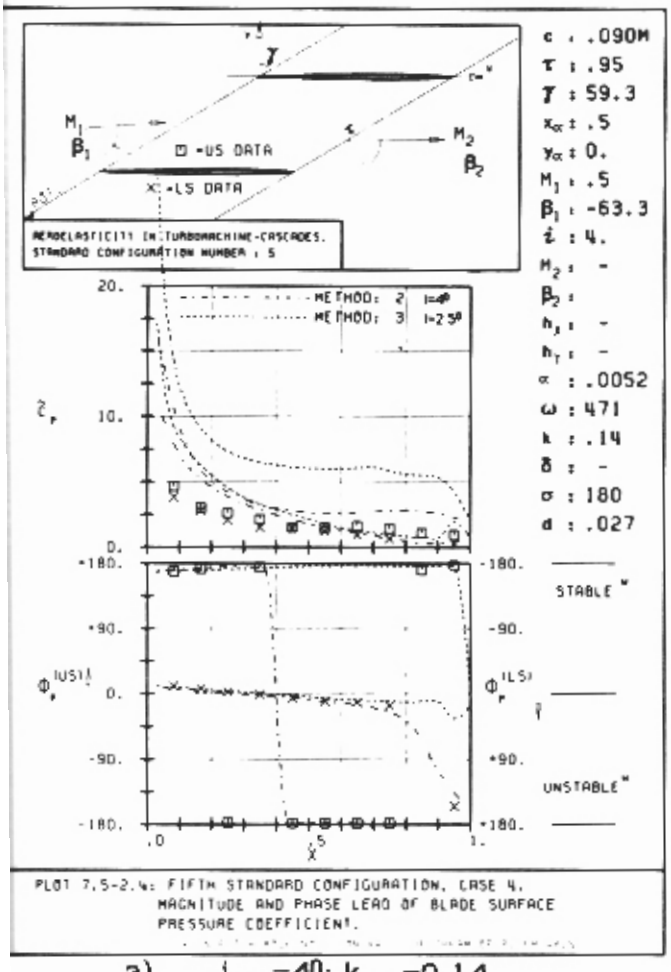


a) $i_{exp}=4^0$; $k_{exp}=0.14$

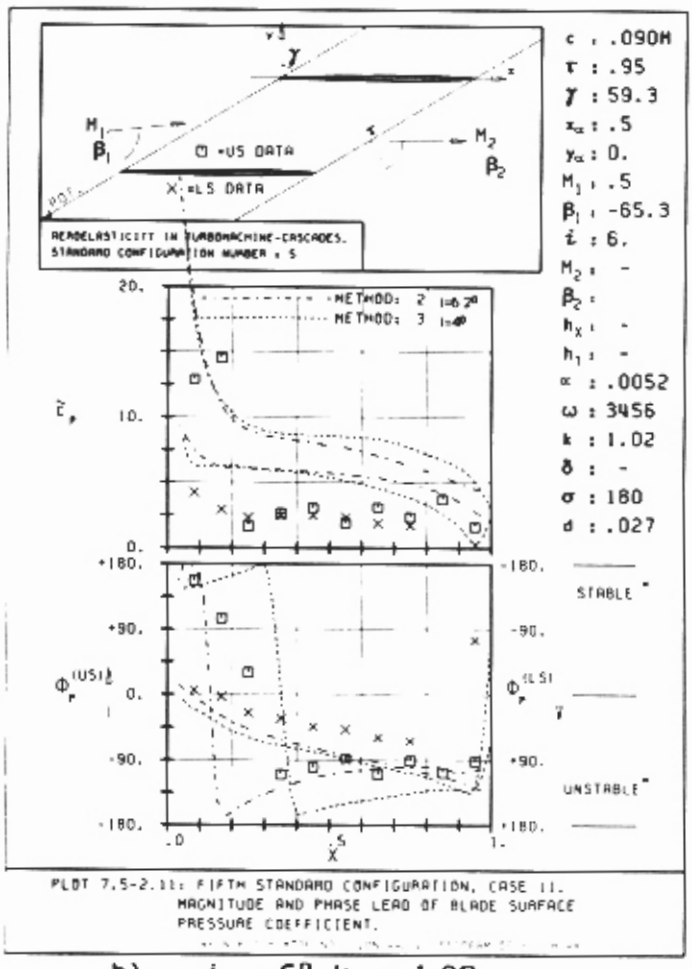


b) $i_{exp}=6^0$; $k_{exp}=1.02$

**Fig. 7.5-10.** Blade surface pressure coefficient versus blade chord at two operating conditions.

Conclusions for unsteady blade surface pressures

- The experimental and theoretical results agree extremely well as far as the phase angles ($\Phi_p^{us}$, $\Phi_p^{ls}$) are concerned.
However, fairly large differences appear in the magnitude of $\tilde{c}_p^{us}$, $\tilde{c}_p^{ls}$ although the trends are identical.

## 7.6. Sixth Standard Configuration (Steam Turbine Tip Section in Transonic Flow)

### Definition

This configuration is directed towards investigations of steam turbine rotor blade tip sections in the transonic flow regime.
The experiments are performed, in air, in the annular cascade test facility at the Swiss Federal Institute of Technology, Lausanne /22/. The data are included in the present study by kind permission of A. Bölcs and the sponsoring company, Brown Boveri Co., Baden /18/.
The cascade configuration consists of twenty vibrating low camber prismatic turbine blades. Each blade has a constant spanwise chord of c=0.0528 m and a span of 0.040 m, with $14^0$ camber and a maximum thickness-to-chord ratio of 0.0526. The stagger angle for the experiments presented here is $73.4^0$, and the gap-to-chord ratio is:

$\tau$ = 0.952 (hub)
1.071 (midspan)
1.190 (tip)

The hub-to-tip ratio of the facility is 0.80.
The cascade geometry is given in Fig. 7.6-1 and the profile coordinates in Table 7.6-1.
Experiments are performed with variable inlet flow velocity, incidence angle, expansion ratio, vibration mode shape, oscillation frequency and interblade phase angle /18/. In the case of self-excited blade vibration tests the blades oscillate without external excitation. Outside these flutter regions all 20 blades in the cascade are vibrated with an electromagnetic excitation system /26/.
Presently, only a limited number of pressure transducers are mounted in the blades, therefore it is not possible at this time to integrate the time-dependent pressure signals to obtain overall unsteady forces. Instead, the self-excited flutter limits of the cascade have been established for several parameters. Furthermore, after the experiments with the true self-excited blade vibrations /18/, another test series with 10 pressure transducers on the blades is scheduled /28/. This will allow for a first approximation of the overall unsteady forces and a comparison with the previously determined flutter boundaries.

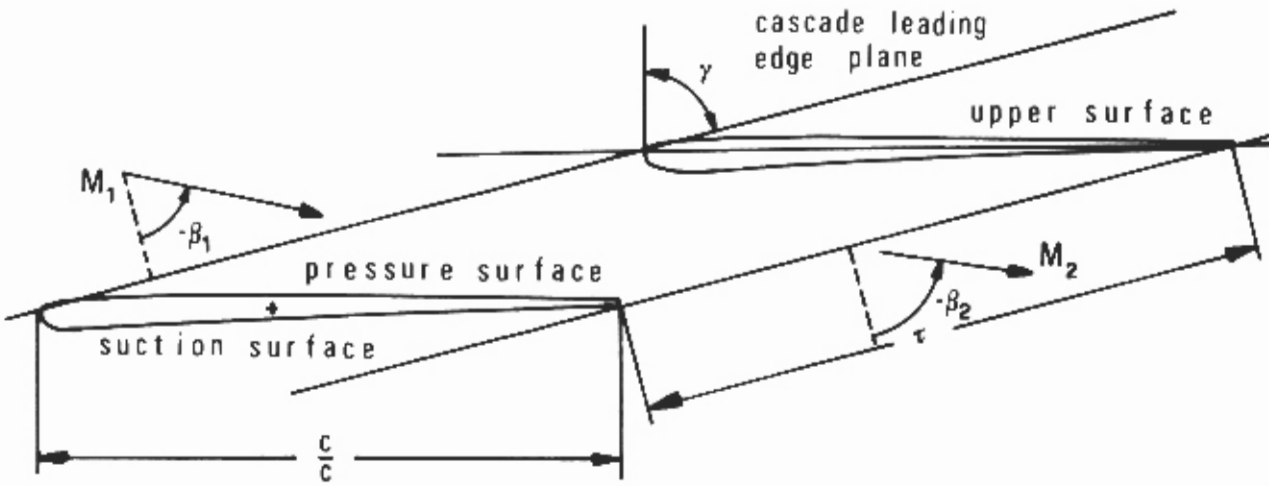


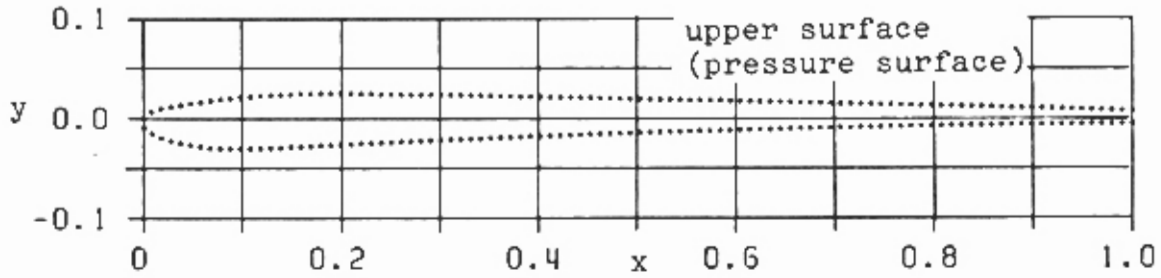


**Transonic Steam Turbine Profiles.**

Vibration in first bending mode
d = (thickness/chord)
γ = 73.4°
c = 0.0528 m
τ = 0.952 (hub)
1.071 (midspan)
1.190 (tip)
$M_2$ = varied
σ = varied

δ = 43.2°
= 0.0526
k = variable
span = 0.040 m
camber = 14.°
hub/tip = 0.8
f = 226 Hz
$\beta_1$ = varied

Nominal values: $M_1$=0.40; $\beta_1$=-62°; $M_2$=1.34; $\beta_2$=-71°
Working fluid: Air

Fig. 7.6-1. Sixth standard configuration: Cascade geometry

C = 0.05277 M

| UPPER SURFACE | | | | LOWER SURFACE | | | |
|---|---|---|---|---|---|---|---|
| X | Y | X | Y | X | Y | X | Y |
| 0.0000 | 0.0000 | .5033 | .0191 | 0.0000 | 0.0000 | .4930 | -.0151 |
| .0078 | .0063 | .5135 | .0189 | .0008 | -.0097 | .5032 | -.0148 |
| .0176 | .0090 | .5236 | .0187 | .0085 | -.0161 | .5133 | -.0145 |
| .0275 | .0109 | .5338 | .0185 | .0178 | -.0202 | .5234 | -.0142 |
| .0375 | .0127 | .5439 | .0183 | .0275 | -.0232 | .5336 | -.0138 |
| .0475 | 0143 | .5540 | .0181 | .0373 | -.0256 | .5437 | -.0135 |
| .0575 | .0157 | .5642 | .0179 | .0473 | -.0274 | .5538 | -.0132 |
| .0676 | .0171 | .5743 | .0177 | .0573 | -.0288 | .5640 | -.0130 |
| .0777 | .0184 | .5845 | .0175 | .0674 | -.0298 | .5741 | -.0127 |
| .0877 | .0195 | .5946 | .0173 | .0775 | -.0305 | .5843 | -.0124 |
| .0978 | .0204 | .6047 | .0171 | .0877 | -.0309 | .5944 | -.0121 |
| .1079 | .0213 | .6149 | .0169 | .0978 | -.0311 | .6045 | -.0119 |
| .1181 | .0221 | .6250 | .0167 | .1080 | -.0310 | .6147 | -.0116 |
| .1282 | .0225 | .6352 | .0165 | .1181 | -.0307 | .6248 | -.0113 |
| .1383 | .0230 | .6453 | .0162 | .1282 | -.0303 | .6349 | -.0111 |
| .1484 | .0235 | .6554 | .0160 | .1384 | -.0298 | .6451 | -.0108 |
| .1586 | .0239 | .6656 | .0158 | .1485 | -.0294 | .6552 | -.0106 |
| .1687 | .0242 | .6757 | .0156 | .1586 | -.0289 | .6654 | -.0104 |
| .1789 | .0243 | .6859 | .0153 | .1688 | -.0284 | .6755 | -.0101 |
| .1890 | .0243 | .6960 | .0151 | .1789 | -.0278 | .6856 | -.0099 |
| .1991 | .0243 | .7061 | .0149 | .1890 | -.0274 | .6958 | -.0097 |
| .2093 | .0242 | .7163 | .0147 | .1991 | -.0269 | .7059 | -.0095 |
| .2194 | .0240 | .7264 | .0144 | .2093 | -.0264 | .7161 | -.0093 |
| .2296 | .0239 | .7366 | .0142 | .2194 | -.0259 | .7262 | -.0091 |
| .2397 | .0237 | .7467 | .0140 | .2295 | -.0254 | .7363 | -.0089 |
| .2498 | .0236 | .7568 | .0137 | .2397 | -.0250 | .7465 | -.0087 |
| .2600 | .0235 | .7670 | .0135 | .2498 | -.0245 | .7566 | -.0085 |
| .2701 | .0235 | .7771 | .0133 | .2599 | -.0240 | .7668 | -.0083 |
| .2803 | .0234 | .7873 | .0130 | .2701 | -.0236 | .7769 | -.0082 |
| .2904 | .0233 | .7974 | .0128 | .2802 | -.0232 | .7870 | -.0080 |
| .3006 | .0232 | .8075 | .0125 | .2903 | -.0227 | .7972 | -.0078 |
| .3107 | .0231 | .8177 | .0123 | .3005 | -.0223 | .8073 | -.0077 |
| .3208 | .0229 | .8278 | .0120 | .3106 | -.0219 | .8175 | -.0075 |
| .3310 | .0227 | .8380 | .0118 | .3207 | -.0214 | .8276 | -.0074 |
| .3411 | .0225 | .8481 | .0115 | .3309 | -.0210 | .8377 | -.0072 |
| .3513 | .0223 | .8582 | .0112 | .3410 | -.0206 | .8479 | -.0071 |
| .3614 | .0220 | .8684 | .0110 | .3511 | -.0202 | .8580 | -.0070 |
| .3715 | .0218 | .8785 | .0107 | .3613 | -.0198 | .8682 | -.0068 |
| .3817 | .0215 | .8886 | .0104 | .3714 | -.0194 | .8783 | -.0067 |
| .3918 | .0213 | .8988 | .0102 | .3815 | -.0190 | .8884 | -.0066 |
| .4019 | .0211 | .9089 | .0099 | .3917 | -.0186 | .8986 | -.0065 |
| .4121 | .0210 | .9191 | .0096 | .4018 | -.0183 | .9087 | -.0064 |
| .4222 | .0208 | .9292 | .0093 | .4119 | -.0179 | .9189 | -.0063 |
| .4324 | .0206 | .9393 | .0090 | .4221 | -.0175 | .9290 | -.0062 |
| .4425 | .0204 | .9495 | .0088 | .4322 | -.0172 | .9392 | -.0061 |
| .4526 | .0202 | .9596 | .0085 | .4423 | -.0168 | .9493 | -.0060 |
| .4628 | .0200 | .9697 | .0082 | .4525 | -.0164 | .9594 | -.0060 |
| .4729 | .0198 | .9799 | .0079 | .4626 | -.0161 | .9696 | -.0059 |
| .4831 | .0195 | .9900 | .0076 | .4727 | -.0158 | .9797 | -.0058 |
| .4932 | .0193 | 1.0002 | .0073 | .4829 | -.0154 | 1.0000 | -.0057 |

**Table 7.6-1.** Sixth standard configuration: Dimensionless airfoil coordinates (spanwise identical)

## Aeroelastic Test Cases.

From the tests, 12 have been selected as test cases. These correspond to five separate time-averaged flow conditions where the outlet Mach number has been varied from sub- to supersonic (see Table 7.6-2), and they represent cases both inside and outside the experimentally-determined flutter limits of the cascade /18/. As the cascade exhibited flutter in the first bending mode, the cases reported here are in this mode, with a vibration direction of $\delta=43.2^0$.

All the experiments presented here have been performed with constant spanwise upstream flow conditions.

| | Time Averaged | | | | Time Dependent Parameters | | | | |
|---|---|---|---|---|---|---|---|---|---|
| Aeroelastic Test Case No. | $M_1$ (-) | $\beta_1$ (°) | $p_2/p_1$ (-) | $M_{2is}$ (-) | $h^o$ (-) | f (Hz) | k (-) | $\sigma$ (°) | $\delta$ (°) |
| 1 | 0.53 | 70 | 0.27 | 1.63 | 0.0030 | 226 | 0.068 | 0 | +43.2 |
| 2 | " | " | " | " | " | " | " | + 45 | " |
| 3 | " | " | " | " | " | " | " | + 90 | " |
| 4 | " | " | " | " | " | " | " | +135 | " |
| 5 | " | " | " | " | " | " | " | -180 | " |
| 6 | " | " | " | " | " | " | " | +135 | " |
| 7 | " | " | " | " | " | " | " | - 90 | " |
| 8 | " | " | " | " | " | " | " | - 45 | " |
| 9 | 0.52 | " | 0.50 | 1.20 | " | " | 0.092 | - 90 | " |
| 10 | " | " | 0.54 | 1.14 | " | " | 0.097 | " | " |
| 11 | " | " | 0.62 | 1.02 | " | " | 0.108 | " | " |
| 12 | " | " | 0.65 | 0.98 | " | " | 0.113 | " | " |

**Table 7.6-2.** Sixth standard configuration: Recommended aeroelastic test cases.

**Discussion of Time-Averaged Results.**

Fig. 7.6-2 shows the experimental time-averaged blade surface pressure distribution for the different backpressures. Due to the high expansion present in the leading edge region, major difficulties may arise in the numerical prediction of the steady-state flow conditions. Up to now, no theoretical steady-state results for this standard configuration have been obtained.

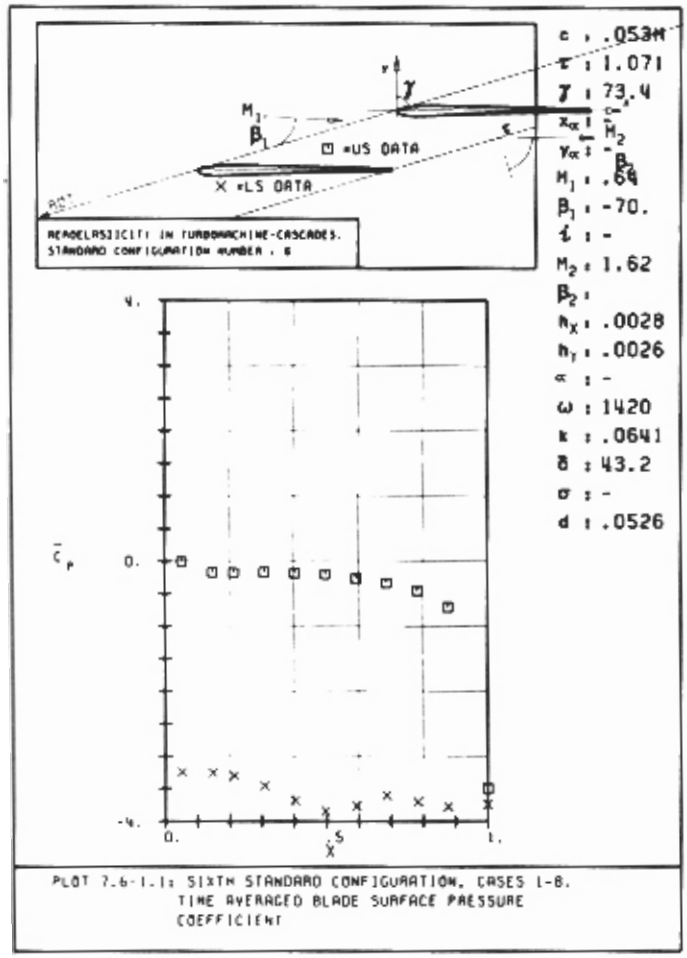


a) $M_{2is}$=1.63

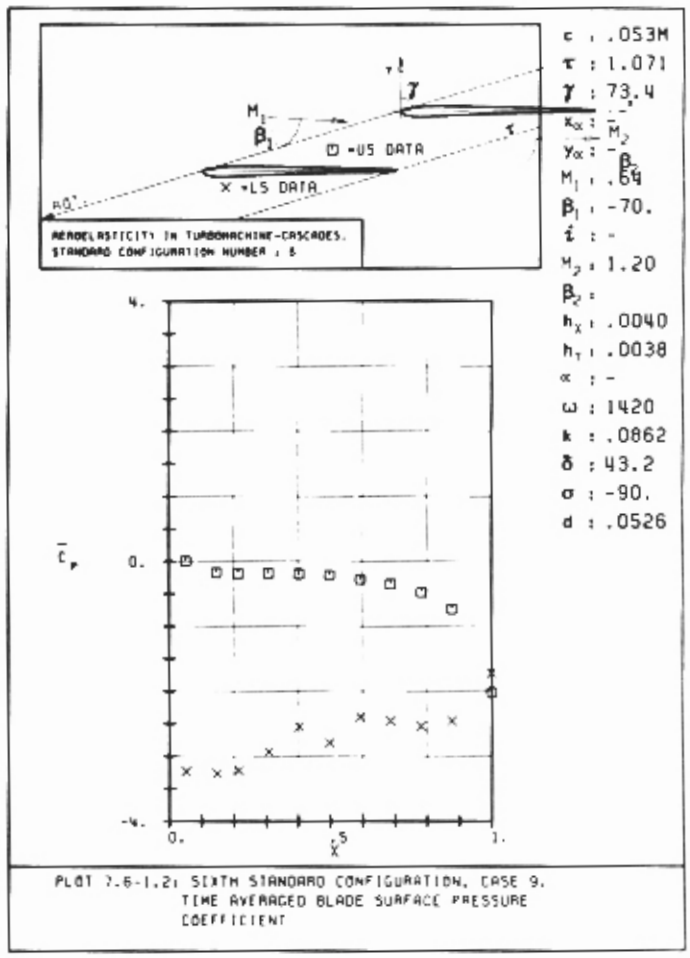


b) $M_{2is}$=1.20

**Fig. 7.6-2.** Continued on next page

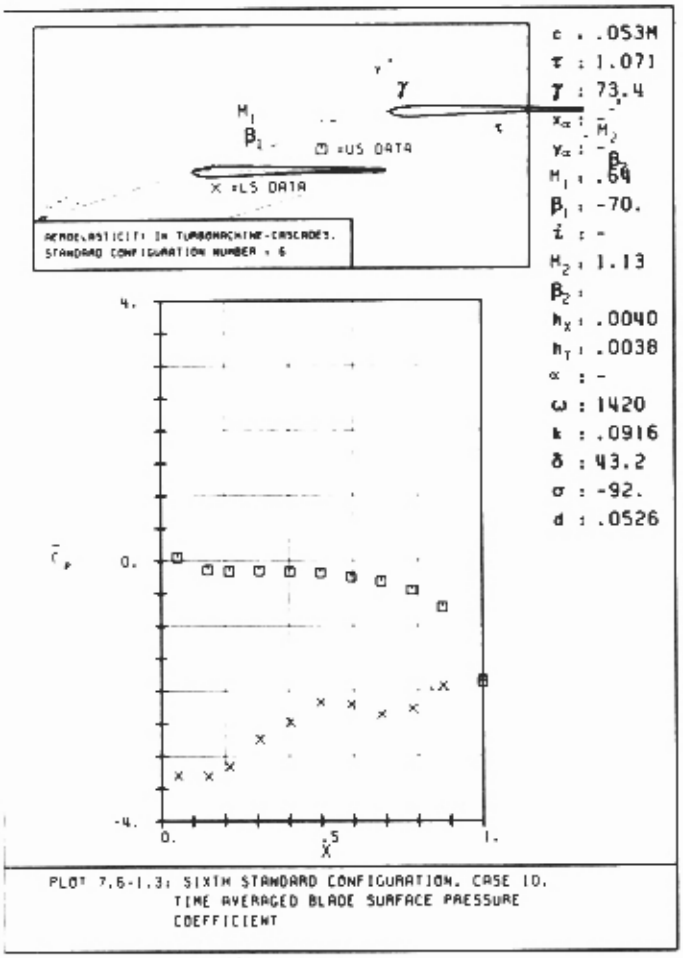


PLOT 7.6-1.3: SIXTH STANDARD CONFIGURATION, CASE 10. TIME AVERAGED BLADE SURFACE PRESSURE COEFFICIENT

c) $M_{2is}$=1.14

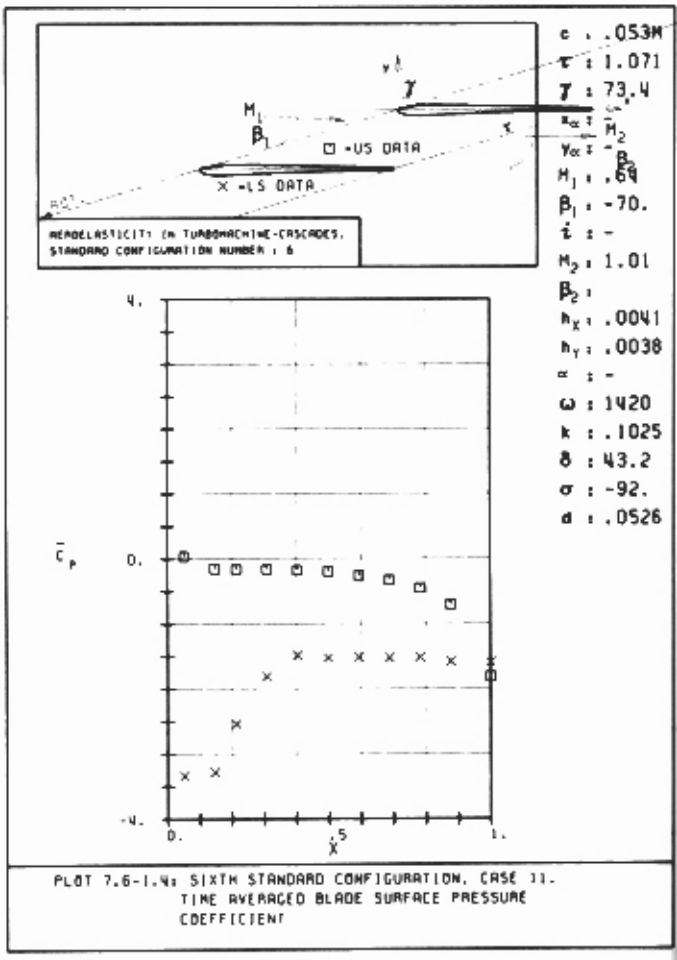


PLOT 7.6-1.4: SIXTH STANDARD CONFIGURATION, CASE 11. TIME AVERAGED BLADE SURFACE PRESSURE COEFFICIENT

d) $M_{2is}$=1.02

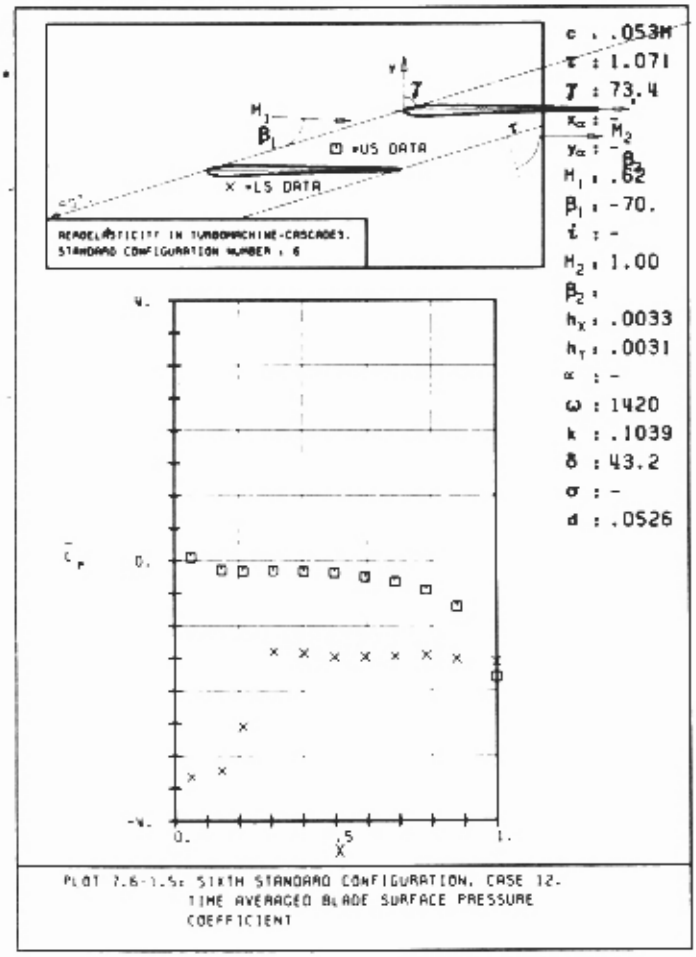


PLOT 7.6-1.5: SIXTH STANDARD CONFIGURATION, CASE 12. TIME AVERAGED BLADE SURFACE PRESSURE COEFFICIENT

e) $M_{2is}$=0.98

**Fig. 7.6-2.** Time-averaged blade surface pressure distribution for the aeroelastic test cases.

**Discussion of Time-Dependent Results.**

At this time, as mentioned above, the aeroelastic forces have not been determined experimentally. However, the experiments indicate regions of self-started blade vibrations, i.e. domains where the aeroelastic forces are large enough to overcome the mechanical damping of the system. These flutter limits are shown in Fig. 7.6-3, for three different aerodynamic excitations. In the first, a well-tuned cascade (blade vibration frequency f=230±0.5Hz) was used, with endplates at the tip of the blades to decrease the aerodynamic excitation from tip-clearance flow. In the second, the same cascade was tested, but without the endplates. Finally, in the third, the cascade was randomly mistuned (f=223±5Hz). It can be concluded that the mistuning, and the reduction of the secondary flow in the tip-clearance, damp the blade vibrations.

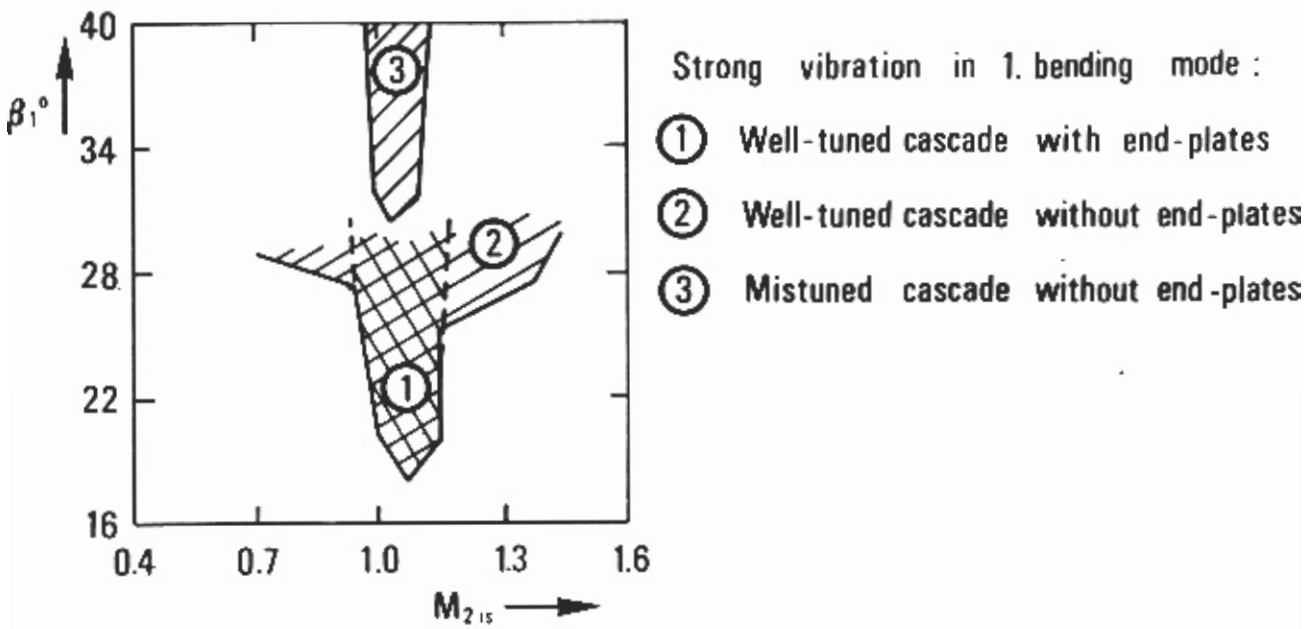


**Fig. 7.6-3.** Experimentally determined regions of self-started blade vibrations (copied from /18/, Fig. 11).

Theoretical results obtained from Method 10 indicate the same trend as the experiments. This can be concluded from Fig. 7.6-4. Here, the blade vibration is stable for subsonic, and unstable for supersonic, outlet flow conditions at a $-90^0$ interblade phase angle (Fig. 7.6-4a; compare Fig. 7.6-3). At the supersonic velocities the vibration is unstable for $-180^0<\sigma<0^0$, whereas for subsonic outlet flow conditions the vibration is stable for all interblade phase angles (Figs. 7.6-4b,c). The reasons for this instability are explained in /18/ to come mainly from instability on the blade suction surface in the throat region (Fig. 7.6-5).

## Conclusions for the Sixth Standard Configuration

The results of both the experiments and one prediction model(semi-actuator disk theory, Method 10) indicate that the blade vibration in the sixth configuration is unstable for supersonic outlet flow velocities in the interblade phase angle range $-180^0<\sigma<0^0$. The stability limits are accurately determined by Method 10[13] .
No comparisons between theoretical and experimental local blade surface pressures could be made in the present study.

13 This is somewhat surprising as for the fourth standard configuration this method showed large discrepancies between both the data and Method 7 (compare section 7.4). A possible explanation for this is the difference in camber between the fourth (camber=45°) and sixth (camber=14°) configurations.

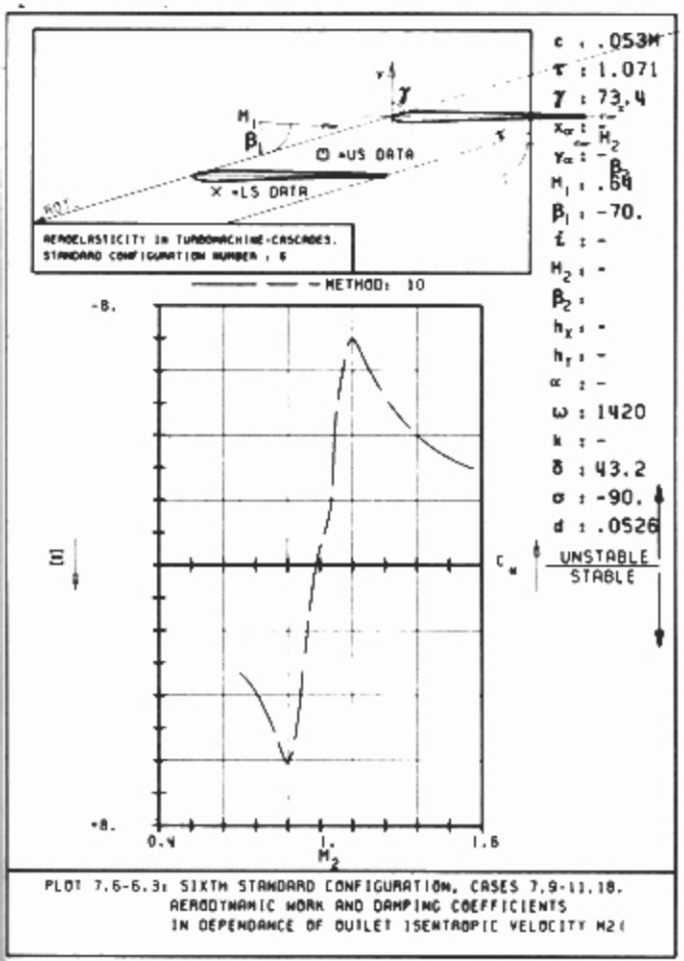


PLOT 7.6-6.3: SIXTH STANDARD CONFIGURATION, CASES 7,9-11,18.
AERODYNAMIC WORK AND DAMPING COEFFICIENTS
IN DEPENDANCE OF OUTLET ISENTROPIC VELOCITY M2(

a) $\sigma=-90^0$

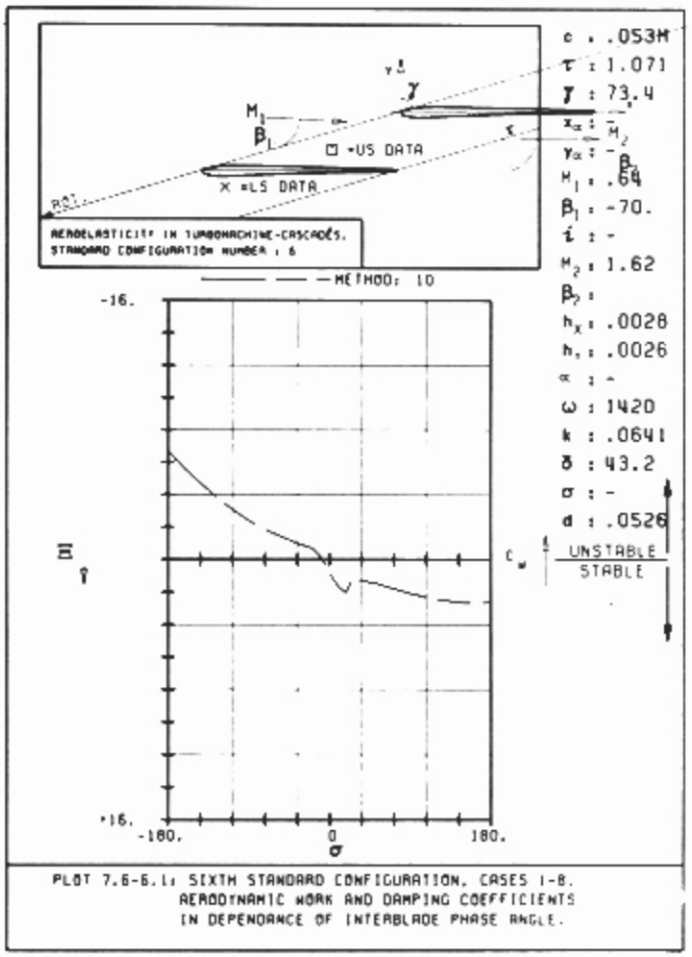


PLOT 7.6-6.1: SIXTH STANDARD CONFIGURATION, CASES 1-8.
AERODYNAMIC WORK AND DAMPING COEFFICIENTS
IN DEPENDANCE OF INTERBLADE PHASE ANGLE.

b) $M_{2is}=1.63$

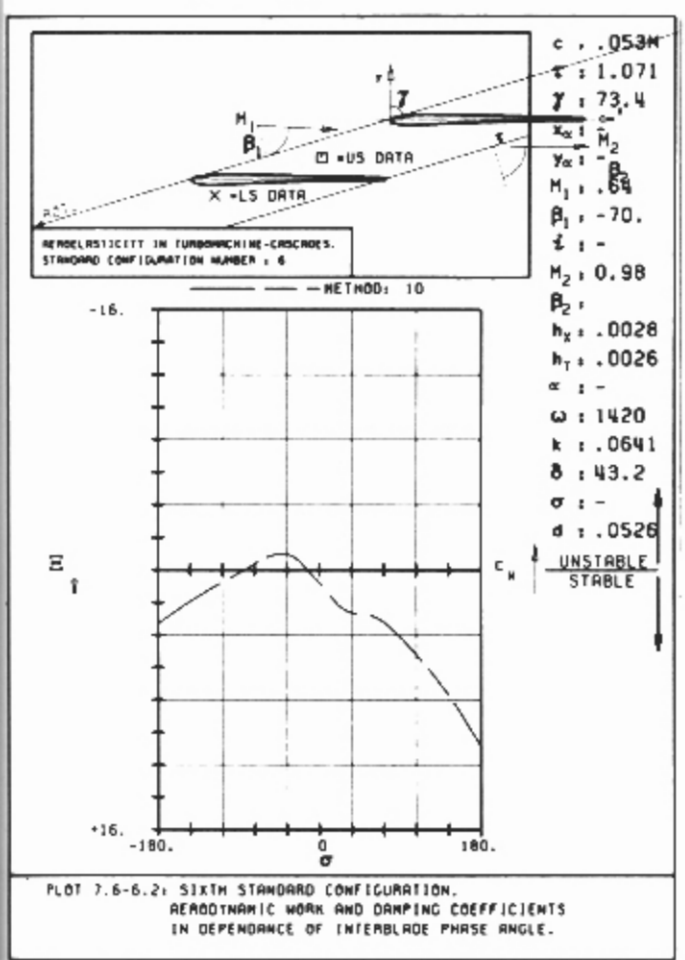


PLOT 7.6-6.2: SIXTH STANDARD CONFIGURATION.
AERODYNAMIC WORK AND DAMPING COEFFICIENTS
IN DEPENDANCE OF INTERBLADE PHASE ANGLE.

c) $M_{2is}=0.98$

Fig. 7.6-4. Theoretically determined aeroelastic damping coefficient versus isentropic outlet Mach number and interblade phase angle.

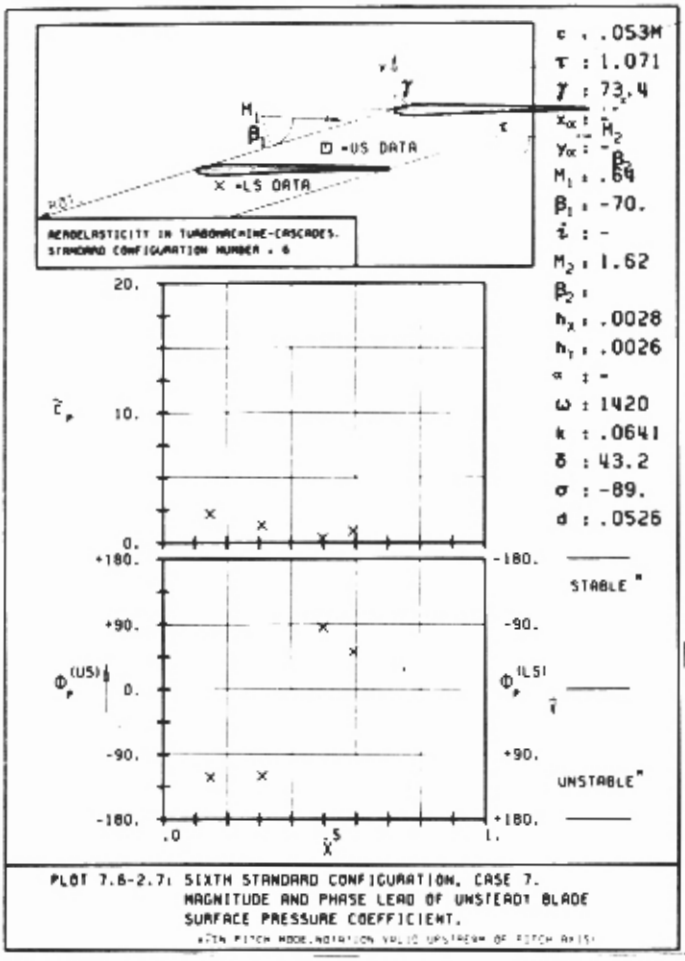


PLOT 7.6-2.7: SIXTH STANDARD CONFIGURATION, CASE 7.
MAGNITUDE AND PHASE LEAD OF UNSTEADY BLADE SURFACE PRESSURE COEFFICIENT.

a) $M_{2is}$=1.62

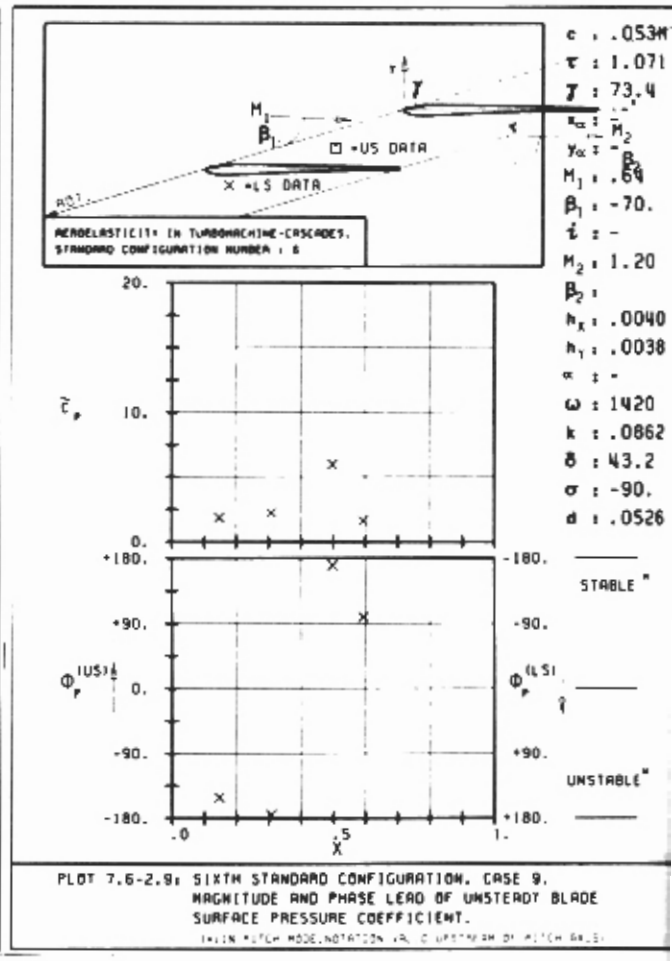


PLOT 7.6-2.9: SIXTH STANDARD CONFIGURATION, CASE 9.
MAGNITUDE AND PHASE LEAD OF UNSTEADY BLADE SURFACE PRESSURE COEFFICIENT.

b) $M_{2is}$=1.20

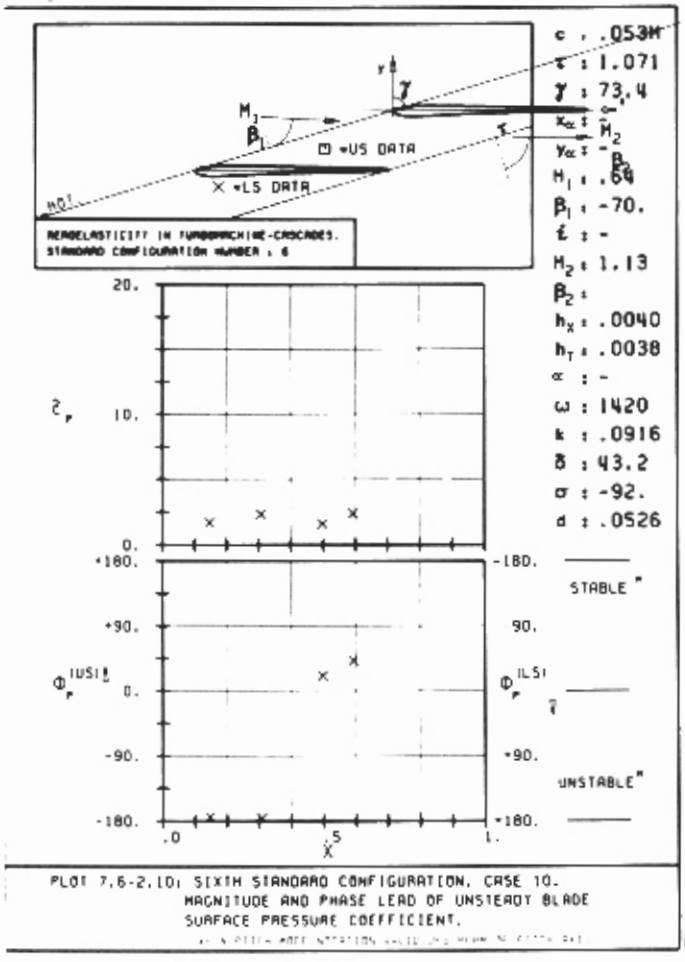


PLOT 7.6-2.10: SIXTH STANDARD CONFIGURATION, CASE 10.
MAGNITUDE AND PHASE LEAD OF UNSTEADY BLADE SURFACE PRESSURE COEFFICIENT.

c) $M_{2is}$= 1.13

**Fig. 7.6-5.** Time-dependent blade surface pressure coefficient.

## 7.7 Seventh Standard Configuration (Compressor Cascade in Supersonic Flow).

### Definition

The seventh standard configuration has been tested in the detroit Diesel Allison rectilinear air test facility, and the results are included here by courtesy of the sponsoring agent, D.R. Boldman at NASA Lewis Research Center [48, 49]. The configuration is representative for the tip sections of turboreactor fan stages (multiple circular arc transonic profiles. The profiles are taken from the 86.7% span section of the second stage of the five-stage TF41-A100 LP-IP compressor rig). Each blade (5 blades in the cascade) has a chord of c=0.0762 m and a span of 0.0762 m, with a -1.30° net camber and a maximum thickness-to-chord ratio of 0.034. The gap-to-chord ratio is 0.855 and the stagger angle 61.55°.
The cascade geometry is given in Figure 7.7-1 and the profile coordinates in Table 7.7-1.
The airfoils oscillate in pitching mode round a pivot axis at (0.50, 0.00), with a frequency between 710 Hz and 730 Hz. The pitching amplitude of the reference blade lies between 0.06° and 0.2°, depending on the test conditions, with some scatter in the motion amplitudes between neighboring blades (due to the high realistic frequencies).
Both the time-averaged and time-dependent instrumentation on this cascade is extensive, and data have been obtained of different interblade phase angles and axial velocity ratios. 20 blade surface pressure tappings were used (10 on each surface) to determine the steady-state blade surface pressure distribution and 12 dynamic pressure transducers were mounted on one blade (6 on each surface) to determinate the unsteady flow conditions.

### Aeroelastic Test Cases

From the tests, a total of 12 aeroelastic test cases are presented here for analyses.
These cases are included in Table 7.7-2, and they correspond to two different time-averaged flow conditions. The inlet Mach number is the same in both cases ($M_1$=1.315) and the outlet pressure ratio varies, corresponding to $M_2$=1.25 and $M_2$=0.99.
The blade vibration frequencies of the tests are very high (f=725 Hz), corresponding to reduced frequencies (based on semi-chord and inlet flow

## Supersonic Compressor Profiles.

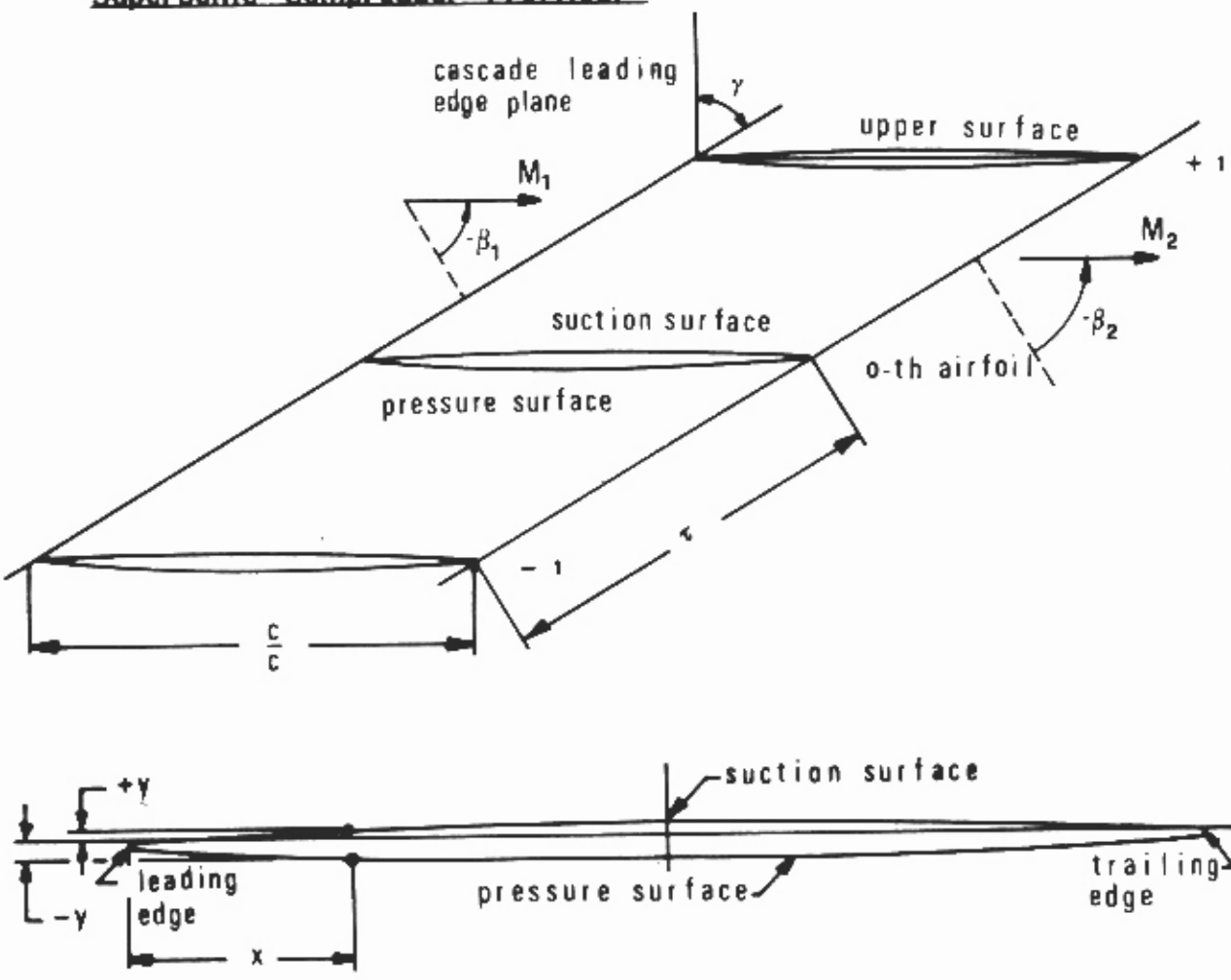


| | | | |
|---|---|---|---|
| Vibration in pitch around $(x_\alpha, y_\alpha)$ | | | = (0.5,0.0) |
| d | = (thickness/chord) | | = 0.034 |
| α | = 0.06-0.2° | $M_2$ | = variable |
| c | = 0.0762 m | $\beta_1$ | = 64.0° |
| τ | = 0.855 | camber | = -1.30° |
| k | = variable | γ | = 61.55° |
| span | = 0.0762 m | f | = 710-730 Hz |
| Working fluid: Air | | | |

Fig. 7.7-1. Seventh standard configuration: Cascade geometry

C = 0.0762 m (3.00 in)

| Upper surface (SUCTION SURFACE) | | Lower surface (PRESSURE SURFACE) | |
|---|---|---|---|
| X | +Y | X | -Y |
| 0 | -0.0029 | 0 | 0.0029 |
| 0.0026 | -0.0004 | 0.0027 | 0.0056 |
| 0.0278 | 0.0015 | 0.0279 | 0.0066 |
| 0.0655 | 0.0041 | 0.0657 | 0.0079 |
| 0.1032 | 0.0065 | 0.1035 | 0.0092 |
| 0.1410 | 0.0087 | 0.1412 | 0.0103 |
| 0.1788 | 0.0107 | 0.1790 | 0.0113 |
| 0.2165 | 0.0124 | 0.2168 | 0.0123 |
| 0.2543 | 0.0139 | 0.2546 | 0.0131 |
| 0.2921 | 0.0152 | 0.2923 | 0.0138 |
| 0.3299 | 0.0162 | 0.3301 | 0.0144 |
| 0.3551 | 0.0168 | 0.3552 | 0.0148 |
| 0.3929 | 0.0175 | 0.3930 | 0.0152 |
| 0.4307 | 0.0179 | 0.4308 | 0.0155 |
| 0.4685 | 0.0181 | 0.4685 | 0.0158 |
| 0.5063 | 0.0181 | 0.5063 | 0.0159 |
| 0.5441 | 0.0179 | 0.5440 | 0.0159 |
| 0.5820 | 0.0174 | 0.5818 | 0.0158 |
| 0.6198 | 0.0167 | 0.6195 | 0.0156 |
| 0.6576 | 0.0158 | 0.6573 | 0.0153 |
| 0.6828 | 0.0150 | 0.6824 | 0.0151 |
| 0.7205 | 0.0137 | 0.7202 | 0.0146 |
| 0.7583 | 0.0122 | 0.7580 | 0.0140 |
| 0.7961 | 0.0105 | 0.7958 | 0.0133 |
| 0.8338 | 0.0087 | 0.8336 | 0.0124 |
| 0.8716 | 0.0067 | 0.8714 | 0.0112 |
| 0.9093 | 0.0047 | 0.9092 | 0.0098 |
| 0.9471 | 0.0026 | 0.9470 | 0.0082 |
| 0.9848 | 0.0003 | 0.9848 | 0.0063 |
| 0.9974 | -0.0005 | 0.9974 | 0.0057 |
| 1.0000 | -0.0029 | 1.0000 | 0.0029 |

L.E. RADIUS/C= 0.0027
T.E. RADIUS/C= 0.0027

**Table 7.7-1.** Seventh standard configuration: Dimensionless airfoil coordinates

| Aeroelastic Test Case No | Time-averaged parameters $M_1$ (-) | $\beta_1$ (°) | $P_{w2}/P_{w1}$ (-) | $P_2/P_1$ (-) | $M_2$ (-) | $\beta_2$ (°) |
|---|---|---|---|---|---|---|
| 1-6 | 1.315 | - 64.0 | 0.958 | 1.04 | 1.25 | - 62.8 |
| 7-12 | " | " | 0.957 | 1.45 | 0.99 | - 63.6 |

| Aeroelastic Test Case No | Time-Dependent Parameters $f^{nominal}$ (Hz) | f (Hz) | k (-) | $\sigma^{nominal}$ (°) | $\sigma^{-1}$ (°) | $\sigma^{*}$ (°) | $\sigma^{+1}$ (°) | $\sigma^{+2}$ (°) | $\alpha^{nominal}$ (rad) | $\alpha^{-2}/\alpha^{*}$ (-) | $\alpha^{-1}/\alpha^{*}$ (-) | $\alpha^{*}$ (rad) | $\alpha^{+1}/\alpha^{*}$ (-) | $\alpha^{+2}/\alpha^{*}$ (-) |
|---|---|---|---|---|---|---|---|---|---|---|---|---|---|---|
| 1 | 725 | 725 | 0.44 | -180 | -173 | -187 | -178 | -180 | 0.00349 | 0.76 | 0.52 | 0.00122 | 1.27 | 0.0 |
| 2 | " | 714 | 0.43 | - 90 | - 91 | - 65 | - 81 | - 80 | " | 0.87 | 0.20 | " | 0.67 | " |
| 3 | " | - | 0.44 | - 45 | - | - | - | - | " | - | - | - | - | - |
| 4 | " | 724 | " | 0 | + 4 | + 6 | - 8 | 0 | " | 0.34 | 0.61 | 0.00379 | 0.75 | " |
| 5 | " | 745 | 0.45 | + 45 | + 48 | + 53 | + 54 | + 50 | " | 0.71 | 0.78 | 0.00206 | 0.32 | " |
| 6 | " | 724 | 0.44 | + 90 | + 91 | + 91 | + 84 | + 90 | " | 0.56 | 0.59 | 0.00187 | 0.97 | " |
| 7 | " | " | " | -180 | -172 | -168 | -163 | -170 | " | 1.21 | 0.85 | 0.00131 | 0.60 | " |
| 8 | " | 725 | " | - 45 | - 66 | - 69 | - 61 | - 66 | " | 0.54 | 0.44 | 0.00178 | 0.34 | " |
| 9 | " | 724 | " | 0 | - 4 | + 8 | - 5 | 0 | " | 0.64 | 0.96 | 0.00202 | 1.11 | " |
| 10 | " | " | " | + 45 | + 66 | + 59 | + 60 | + 60 | " | 0.36 | 0.65 | 0.00386 | 0.50 | " |
| 11 | " | 725 | " | + 90 | + 92 | + 74 | + 86 | + 85 | " | 0.66 | 0.96 | 0.00227 | 0.73 | " |
| 12 | " | " | " | +120 | + 96 | +115 | + 98 | +100 | " | 0.35 | 0.40 | 0.00129 | 0.25 | " |

**Table 7.7-2** Seventh standard configuration. 12 experimental aeroelastic test cases (defined from /57,58/)

velocity) of approximately k=0.45. However, due to these high vibration frequencies, a certain amount of difficulty was encountered in the nominal amplitudes and interblade phase angles, and in keeping these constant over the five blades in the cascade [48, 49]. Therefore, both the nominal and measured amplitudes and interblade phase angles are given in Table 7.7-2. As the prediction models used for calculating the aeroelastic behavior of the cascade consider travelling wave modes over a large number of blades it is expected that some discreapancies between the experimental data and the theoretical results will be present. Therefore, good agreement is hardly to be expected. However, it should be noted that due to the considerable complications involved in measuring unsteady transonic flow in cascades, the data presented are representative for the state-of-the-art of aeroelastic investigations on compressors in the transonic flow region.

**Discussion of Time-Averaged Results**

The 12 aeroelastic cases correspond, as mentioned above, to 2 steady-state conditions ($M_1$=1.315; $M_2$=1.25 and 0.99). The time-averaged data are given, together with the results obtained from Methods 7 and 18, in Fig. 7.7-2. It is seen that the trend of the predicted time-averaged blade surface pressure coefficient agrees with the experimental data. However, absolute values do not agree well, either for the low ($M_2$=1.25) or the high ($M_2$=0.99) pressure ratio case.

For the lower pressure ratio, the Schlieren pictures indicate that the leading edge shock is slightly detached and that it impinges on the blade suction surface at about 90% chordwise position.

In the case of the higher pressure ratio, the Schlieren pictures indicate instead a boundary layer separation downstream of the shock wave intersection of the airfoil (at about 40% chord) [48]. This separation was taken into account in Method 7 by performing a boundary layer analyses and then correcting the blade geometry to consider the increase in the displacement thickness of the boundary layer [40]. The correct shock position and exit flow conditions were obtained in Method 7 by adding this extra thickness onto the aerofoil. However, no such attempt to match the experimental data was made in Method 18, which to some extent may explain the large differences between the two predicted results.

## Discussion of Time-Dependent Results

When discussing the time-dependent results the experimentally determined steady-state boundary layer separation at about 40% chord for the high pressure ratio should be kept in mind. Both prediction models 7 and 18 are inviscid and cannot deal with unsteady response to shock/boundary layer interactions.

The non-constant blade vibration amplitudes and interblade phase angles in the experiments also influence to a certain extent the agreement between the data and the traveling wave analyses. It was shown in [40] that a flat plate theory with variable blade vibration amplitudes agreed better with the data than the same model assuming a constant blade vibration amplitude [40, 64].

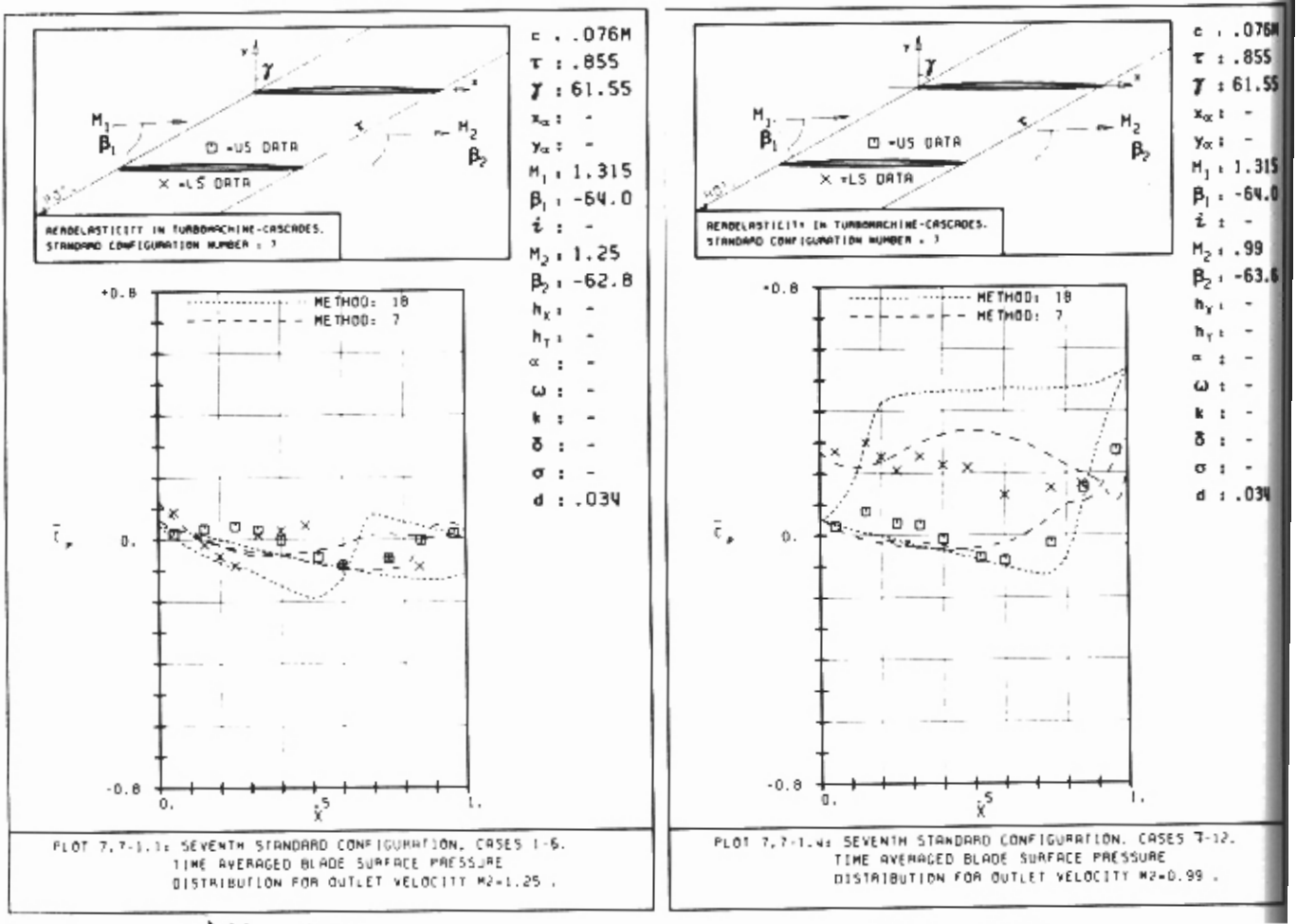


a) $M_2 = 1.25$ b) $M_2 = 0.99$

**Fig. 7.7-2.** Steady-state blade surface pressure distribution at $M_1$=1.315, $\beta_1$=-64.0°.

Intergrated values

The aeroelastic lift, moment and damping coefficients were calculated in the experiments from the measured blade amplitude and the unsteady pressure coefficient and its phase angle relative to the blade motion. The leading edge and trailing edge values were obtained by extrapolating the 15% and 85% chord data.

For the low pressure ratio ($M_2$=1.25, Fig. 7.7-3a) the trend of the aeroelastic damping coefficient $\Xi$, versus the interblade phase angle, is correctly given by the two models (7, 18) using the full blade geometry. This is also the case for a flat plate analyses (Method 5), using a zero mean incidence angle (i.e. $\beta_1$=-61.55°). All the theories predict the most stable situation around $\sigma$=-120°, and the most unstable around $\sigma$=+45°. This is also seen to be the case for the data. However, the magnitude is different according to the different theories.

Also at the high pressure ratio ($M_2$=0.99, Fig. 7.7-3b), the trend of the thoeries agrees well with the data. In the least stable position ($\sigma$=+90°) the data and Method 18 indicate a slight instability, whereas Method 7 lies just at the stability-line. It should be noted here that the stage was believed to be deeply into flutter at $M_2$=0.99 and out of flutter at $M_2$=1.25 [40].

Considering the theoretical and experimental difficulties involved in determining the unsteady flow in the transonic flow regime, and the experimental accuracy (especially while integrating with 12 transducers at the high pressure ratio), the results are encouraging.

Also the calculation of the magnitude of the moment coefficient ($\tilde{c}_m$) shows a good agreement between the trend of the data and the theories, especially at the low pressure ratio (Fig. 7.7-3c,d). However, a discrepancy can be found in the phase angle. It is especially interesting to note that, although the aerodynamic damping coefficient from Method 7 agrees well with the data at the high pressure ratio ($M_2$=1.25, Fig. 7.7-3b), a fairly large difference is found in the moment coefficient (Fig. 7.7-3d). In the phase angle $\Phi_m$, differences of up to $\Delta\Phi_m(=\Phi_{m,Theory} - \Phi_{m,Exp})$=180° are noted.

The aeroelastic lift coefficient ($\tilde{c}_l(t)$) does not influence the stability of a pure harmonic pitching motion. This information is given in Fig. 7.7-4. It is concluded that the trend of the magnitude ($\tilde{c}_l$) is correct, but that the phase angle ($\Phi_l$) shows a general discrepancy of up to $\Delta\Phi_l=\Phi_{l,Theory}-\Phi_{l,Exp}$=180°.

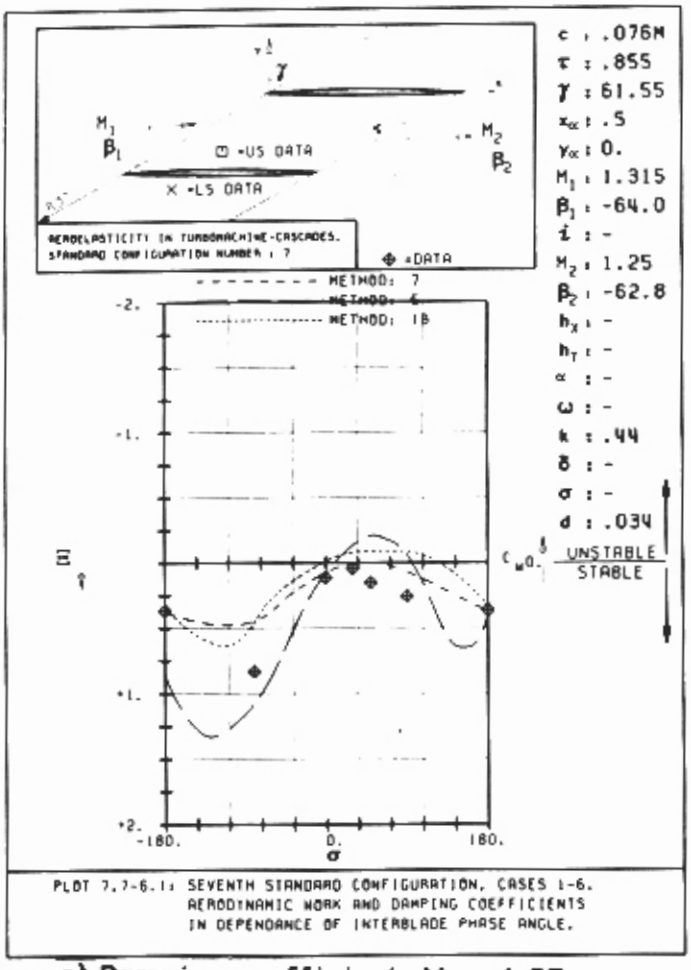


PLOT 7.7-6.1: SEVENTH STANDARD CONFIGURATION, CASES 1-6. AERODYNAMIC WORK AND DAMPING COEFFICIENTS IN DEPENDANCE OF INTERBLADE PHASE ANGLE.

a) Damping coefficient, $M_2 = 1.25$

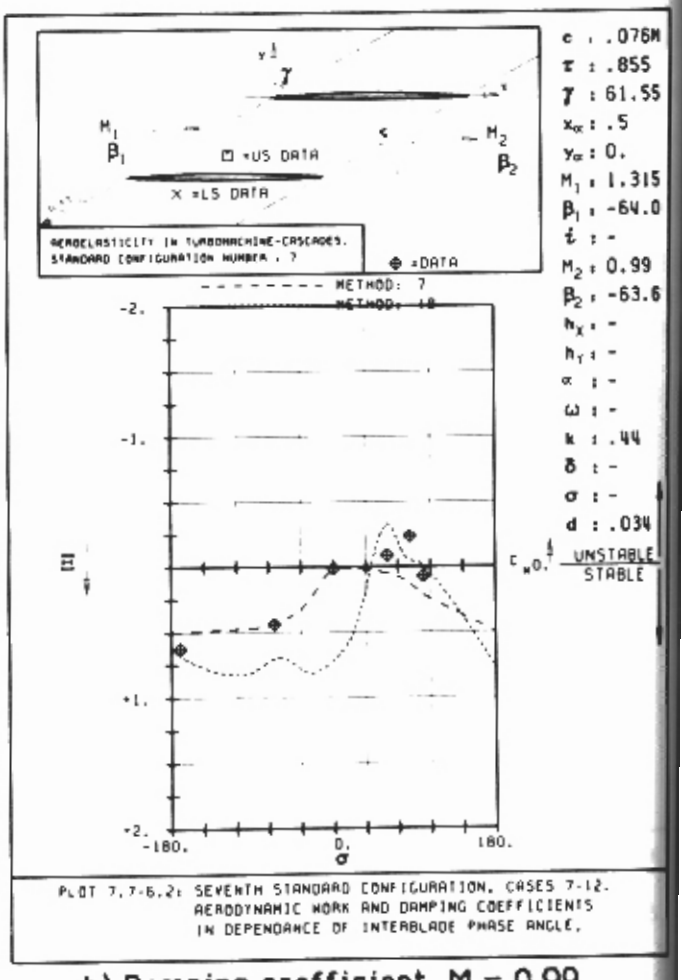


PLOT 7.7-6.2: SEVENTH STANDARD CONFIGURATION, CASES 7-12. AERODYNAMIC WORK AND DAMPING COEFFICIENTS IN DEPENDANCE OF INTERBLADE PHASE ANGLE.

b) Damping coefficient, $M_2 = 0.99$

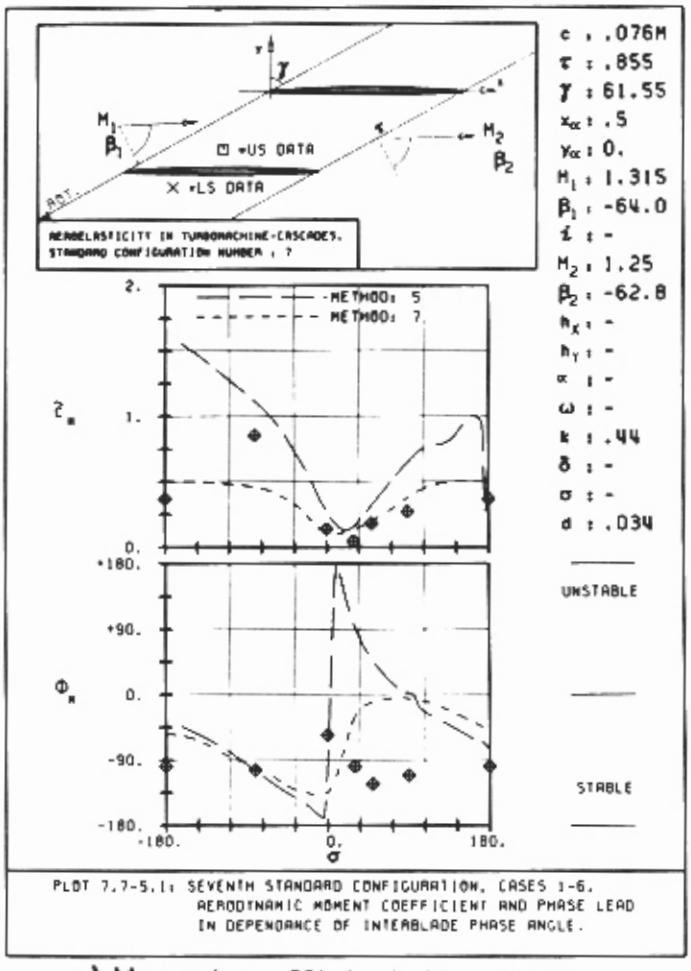


PLOT 7.7-5.1: SEVENTH STANDARD CONFIGURATION, CASES 1-6. AERODYNAMIC MOMENT COEFFICIENT AND PHASE LEAD IN DEPENDANCE OF INTERBLADE PHASE ANGLE.

c) Moment coefficient, $M_2 = 1.25$

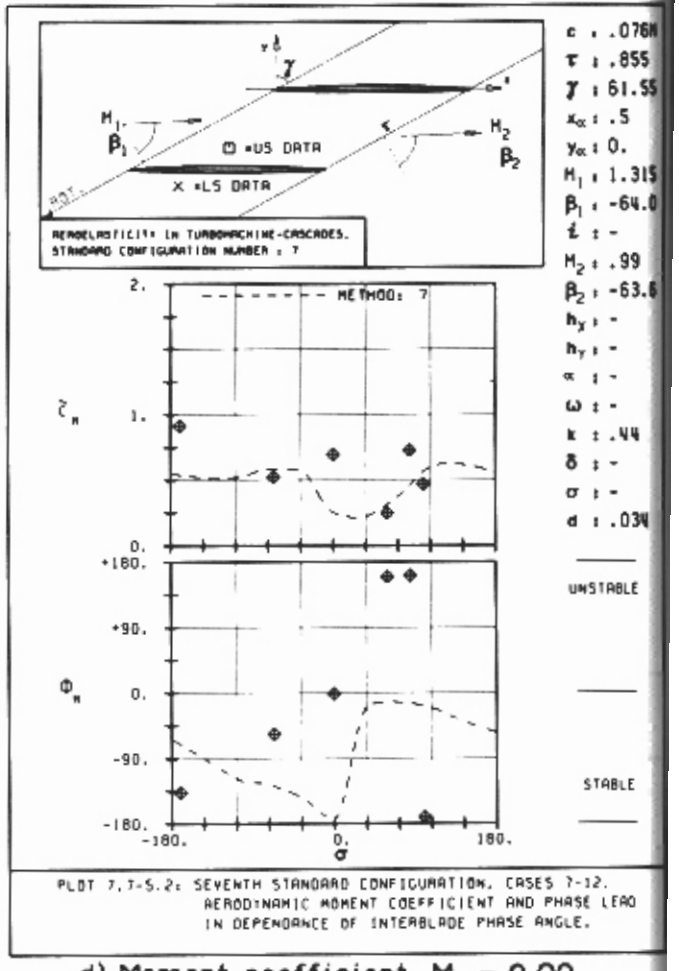


PLOT 7.7-5.2: SEVENTH STANDARD CONFIGURATION, CASES 7-12. AERODYNAMIC MOMENT COEFFICIENT AND PHASE LEAD IN DEPENDANCE OF INTERBLADE PHASE ANGLE.

d) Moment coefficient, $M_2 = 0.99$

**Fig. 7.7-3.** Aerodynamic damping and moment coefficients versus interblade phase angle for $M_2 = 1.25$ and $M_2 = 0.99$.

Blade Surface Pressure Differences

The trend of the magnitude of the time-dependent blade surface pressure diference coefficient ($\Delta\tilde{c}_p$) is correctly predicted at the low pressure ratio ($M_2$=1.25, Fig. 7.7-5). However, the predicted phase angles disagree with the measured ones, along the whole chord, while the theories agree well with each other.

The flat plate analyses (Method 5) predicts a discontinuity in $\Delta\tilde{c}_p$ at the position where the trailing edge shock impinges on the blade pressure surface ($x_{shock}$=0.55).

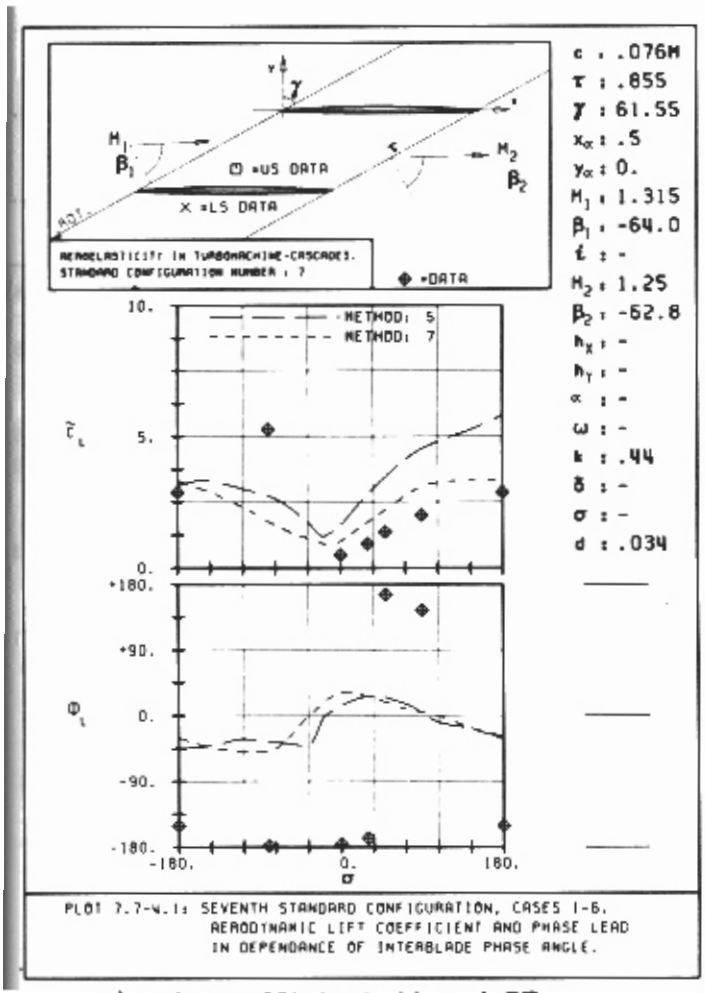


a) Lift coefficient, $M_2$ = 1.25

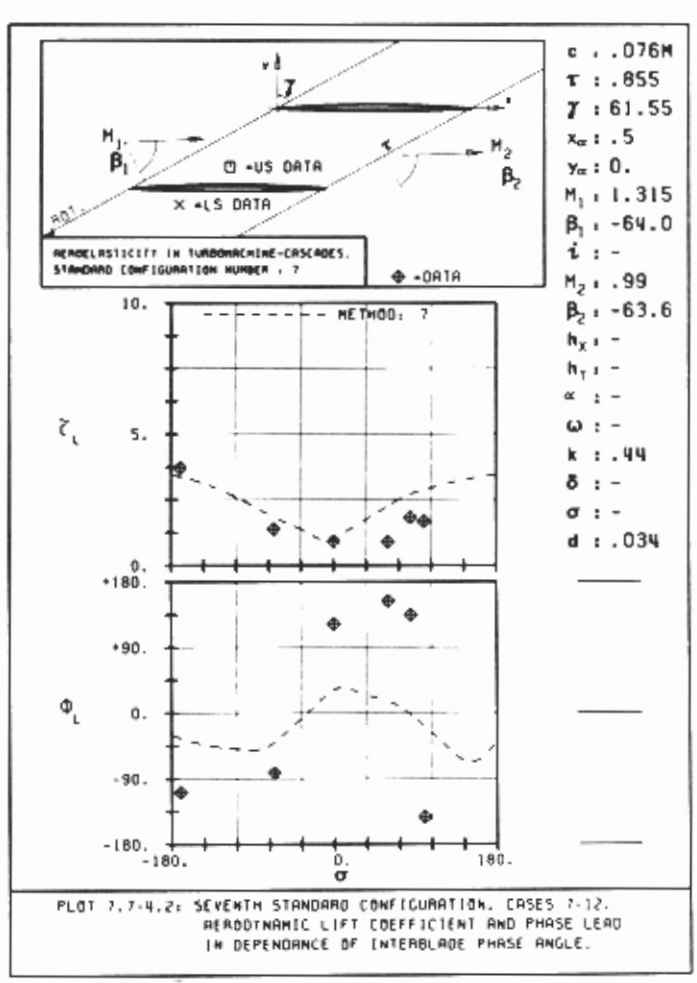


b) Lift coefficient, $M_2$= 0.99

**Fig. 7.7-4.** Aerodynamic lift coefficient versus interblade phase angle for $M_2$ = 1.25 and $M_2$ = 0.99.

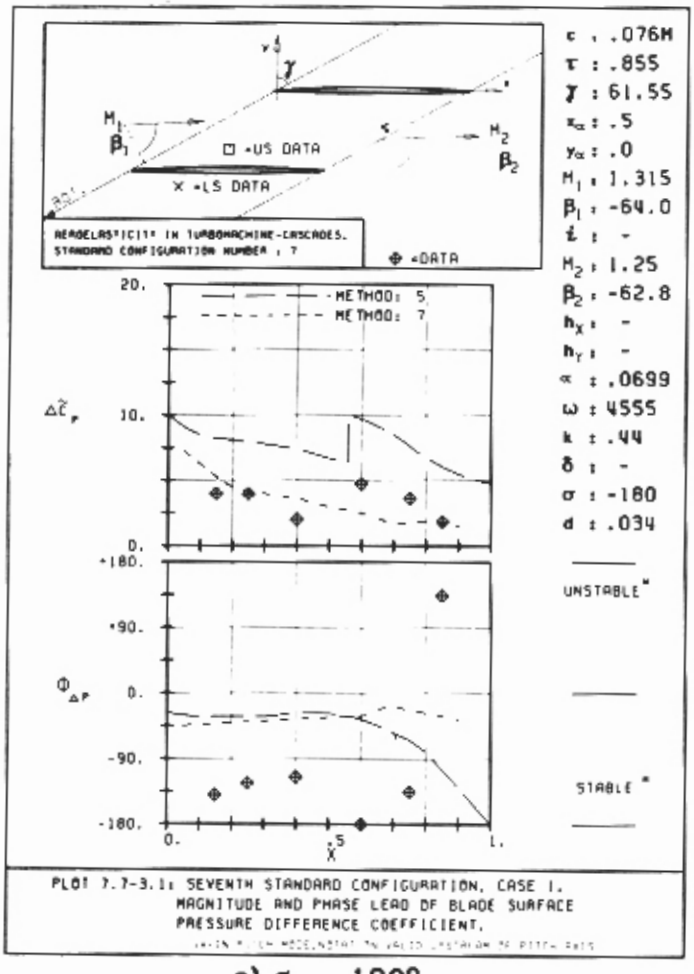


PLOT 7.7-3.1: SEVENTH STANDARD CONFIGURATION, CASE 1. MAGNITUDE AND PHASE LEAD OF BLADE SURFACE PRESSURE DIFFERENCE COEFFICIENT.

a) $\sigma = -180^0$

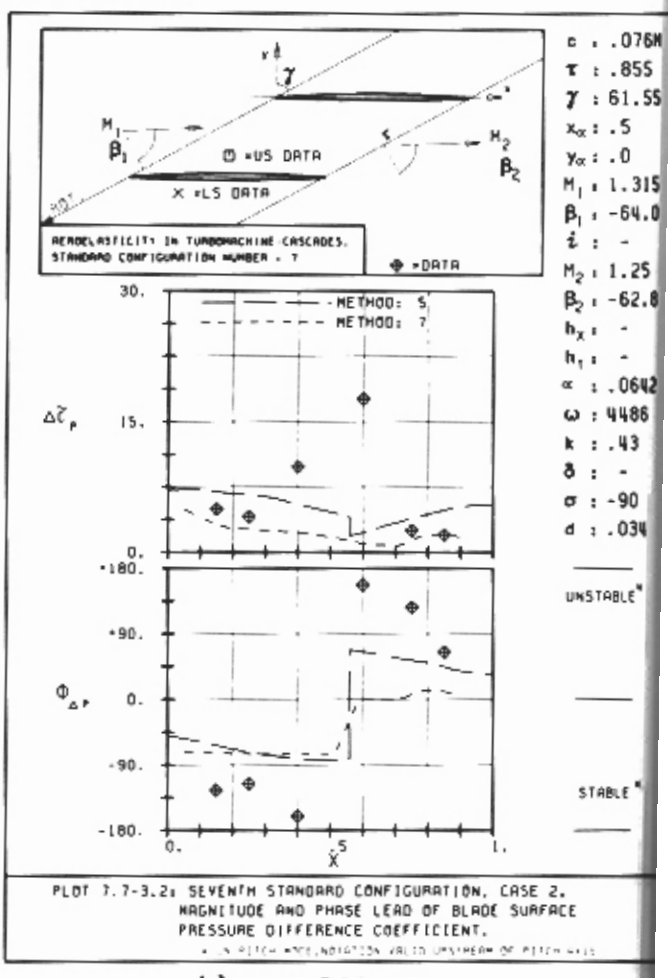


PLOT 7.7-3.2: SEVENTH STANDARD CONFIGURATION, CASE 2. MAGNITUDE AND PHASE LEAD OF BLADE SURFACE PRESSURE DIFFERENCE COEFFICIENT.

b) $\sigma = -90^0$

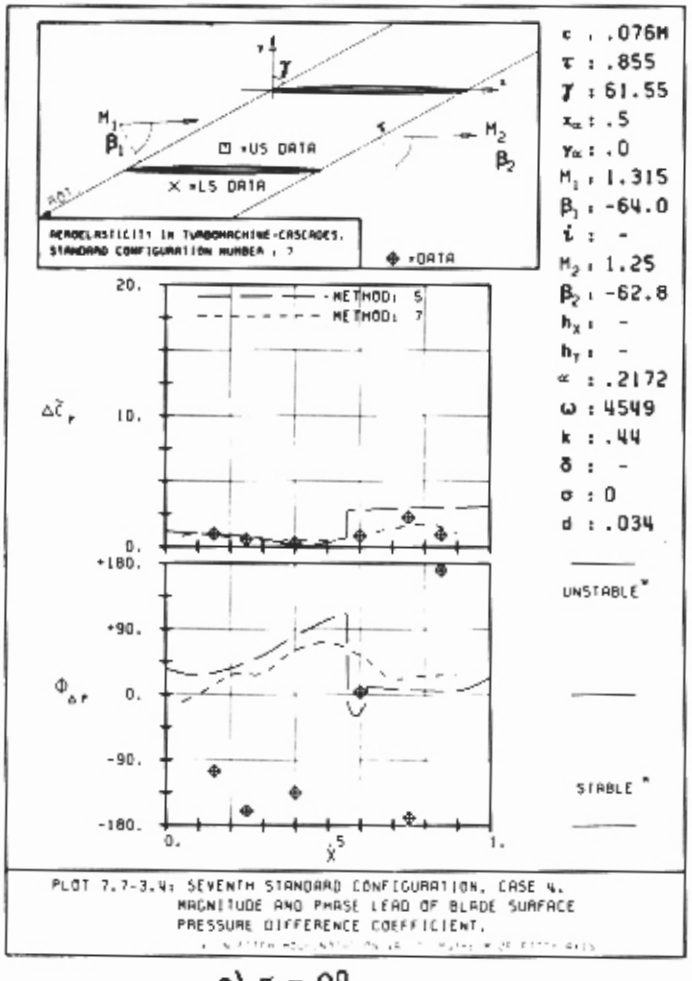


PLOT 7.7-3.4: SEVENTH STANDARD CONFIGURATION, CASE 4. MAGNITUDE AND PHASE LEAD OF BLADE SURFACE PRESSURE DIFFERENCE COEFFICIENT.

c) $\sigma = 0^0$

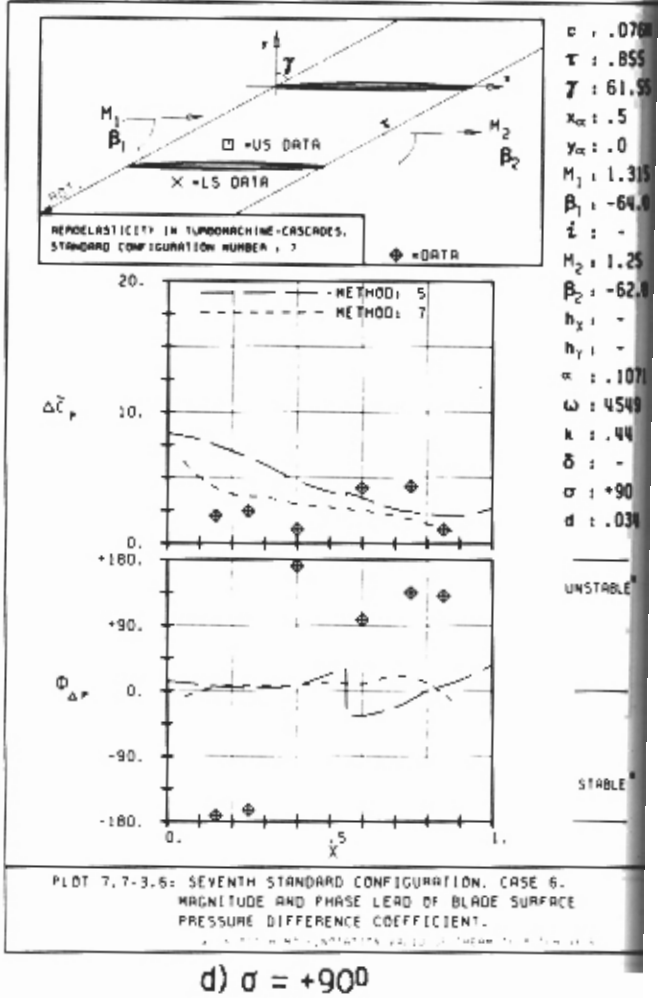


PLOT 7.7-3.6: SEVENTH STANDARD CONFIGURATION, CASE 6. MAGNITUDE AND PHASE LEAD OF BLADE SURFACE PRESSURE DIFFERENCE COEFFICIENT.

d) $\sigma = +90^0$

**Fig. 7.7-5.** Time-dependent blade surface pressure difference coefficient along blade chord at $M_2 = 1.25$.

Some slight indication of this can possibly also be found in the experimental data, whereas Method 7 smears out the unsteady response of the shock impingement on the blade. Away from this region, the flat plate analyses (Method 5) and the full geometry, potential flow solver (Method 7) give similar results.

Also at the higher pressure ratio the trend of the magnitude ($\Delta\tilde{c}_p$) as predicted by the theories agrees well with the data, both for the flat plate and full geometry solvers. Again, the phase angle ($\Phi_{\Delta p}$) is not well predicted.

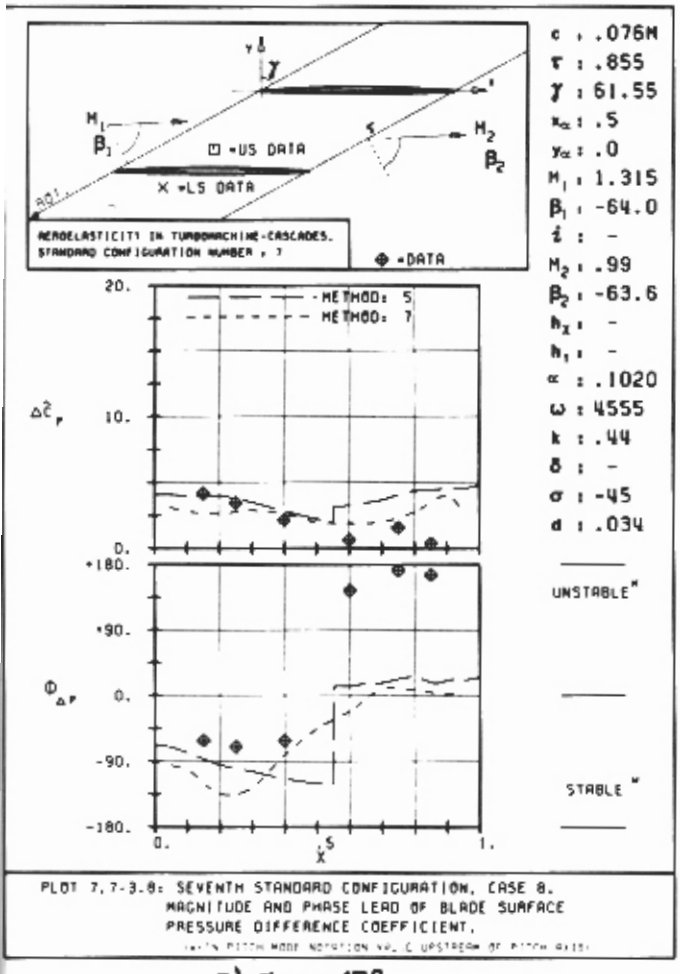


PLOT 7.7-3.8: SEVENTH STANDARD CONFIGURATION, CASE 8.
MAGNITUDE AND PHASE LEAD OF BLADE SURFACE
PRESSURE DIFFERENCE COEFFICIENT.

a) $\sigma = -45^0$

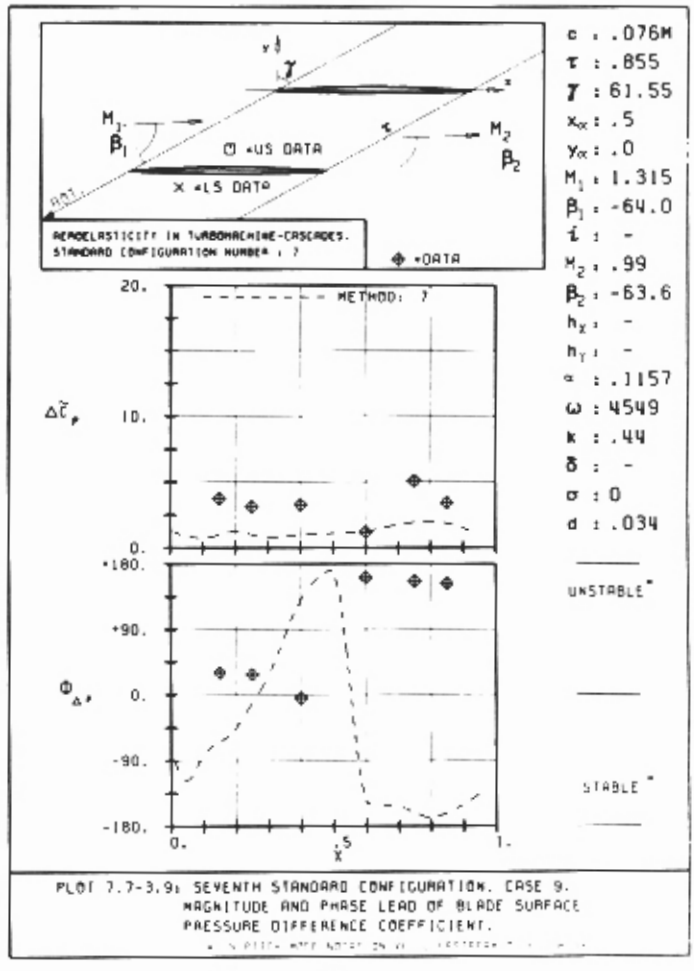


PLOT 7.7-3.9: SEVENTH STANDARD CONFIGURATION, CASE 9.
MAGNITUDE AND PHASE LEAD OF BLADE SURFACE
PRESSURE DIFFERENCE COEFFICIENT.

b) $\sigma = 0^0$

**Fig. 7.7-6.** Time-dependent blade surface pressure difference coefficient along blade chord at $M_2 = 0.99$.

Blade Surface Pressures

From the few predicted blade surface pressure results obtained on this cascade, a modest agreement is found in the magnitude ($\tilde{c}_p^{us}$, $\tilde{c}_p^{ls}$) both for $M_2$=1.25 and $M_2$=0.99. Again, discrepancies are found in the phase angles (Fig. 7.7-7), especially towards the trailing edge region where the experiments indicate a boundary layer separation. However, these differences seem to be smaller than the corresponding ones for the pressure difference ($\Phi_{\Delta p}$).

## Conclusions for the Seventh Standard Configuration

From the study on a 3% thick, low cambered compressor profile in supersonic flow at a high reduced frequency, oscillating in pitching mode, it can be concluded that:

- The experimental steady-state blade surface pressure distribution cannot be fully reproduced by theoretical methods. Indications of the boundary layer separations on the suction surface on the aft part of the blade exist. This phenomenon certainly influences both the steady-state and time-dependent flow response.
- The experimental blade vibration amplitudes and interblade phase angles were not constant between the 5 blades in the cascade (Table 7.7-2). This fact influences the agreement with the traveling wave analyses. It is expected that the agreement would be better if the prediction models also considered non-constant blade vibration amplitudes and interblade phase angles.
- Both the experiment and the available theories indicate the same trends for the aeroelastic damping coefficient versus the interblade phase angle and outlet flow velocity. The magnitude is however not fully predictable.
- The range of predicted instabilities, or near instabilities, agrees well with the experimenta data.
- For low pressure ratios the stability margins are predicted just as well with a flat plate anlyses as with models considering the full blade geometry.
- The amplitudes of $\tilde{c}_m(t)$, $\Delta\tilde{c}_p(x,t)$ and $\tilde{c}_p^{us,ls}(x,t)$ are modestly well predicted. However, the corresponding phase angles do not agree with the data. Again, for low pressure ratios, the flat plate analyses agree well with the full geometry solvers.
- Further work, both experimental and theoretical, is necessary to establish the origin of the differences found in this standard configuration.

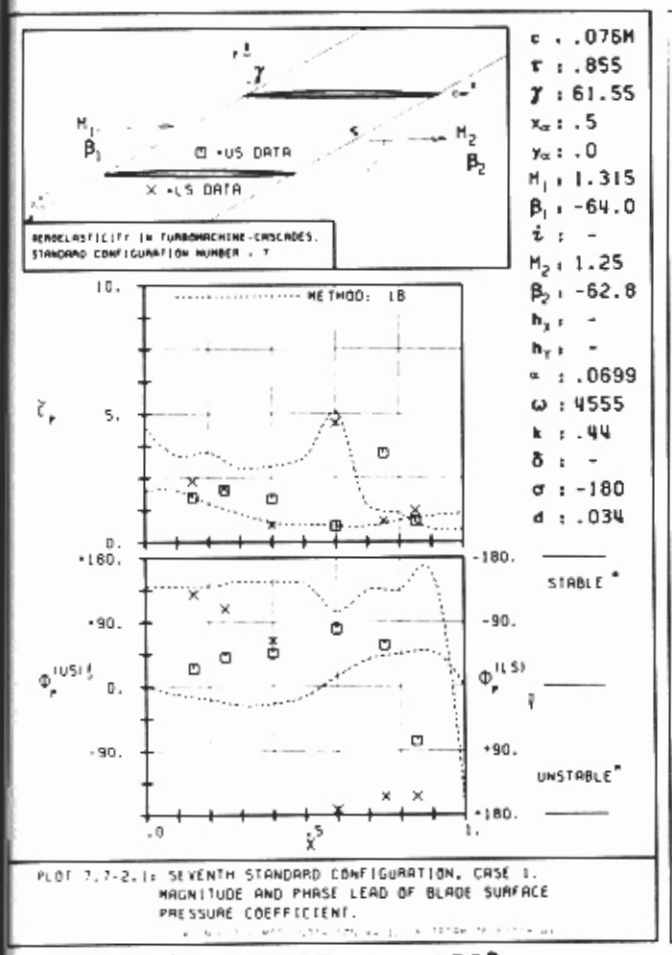


a) $M_2 = 1.25$, $\sigma = -180^0$

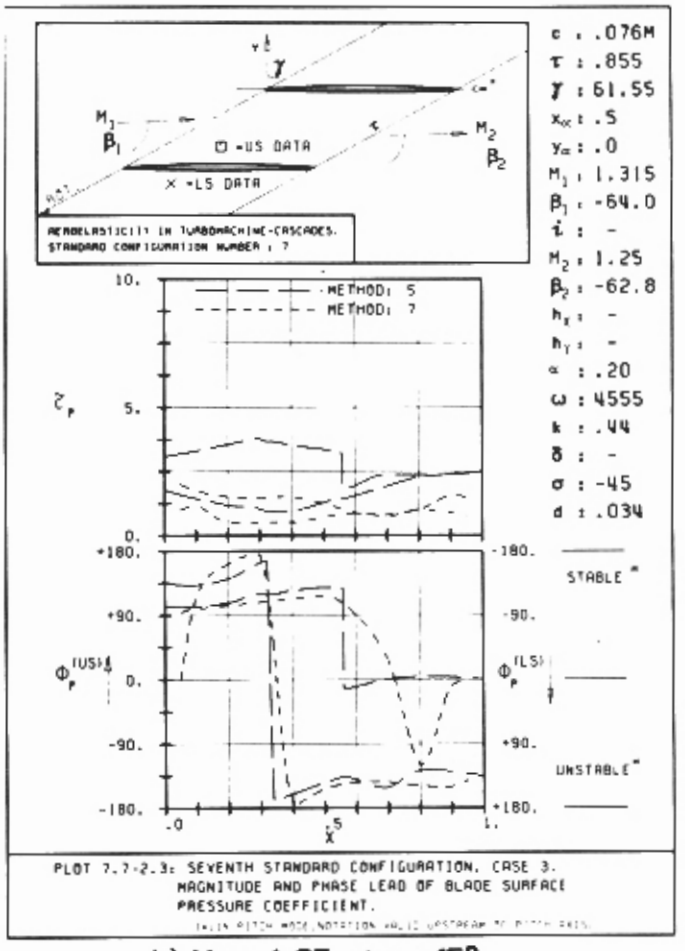


b) $M_2 = 1.25$, $\sigma = -45^0$

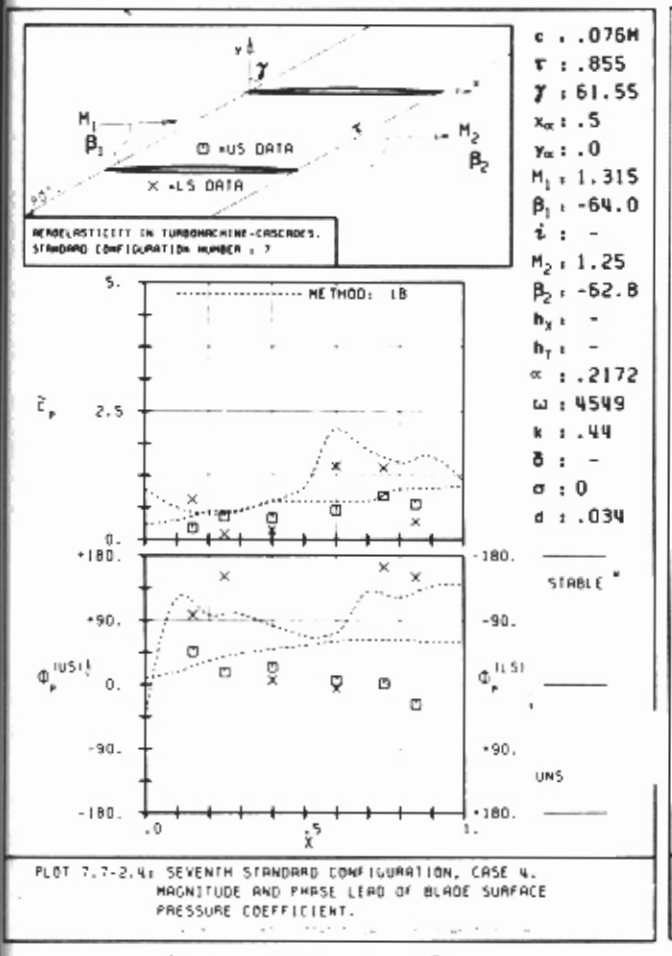


c) $M_2 = 1.25$, $\sigma = 0^0$

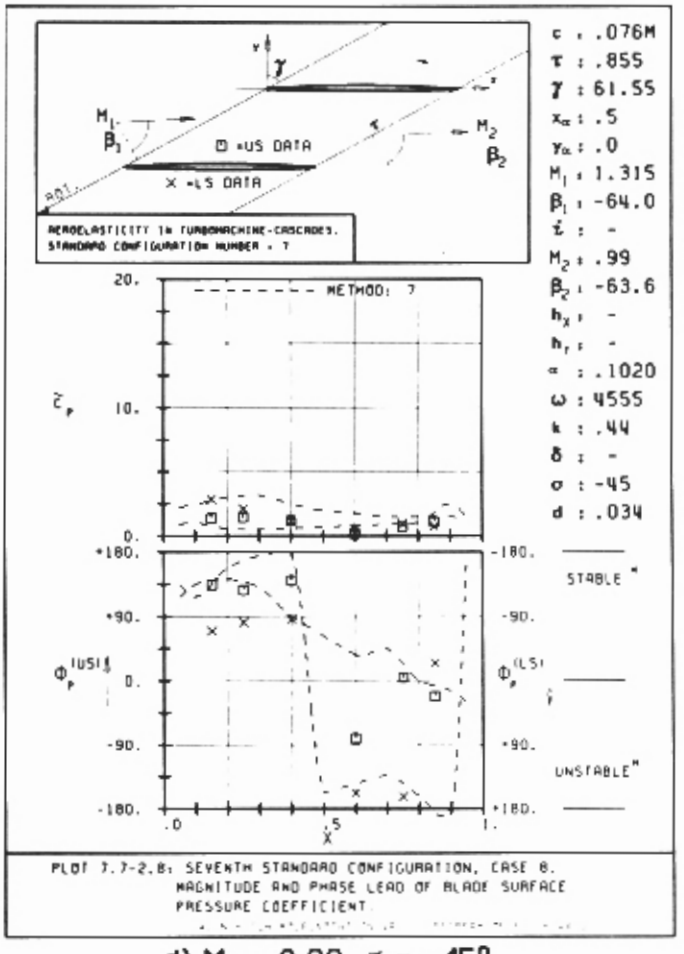


d) $M_2 = 0.99$, $\sigma = -45^0$

**Fig. 7.7-7.** Time-dependent blade surface pressure coefficient along blade chord at $M_2 = 1.25$ and $M_2 = 0.99$.

## 7.8 Eighth Standard Configuration (Flat Plate Cascade in Subsonic and Supersonic Flow)

### Definition

The eighth and ninth standard configurations are directed towards the investigation of basic aeroelastic phenomena and the influence of thickness effects on numerical calculations, especially in the transonic flow region.
Configuration number eight deals with a two-dimensional cascade of flat plates. Theoretical analyses of such unsteady configurations have been performed for many years now, but the problem is still of great interest, mainly due to the following factors:

- In modern compressors, operating in the transonic and supersonic flow regimes, the actual blades are rather thin and have a low camber. They can thus mostly be fairly well approximated as flat plates.
- Supersonic two-dimensional flat plate prediction models are often one of the main aeroelastic tools used by the designer of large turboreactors.
- In the incompressible flow domain, analytical flat plate solutions are available.
- It is possible to establish, with different theories and for the purposes of the present comparative work, the aeroelastic response of a flat plate cascade over the whole Mach number range from incompressible to supersonic flow conditions.
- The strip theory assumption should be validated, in the transonic flow domain, in a fairly simple case. This requires validation not only of theoretical results, but also of two-dimensional and quasi three-dimensional experimental data on thin airfoils.

The cascade being investigated as the eight standard configuration is shown in Fig. 7.8-1.

### Aeroelastic Test Cases

In this eight standard configuration, the main emphasis will be laid on the change in the aeroelastic behavior of the cascade in dependance of the inlet flow velocity, pressure ratio through the cascade, stagger angle and solidity. The unsteady blade surface pressure distributions will thus be compared in detail only for a few aeroelastic cases.
It is assumed that the two-dimensional airfoils oscillate in pitch about mid-chord (0.5, 0.), with an amplitude of 2° (0.0349 rad).

As the main interest for this configuration lies in the variation of the time-averaged parameters the calculations should be performed at zero mean incidence, with a constant interblade phase angle of 90° and with a fairly high reduced frequency, k=1.0.

During the project it was found that this high reduced frequency may introduce inaccuracies in the calculated results. However, such problems are of special interest in workshops of the present kind, so the results are presented nonetheless.

35 aeroelastic test cases have been selected for analyses (Table 7.8-1). This is the largest number of test cases for any single standard configuration, which may seem strange for such a simple configuaration. However, as can be seen from Table 6.1, a larger number of predictions were made using this standard configuration than any other. This is clearly the case as more flat plate prediction models exist than methods which take into account the full geometry of the profiles.

**Flat Plate Profiles.**

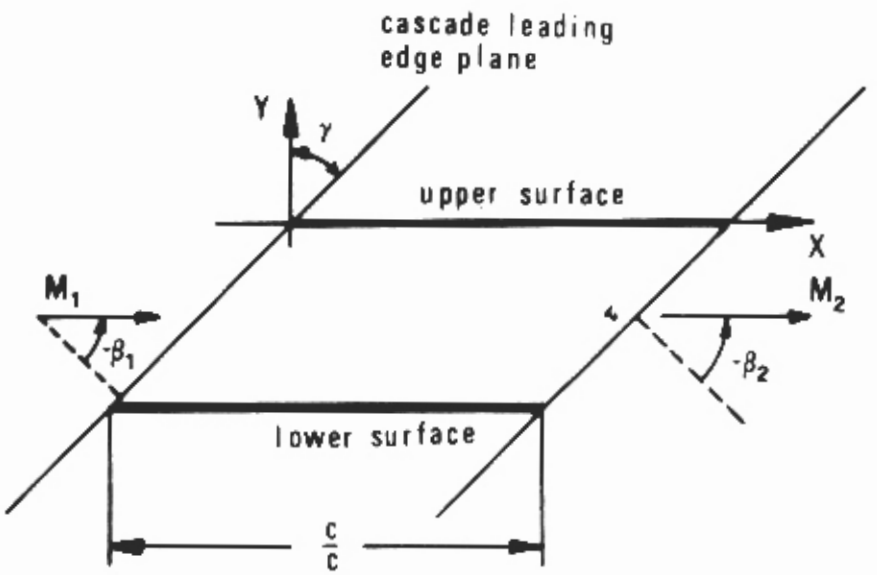


| | | | |
|---|---|---|---|
| Vibration in pitch around $(x_\alpha, y_\alpha)$ | = (0.5,0.) | | |
| $\alpha$ | = 2.0° (=0.0349 rad) | | |
| c | = 0.1 m | i | = 0° |
| $\tau$ | = variable (0.5-1.0) | camber | = 0° |
| k | = 1.0 | $\gamma$ | = variable (0°-60°) |
| $\sigma$ | = 90° | $M_1$ | = variable (0.0-1.5) |

**Fig. 7.8-1.** Eighth standard configuration: Cascade geometry

| Aeroelastic Test Case No | Time - Averaged | | | | |
|---|---|---|---|---|---|
| | $M_1$ (-) | i (°) | Normal Shock ? | $\gamma$ (°) | $\tau$ (-) |
| 1 | Incompressible | 0 | | 60 | 0.75 |
| 2 | ↓ | ↓ | | 45 | ↓ |
| 3 | ↓ | ↓ | | 30 | ↓ |
| 4 | ↓ | ↓ | | 0 | ↓ |
| 5 | 0.5 | ↓ | | 60 | ↓ |
| 6 | 0.6 | ↓ | | ↓ | ↓ |
| 7 | 0.7 | ↓ | | ↓ | ↓ |
| 8 | 0.8 | ↓ | | ↓ | ↓ |
| 9 | 0.9 | ↓ | | ↓ | ↓ |
| 10 | 0.95 | ↓ | | ↓ | ↓ |
| 11 | 0.8 | ↓ | | 45 | ↓ |
| 12 | ↓ | ↓ | | 30 | ↓ |
| 13 | ↓ | ↓ | | 0 | ↓ |
| 14 | ↓ | ↓ | | 60 | 0.5 |
| 15 | ↓ | ↓ | | ↓ | 1.0 |
| 16 | 1.1 | ↓ | - | ↓ | 0.75 |
| 17 | ↓ | ↓ | at L.E. | ↓ | ↓ |
| 18 | ↓ | ↓ | at L.E. | ↓ | ↓ |
| 19 | 1.2 | ↓ | - | ↓ | ↓ |
| 20 | ↓ | ↓ | at L.E. | ↓ | ↓ |
| 21 | ↓ | ↓ | at L.E. | ↓ | ↓ |
| 22 | 1.3 | ↓ | - | ↓ | ↓ |
| 23 | ↓ | ↓ | at L.E. | ↓ | ↓ |
| 24 | ↓ | ↓ | at L.E. | ↓ | ↓ |
| 25 | 1.4 | ↓ | - | ↓ | ↓ |
| 26 | ↓ | ↓ | at L.E. | ↓ | ↓ |
| 27 | ↓ | ↓ | at L.E. | ↓ | ↓ |
| 28 | 1.5 | ↓ | - | ↓ | ↓ |
| 29 | ↓ | ↓ | at L.E. | ↓ | ↓ |
| 30 | ↓ | ↓ | at L.E. | ↓ | ↓ |
| 31 | 1.3 | ↓ | - | ↓ | 0.5 |
| 32 | ↓ | ↓ | - | ↓ | 1.0 |
| 33 | ↓ | ↓ | at L.E. | ↓ | 0.5 |
| 34 | ↓ | ↓ | ↓ | ↓ | 1.0 |
| 35 | ↓ | ↓ | ↓ | 45 | 0.75 |

**Table 7.8-1** Eighth Standard Configuration : 35 recommended aeroelastic test cases

## Discussion of Time-Dependent Results

In total eight models were used to predict the unsteady flow around the flat plate cascade. In general, the results of the different analyses agree well, with a few notable exceptions.

Integrated parameters

The first results presented are taken from the investigation regarding the influence of the steady-state stagger angle on the aerodynamic damping coefficient (Fig. 7.8-2).
It is found that the results obtained from the different prediction models agree extremly well for a low subsonic flow velocity (Fig. 7.8-2a), whereas some

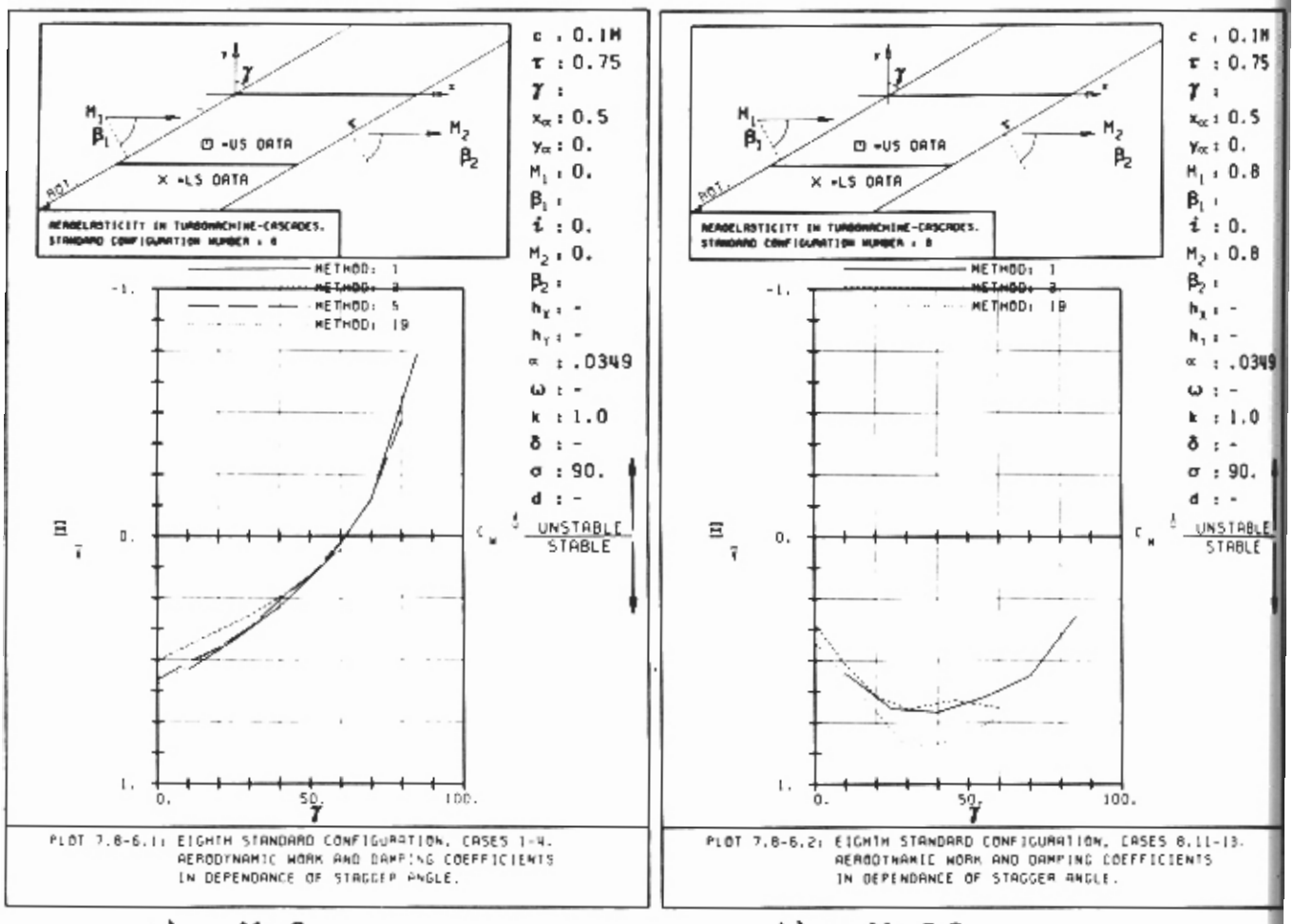


PLOT 7.8-6.1: EIGHTH STANDARD CONFIGURATION, CASES 1-4. AERODYNAMIC WORK AND DAMPING COEFFICIENTS IN DEPENDANCE OF STAGGER ANGLE.

PLOT 7.8-6.2: EIGHTH STANDARD CONFIGURATION, CASES 8,11-13. AERODYNAMIC WORK AND DAMPING COEFFICIENTS IN DEPENDANCE OF STAGGER ANGLE.

a) $M_1$=0. b) $M_1$=0.8

**Fig. 7.8-2.** Aerodynamic damping coefficient versus stagger angle for $M_1$=0. and $M_1$=0.8, respectively.

discrepancies appear at a high subsonic flow velocity ($M_1$=0.8, Fig. 7.8-2b). However, all the methods predict stability for subsonic Mach numbers at the specified time-dependent flow conditions (k=1.0, $\sigma$=90°).
The good agreement between the theories, for subsonic flow, is also seen in the aerodynamic damping coefficient versus Mach number (Fig. 7.8-3a).
Here, the differences in $\Xi$ between $M_1$=0.0 and $M_1$=0.5 come about because of the interpolation-routine in the plot program, and the sharp peak at $M_1$=0.5 depends on the closeness to the acoustic resonance ($M_{1,ac.res}$=0.53). However, some small differences can be found between the different analyses at the higher flow velocities ($M_1$>0.5). These differences become somewhat larger for supersonic flow conditions.
If a strong shock is positioned at the leading or trailing edge (Figs. 7.8-3b,c, respectively) the potential flow solver 7 predicts only a slight change in magnitude of the aerodynamic damping. However, a flat plate anlyses (Method 19), with special care taken in simulating the leading edge shock (Fig. 7.8-3b), predicts instead an instability in the Mach number range 1.3<$M_1$<1.5. The reasons for these differences are not apparent at the present time, but it is found (Fig. 7.8-3d) that differences between Methods 7 and 19 exist in both the magnitude and phase angle of the moment coefficient ($\tilde{c}_m$ and $\Phi_m$, resp.).

Blade surface pressure differences

At low subsonic flow velocities the results obtained from the different prediction models agree extremly well (Fig. 7.8-4a, where $\gamma$=60°, $\tau$=0.75). This is also seen to be the case at higher flow velocities (Fig. 7.8-4b, $M_1$=0.8). Evaluating these results, it can be seen that the differences in aerodynamic damping coefficient at $M_1$=0.8 (Fig.7.8-3a) probably come about because of a slight discrepancy in the magnitude of the blade surface pressure difference ($\Delta\tilde{c}_p$) in the different models.
However, the trend is the same for all models, both as regards the magnitude ($\Delta\tilde{c}_p$) and phase angle ($\Phi_{\Delta p}$).
For supersonic flow velocities a larger disagreement is found in the pressure difference coefficient (Fig. 7.8-5). The trend of $\Delta\tilde{c}_p$ is the same for two flat plate analyses (Methods 5 and 19 in Fig. 7.8-5a), whereas a finite element potential flow solver ( Method 7 ) does not indicate any specific

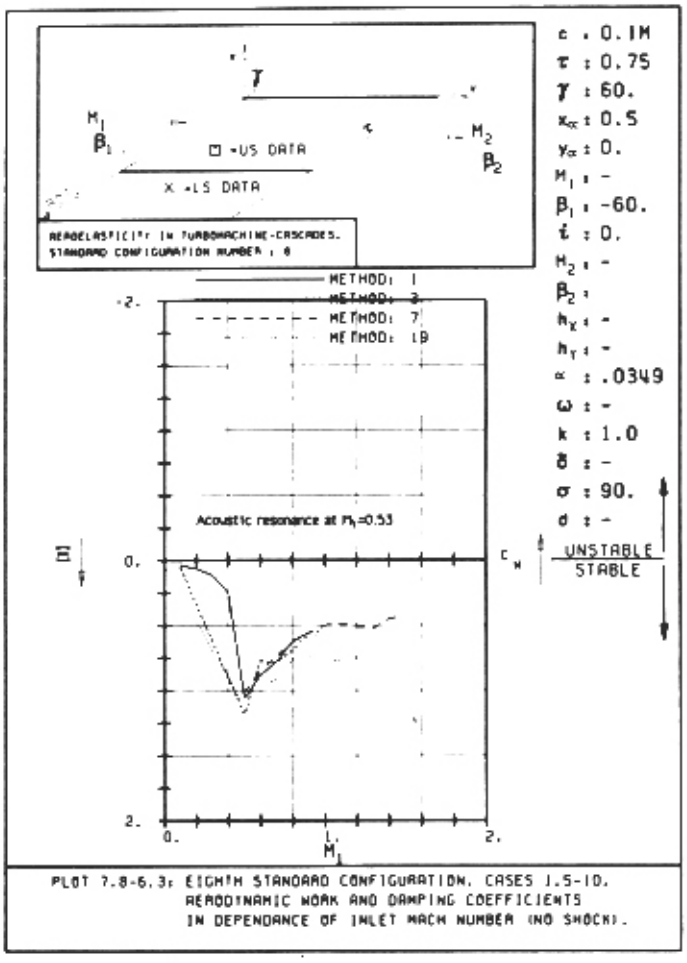


PLOT 7.8-6.3: EIGHTH STANDARD CONFIGURATION, CASES 1.5-10.
AERODYNAMIC WORK AND DAMPING COEFFICIENTS
IN DEPENDANCE OF INLET MACH NUMBER (NO SHOCK).

a) No strong shock

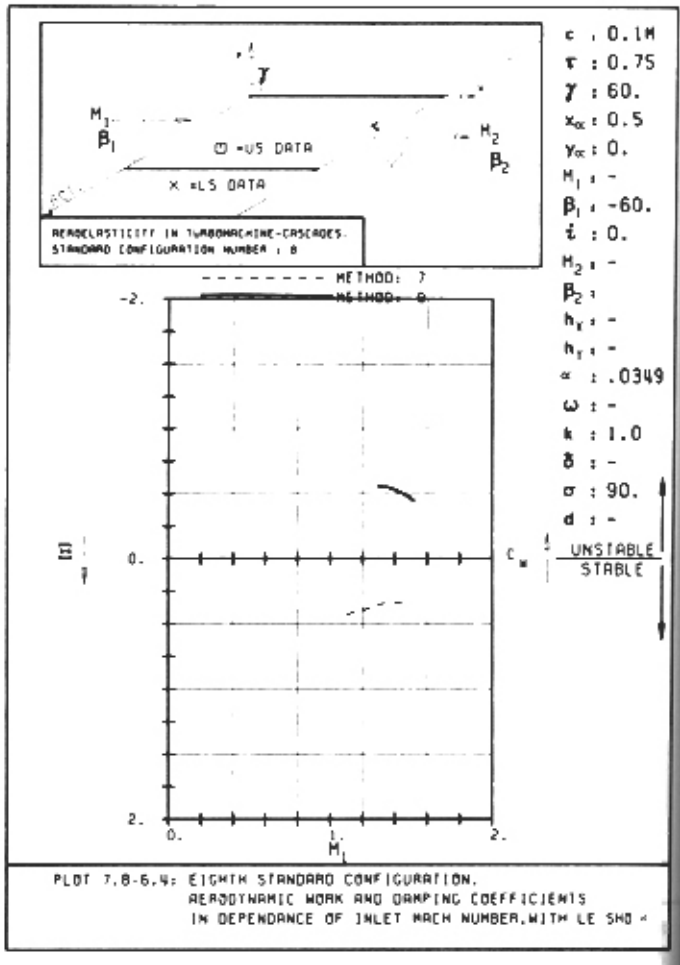


PLOT 7.8-6.4: EIGHTH STANDARD CONFIGURATION.
AERODYNAMIC WORK AND DAMPING COEFFICIENTS
IN DEPENDANCE OF INLET MACH NUMBER, WITH LE SHO

b) Strong leading edge shock

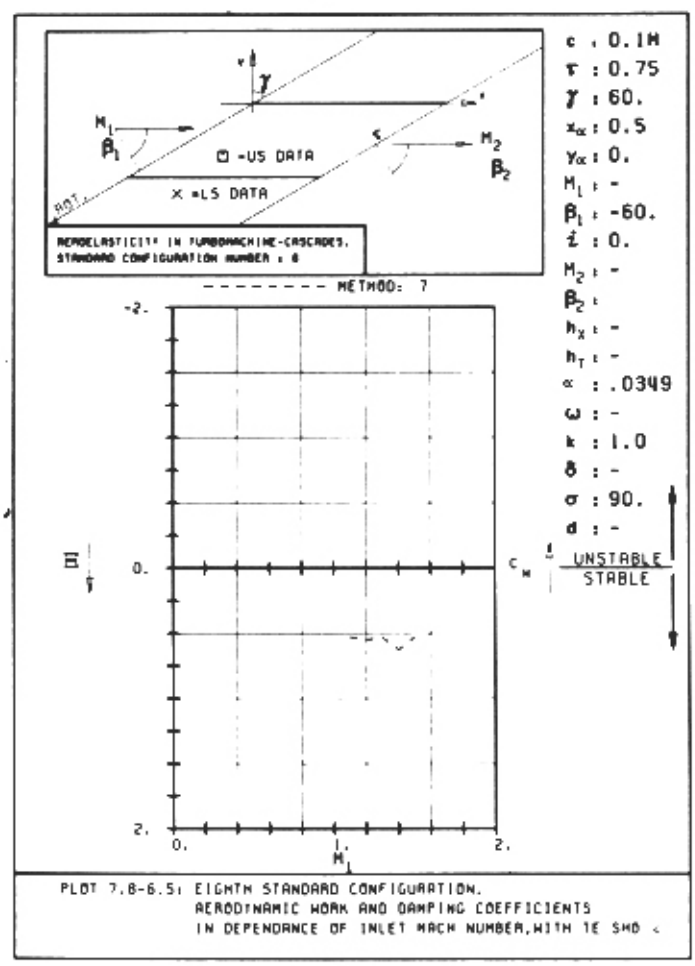


PLOT 7.8-6.5: EIGHTH STANDARD CONFIGURATION.
AERODYNAMIC WORK AND DAMPING COEFFICIENTS
IN DEPENDANCE OF INLET MACH NUMBER, WITH TE SHO

c) Strong trailing edge shock

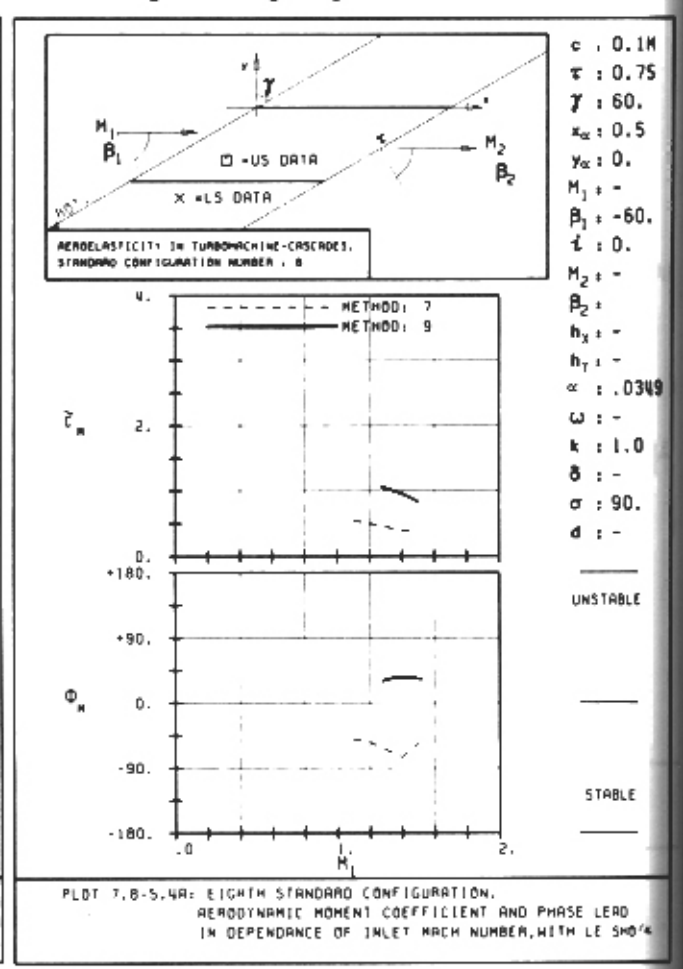


PLOT 7.8-5.4A: EIGHTH STANDARD CONFIGURATION.
AERODYNAMIC MOMENT COEFFICIENT AND PHASE LEAD
IN DEPENDANCE OF INLET MACH NUMBER, WITH LE SHO

d) Strong leading edge shock

**Fig. 7.8-3.** Aerodynamic damping and moment coefficients versus Mach number.

change, either in $\Delta\tilde{c}_p$ or in $\Phi_{\Delta p}$, in the neighborhood of the steady state (weak) shock wave impingement on the blade surfaces (see sketches in Figs. 7.8-5; $x_{Shock}$=0.62 on the lower surface, $x_{Shock}$=0.95 on the upper surface). However, the flat plate analyses also show some disagreement in the case of a detailed comparison.

If a strong shock wave is positioned at the leading edge (Fig. 7.8-5b), the finite element solver (Method 7) indicates some change along the whole chord, both for the magnitude and phase angle ($\Delta\tilde{c}_p$, $\Phi_{\Delta p}$). Here, the differences between the two methods are larger than in the case with weak shocks. The discrepancy is fairly large for both the magnitude and the phase angle. From this Figure, it is clear why the stability of the cascade was different in Methods 7 and 19 (Fig. 7.8-3b). In the forward part of the blade the phase angle $\Phi_{\Delta p}$ indicates instability for both methods. However, for Method 7 this phase angle is close to

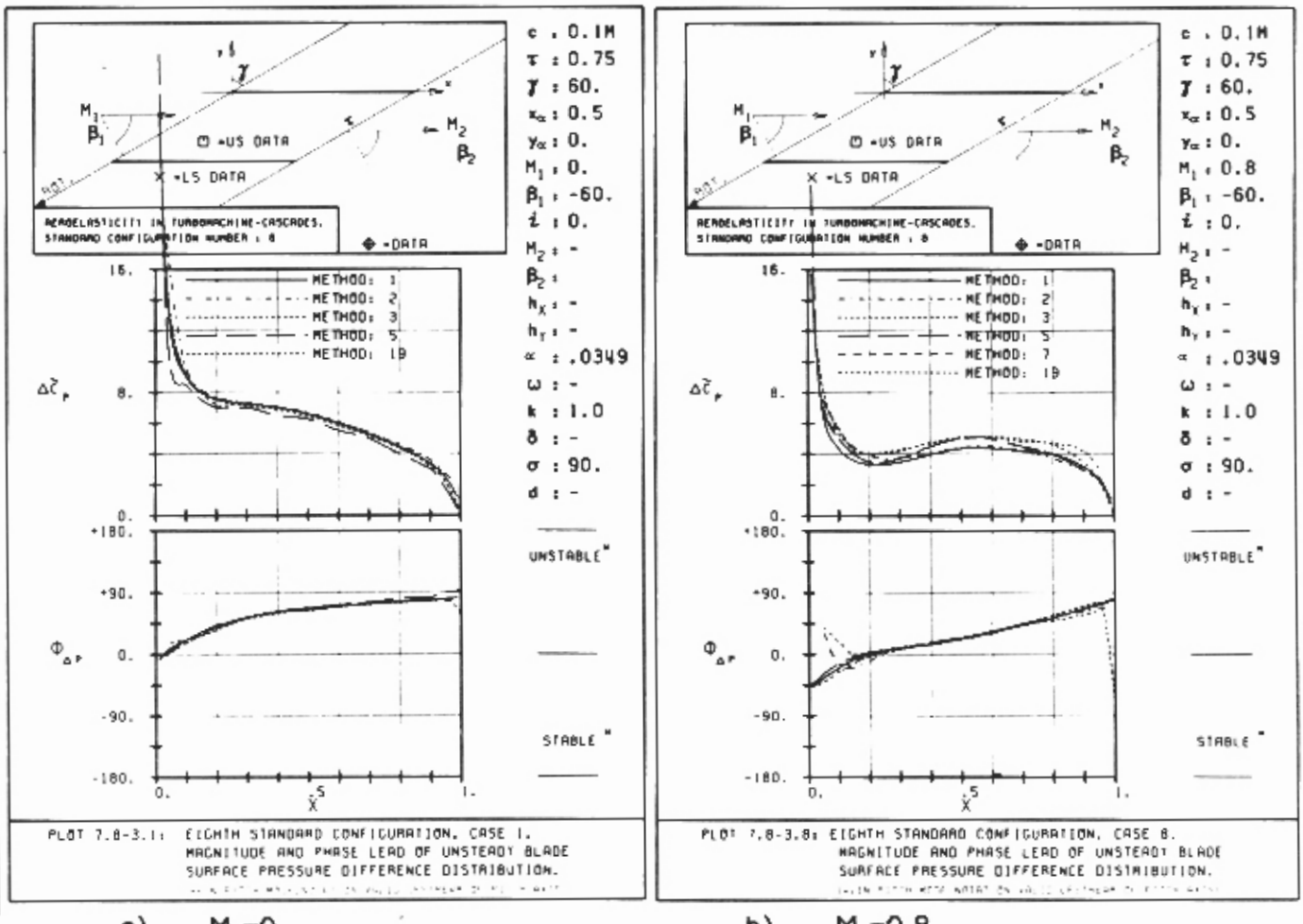


a) $M_1$=0. b) $M_1$=0.8

**Fig. 7.8-4.** Blade surface pressure difference coefficient for different subsonic flow velocities.

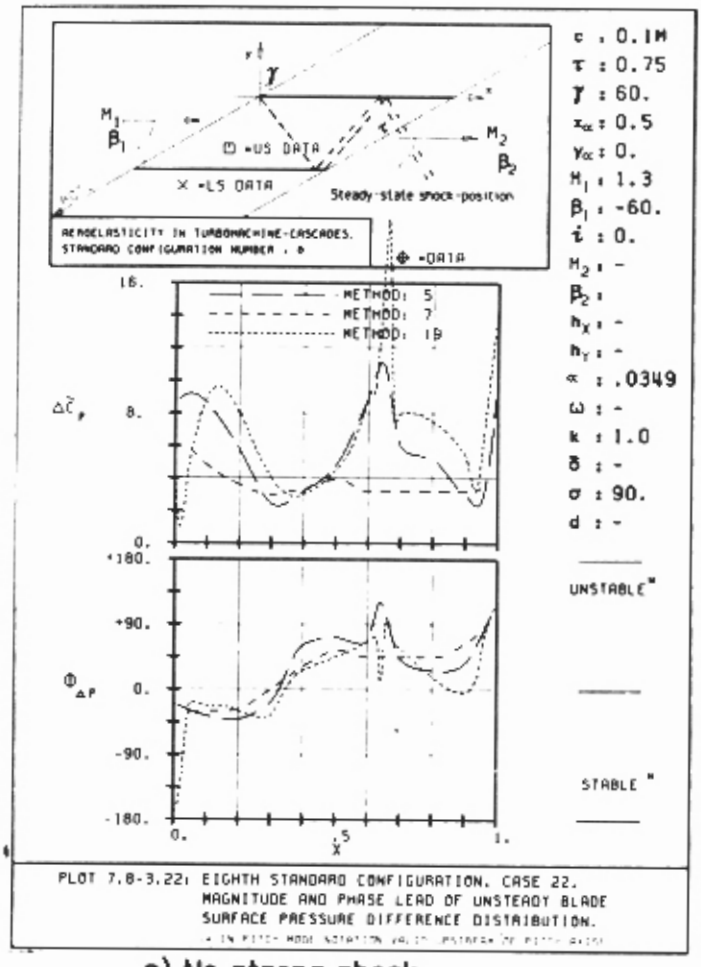


PLOT 7.8-3.22: EIGHTH STANDARD CONFIGURATION, CASE 22.
MAGNITUDE AND PHASE LEAD OF UNSTEADY BLADE
SURFACE PRESSURE DIFFERENCE DISTRIBUTION.

a) No strong shock

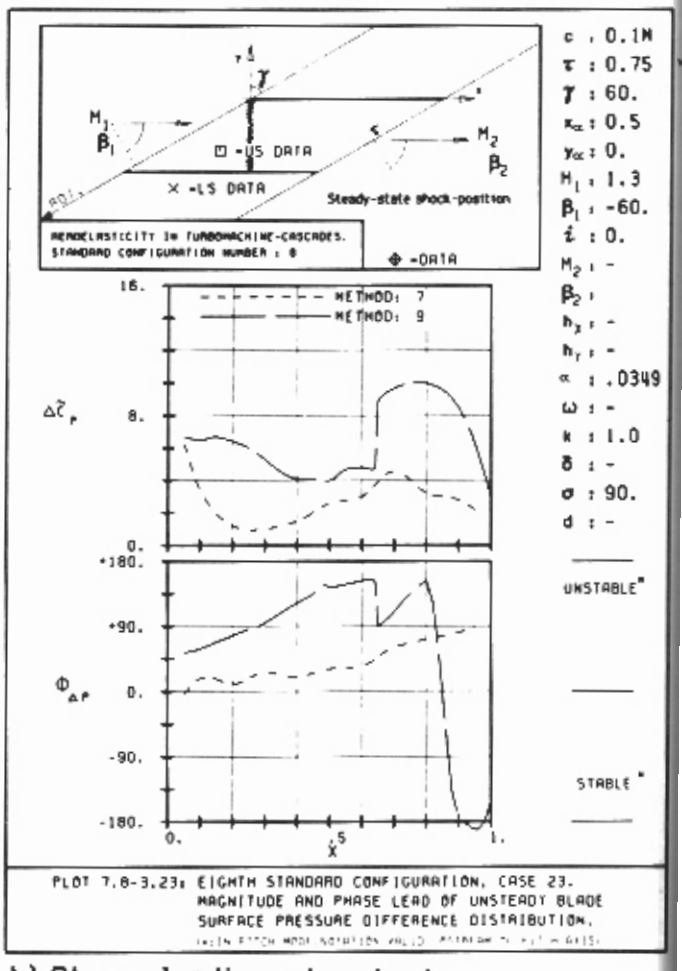


PLOT 7.8-3.23: EIGHTH STANDARD CONFIGURATION, CASE 23.
MAGNITUDE AND PHASE LEAD OF UNSTEADY BLADE
SURFACE PRESSURE DIFFERENCE DISTRIBUTION.

b) Strong leading edge shock

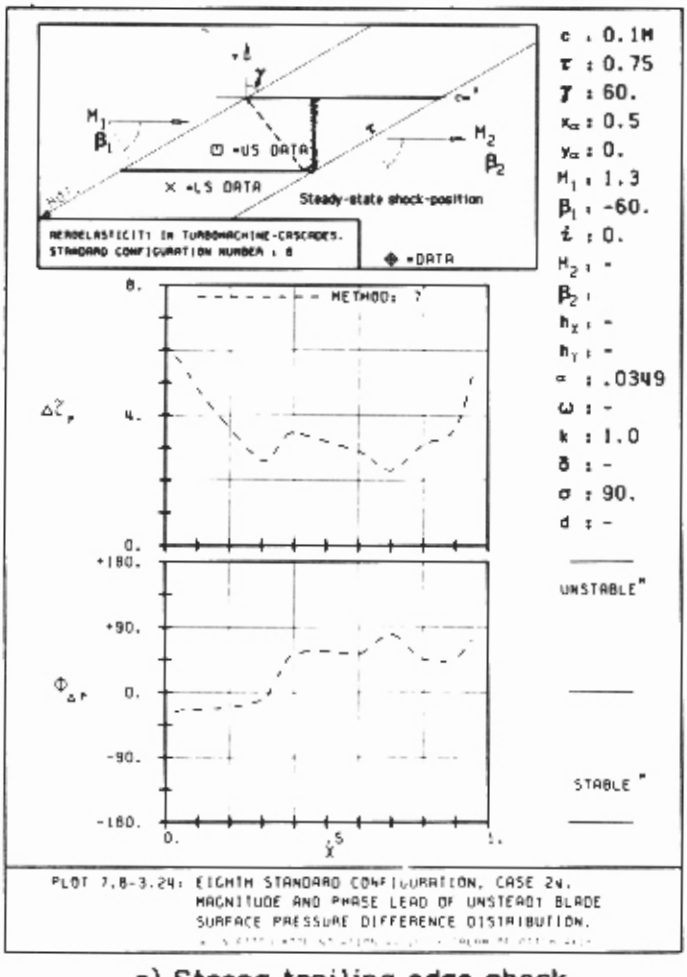


PLOT 7.8-3.24: EIGHTH STANDARD CONFIGURATION, CASE 24.
MAGNITUDE AND PHASE LEAD OF UNSTEADY BLADE
SURFACE PRESSURE DIFFERENCE DISTRIBUTION.

c) Strong trailing edge shock

**Fig. 7.8-5.** Blade surface pressure difference coefficient for different shock positions.

0°, whereas for Method 19 it is close to +90°. Therefore, the forward part of the blade does not contribute to any large extent to the aerodynamic damping for Method 7, whereas it does for Method 19. For both methods, the leading edge shockwave is clearly seen as an increase in magnitude ($x_{shock}$=0.65, Fig. 7.8-5b), although to a smaller extent for the potential flow solver than for the analytical flat plate model. In the latter, the shock wave is also noticeable as a jump in the phase angle, whereas the former does not show any significant influence.

In Fig. 7.8-5c the same calculation is presented, but with a strong trailing edge shock wave instead of a leading edge one. Here, results are available for the potential flow solver only. The impingment of the shockwave on the blade surfaces is noted ($x_{shock}$=0.35), both in magnitude and phase. It is interesting to note that, although the aerodynamic damping coefficient did not change significantly (according to Method 7) if the steady-state shock wave was positioned at the leading or trailing edge (Fig. 7.8-3b,c), the blade surface pressure difference coefficient changed along the whole chord, in a non-negligible manner, for both the magnitude and phase angle (Fig. 7.8-5b,c; note however the difference in scale in $\Delta\tilde{c}_p$).

Blade surface pressures

As for $\Delta\tilde{c}_p(x, t)$, the local surface pressures ($\tilde{c}_p^{us}(x,t)$, $\tilde{c}_p^{ls}(x,t)$ agree extremely well in two different potential flow methods for subsonic Mach numbers (Fig. 7.8-6), both as regards the magnitude and phase angle.

For supersonic velocities, only two results (Methods 7 and 9) were submitted (for all results, see Appendix A5).

The potential flow solver (Method 7) gives almost identical results for the case with weak shocks (Fig. 7.8-7a) and with a strong trailing edge shock (Fig. 7.8-7c), apart from the lower surface in the vicinity of the strong shock wave ($x_{shock}$=0.35).

However, for a leading edge shock wave the response is quite different (Fig. 7.8-7b). Here, as already found for $\Delta\tilde{c}_p(x,t)$, there are some large differences between the Methods 7 and 19. Presently, no explanation for this can be given.

## Conclusions for the Eighth Standard Configuration

From the comparisons on a flat plate cascade in sub- and supersonic flow (k=1.0, $\varepsilon$=0°, $\gamma$ and $\tau$ variable) it can be concluded that:

- The different prediction models presented agree extremely well for low subsonic flow velocities, as regards the aerodynamic damping, moment, pressure difference and pressure coefficients.
- For high subsonic flow velocities a discrepancy is found between the different analyses.
- In supersonic flow the results become ambiguous if strong shock waves are considered. Different theories indicate different stability margins of the cascade, and the local blade surface pressure amplitudes and phase angles are very different. A possible explanation for the differences is the high value of the reduced frequency (k=1.0). However, the differences are too large to be neglected.

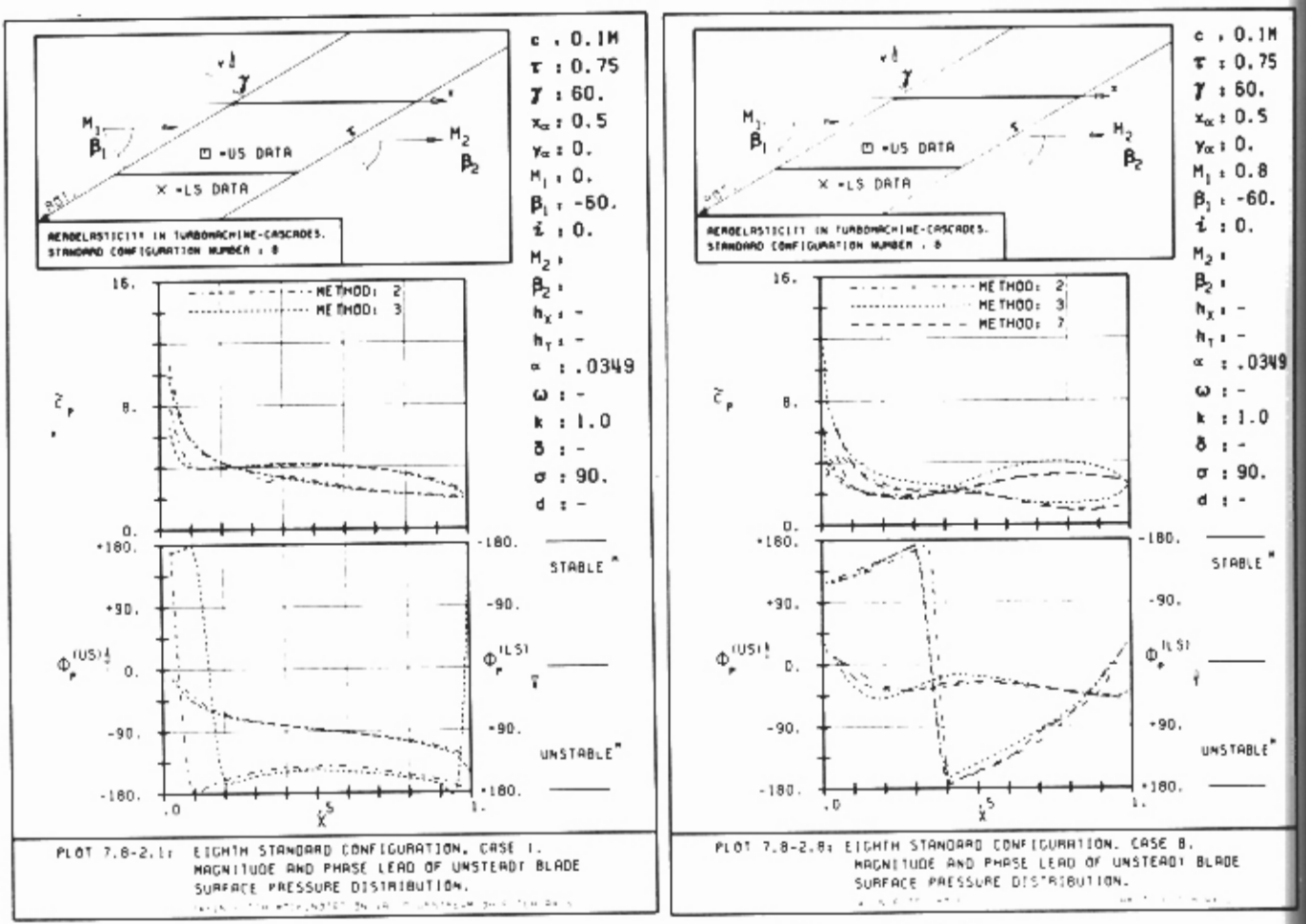


a) $M_1$=0. b) $M_1$=0.8

**Fig. 7.8-6.** Blade surface pressure coefficient for different subsonic flow velocities.

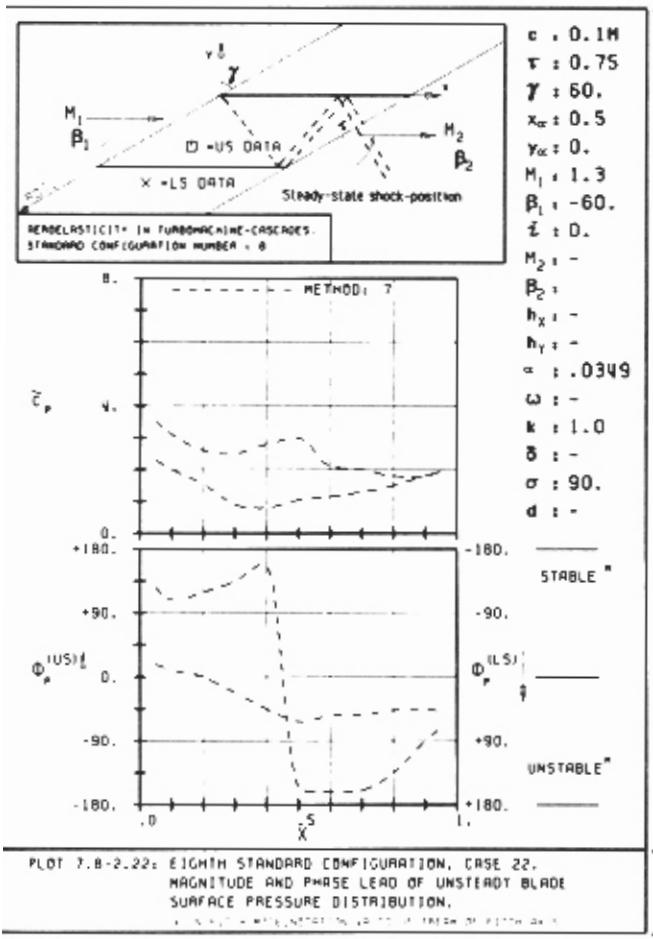


PLOT 7.8-2.22: EIGHTH STANDARD CONFIGURATION, CASE 22.
MAGNITUDE AND PHASE LEAD OF UNSTEADY BLADE
SURFACE PRESSURE DISTRIBUTION.

a) No strong shock

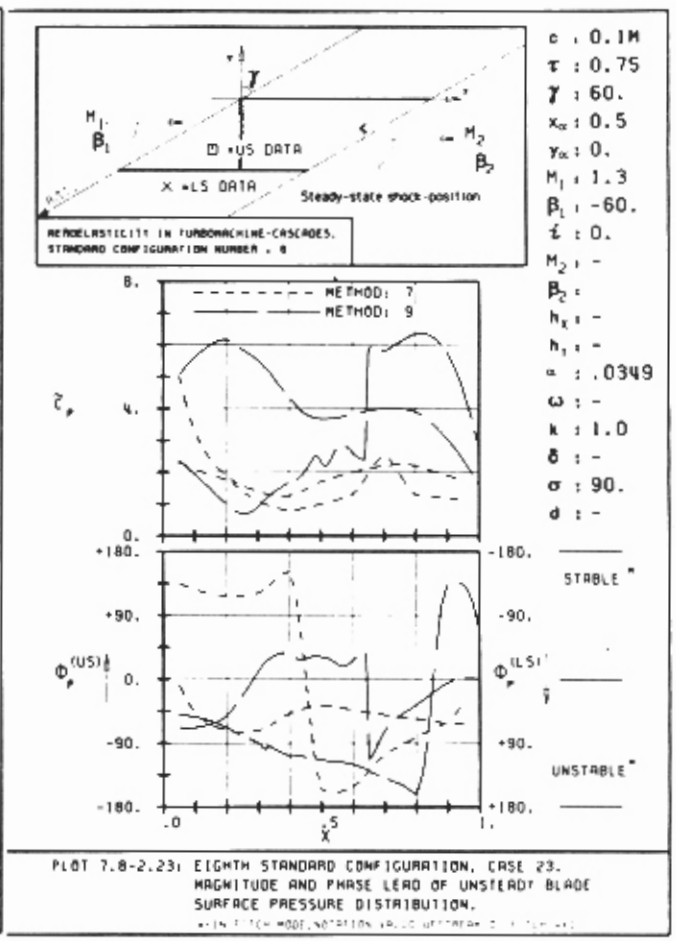


PLOT 7.8-2.23: EIGHTH STANDARD CONFIGURATION, CASE 23.
MAGNITUDE AND PHASE LEAD OF UNSTEADY BLADE
SURFACE PRESSURE DISTRIBUTION.

b) Strong leading edge shock

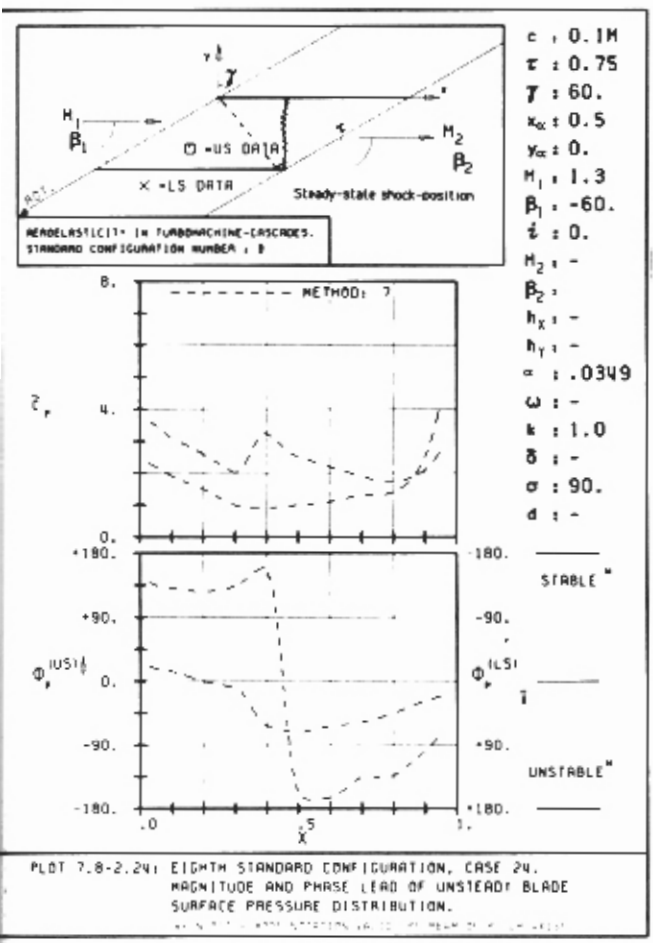


PLOT 7.8-2.24: EIGHTH STANDARD CONFIGURATION, CASE 24.
MAGNITUDE AND PHASE LEAD OF UNSTEADY BLADE
SURFACE PRESSURE DISTRIBUTION.

c) Strong trailing edge shock

**Fig. 7.8-7.** Unsteady blade surface pressure difference coefficient for different shock positions at $M_1$=1.3.

## 7.9 Ninth Standard Configuration (Double Circular Arc Profiles in Subsonic and Supersonic Flow).

### Definition

The ninth standard configuration is selected to be a continuation of the flat plate investigation. The emphasis is now placed on blade thickness influence, especially in the high subsonic flow region, on the numerical results from the different prediction models.
To this end, Double Circular Arc profiles, with thickness/chord ranging from 0.01 to 0.10, are defined (see Figure 7.9-1).
Apart from the profile thickness, the influence of the inlet Mach number on the aeroelastic response of the cascade will be investigated.
For this configurtaion, the same vibration mode, reduced frequency and interblade phase as in the eighth configuration (1.0 and 90° resp.) are chosen.
The stagger angle has been defined to be 45 and 60°, mainly to allow for realistic conditions at high velocities, although in some computations they may introduce influence of distorted calculation grids.

### Aeroelastic Test Cases

In the configuration, 21 aeroelastic cases are defined for comparison (see Table 7.9-1).
For the subsonic cases the incidence should be close to 0°, and for the supersonic cases it should satisfy the unique incidence condition.

Discussion of Time-Averaged Results

Time-averaged results were received from one prediction model (Method 3), for the flat-bottomed test cases in high subsonic flow. These are given in Fig. 7.9-2. It should be noted that Method 3 predicts a shock at 40% chord for an inlet Mach number M=0.9 (Fig. 7.9-2d).

Discussion of Time-Dependent Results

Time-dependent results have been submitted from two prediction models (Methods 2 and 3). Furthermore, for comparison with the flat-plate cascade in the previous section results of a flat-plate analyses (Method 1) are given when available.

## Symmetric/Flat-Bottomed Circular Arc Profiles.

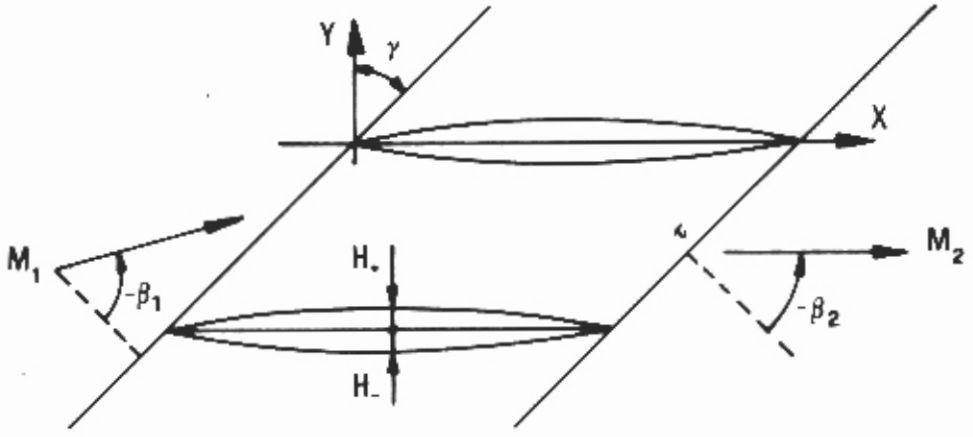


Equation:

$y_{\pm}(x) = \mathrm{sgn}(H_{\pm})[|H_{+/-}| - R_{\pm} + (R_{\pm}^2 - (x-0.5)^2)^{0.5}]$ if $H_{\pm} \neq 0$.

$= 0$ if $H_{\pm} = 0$.

$R = (H^2 + 0.5^2)/(2|H|)$

$\mathrm{sgn}(H) = \pm 1$ for H>/<0.

\+ = upper surface

\- = lower surface

Maximum thickness at x = 0.5

Vibration in pitch around $(x_\alpha, y_\alpha)$ = (0.5,camber-line)

d = (thickness/chord) = 0.01 - 0.1

$\alpha = 2.0^0$ (=0.0349 rad)

c = 0.1 m

τ = 0.75

k = 1.0

$M_1$ = variable (0.0-1.5)

$\sigma = 90^0$

i = $0^0$ (for $M_1$<1.)

camber = $0^0$ (for symmetric profiles)

γ = $45^0$, $60^0$

**Fig. 7.9-1.** Ninth standard configuration: Cascade geometry

| Aeroelastic Test Case No | Time-Averaged Parameters | | | | | |
|---|---|---|---|---|---|---|
| | $M_1$ (-) | $\gamma$ (°) | $\beta_1$ (°) | $H_+$ (-) | $H_-$ (-) | d (-) |
| 1 | 0.0 | 60 | - 60 | 0.01 | 0.01 | 0.02 |
| 2 | " | " | " | 0.02 | 0.02 | 0.04 |
| 3 | " | " | " | 0.03 | 0.03 | 0.06 |
| 4 | " | " | " | 0.05 | 0.05 | 0.10 |
| 5 | 0.5 | " | " | 0.01 | 0.01 | 0.02 |
| 6 | 0.7 | " | " | 0.005 | 0.005 | 0.01 |
| 7 | " | " | " | 0.01 | 0.01 | 0.02 |
| 8 | " | " | " | 0.0015 | 0.0015 | 0.03 |
| 9 | " | " | " | 0.02 | 0.02 | 0.04 |
| 10 | 0.8 | " | " | 0.01 | 0.01 | 0.02 |
| 11 | 1.3 | " | " | " | " | " |
| 12 | 1.4 | " | " | " | " | " |
| 13 | 1.5 | " | " | " | " | " |
| 14 | 0.0 | 45 | - 45 | " | " | " |
| 15 | 0.5 | " | " | " | " | " |
| 16 | 0.7 | " | " | " | " | " |
| 17 | 0.8 | " | " | " | " | " |
| 18 | 0.5 | " | " | 0.05 | 0.0 | 0.05 |
| 19 | 0.7 | " | " | " | " | " |
| 20 | 0.8 | " | " | " | " | " |
| 21 | 0.9 | " | " | " | " | " |

**Table 7.9-1** Ninth standard configuration. 21 aeroelastic test cases

Integrated Parameters

The trend and magnitude of the aerodynamic damping coefficient of the different models versus inlet Mach number agree well for a 2% thick symmetric double circular arc profile (Fig. 7.9-3a)[14]. In the high subsonic flow region the flat plate analyses predicts a somewhat higher aerodynamic damping than the potential flow models. Or a flat-bottomed, 5% thick, profile some larger differences are found (Fig. 7.9-3b).

Blade Surface Pressure Differences

The unsteady blade surface pressure difference distribution was submitted for several aeroelastic test cases. For moderate thicknesses, symmetric blades, and low Mach numbers ($M \approx 0.0$) the full geometry models predict the same unsteady behavior as the flat-plate analyses (Fig. 7.9-4a). For 10% thickness, a slight difference is found (Fig. 7.9-4b).
At higher Mach numbers, differences are found at lower thicknesses (Fig. 7.9-5).
For the supersonic inlet flow conditions, only one prediction model was submitted (Fig. 7.9-6). This model indicates the same pressure response for $1.3 < M_1 < 1.5$, with a 2% thick airfoil. This is clearly the case as, for Mach numbers larger than $M_1 = 1.3$, the leading edge shock wave passes downstream of the trailing edge of the neighboring blade (compare Fig. 7.8-5a). The results obtained from a 5% thick flat-bottomed DCA-cascade, at high subsonic inlet flow conditions, show larger differences between the flat-plate analyses (Method 1) and a potential flow solver (Method 3) than on the symmetric profiles. These results are given in Fig. 7.9-7.
As the Mach number increases from $M_1 = 0.5$ (Fig. 7.9-7a) to $M_1 = 0.9$ (Fig.7.9-7d), it is found that the differences between the flat plate analyses and the potential flow theory increase, both in magnitude ($\Delta\tilde{c}_p$) and phase angle ($\Phi_{\Delta p}$). For the highest Mach number the influence of the shock (at $x_{shock} = 0.4$) is clearly seen with the potential flow solver (method 3), whereas the flat plate anlyses indicates different distributions for $\Delta\tilde{c}_p$ and $\Phi_{\Delta p}$ (Fig. 7.9-7d).

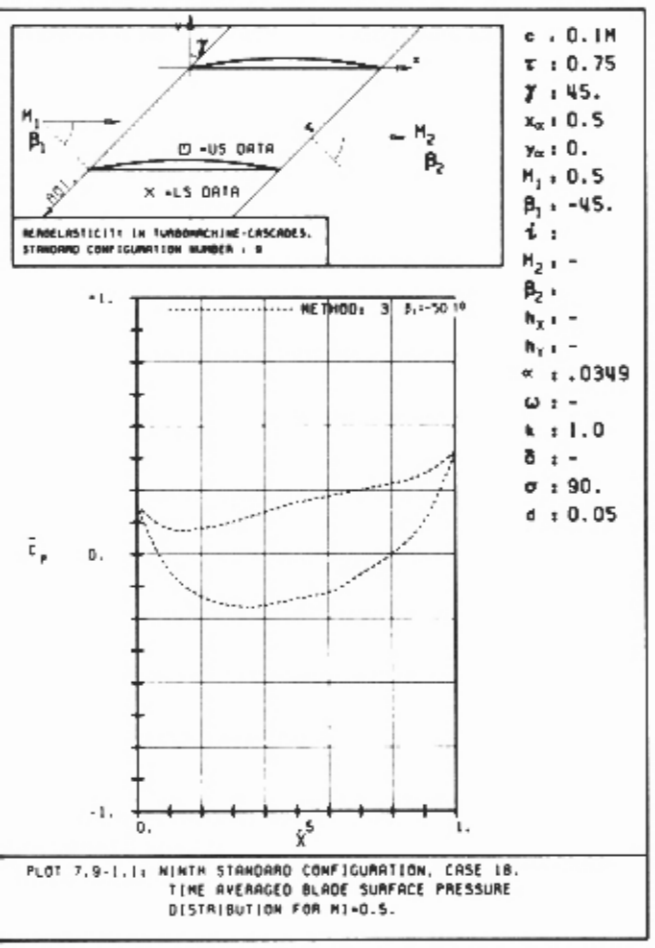


c : 0.1M
τ : 0.75
γ : 45.
$x_\alpha$ : 0.5
$y_\alpha$ : 0.
$M_1$ : 0.5
$\beta_1$ : -45.
i :
$M_2$ : -
$\beta_2$ :
$h_x$ : -
$h_y$ : -
α : .0349
ω : -
k : 1.0
δ : -
σ : 90.
d : 0.05

PLOT 7.9-1.1: NINTH STANDARD CONFIGURATION, CASE 18.
TIME AVERAGED BLADE SURFACE PRESSURE
DISTRIBUTION FOR M1=0.5.

a) $M_1$=0.5

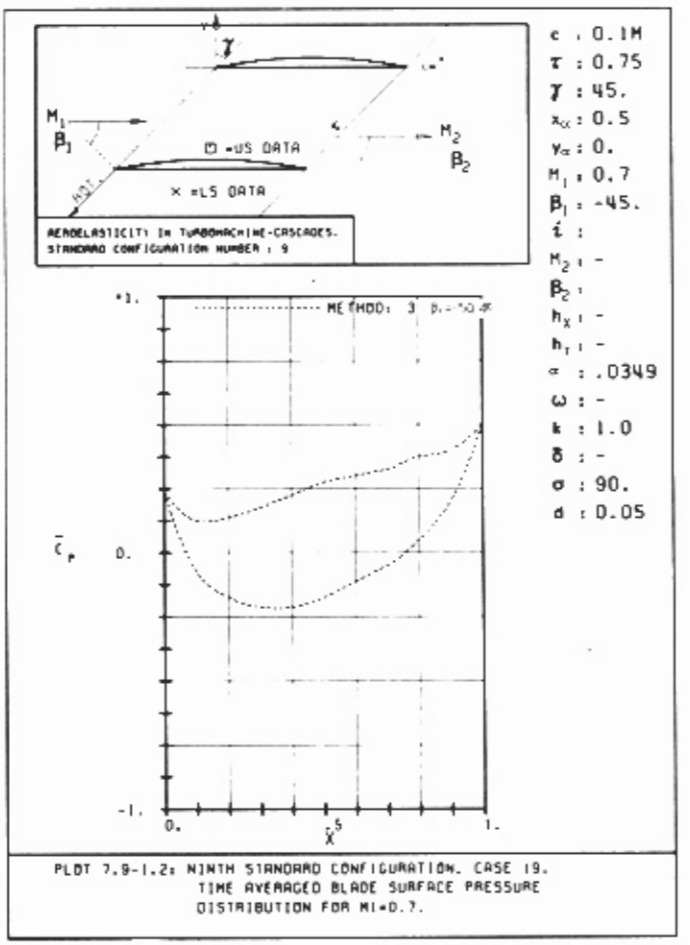


c : 0.1M
τ : 0.75
γ : 45.
$x_\alpha$ : 0.5
$y_\alpha$ : 0.
$M_1$ : 0.7
$\beta_1$ : -45.
i :
$M_2$ : -
$\beta_2$ :
$h_x$ : -
$h_y$ : -
α : .0349
ω : -
k : 1.0
δ : -
σ : 90.
d : 0.05

PLOT 7.9-1.2: NINTH STANDARD CONFIGURATION, CASE 19.
TIME AVERAGED BLADE SURFACE PRESSURE
DISTRIBUTION FOR M1=0.7.

b) $M_1$=0.7

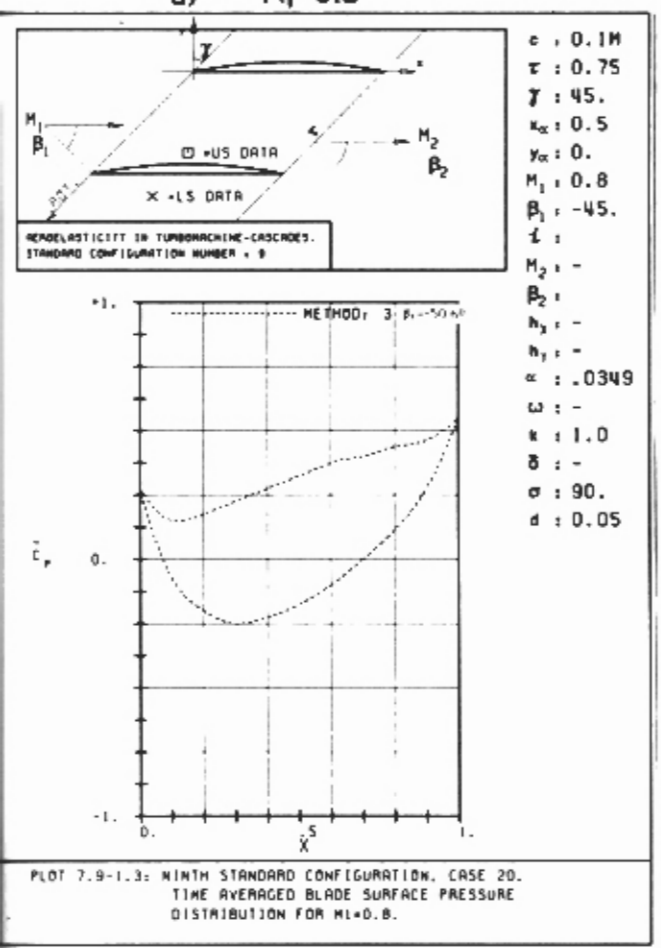


c : 0.1M
τ : 0.75
γ : 45.
$x_\alpha$ : 0.5
$y_\alpha$ : 0.
$M_1$ : 0.8
$\beta_1$ : -45.
i :
$M_2$ : -
$\beta_2$ :
$h_x$ : -
$h_y$ : -
α : .0349
ω : -
k : 1.0
δ : -
σ : 90.
d : 0.05

PLOT 7.9-1.3: NINTH STANDARD CONFIGURATION, CASE 20.
TIME AVERAGED BLADE SURFACE PRESSURE
DISTRIBUTION FOR M1=0.8.

c) $M_1$=0.8

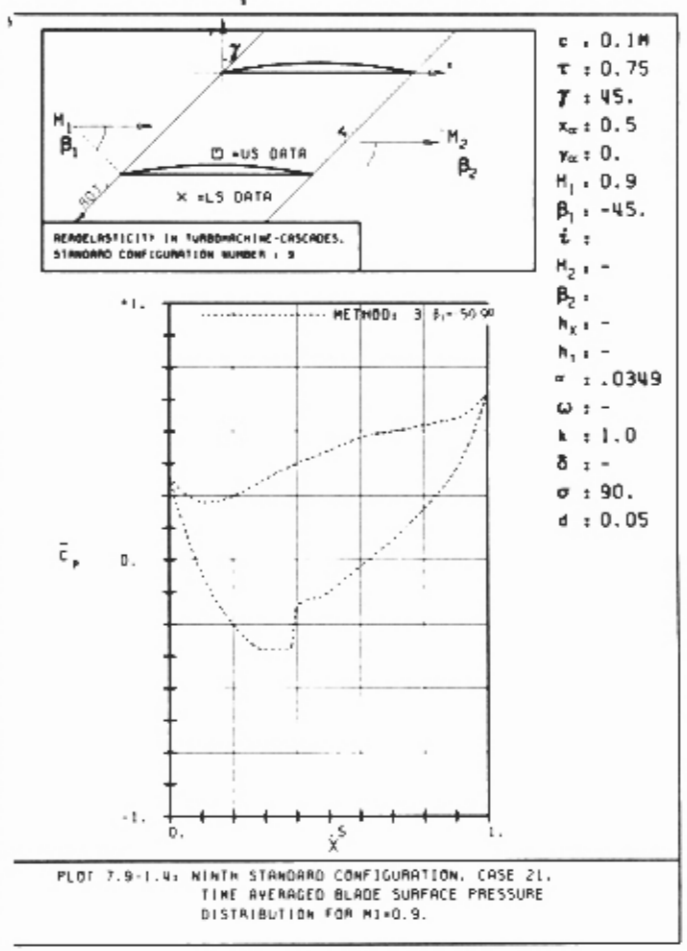


c : 0.1M
τ : 0.75
γ : 45.
$x_\alpha$ : 0.5
$y_\alpha$ : 0.
$M_1$ : 0.9
$\beta_1$ : -45.
i :
$M_2$ : -
$\beta_2$ :
$h_x$ : -
$h_y$ : -
α : .0349
ω : -
k : 1.0
δ : -
σ : 90.
d : 0.05

PLOT 7.9-1.4: NINTH STANDARD CONFIGURATION, CASE 21.
TIME AVERAGED BLADE SURFACE PRESSURE
DISTRIBUTION FOR M1=0.9.

d) $M_1$=0.9

**Fig. 7.9-2.** Time-averaged pressure distribution for a 5% thick flat-bottomed DCA-cascade ($\gamma$=45$^0$).

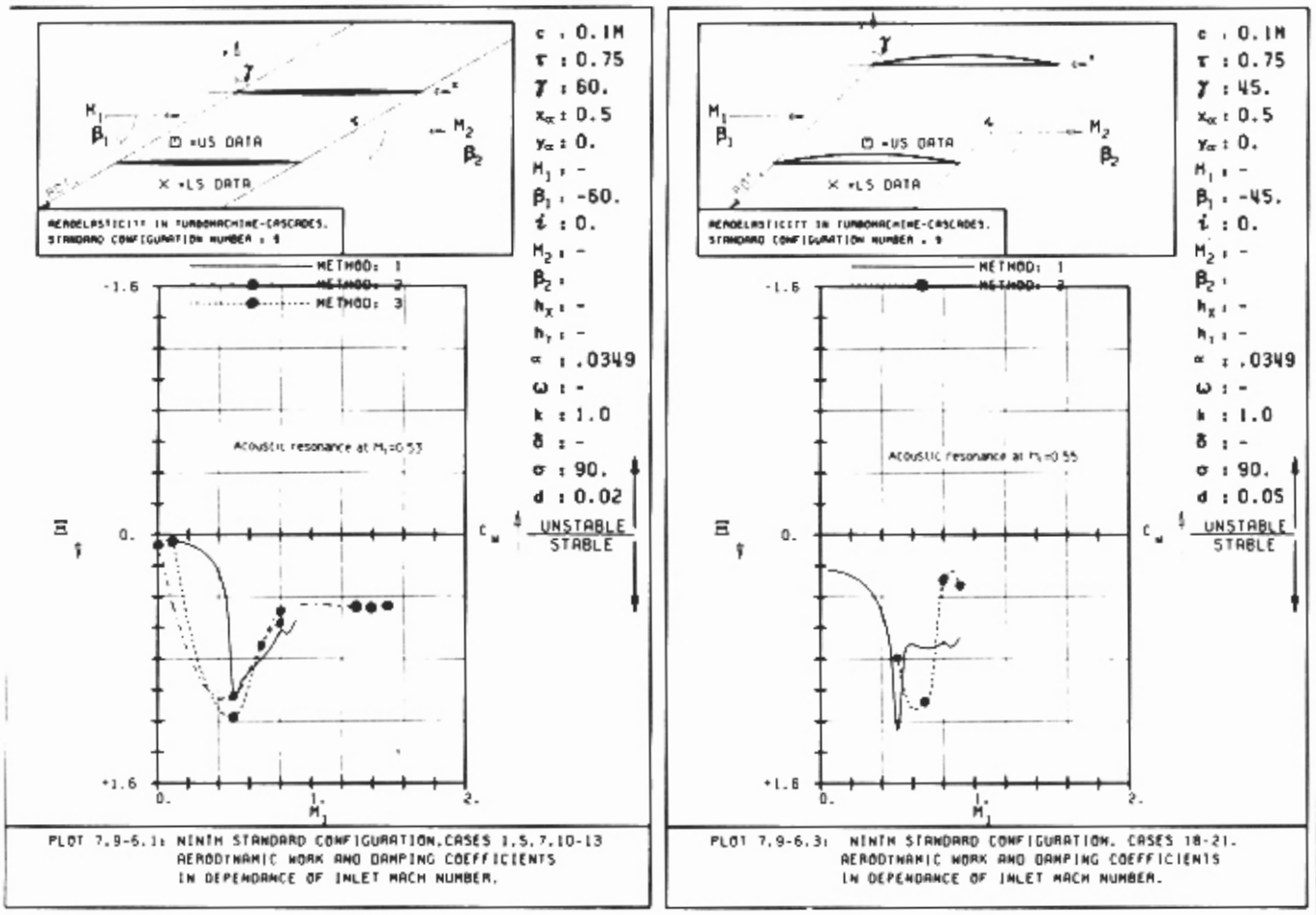


a) d=0.02 b) d=0.05

**Fig. 7.9-3.** Ninth standard configuration. Aerodynamic damping coefficient.

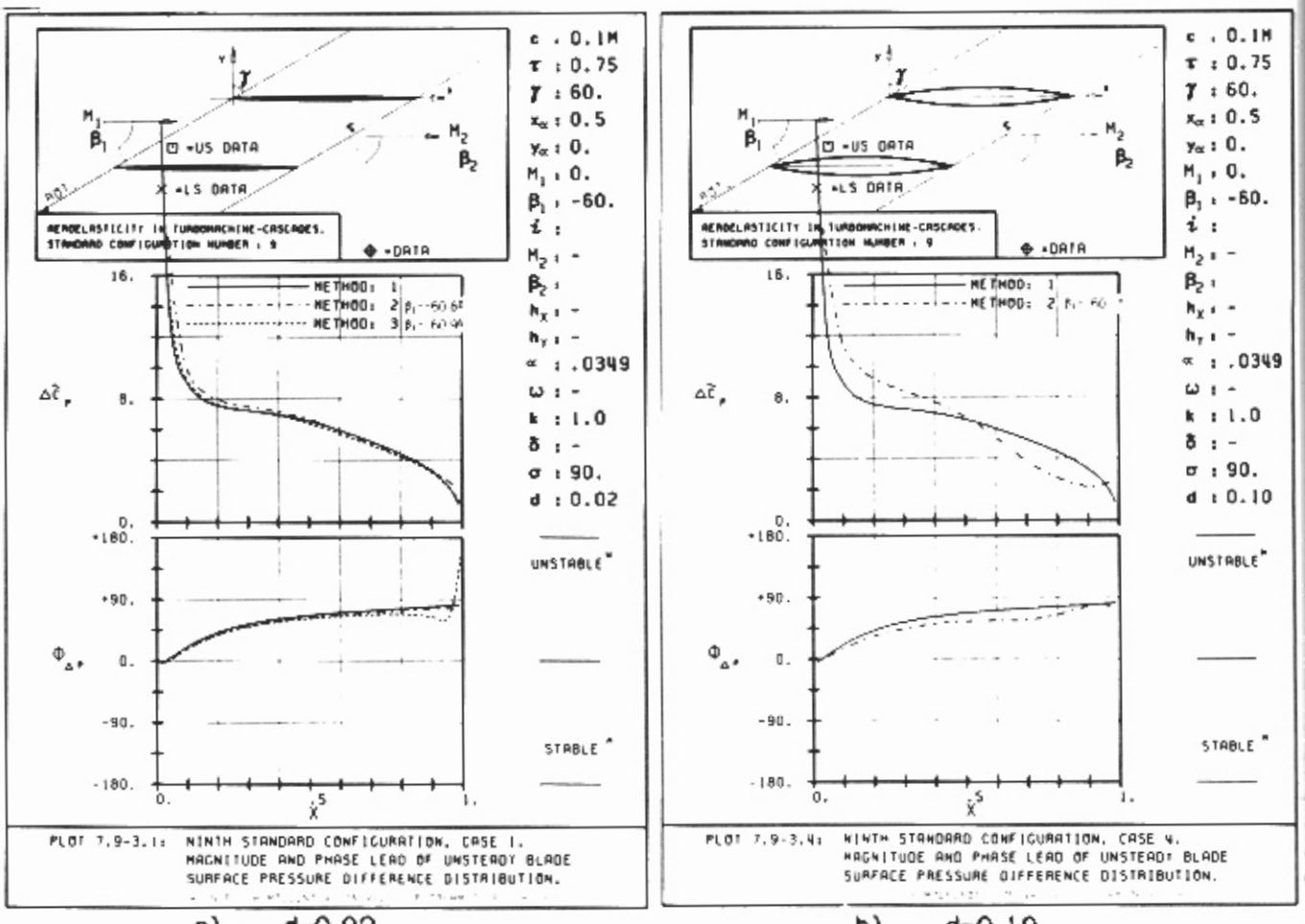


a) d=0.02 b) d=0.10

**Fig. 7.9-4.** Time-dependent blade surface pressure difference coefficient for different blade thicknesses (symmetrical profiles, M=0.0).

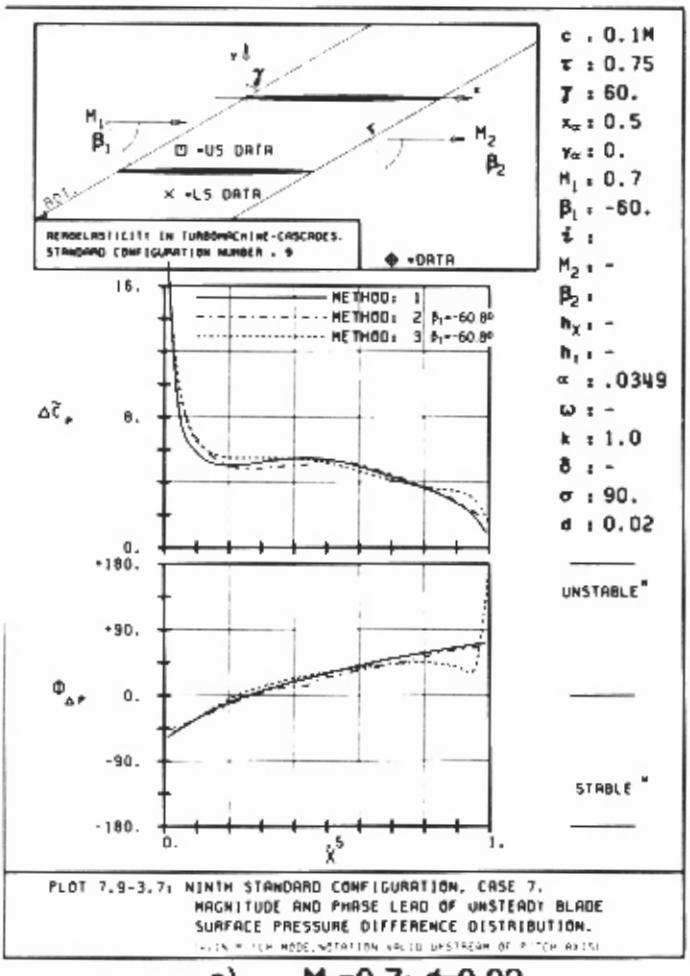


PLOT 7.9-3.7: NINTH STANDARD CONFIGURATION, CASE 7.
MAGNITUDE AND PHASE LEAD OF UNSTEADY BLADE
SURFACE PRESSURE DIFFERENCE DISTRIBUTION.

a) $M_1$=0.7; d=0.02

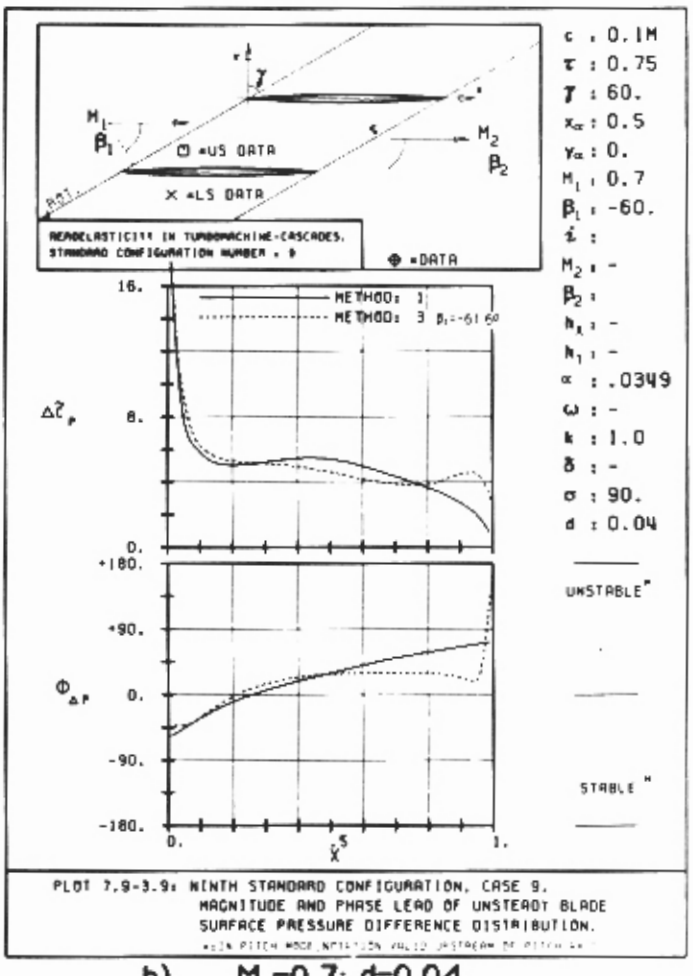


PLOT 7.9-3.9: NINTH STANDARD CONFIGURATION, CASE 9.
MAGNITUDE AND PHASE LEAD OF UNSTEADY BLADE
SURFACE PRESSURE DIFFERENCE DISTRIBUTION.

b) $M_1$=0.7; d=0.04

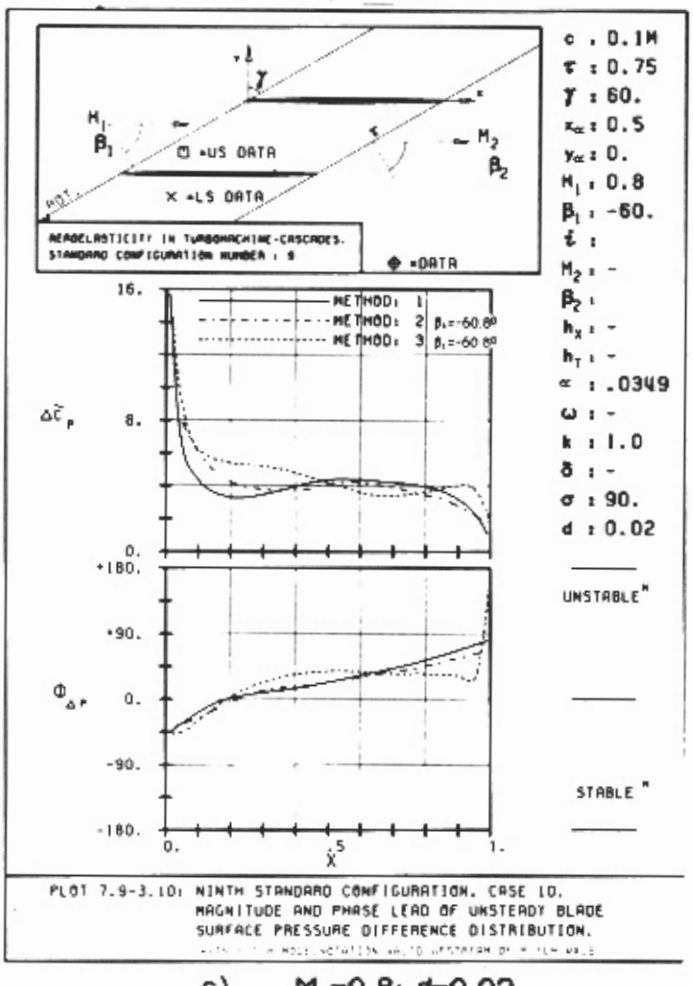


PLOT 7.9-3.10: NINTH STANDARD CONFIGURATION, CASE 10.
MAGNITUDE AND PHASE LEAD OF UNSTEADY BLADE
SURFACE PRESSURE DIFFERENCE DISTRIBUTION.

c) $M_1$=0.8; d=0.02

**Fig. 7.9-5.** Time-dependent blade surface pressure difference coefficient for various steady-state flow conditions (symmetrical profiles).

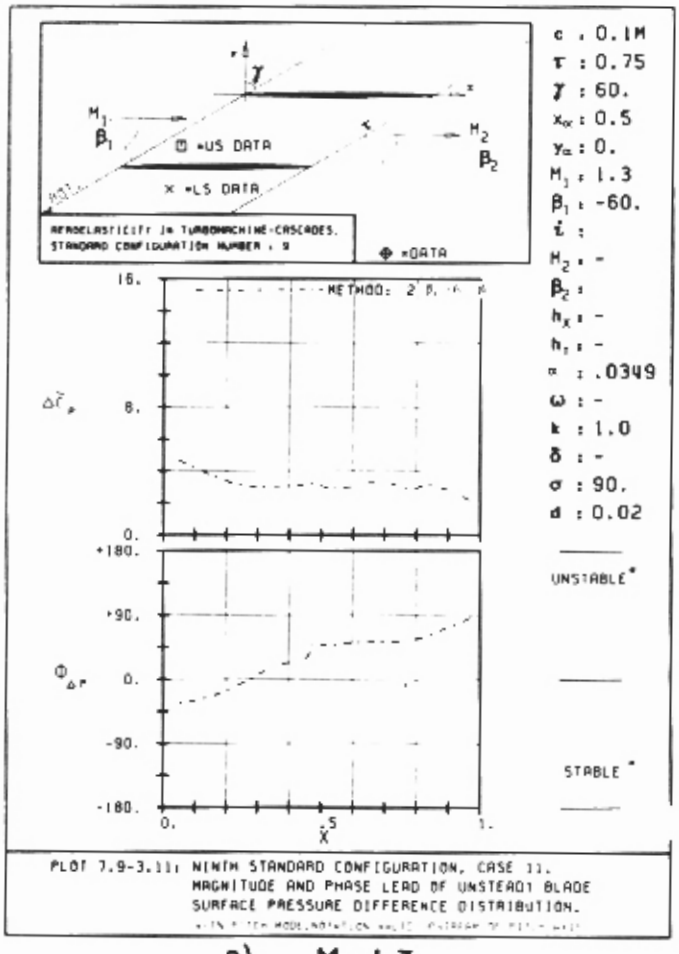


PLOT 7.9-3.11: NINTH STANDARD CONFIGURATION, CASE 11.
MAGNITUDE AND PHASE LEAD OF UNSTEADY BLADE SURFACE PRESSURE DIFFERENCE DISTRIBUTION.

a) $M_1 = 1.3$

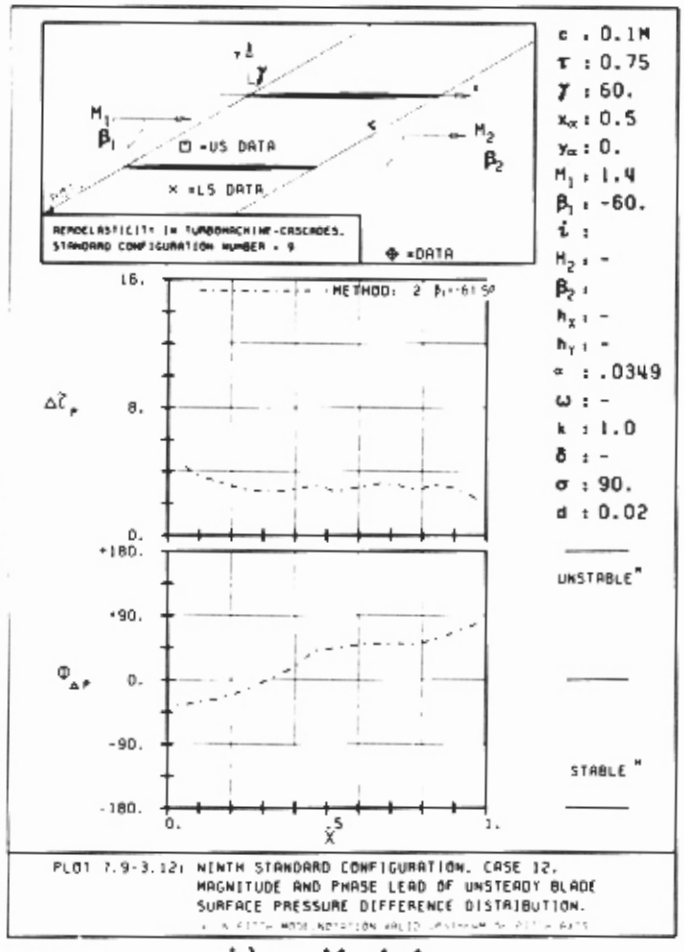


PLOT 7.9-3.12: NINTH STANDARD CONFIGURATION, CASE 12.
MAGNITUDE AND PHASE LEAD OF UNSTEADY BLADE SURFACE PRESSURE DIFFERENCE DISTRIBUTION.

b) $M_1 = 1.4$

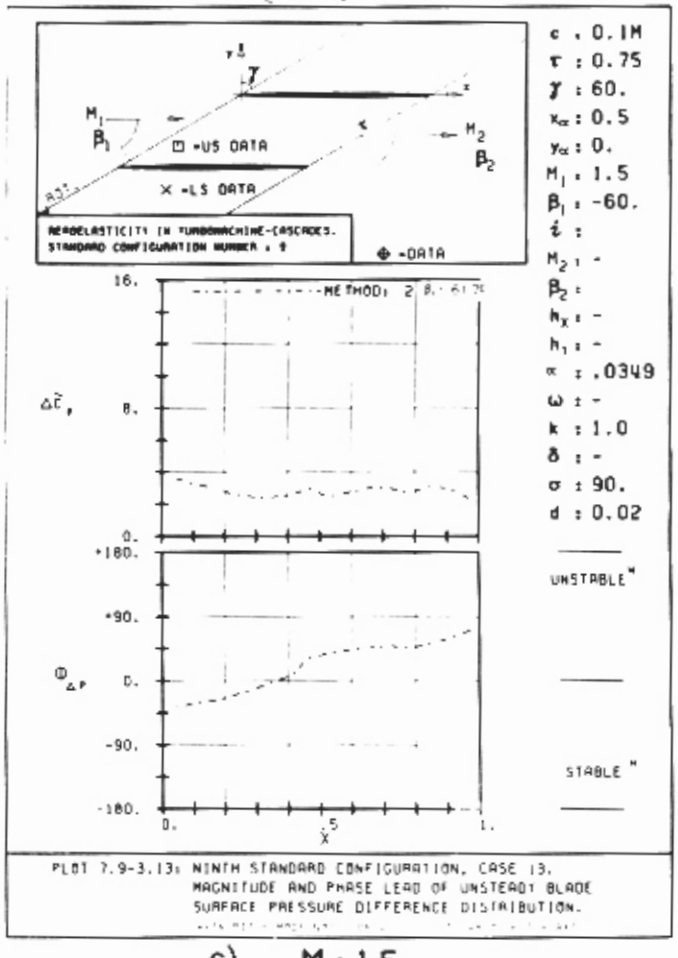


PLOT 7.9-3.13: NINTH STANDARD CONFIGURATION, CASE 13.
MAGNITUDE AND PHASE LEAD OF UNSTEADY BLADE SURFACE PRESSURE DIFFERENCE DISTRIBUTION.

c) $M_1 = 1.5$

**Fig. 7.9-6.** Time-dependent blade surface pressure difference coefficient at various steady-state Mach numbers (symmetrical profiles, d=0.02).

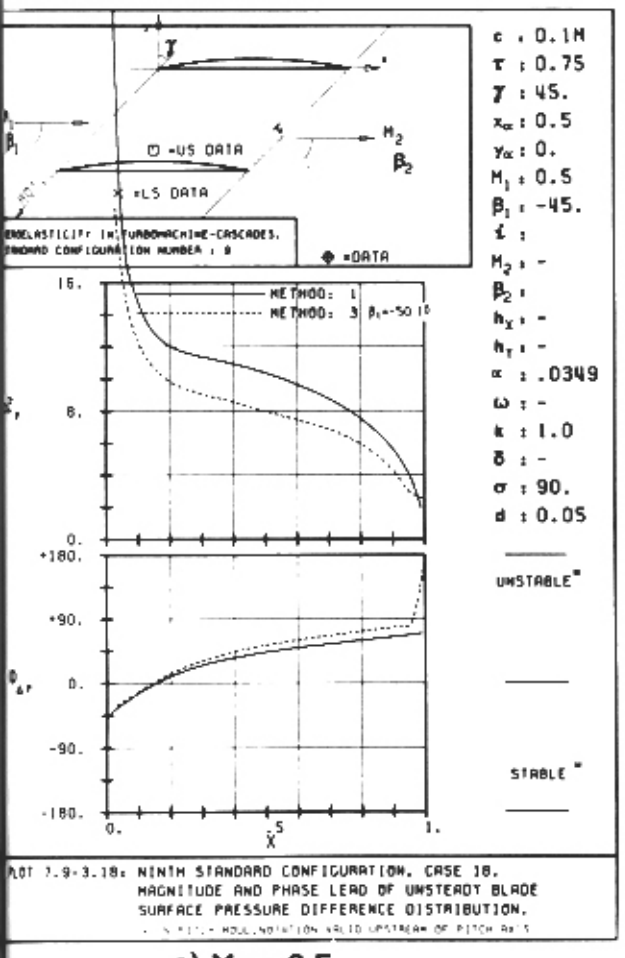


PLOT 7.9-3.18: NINTH STANDARD CONFIGURATION, CASE 18.
MAGNITUDE AND PHASE LEAD OF UNSTEADY BLADE
SURFACE PRESSURE DIFFERENCE DISTRIBUTION.

a) $M_1 = 0.5$

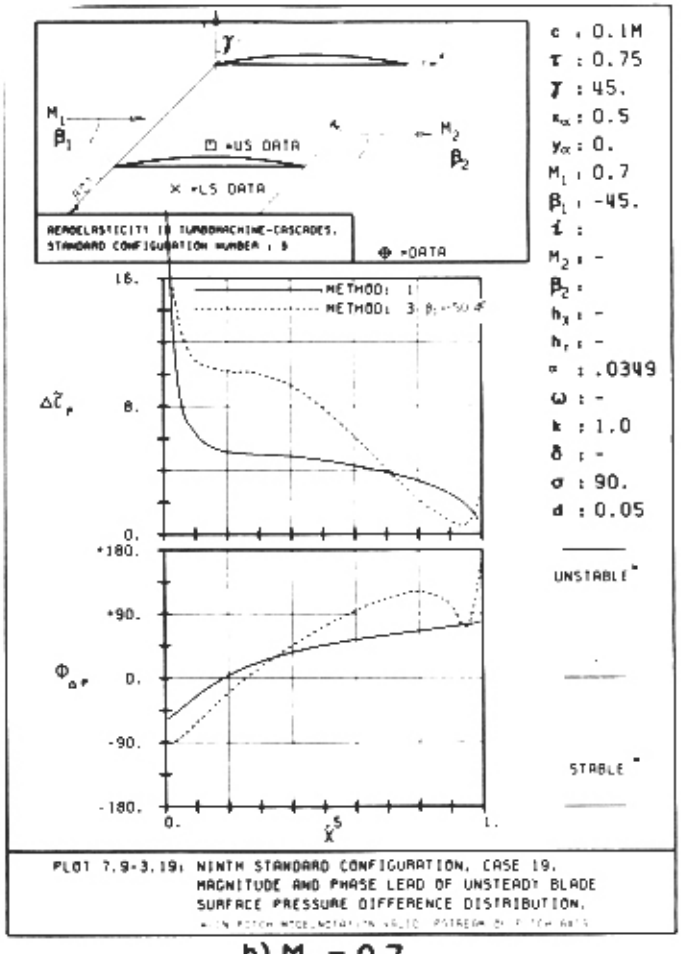


PLOT 7.9-3.19: NINTH STANDARD CONFIGURATION, CASE 19.
MAGNITUDE AND PHASE LEAD OF UNSTEADY BLADE
SURFACE PRESSURE DIFFERENCE DISTRIBUTION.

b) $M_1 = 0.7$

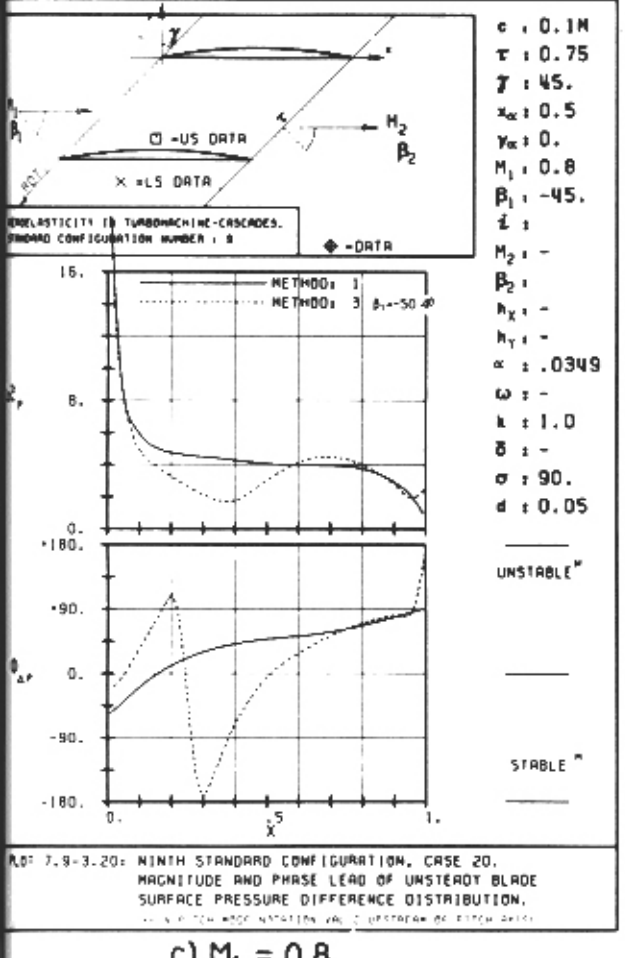


PLOT 7.9-3.20: NINTH STANDARD CONFIGURATION, CASE 20.
MAGNITUDE AND PHASE LEAD OF UNSTEADY BLADE
SURFACE PRESSURE DIFFERENCE DISTRIBUTION.

c) $M_1 = 0.8$

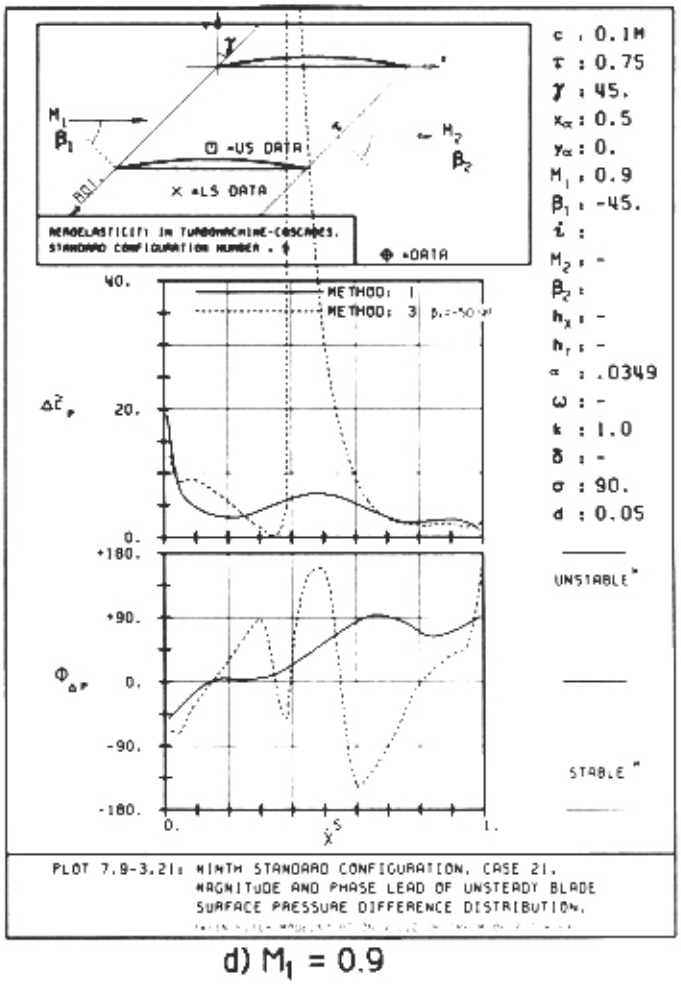


PLOT 7.9-3.21: NINTH STANDARD CONFIGURATION, CASE 21.
MAGNITUDE AND PHASE LEAD OF UNSTEADY BLADE
SURFACE PRESSURE DIFFERENCE DISTRIBUTION.

d) $M_1 = 0.9$

Fig. 7.9-7. Unsteady blade surface pressure difference coefficient for a flat-bottomed DCA-cascade ($\gamma$=45°, $H_+$=0.05,$H_-$=0.0)

Blade Surface Pressures

As for the blade surface pressure difference, the blade surface pressures agree well for the Methods 2 and 3 for low Mach numbers and moderate thickness (Fig. 7.9-8a). However, although $\Delta\tilde{c}_p$ agreed well, some slight discrepancy is found in the local pressure values at a moderate inlet Mach number and blade thickness ($M_1$=0.5, d=0.02; Fig. 7.9-8b). This discrepancy can possibly be explained by the fact that the theoretically determined acoustic resonance is situated close to M=0.50 ($M_{ac.res}$=0.53). At higher Mach numbers ($M_1$=0.7, 0.8) the discrepancy is also present, although now rather in the phase angle than in the magnitude (Fig. 7.9-8c,d).
For the supersonic cases, only one model (Method 2) was applied (Fig. 7.9-9). As for the pressure difference coefficient, only small differences are found in the region $1.3<M_1<1.5$. It is seen that both the upper and lower surface values ($\tilde{c}p$) decrease with increasing Mach number. This simultaneous change is the reason for the fact that $\Delta\tilde{c}_p$ is practically constant for these different Mach numbers.
For the flat-bottomed DCA-cascade, the local blade surface pressure coefficient is largely influenced by the inlet flow conditions (Fig. 7.9-10)[15]. As the Mach number increases, the phase angle encounters phase shiffs. This is especially clear at $M_1$=0.9, where the suction (upper) surface phase angle ($\Phi_p^{us}$) performs three shifts over the chord (Fig. 7.9-10d).

Recent Experimental Results

Recently, time-dependent experiments on cascades with Double Circular Arc profiles in the high subsonic velocity domain have been started [46,60,62]. Some theoretical results on the experiments presented in [60] have also recently become available [5,61,63]. Both the experimental and theoretical difficulties in this velocity domain are considerable, and it is our hope that some of these new investigations may be presented and discussed in detail at the Aachen Symposium on Aeroelasticity in 1987.

15 The results at $M_1$=0.5 may be influenced by the acoustic resonance at $M_{ac.res}$=0.55.

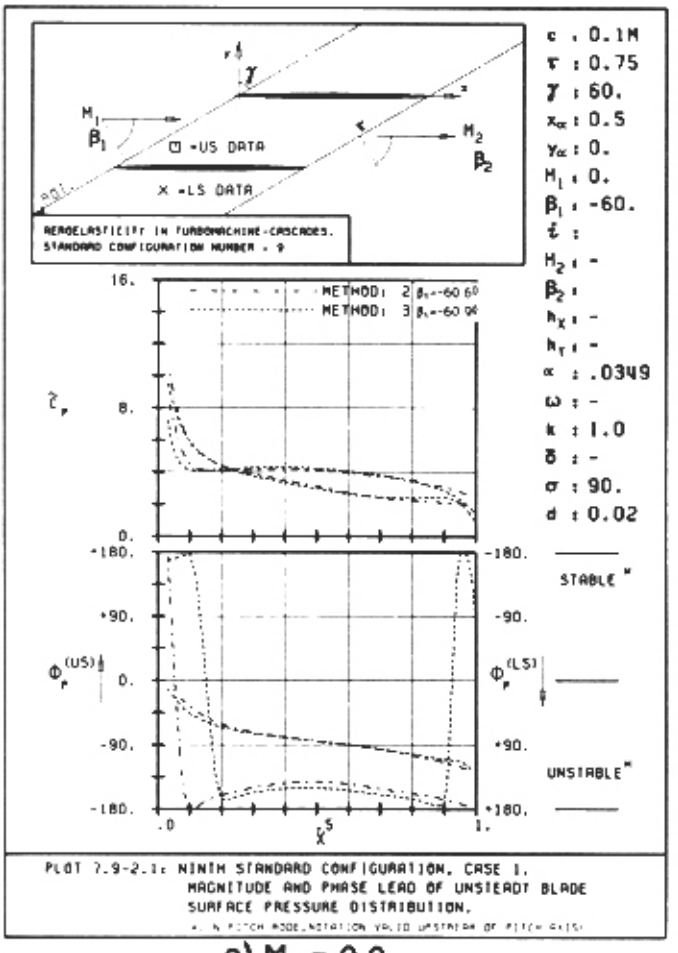


PLOT 7.9-2.1: NINTH STANDARD CONFIGURATION, CASE 1.
MAGNITUDE AND PHASE LEAD OF UNSTEADY BLADE SURFACE PRESSURE DISTRIBUTION.

a) $M_1 = 0.0$

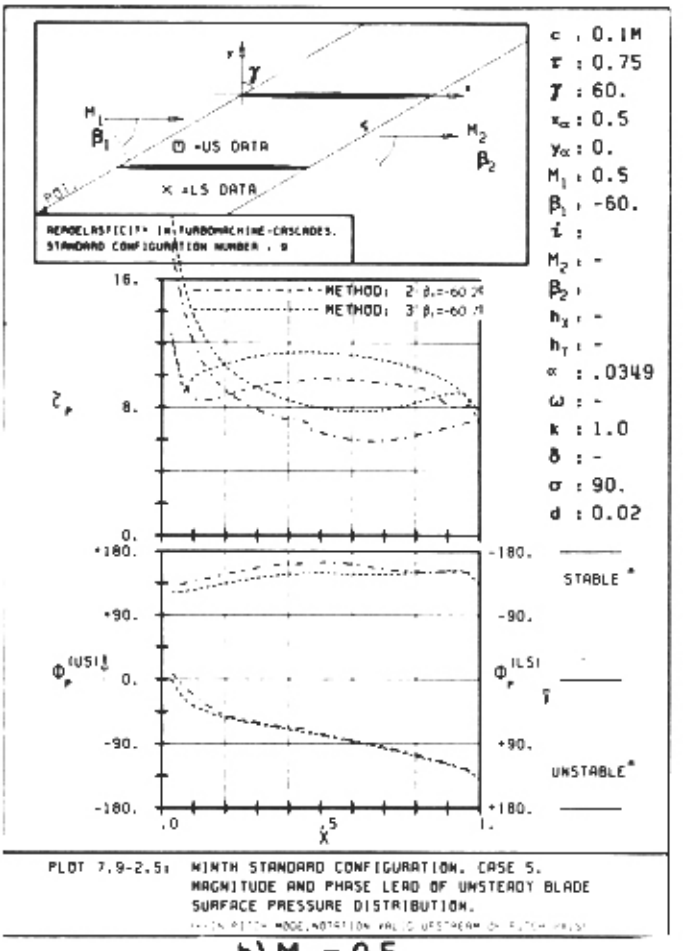


PLOT 7.9-2.5: NINTH STANDARD CONFIGURATION, CASE 5.
MAGNITUDE AND PHASE LEAD OF UNSTEADY BLADE SURFACE PRESSURE DISTRIBUTION.

b) $M_1 = 0.5$

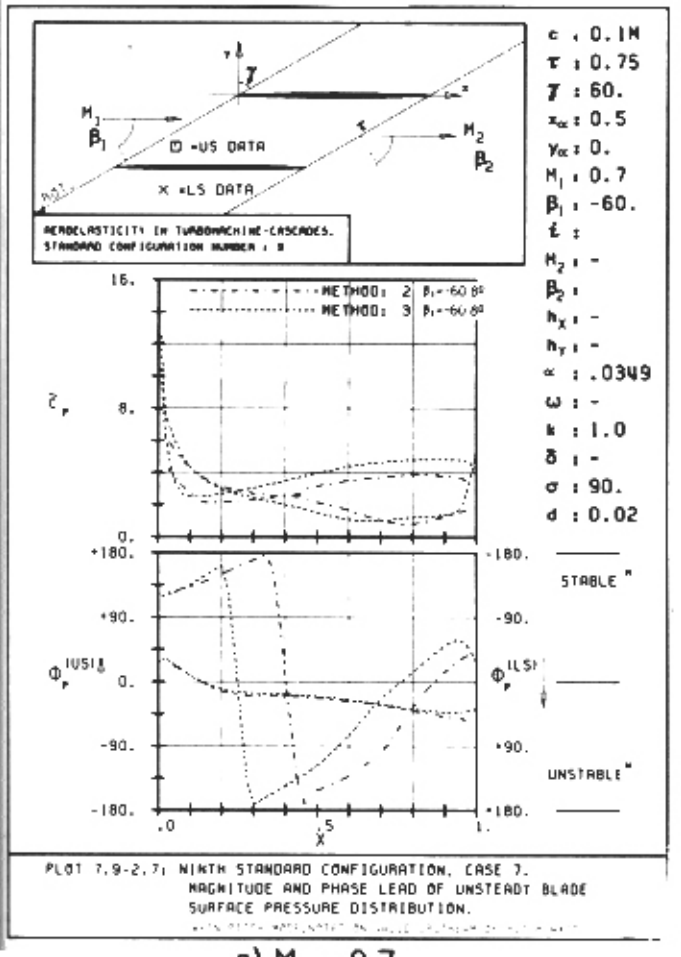


PLOT 7.9-2.7: NINTH STANDARD CONFIGURATION, CASE 7.
MAGNITUDE AND PHASE LEAD OF UNSTEADY BLADE SURFACE PRESSURE DISTRIBUTION.

c) $M_1 = 0.7$

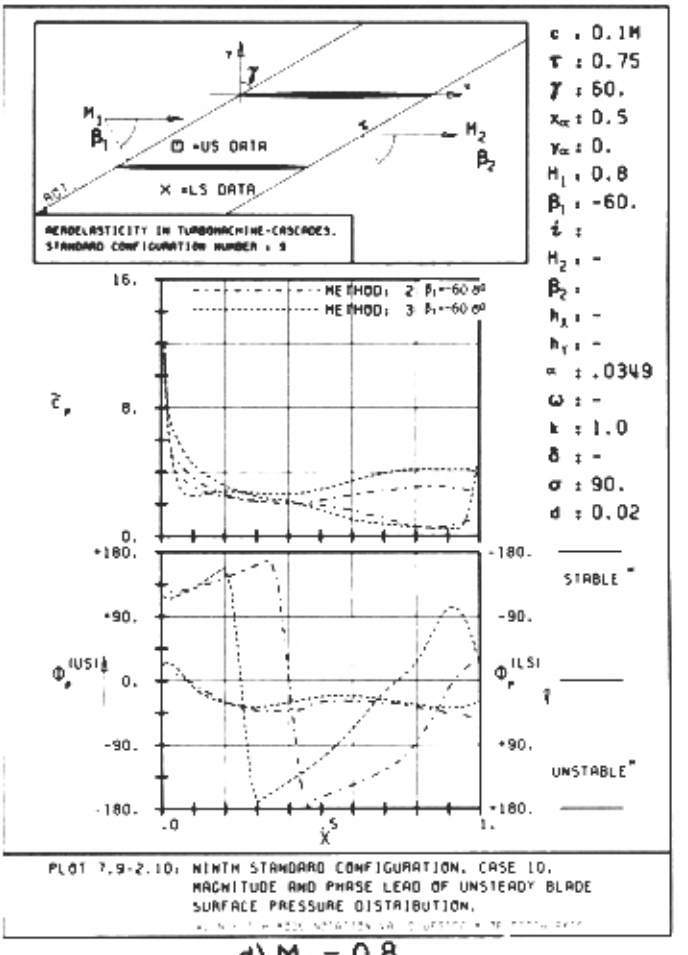


PLOT 7.9-2.10: NINTH STANDARD CONFIGURATION, CASE 10.
MAGNITUDE AND PHASE LEAD OF UNSTEADY BLADE SURFACE PRESSURE DISTRIBUTION.

d) $M_1 = 0.8$

**Fig. 7.9-8.** Time-dependent blade surface pressure coefficient for a symmetric DCA-profile at different subsonic inlet Mach numbers (d=0.02)

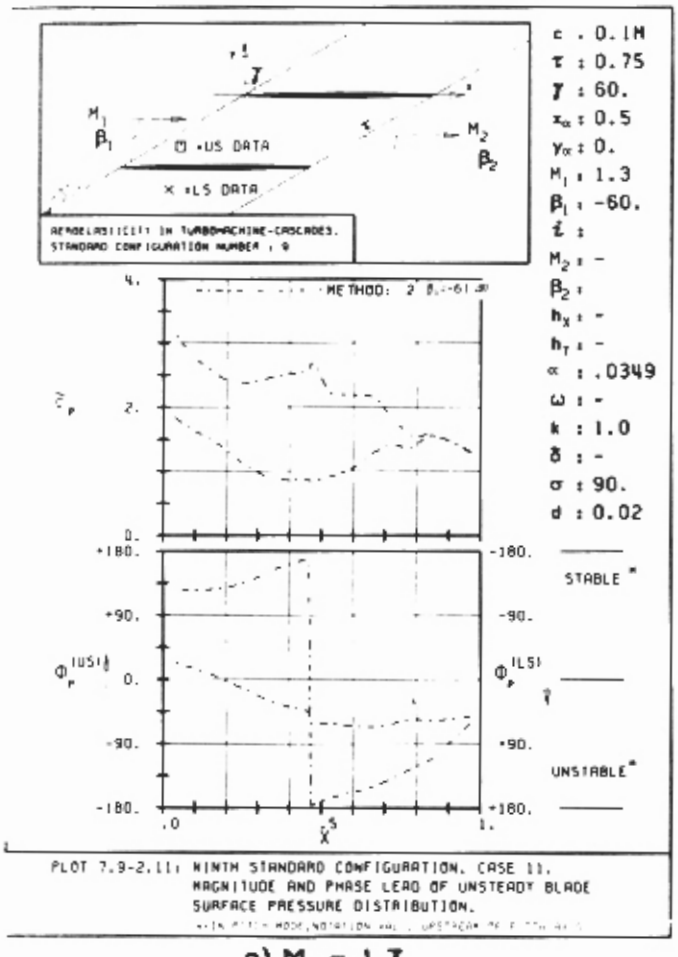


PLOT 7.9-2.11: NINTH STANDARD CONFIGURATION, CASE 11. MAGNITUDE AND PHASE LEAD OF UNSTEADY BLADE SURFACE PRESSURE DISTRIBUTION.

a) $M_1 = 1.3$

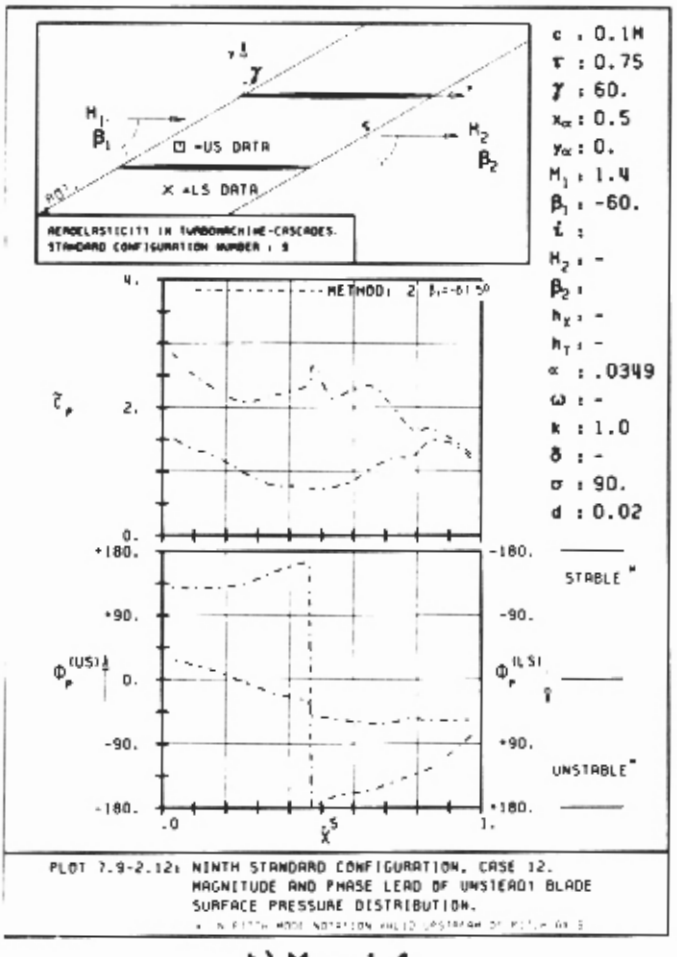


PLOT 7.9-2.12: NINTH STANDARD CONFIGURATION, CASE 12. MAGNITUDE AND PHASE LEAD OF UNSTEADY BLADE SURFACE PRESSURE DISTRIBUTION.

b) $M_1 = 1.4$

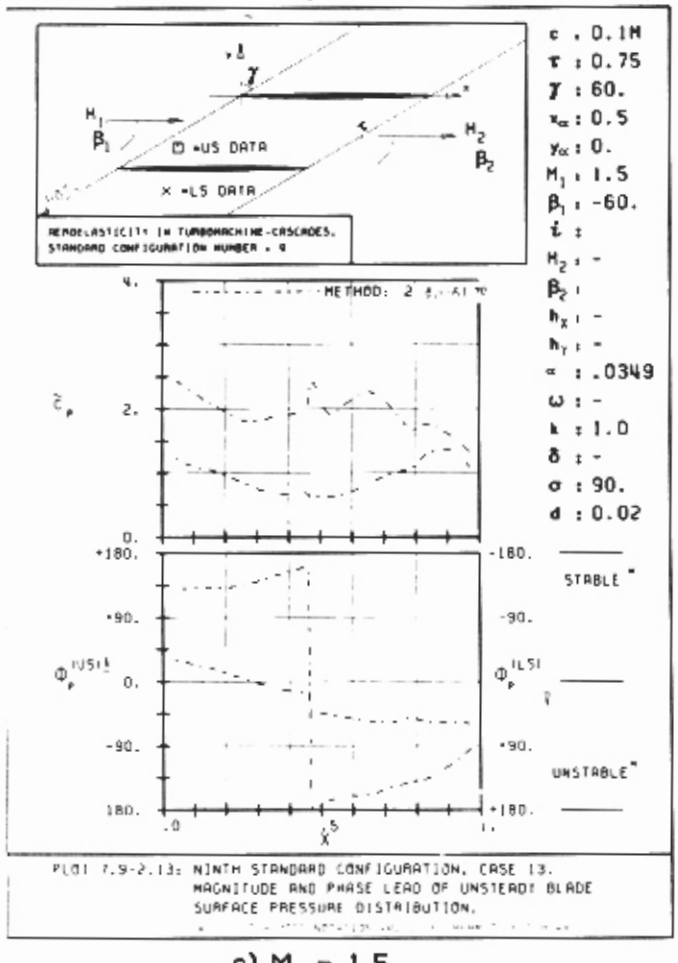


PLOT 7.9-2.13: NINTH STANDARD CONFIGURATION, CASE 13. MAGNITUDE AND PHASE LEAD OF UNSTEADY BLADE SURFACE PRESSURE DISTRIBUTION.

c) $M_1 = 1.5$

**Fig. 7.9-9.** Time-dependent blade surface pressure coefficient for a symmetric DCA-profile at different supersonic inlet Mach numbers (d=0.02)

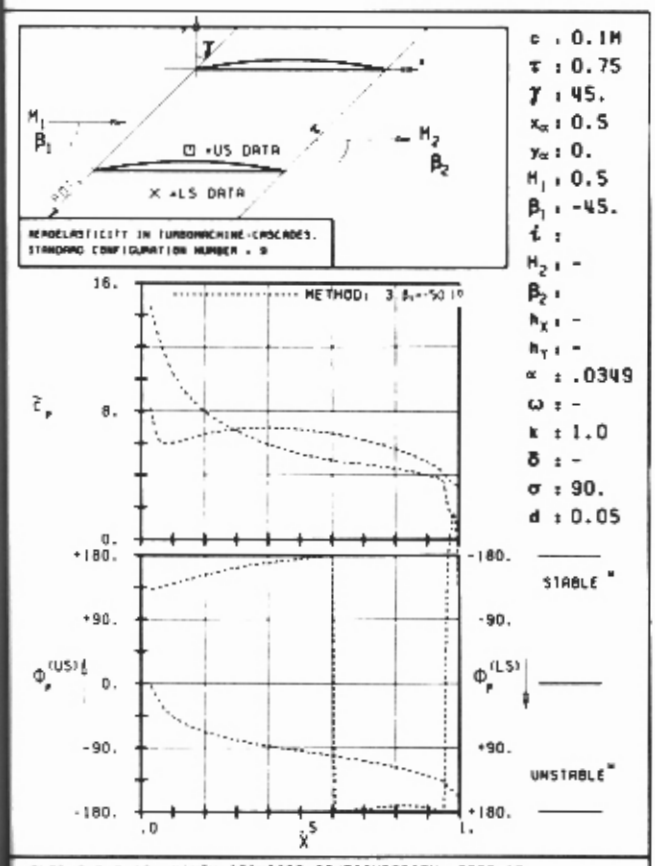


a) $M_1 = 0.5$

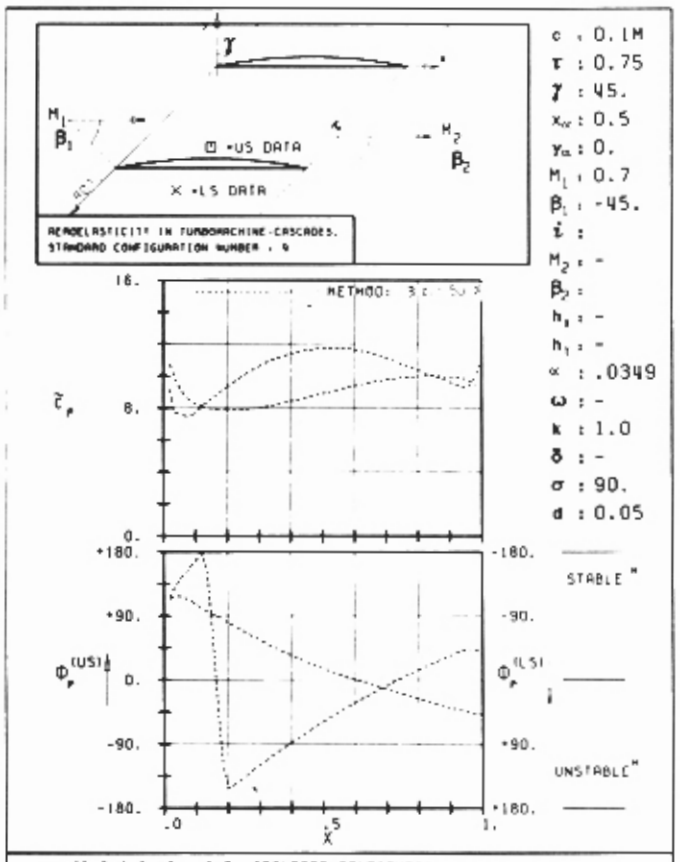


b) $M_1 = 0.7$

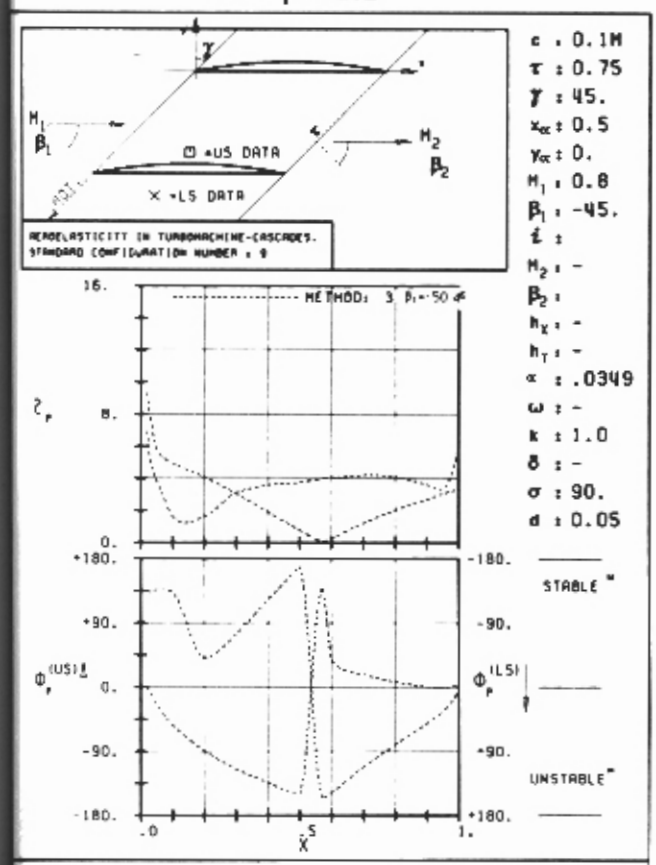


c) $M_1 = 0.8$

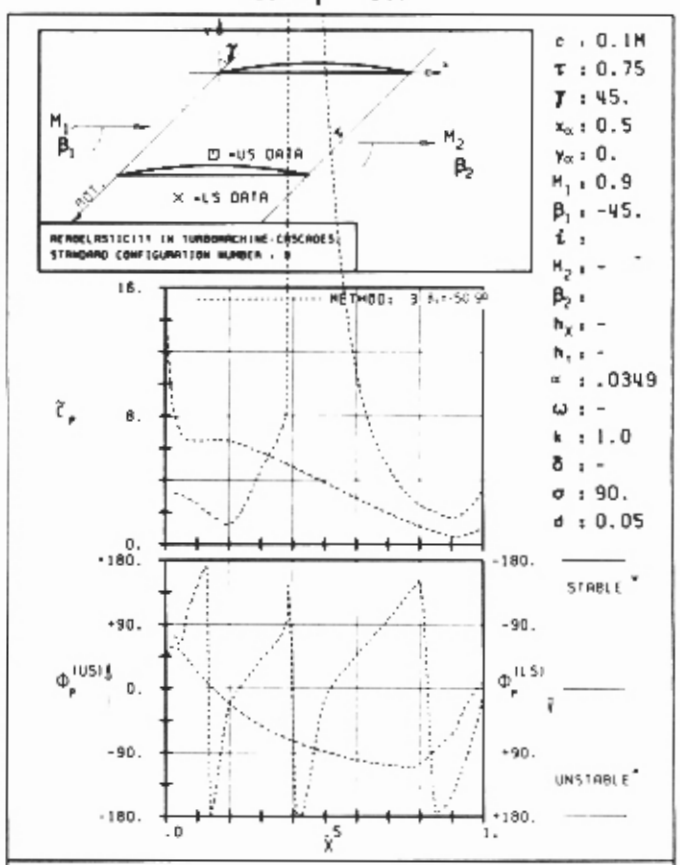


d) $M_1 = 0.9$

**Fig. 7.9-10.** Time-dependent blade surface pressure coefficient for a symmetric DCA-profile at different subsonic inlet Mach numbers (flat-bottomed DCA-cascade, $H_+ = 0.05$, $H_- = 0.0$)

Conclusions for the Ninth Standard Configuration

The study on Double Circular Arc profiles in sub- and supersonic flow indicates that only a few prediction models which consider the full blade geometry outside of the incompressible flow domain presently exist. For the study, two methods were used (Methods 2 and 3). The results from these two methods agree well in most cases presented. However, discrepancies can be found at high subsonic Mach numbers. These increase with increasing Mach number and/or thickness ratio.

It would be of large interest to the aeroelasticity community if the present experimental and theoretical efforts [5,60-63] could be coordinated as to simultaneously perform both experiments and predictions.

## 8. Summary and Conclusions

### Summary

An international study to define the state-of-the-art of theoretical and experimental aeroelastic investigations in turbomachine-cascades has been conducted.
The project, which was initiated during the second Symposium on Aeroelasticity [2], has given the first general comparison of aeroelastic information between a larger set of experimental data and the major theoretical prediction models available presently.
Through the interest shown by both industrial and governemental institutions, it has become clear that the study corresponds to an urgent need for establishing the state-of-the-art of aeroelastic investigations in turbomachines, and to coordinate and initiate new experimental and theoretical projects. This is especially important as the understanding of the physical phenomena causing flutter, especially in the transonic flow domain, can be achieved only by mutual experimental and theoretical approaches.
The configurations under investigation consist of different blade and cascade geometries, various steady-state and time-averaged flow conditions, and different blade vibration modes. However, as no prediction models for separated flow were offered for analyses, the study was confined to attached flow conditions. Furthermore, all experiments offered as test cases considered rigid, uncoupled, body motions in either torsion or bending, therefore the conclusions are not valid for coupled and/or non-rigid blade vibrations.
The study indicates well in which flow domains, and on which sort of profiles, present two-dimensional theoretical models can accurately predict the aeroelastic behavior of a vibrating cascade and, in particular, its stability margins.

### State-of-the-Art of Aeroelasticity in Turbomachine-Cascades

With present experimental methods it is possible to measure accurately the time-dependent pressure fluctuations on vibrating turbomachine blades, as well as in the blade-passage between the blades, in linear and annular wind tunnels in the subsonic attached flow domain. However, the procedures are costly, far from routine, and considerable efforts are necessary to guarantee the accuracy of the results. Among the difficulties to consider can be

mentioned, apart from the problems in establishing periodic steady-state flow conditions in cascades:

- establishment of unsteady flow periodicity conditions
- realization of sufficiently high blade vibration amplitudes
- control of interblade phase angles
- determination of data accuracy
- determination of unsteady boundary layer separations, especially local separation bubbles.

Also in the transonic and supersonic flow regimes it is today possible to obtain highly accurate data. However, shock waves and shock/boundary layer interactions can considerably complicate the measurement accuracy. Furthermore, the manner of integrating the aeroelastic damping coefficient, and the number of pressure transducers used, may influence the magnitude and stability limits, especially in the transonic flow region where strong, mostly unsteady, shocks are present.

As regards the theoretical methods, it is today possible to predict accurately the local blade surface pressure distribution, aeroelastic lift and moment coefficients, as well as the aeroelastic damping coefficients, for blades of different shapes in two-dimensional subsonic, attached flow. This has clearly been demonstrated in the first (6% thick; 10° camber; M=0.2; compressor cascade) and fourth (17% thick; 45° camber; $M_1$=0.2; turbine cascade) standard configurations. Different theories (including flat plate methods) predict similar results in the low subsonic flow regions on thin airfoils (first standard configuration), whereas discrepancies are apparent for higher flow velocities with thin (eighth standard configuration) or moderately thick (fifth and ninth standard configurations) blades at high reduced frequencies.

At lower reduced frequencies it is possible to predict very accurately the unsteady pressures on thick, cambered turbine blades in bending vibration (fourth standard configuration).

Local pressure differences (on the blade surface) between experimental data and predicted results on a compressor cascade in moderate subsonic flow (fifth standard configuration) may possibly be explained by local unsteady separation bubbles, as well as by the fact that only one blade was considered to vibrate in the experiment.

Also in the supersonic flow domain the prediction methods (including flat plate anlyses) seem able to predict fairly accurately the aeroelastic damping coefficient (seventh standard configuration). This is clearly the case as compressor blades in this flow region are thin and moderately cambered.

However, in this flow regime major discrepancies are found between the predicted and the experimental pressure and moment coefficients, especially in the phase angles (seventh standard configuration). It is not clear a priori whether these discrepancies should be attributed to the theoretical models or if scatter in the data, as well as shock/boundary layer interactions and boundary layer separations, plays a significant role.
Indications that a strong leading edge shock wave may significantly alter the aeroelastic behavior of a flat plate cascade in supersonic flow at high reduced frequencies were given (eighth standard configuration). However, a more detailed study should be performed before any conclusions about these results are drawn.
The trends of the aeroelastic behavior of thick, cambered turbine blades in the transonic flow domain are predicted (fourth standard configuration). The agreement between the data and the predicted results ranges from extremly good (subsonic flow) to moderate (transonic flow).
In general it can be concluded that although the fundamental physical reasons for the flutter are not fully understood, present two-dimensional prediction models give good approximations for test cases in attached two-dimensional and quasi three-dimensional flow. However, no fully three-dimensional models (with blade thickness taken into account) exist, and no attempts were made to predict the aeroelastic behavior of stalled flow.

**Further Work**

The results of the study are encouraging, but a lack of understanding of flutter phenomena exists in several domains. The project has shown that it is presently possible to predict flutter in some cases, at least in two-dimensional attached flows. However, the detailed pressure distribution on the blades cannot be predicted as well, especially in transonic flows. Furthermore, three-dimensional effects and their influence on the stability of turbomachine-blades are not well known.
Hence, to model the physical aspects of flutter better, projects in the following domains are solicited:

- transonic two-dimensional attached flow in turbines and compressors
- quasi three-dimensional and three-dimensional investigations in attached flow, throughout all velocity domains
- stalled two-dimensional flow
- rotating machines

- accuracy analyses of time-dependent pressures and their phase angles towards the blade motion
- experimental techniques to evaluate the unsteady pressures in rotating machines
- experimental determination of unsteady wave propagations up- and downstream of blade rows in linear and annular cascade facilities
- experiments with coupled blade vibration modes
- unsteady boundary layer investigations

During the project, several interesting experimental and theoretical investigations were started. One of these concerns experiments on transonic turbine profiles, and the results are included here as the fourth standard configuration. Among the others can be mentioned:

- In the experimental domain:

  - two-dimensional and quasi three-dimensional studies on Double Circula Arc profiles in high subsonic and transonic flow domains [46, 49, 60, 62]

  - two-dimensional and quasi three-dimensional studies on a fan section in the high subsonic, transonic and supersonic flow domains [65].

  - flat plate investigations (turbine) in the transonic flow region [69].

- In the theoretical domain:

  - two-dimensional unsteady perturbation solvers, based on the Euler equations.

  - two-dimensional fully unsteady Euler solvers [47, 67, 68].

Simultaneously, considerable improvements have been made on experimental and theoretical projects already started.

It is hoped that new results will continue to be introduced in the workshop so as to continue the international collaboration which has now been established. Such a collaboration will certainly make aeroelastic knowledge progress faster than if only individual and independent projects are considered.

## Applicability to Flutter in Rotating Machines

The final objective of the aeroelastician is obviously to give the designer the necessary tools for preventing flutter in rotating machines. However, such a far-reaching objective does not correspond to the state-of-the-art of aeroelastic knowledge, either for prediction models or as regards well-documented experimental data to be used for the validation of theoretical models. The best approach today to blade flutter prevention in turbomachines is to use existing two-dimensional prediction models, couple them extensively with in-house empirical data and then perform comprehensive

tests on the machine. However, this procedure is extremly costly, and will give an answer only for the aeroelastic response of the machine being tested. This has especially been seen in the present study, as prediction models gave correct stability limits in some cases, while being far out in the prediction of the unsteady pressure forces acting on the blades. Furthermore, most flutter failures seem to appear in the transonic and/or stalled flow regions, for which only a few prediction models (mostly empirical) and experimental set-ups exist today.

It thus seems to the editors of the present study that several basic experimental and theoretical research projects still have to be carried out to clarify the flutter phenomena in cascades (see the previous section). Only with such an approach will it be possible to find out exactly why a certain stage fluttered although it was perhaps predicted to be stable. Simultaneously, detailed flow surveys in the machine under flutterconditions, which are very difficult, and especially the feedback of this information into cascade tests and prediction models, are necessary. Obviously, this last piece information will mostly be of a proprietary nature.

It is the editors belief that although cascade experiments and two-dimensional prediction models can replace full-scale machine tests only to a small extent, a continued, long-term joint scientific collboration of the present kind will, be of benefit to the designer of turbomachines, especially as long as a large data-bank of detailed three-dimensional unsteady blade surface pressure data is not available.

**Acknowledgement**

This research project was sponsored in part by the United States Air Force under Grants AFOSR 81-0251, AFOSR 83-0063, AFOSR 84-0105 with Dr. Anthony Amos as program manager, and in part by the Swiss Federal Institute of Technology, Lausanne. The kind support of the European Office of Scientific Research, under the direction of Colonel W. K. Pendleton, Colonel O. Mancarella and Captain A. R. Hoyt is gratefully acknowledged.

The editors express their particular thanks to all the research colleagues who have participated, either directly or indirectly, in the project. Needless to say, without their understanding, patience and goodwill, this state-of-the-art of aeroelasticity in turbomachine-cascades would never have been compiled. It is also thanks to their scientific interest and considerable efforts that the study has been given a truly international character. It is our hope that scientific exchanges on this subject can continue in a similar spirit with a view to the next Symposium.

Thank you (in alphabetical order):

- Dr. T. Araki, Toshiba Corporation, Kawasaki, Japan
- Prof. Dr. H. Atassi, University of Notre Dame, Notre Dame, USA
- Prof. Dr. O. O. Bendiksen, Princeton University, Princeton USA
- Dr. D. Bohn, Kraftwerkunion AG, Mülheim/Ruhr Germany
- Mr. D. R. Boldman, NASA Lewis Research Center, Cleveland, Ohio, USA
- Dr. P. Bublitz, Deutsche Forschungsverein für Luft- und Raumfahrt, Göttingen, Germany
- Dr. V. Carstens, Deutsche Forschungsverein für Luft- und Raumfahrt, Göttingen Germany
- Dr. F. O. Carta, United Technologies Research Center, East Hartford, Conneticut, USA
- Prof. Dr. J. Caruthers, University of Tennessee Space Institute, Tullahoma, Tennessee USA
- Mr. R. Cedar, Rolls Royce Ltd, Derby, UK
- Prof. Dr. E.F. Crawley, Massachussets Institute of Technology, Cambridge, Massachussets, USA
- Prof. Dr. H.E. Gallus, Rhein-Westphalische Technische Hochschule, Aachen, Germany
- Dr. J. M. R. Graham, Imperial College, London UK
- Dr. D. G. Halliwell, Rolls Royce Ltd, Derby, UK
- Dr. M. Honjo, Mitsubishi Heavy Industries Ltd., Japan

- Mr. R.L. Jay, Detroit Diesel Allison, Indianapolis, Indiana, USA
- Dr. H. Joubert, SNECMA, Moisy Crayamel, France
- Dr. R. Jutras, General Electric, Cincinatti, USA
- Prof. Dr. S. Kaji, Tokyo University, Tokyo, Japan
- Dr. N. H. Kemp, Physical Science Incorporation, Andover, Massachussets, USA
- Mr. A. Kirschner, Brown Boveri Company, Baden, Switzerland
- Dr. H. Kobayashi, National Aerospace Laboratory, Tokyo Japan
- Mr. Z. Kovatz, Westinghouse Electric Corporation, Pittsburg, Pennsylvania, USA
- Prof. Dr. M. Kurosaka, University of Tennessee Space Institute, Tullahoma, Tennessee USA
- Prof. F. Martelli, University of Florence, Florence Italy
- Dr. J.-L. Meurzec, Office National d'Etudes et de la Recherche Aerospatiale, Chattillon, France
- Dr. F. B. Molls, NASA Lewis Research Center, Cleveland, Ohio, USA
- Dr. S. Nagano, Ishikawajima-Harima Heavy Industries, Tokyo, Japan
- Prof. Dr. M. Namba, Kuyushu University, Fukuoka, Japan
- Dr. S. G. Newton, Rolls Royce Ltd, Derby, UK
- Mr. P. Niscode, General Electric, Cincinnatti, Ohio USA
- Dr. D. Nixon,Nielsen Engineering and Research Inc., Mountain View, California USA
- Prof. Dr. M. F. Platzer, Naval Postgraduate School, Monterey, California, USA
- Dr. P. Salaün, Office National d'Etudes et de la Recherche Aerospatiale, Chatillon, France
- Mr. D. Schläfli, Swiss Federal Institute of Technology, Lausanne, Switzerland
- Dr. H. Shoji, Tokyo University, Tokyo, Japan
- Prof. Dr. F. Sisto, Stevens Institute of Technology, Hobroken, New Jersey, USA
- Prof. Dr. S. Stecco, University of Florence, Florence, Italy
- Dr. E. Szecheneyi, Office National d'Etudes et de la Recherche, Chatillon France
- Dr. S. Takahara, Mitsubishi Heavy Industries Ltd., Nagasaki, Japan
- Prof. Dr. H. Tanaka, Tokyo University, Tokyo Japan
- Prof. Dr. H. Tanida, Tokyo University, Tokyo, Japan

- Dr. H. Triebstein, Deutsche Forschungsverein für Luft- und Raumfahrt, Göttingen, Germany
- Dr. J. M. Verdon, United Technologies Research Center, East Hartford, Connetticut, USA
- Dr. K. Vogeler, Rhein-Westphalische Technische Hochschule, Aachen, Germany
- Dr. D. S. Whitehead, Cambridge University, Cambridge UK
- Prof. Sheng Zhou, Beijing Institute of Aeronautics and Astronautics, Beijing, China

## References

**[1]**
"Aéroélasticité dans les turbomachines"
*Proceedings of the Symposium held in Paris, France, 1976*
*Revue Mécanique Française, Numéro spécial 1976*

**[2] P. Suter (Editor)**
"Aeroelasticity in Turbomachines"
*Proceedings of the Symposium held in Lausanne, Sept. 8-12, 1980.*
*Communication du Laboratoire de Thermique Appliquée N° 10, Lausanne Institute of Technology, Switzerland*

**[3]**
"Unsteady Aerodynamics of Turbomachines and Propellers"
*Proceedings of the Symposium held in Cambridge, UK, September 24-27, 1984*

**[4] T. Fransson, P. Suter**
"Two-Dimensional and Quasi-Three-Dimensional Experimental Standard Configurations for Aeroelastic Investigations in Turbomachine-Cascades".
*Report LTT 83-2, Ecole Polytechnique Fédérale de Lausanne,Switzerland, 1983.*
*+ Errata to configurations 2, 5 and 9.*

**[5] J. M. Verdon, W. J. Usab**
"Application of a Linearized Unsteady Aerodynamic Analysis to Standard Cascade Configurations"
*NASA Contractor Report, 1985*

**[6] S. Fleeter**
"Aeroelasticity Research for Turbomachine Applications"
*Journal of Aircraft, Vol. 16, N° 5, 1979*

**[7] T. Fransson**
"Two-Dimensional and Quasi-Three-Dimensional Experimental Standard Configurations for Aeroelastic Investigations in Turbomachine-Cascades."
*Proceedings of the Symposium on "Unsteady Aerodynamics of Turbomachines and Propellors", Cambridge, UK, September 24-27, 1984, p.p. 361-396.*

**[8] F.O. Carta**
"Unsteady Gapwise Periodicity of Oscillating Cascaded Airfoils"
*ASME Paper 82-GT-286, 1982*

**[9] J.M. Verdon, J.R. Caspar**
"Development of a Linear Unsteady Aerodynamic Analysis for Finite-Deflection Subsonic Cascades"
*AIAA Paper 81-1290, 1981*

**[10] Y.C. Fung**
"An introduction to the Theory of Aeroelasticity"
*Dover Publications, Inc., New-York, 1969, page 82*

**[11] H. Ashley, R.L. Bisplinghoff**
"Principles of Aeroelasticity"
*Dover Publications, Inc., New-York, 1969, page 202*

**[12] F.O. Carta**
"Coupled Blade-Disk-Shroud Flutter Instabilities in Turbojet Engine Motors"
*Journal of Engineering for Power, July 1967, p.p. 419-426*

**[13] S.R. Bland (Coordinator)**
"AGARD Two-Dimensional Aeroelastic Configurations"
*AGARD Advisory Report N° 156, 1979*

**[14] J.M. Verdon, J.E. Mc Cune**
"Unsteady Supersonic Cascade in Subsonic Axial Flow"
*AIAA Journal Vol. 13, N° 2, 1975, pp. 193-201*

**[15] F. O. Carta**
"An Experimental Investigtion of Gapwise Periodicity and Unsteady Aerodynamic Response in an Oscillating Cascade:
I - Experimental and Theoretical Results
II - Data Report, Vol. 1.
III- Data Report, Vol. 2."
*NASA Contractor Report 3513, June 1982.*

**[16] F. O. Carta**
Private Communication, 1984

**[17] E. L. Davis,Jr.**
"The Measurement of Unsteady Pressures in Wind Tunnels"
*AGARD Report 169, March 1958*

**[18] A. Bölcs, D. Schläfli**
"Flutter Phenomena in a Transonic Turbine Cascade"
*Proceedings of the Symposium on "Unsteady Aerodynamics of Turbomachines and Propellors", Cambridge, UK, September 24-27, 1984, p.p. 411-426.*

**[19] Y. Hanamura, H. Tanaka**
"The Flexure-Torsion Flutter of Airfoils in Cascade"
*Bulletin of JSME, Vol. 10, N° 40, 1967 pages 647-662 + pages 939-952*

**[20] H. Tanaka**
Private Communication, 1984

**[21] A. Bölcs, M. Degen, D. Schläfli**
"Experimental Data for the Fourth Standard Configuration in the Workshop on Aeroelasticity in Turbomachine-Cascades"
*Proceedings of the Symposium on "Unsteady Aerodynamics of Turbomachines and Propellors", Cambridge, UK, September 24-27, 1984, p.p. 601-607*

**[22] A. Bölcs**
"A Test Facility for the Investigation of Steady and Unsteady Transonic Flows in Annular Cascades"
*ASME paper 83-GT-34, 1983*

**[23] A. Bölcs, M. Degen, D. Schläfli**
"Flutter Investigation of a Highly Cambered Turbine Cascade in Sub- and Supersonic Flow" + Appendix A1-A3,
*Report LTT - 2 - 85, 1985, Ecole Polytechnique Fédérale de Lausanne, Switzerland*

**[24] F. Beretta-Piccoli, P. Ott**
"Three-Dimensional Laser Holography Visualization of a Highly Cambered Turbine Cascade"
Private Communication, 1985

**[25] A. Bölcs, O. Sari**
"Investigation of a Highly Cambered Turbine Cascade in a Linear Test Facility"
*Report LTT - 6 - 85, 1985, Ecole Polytechnique Fédérale de Lausanne, Switzerland*

**[26] B. Fosco, A. Kirschner**
"Control of Vibration in Aeroelastic Cascade Experiments"
*Proceedings of the Symposium on "Aeroelasticity in Turbomachines", held in Lausanne, Sept. 8-12, 1980, p.p. 285-296*
*Communication du Laboratoire de Thermique Appliquée N° 10, Ecole Polytechnique Fédérale de Lausanne, Switzerland*

**[27] D. Schläfli**
"Acquisition des données et méthodes de dépouillement des mesures instationnaires des essais de flottement"
*Report LTT-3-83, 1983 Ecole Polytechnique Fédérale de Lausanne, Switzerland*

**[28] D. Schläfli**
Private Communication, 1985

**[29] E. Szechenyi, R. Finas**
"Aeroelastic Testing in a Straight Cascade Wind-Tunnel"
*Proceedings of the Symposium on "Aeroelasticity inTurbomachines", held in Lausanne, Sept. 8-12, 1980, p.p. 143-150*

**[30] E. Szechenyi,J. Ph. Girault**
"A Study of Compressor Blade Stall Flutter in a Straight Cascade Wind-Tunnel"
*Proceedings of the Symposium on "Aeroelasticity in Turbomachines", held in Lausanne, Sept. 8-12, 1980, p.p. 163-170*

**[31] E. Szechenyi**
Private Communication, 1984

**[32] J. P. Christiansen**
*1973, J. Comp. Phys 13, 363*

**[33] J.L.Kennedy, D.M. Marsden**
*1976 Canadian Aero. and Space Jnl. 22, 243*

**[34] R.J. Grant, D.S. Whitehead**
"Force and Moment coefficients for High-Deflection Cascades"
*Proceedings of the Symposium on "Aeroelasticity in Turbomachines", held in Lausanne, Sept. 8-12, 1980, p.p. 85-128*

**[35] H. Kobayashi**
"Unsteady Aerodynamic Force Acting on Controlled-oscillating Transonic Annular Cascade"
*Proceedings of the Symposium on "Unsteady Aerodynamics of Turbomachines and Propellors", Cambridge, UK, September 24-27, 1984, p.p. 343-359*

**[36] S. Fleeter, V. Capece**
"Stator Row Aerodynamic Due To Wake Excitations"
*Proceedings of the Symposium on "Unsteady Aerodynamics of Turbomachines and Propellors", Cambridge, UK, September 24-27, 1984, p.p. 427-446*

**[37] F. Molls**
*NASA Contractor Report 3925, September 1985*

**[38] H. Atassi**
Private Communication, 1985

**[39] J.M. Verdon**
"Further Development in the Aerodynamic Analysis of Unsteady Supersonic Cascades" *ASME Paper N° 77-GT-44, 77-GT-45, 1977*

**[40] H.A. Barton, M.M. Nagui, S.G. Newton**
"An Evaluation of a Finite Element Calculation Method for Unsteady Transonic Flows Against Cascade Test Data"
*"Unsteady Aerodynamics of Turbomachines and Propellors", Cambridge, UK, September 24-27, 1984, p.p. 307-330*

**[41] J. D. Denton**
"An Improved Time Marching Method for Turbomachinery Flow Calculation"
*ASME Paper 82-GT-239, 1982*

**[42] A. Bölcs, F. Jolles**
"Hybrid Method for Calculation of the Two-Dimensional Transonic Steady-State Cascade Flows"
*Report LTT, Ecole Polytechnique Fédérale de Lausanne, Switzerland, 1986*

**[43] S. Newton, D.S. Whitehead**
"A finite element method for the solution of two-dimensional transonic and supersonic flows"
*International Journal for Numerical Methods in Fluids, Vol. 5, pp. 115-132, 1985*

**[44] D.S. Whitehead**
*Cambridge University Engineering Department Report CUED/A-Turbo/TR 118, 1982*

**[45] H. Kobayashi**
"Unsteady Aerodynamic Force Acting on Controlled-Oscillating Transonic Annular Cacade"
*"Unsteady Aerodynamics of Turbomachines and Propellors", Cambridge, UK, September 24-27, 1984, p.p. 343-359*

**[46] H. Kobayashi**
Private Communication, 1984, 1985

**[47] H. Joubert**
"Supersonic Flutter in Axial Flow Compressors"
*"Unsteady Aerodynamics of Turbomachines and Propellors", Cambridge, UK, September 24-27, 1984, p.p. 231-254*

**[48] R.E. Riffel, M.D. Rothrock**
"Experimental Determination of Unsteady Blade Element Aerodynamics in Cascades; Torsional Mode Final Report"
*NASA Contractor Report 159831, 1980*

**[49] D. Boldman**
Private Communication, 1983

**[50] S. N. Smith**
"Discrete Frequency Sound Generation in Axial Flow Turbomachines"
*Reports and Memoranda No. 3709, Great Britain, March, 1972.*

**[51] R.D. Cedar, P. Stow**
"The addition of the quasi-three-dimensional terms into a finite element method for transonic turbomachinery blade-to-blade flows"
*International Journal for Numerical Methods in Fluids, Vo.5, 101-114 (1985)*

**[52] I.K. Jennions, P. Stow**
"A quasi-three-dimensional turbomachinery blade design system"
*Part I - Through-flow analysis, ASME 84-GT-26*
*Part II - Computerised System ASME 84-GT-27*

**[53] S.P. Newman, P. Stow**
"Semi-inverse mode boundary layer coupling"
*Proceedings of the conference on Numerical Methods for Fluid Dynamics, Reading, 1985*

**[54] R.D. Cedar, P. Stow**
"A compatible mixed design and analysis finite element method for the design of turbomachinery blades"
*International Journal for Numerical Methods in Fluids, Vol. 5, 331-345 (1985)*

**[55] J. M. R. Graham**
Private Communication, 1986

**[56] S. Kaji**
Private Communication, 1986

**[57] D. Boldman**
Private Communication, 1984

**[58] G.Samolovich**
"Resonance Phenomena in Sub- and Supersonic Flow Through an Aerodynamic Cascade"
*Mekhanika Zhidkosti i Gaza, Vol.2, N° 3, pp. 143-144, 1967*

**[59] T.H. Fransson, N. Sayari, D. Schläfli**
"Decomposition of Unsteady Results from a Traveling Wave Mode Formulation into Individual Influence Coefficients"
*Internal Report, LTT-EPF-Lausanne, Switzerland, 1986.*

**[60] L.M. Shaw, D.R. Boldman , A.E. Buggele, D.H. Buffum**
"Unsteady Pressure Measurements on a Biconvex Airfoil in a Transonic Oscillating Cascade"
*ASME Paper N° 85-GT-212, 1985*

**[61] W. Usab, Jr., J.M. Verdon**
"On the Application of a Linearized Unsteady Potential-Flow Analysis to Fan-Tip Cascades"
*ASME Paper N° 86-GT-87, 1986*

**[62] K. Broichhausen, H. E. Gallus, J. M. Hehne**
"Experimental Unsteady Shock-Boundary Layer Interaction at Single Blades in Linear Cascades"
*ASME Paper N° 86-GT-218, 1986*

**[63] D.S. Whitehead**
Private Communication, 1985

**[64] J.E. Caruthers**
"Theoretical Analyses of Unsteady Supersonic Flow Through Harmonically Oscillating Turbofan Cascades"
*PhD Thesis, Georgia INstitute of Technology, June 1976*

**[65] A. Bölcs, F. Folchi-Vici, T.H. Fransson, K. Schulz**
Private Communication, 1985
To be published

**[66] F.O. Carta**
Private Communication, 1983, 1986
To be published

**[67] H. Holtmann, S. Servaty, H.E. Gallus**
"Computation of the subsonic flow field through oscillating compressor and turbine cascades"
*"Unsteady Aerodynamics of Turbomachines and Propellors", Cambridge, UK, September 24-27, 1984, p.p. 73-92*

**[68] T.H. Fransson, M. Pandolfi**
"Numerical Investigation of Unsteady Subsonic Compressible Flows through an Oscillating Cascade"
*ASME Paper 86-GT-304, 1986*

**[69] T. Araki**
Private Communication, 1986
To be published

**[70] E. Széchényi, I. Cafarelli, C. Notin, J.P. Girault**
"A Straight Cascade Wind-Tunnel Study of Fan Blade Flutter in Starded Supersonic Flow"
*"Unsteady Aerodynamics of Turbomachines and Propellors", Cambridge, UK, September 24-27, 1984, p.p. 447-458*

**[71] E. Széchényi**
"Fan blade flutter-single degree of freedom instability or blade-to-blade coupling"
*ASME Paper 85-GT-216, 1985*

**[72] J.M. Verdon**
"Analysis of Unsteady Supersonic Cascades"
*ASME Paper 77-GT-44, 77-GT-45, 1977*

## Appendix A1: Pressure Response Spectra Contributing to the Aerodynamic Work in Two-dimensional Flow With Rigid Body Motions.

The fundamental consideration of the data reduction processes most often used for evaluation of aeroelastic experiments is that, although the pressure response on the vibrating blades may be highly non-harmonic, it is only the frequency (or frequencies in the case of higher harmonics), of the pressure response spectra corresponding to the blade vibration that contributes to the aerodynamic work. This follows from the orthogonality, over a period, of the components of the Fourier series expansions, and can be demonstrated as follows /15,28/.

Assume a blade vibration, in pitching mode, $\tilde{\alpha}(t)$ and an unsteady perturbation moment signal $\tilde{c}_m(t)$, which can both be expressed as Fourier series with $\omega$ as the fundamental frequency:

$$\tilde{\alpha}(t) = \sum_{n=1}^{\infty} \alpha_n e^{i\cdot[n\,\omega\,t+n\,\Phi_\alpha]}$$

$$\tilde{c}_m(t) = \sum_{k=1}^{\infty} c_{mk}\, e^{i\cdot[k\,\omega\,t+k\,\Phi_m]}$$

With $\quad d\tilde{\alpha}(t) = [d\tilde{\alpha}/d(\omega t)]\cdot d(\omega t)$

the aerodynamic work $c_w$ becomes, according to (Eq. 13)

$$c_w = \int_0^{2\pi} \mathrm{Re}\{\sum_{k=1}^{\infty} \alpha_k \cdot c_{mk}\, e^{i\cdot[k\,\omega\,t+k\,\Phi_m]}\}\cdot \mathrm{Re}\{i\cdot\sum_{n=1}^{\infty} n\cdot\alpha_n e^{i\cdot[n\,\omega\,t+n\,\Phi_\alpha]}\}\cdot d(\omega t) =$$

$$= - \int_0^{2\pi} \{\sum_{k=1}^{\infty} \alpha_k \cdot c_{mk} \cdot \cos[k\omega t + k\Phi_m]\}\cdot$$

$$\{\sum_{n=1}^{\infty} n\alpha_n \cdot \sin[n\omega t + n\Phi_\alpha]\} \quad d(\omega t) =$$

$$= - \sum_{k=1}^{\infty} \sum_{n=1}^{\infty} n\,\alpha_k c_{mk} h_n \int_0^{2\pi} \cos(k\omega t + k\Phi_m)\cdot\sin(n\omega t + n\Phi_\alpha)\, d(\omega t)$$

With the abbreviation $f(\Sigma) = - \sum_{k=1}^{\infty} \sum_{n=1}^{\infty} n\,\alpha_k c_{mk} \alpha_n$

we obtain:

$$c_w = f(\Sigma)\cdot \int \{\cos(k\omega t)\cdot\cos(k\Phi_m) - \sin(k\omega t)\cdot\sin(k\Phi_m)\}\cdot$$
$$\{\sin(n\omega t)\cdot\cos(n\Phi_\alpha) + \cos(n\omega t)\cdot\sin(n\Phi_\alpha)\} \cdot d(\omega t) =$$
$$= f(\Sigma)\cdot \int \{\cos(k\omega t)\cdot\sin(n\omega t)\cdot\cos(k\Phi_m)\cdot\cos(n\Phi_\alpha) +$$
$$\cos(k\omega t)\cdot\cos(n\omega t)\cdot\cos(k\Phi_m)\cdot\sin(n\Phi_\alpha) -$$
$$\sin(k\omega t)\cdot\sin(n\omega t)\cdot\sin(k\Phi_m)\cdot\cos(n\Phi_\alpha) -$$
$$\sin(k\omega t)\cdot\cos(n\omega t)\cdot\sin(k\Phi_m)\cdot\sin(n\Phi_\alpha)\}\, d(\omega t) =$$
$$= 0.5\cdot f(\Sigma)\cdot \int \{[\sin(\omega t[k+n]) - \sin(\omega t[k-n])]\cdot\cos(k\Phi_m)\cdot\cos(n\Phi_\alpha) +$$
$$[\cos(\omega t[k+n]) + \cos(\omega t[k-n])]\cdot\sin(k\Phi_m)\cdot\cos(n\Phi_\alpha) -$$
$$[\sin(\omega t[k+n]) + \sin(\omega t[k-n])]\cdot\sin(k\Phi_m)\cdot\sin(n\Phi_\alpha)\}\, d(\omega t) =$$

$$= -0.5 \sum_{k=1}^{\infty} k\,\alpha_k^2 c_{mk}\cdot 2\pi\cdot[\cos(k\Phi_m)\cdot\sin(k\Phi_\alpha) - \sin(k\Phi_m)\cdot\cos(k\Phi_\alpha)] =$$

$$= \pi\cdot \sum_{k=1}^{\infty} k\,\alpha_k^2 c_{mk}\cdot\sin(k[\Phi_m - \Phi_\alpha])$$

as only the integrals

$$\int_0^{2\pi} \ldots\ldots(k-n) \neq 0 \quad \text{if and only if } k=n.$$

Thus, in computation of the aerodynamic work and damping coefficients, only the frequencies of the pressure response spectra corresponding to the blade vibration frequencies contribute to the resulats.

## Appendix A2. Definition of Positive and Negative Aerodynamic Work. Stability Limits.

Depending on the geometry of the blades and the stagger angle, as well as on the time-averaged and time-dependent flow conditions, the aerodynamic work done by the flow on the blade can be either positive or negative. If the work is positive, the flow gives energy to the blade every vibration cycle, which implies that the blade vibration amplitude will increase every cycle. If, on the other hand, the work is negative the blade gives energy to the flow which implies that the flow damps the blade vibration.

The sign of the aerodynamic work depends on the phase angle between the blade vibration and the time-dependent force acting on it. This is clearly seen in the case of harmonic blade vibration and force response $\omega$:

$$h(t) = h \cdot e^{i\omega t} \qquad \text{(Translation mode)}$$
$$c_h(t) = c_h \cdot e^{i(\omega t+\Phi_h)}$$

where $\Phi_h$ is the phase angle between the blade motion and the force response (positive when the force leads the motion).

By considering the aerodynamic work over a cycle of vibration as the integral of the product of blade velocity and force, we obtain:

$$c_{wh} = \oint \mathrm{Re}\{dh(t)\} \cdot \mathrm{Re}\{hc_h(t)\} = -h^2 \cdot c_h \cdot \int_0^{2\pi} \sin(\omega t) \cdot \cos(\omega t+\Phi_h) =$$
$$= \pi \cdot h^2 \cdot c_h \cdot \sin\Phi_h$$

**Therefore, the blade vibration is**

**unstable** if $0^\circ < \Phi_h < 180^\circ$

**stable** if $180^\circ < \Phi_h < 360^\circ$

The **stability limits** ($c_{wh}=0$) are thus found to be $\Phi_h = 0^\circ$ **and** $180^\circ$.

The same result is found also if a non-harmonic force response is assumed (compare Appendix A1).

## Appendix A3: Acoustic Resonance.

The acoustic resonance is a phenomenon which theoretically puts an infinite cascade of flat plates into resonance. It appears (for linearized theories) when the interblade phase angle corresponds to the time a perturbation takes to travel from one point on blade "0" to a corresponding point on blade "+1" (Fig. A3.1).
Two different methods of approach for explaining this phenomenon are given in the following. The first is a purely geometrical interpretation, whereas the second introduces a small perturbation theory.

Geometrical interpretation.

If the blade movements are assumed to be simple harmonics with constant interblade phase angles ($\sigma$), then

$$h_0 = h \cdot \sin(\omega t) \qquad (A3.1)$$
$$h_1 = h \cdot \sin(\omega t + \sigma)$$

where the indexes $_0$ and $_1$ denote the blades "0" and "+1", respectively.
A perturbation propagates from blade "0" toward blade "+1" along the pitch with the velocity (Fig. A3.1):

$$qp\pm = q1 \cdot \cos(90-\gamma) \pm a \cdot \cos\alpha \qquad (A3.2)$$

where

$a$ = velocity of sound.
$\cos\alpha = \{1-M12 \cdot \sin2(90-\gamma)\}0.5$

Thus, the time for a perturbation from blade "0" to reach blade "+1" is

$$\Delta t = \tau / qp\pm = \tau / \{a \cdot [M1 \cdot \cos(90-\gamma) \pm (1-M12 \cdot \sin2(90-\gamma))0.5]\} \qquad (A3.3)$$

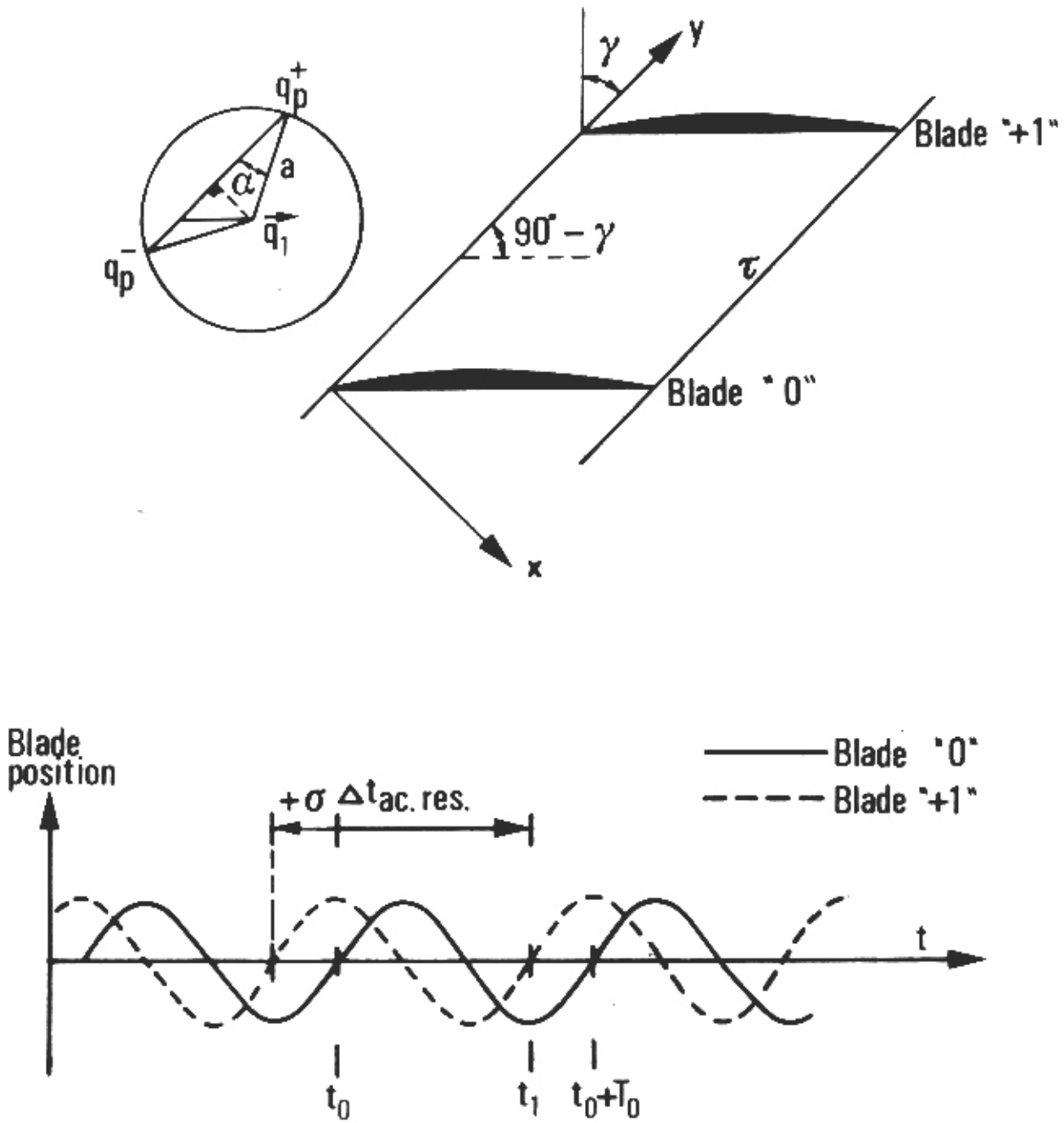


**Fig. A3.1.** Illustration of acoustic resonance.

A perturbation leaving blade "0" at time t=t0 will thus reach blade "+1" at time t=t1=t0+$\Delta t$.
If the interblade phase angle is such that blade "+1" is in the same position at time t1 as blade "0" was at time t0, then (Fig. A3.1)

$$\sigma + \omega\Delta t = n \cdot \omega T_0 \quad \text{, where n is an integer.} \qquad \text{(A3.4)}$$

Thus, $\sigma_{ac.res} = -\omega \cdot \Delta t$ (as $T_0$ is the period of a cycle) (A3.5)

wherefore

$$\sigma_{ac.res\pm} = -\omega\tau/\{a\cdot[M1\cdot\cos(90-\gamma) \pm (1-M12\cdot\sin 2(90-\gamma))0.5]\} \qquad \text{(A3.6)}$$

The acoustic resonance can thus be predicted analytically.
In linearized theories (see below), the infinity number of blades leads to an infinite series expression for the unsteady pressure field. This serie has a singular term as the interblade phase angle approaches $\sigma_{ac.res\pm}$ and resonance is observed /72/.
From eq. (A3.6) it is concluded that for every blade vibration frequency, two phase angles exist when the cascade comes into resonance condition ($\omega_{ac.res}$). If, for a certain interblade phase angle in subsonic flow the vibration frequency is less than this value, i.e. $\omega<\omega_{ac.res}$, Verdon /72/ and Samoilovich /58/ have classified the blade vibration as subresonant. Similarly, if $\omega>\omega_{ac.res}$ the vibration is said to be superresonant. (This classification is only valid in the subsonic flow domain /72/.)
According to linearized theory in subsonic flow, unsteady disturbances attenuate for subresonant motions, but they persist in the far field when the blade vibration is superresonant (/72,58/).

Interpretation based on small perturbation theory.

Departing from the full Euler equations describing the two-dimensional unsteady, inviscid, compressible flow through a cascade, written in differential form as in eq. (4.1), and performing a small perturbation on an otherwise undisturbed flow as $g = \bar{g} + \hat{g}$, where $\bar{g}$ is any steady-state flow variable, and $\hat{g}$ the unsteady perturbation part, the following perturbation equation system can be obtained (w = velocity in x direction, v = velocity in y direction):

$$\begin{aligned} \partial\hat{\varrho}/\partial t + \bar{\varrho}\cdot\partial\hat{w}/\partial x + \bar{w}\cdot\partial\hat{\varrho}/\partial x + \bar{\varrho}\cdot\partial\hat{v}/\partial y + \bar{v}\cdot\partial\hat{\varrho}/\partial y &= 0 \\ \partial\hat{w}/\partial t + \bar{w}\cdot\partial\hat{w}/\partial x + \bar{v}\cdot\partial\hat{w}/\partial y + (\partial\hat{p}/\partial x)/\bar{\varrho} &= 0 \\ \partial\hat{v}/\partial t + \bar{w}\cdot\partial\hat{v}/\partial x + \bar{v}\cdot\partial\hat{v}/\partial y + (\partial\hat{p}/\partial y)/\bar{\varrho} &= 0 \end{aligned} \qquad \text{(A3.7)}$$

In this equation system only first order perturbation terms have been retained.

Furthermore, assuming that the unsteady part of the flow variable g can be written as $\hat{g} = \tilde{g}\cdot e^{i\{\omega t + \varepsilon x + \lambda y\}}$, the equation system (A3.7) becomes, together with the isentropic relationship $a^2=\tilde{p}/\tilde{\varrho}$:

$$\begin{aligned} \tilde{p}(\omega+\varepsilon\bar{w}+\lambda\bar{v}) + a^2\bar{\varrho}\varepsilon\tilde{w} + \lambda a^2\bar{\varrho}\tilde{v} &= 0 \\ \tilde{p}\varepsilon/\bar{\varrho} + (\omega+\varepsilon\bar{w}+\lambda\bar{v})\tilde{w} + 0 &= 0 \\ \tilde{p}\lambda/\bar{\varrho} + 0 + (\omega+\varepsilon\bar{w}+\lambda\bar{v})\tilde{v} &= 0 \end{aligned} \qquad \text{(A3.8)}$$

This equation system has a non-trivial solution if, and only if, its determinant is zero, wherefore:

$$(\omega+\varepsilon\bar{w}+\lambda\bar{v})^3 - (a^2\cdot\varepsilon^2 + a^2\lambda^2)\cdot(\omega+\varepsilon\bar{w}+\lambda\bar{v}) = 0 \qquad \text{(A3.9)}$$

In x direction this equation has 3 solutions:

$$\begin{aligned} &\varepsilon = -(\omega+\lambda\bar{v})/\bar{w} \quad ; \text{ i. e. } \varepsilon \text{ is real} \\ &\varepsilon = \{-\bar{w}\cdot(\omega+\lambda\bar{v}) \pm a\cdot[(\omega+\lambda\bar{v})^2 + \lambda^2\cdot(\bar{w}^2-a^2)]^{0.5}\}/\{\bar{w}^2-a^2\}; \ \varepsilon \text{ real or complex} \end{aligned} \qquad \text{(A3.10)}$$

In the case that $\varepsilon$ is complex ($\varepsilon = \varepsilon_R + i\varepsilon_I$), the unsteady perturbations will attenuate in x direction as

$$g = \tilde{g}\cdot e^{i\{\omega t + \varepsilon x + \lambda y\}} = \tilde{g}\cdot e^{i\{\omega t + \varepsilon_R x + \lambda y\}}\cdot e^{-\varepsilon_I x} \qquad \text{(A3.11)}$$

If instead $\varepsilon$ is real, the unsteady perturbations will propagate through the flow field unattenuated.

If the perturbations attenuate, the unsteady flow phenomena is called "subresonant" (or "cut-off condition"). If however the perturbations do not attenuate, the flow is called "superresonant" /72,58/.

From equations (A3.10) and (A3.11) it is seen that the sub- and superresonant regions depend on the factor $f = [(\omega+\lambda\bar{v})^2 + \lambda^2\cdot(\bar{w}^2-a^2)]$. If this value

is f< 0, the flow is subresonant, whereas it is superresonant if the factor is f>0.
Thus, for subresonant flow,

$$[(\omega+\lambda\bar{v})^2 + \lambda^2\cdot(\bar{w}^2-a^2)] < 0 \quad \Rightarrow \quad (a-\bar{w}) > \{(\omega+\lambda\bar{v})^2\}/\{\lambda^2(\bar{w}+a)\}$$

which indicates that the subresonant and superresonant regions are different for sub- and supersonic flows.
At the separation between the two domains, the factor $f= [(\omega+\lambda\bar{v})^2 + \lambda^2\cdot(\bar{w}^2-a^2)]$ is zero. $\varepsilon$ is then real, and the unsteady perturbations can propagate in z direction. In this case, a special phenomena, the acoustic resonance, can appear in y direction (=pitch direction, see Fig. A3.1). If

$$\bar{w} = \bar{q}_1\cdot\cos\gamma$$
$$\bar{v} = \bar{q}_1\cdot\sin\gamma$$
$$\lambda = (\sigma-2\pi n)/\tau, \text{ with n = integer,}$$

then
$$f = [(\omega+\lambda\bar{v})^2 + \lambda^2\cdot(\bar{w}^2-a^2)] = 0 \quad \Rightarrow$$
$$\lambda\pm = \{\omega[-\bar{v} \pm (a^2-\bar{w}^2)^{0.5}]/[\bar{v}^2+\bar{w}^2-a^2]\} \quad \Rightarrow$$
$$\sigma\pm = 2\pi n - \{\omega\tau\}/\{a[M_1\sin\gamma\pm(1-M_1^2\cos^2\gamma)^{0.5}]\}$$

which is the expression for the acoustic resonance in equation (A3.6).

## Appendix A4. Time-Dependent Data Acquisition and Reduction Procedures Used in the Standard Configurations.

### First Standard Configuration.

*(For convenience, this section of the present report has been copied from the NASA Contractor Report 3513 by F. O. Carta [15].)*

During unsteady testing, data are collected by two systems, one which stores and computes pertinent steady-state parameters and provides on-line monitoring of external flow conditions, and one which collects and stores all unsteady, high response data for subsequent processing. The latter is here described briefly.

Unsteady blade and sidewall pressures and blade angular displacement are obtained as time varying voltages which are conditioned and amplified in an instrumentation package mounted close to the wind tunnel (to reduce transmission noise of low level siganals). These high response transducer outputs are acquired and recorded in digital form for subsequent off-line processing by the Aeromechanics Transient Logging and Analysis System (ATLAS) which accepts up to 26 channels of data. Each channel may be amplified and filtered as required. The heart of the system is a 26 channel transient recorder which digitizes and stores each channel simultaneously at sampling rates up to 200 kHz as selected by the operator. System control is provided by a Perkin Elmer 7/16 minicomputer system which interfaces with the operator through graphics display terminal. The data system is capable of self-calibration using a built in programmable voltage standard which is under computer control. The system offers several modes of operation ranging from fully manual, where each step in the sequence (calibration, acquisition, and recording) is under operator control with the capability of aborting at any time, to fully automatic where these tasks are computer controlled according to preset parameters. Data acquisition may be initiated manually, by the computer, or on receipt of an external trigger pulse. For this program, the system was run in the manual-trigger mode. Typically, the operator at the computer console instructs the system to acquire data, using the preprogrammed software on the minicomputer program disk and several specific instructions pertinent to the particular experiment in progress. Acquired data, consisting of 1024 time-correlated samples for each active channel, can be spot-checked by the operator by displaying the contents of the

memory of each channel on a built in scope, or can be recorded directly on a digital magnetic tape for subsequent off-line processing.
The acquisition rate for all unsteady data was set at 1000 samples/sec. Thus, for the three nominal test frequencies, f=9.2, 15.5, 19.2 Hz, there were 9.4, 15.9 and 19.7 cycles of data available for analysis, or conservatively, there were 9, 15, and 19 full cycles available. Data for each channel were Fourier analyzed, primarily to provide first, second, and third harmonic results for ease in analyses, but also to provide a compact means of data storage for subsequent use. These data have been completely tabulated in a companion data report [15] in which each run/point combination is fully documented and described, and the data are arranged in several convenient forms. In each case a total of 10 harmonics are displayed for each unsteady channel. It is seen that this is well within the bounds of the conventional sampling theorem requiring 2 or more samples/cycle in the highest harmonic of interest.

**Third Standard Configuration.**

*(For convenience, this section of the present report has been copied from the publication "Unsteady Aerodynamic Force Acting on Controlled-Oscillating Transonic Annular Cascade" by H. Kobayashi [45].)*

The measurement of time-dependent data includes airfoil oscillatory displacement, unsteady aerodynamic moment and unsteady pressure distribution on the oscillating airfoil surface. All time-dependent data were recorded on FM Magnetic tape recorder with frequency response 2.5 kHz and analyzed with a Fast Fourier Transform (FFT) analyzer.
Instrumented airfoil motion was measured with the combination of a small rod fixed on airfoil tip section and eddy-current type displacement sensors. Unsteady aerodynamic forces are acquired with two measuring methods. One is the net work of dual strain gauges on the cross spring bars machined on the trunnion of instrumented airfoil, which gives the information of unsteady aerodynamic moment caused by aerodynamic force acting on the entire blade surface. This method has the advantage to understand synthetically the unsteady phenomena of oscillating airfoil, but it connot offer the information of local unsteady phenomena on oscillating blade surface. The measuring data obtained by cross spring bars contains the inertia force of blade and so the aerodynamic moment is calculated with the difference between the moment in flow and the moment in vacuum condition.

The other is the measurement of unsteady pressure distribution on an oscillating blade surface, which can offer the unsteady aerodynamic moment per unit span and the unsteady phenomena on the local blade surface. As for the measuring instrument of unsteady pressure, minute pressure transducers are used in combination with probe tubes in blade, because even this thinner transducer cannot be enclosed in a thinner part of the blade section and also transducers have to be used many times for other measurements. 22 probe tube systems were prepared for the measurement of chordwise unsteady pressure distribution.

Now, the measuring time-dependent pressure signals, amplitude $A_0$ and phase lag $\Phi_0$, are necessary to be corrected with the frequency response characteristic data of probe tube measuring system ($A_s$, $\Phi_s$), and that of electronic data acquisition system including DC amplifier ($A_D$, $\Phi_D$), and Data Recorder ($A_r$, $\Phi_r$). Finally, unsteady aerodynamic amplitude $A_p$ and phase lag $\Phi_p$ can be obtained according to:

$$A_p = A_0/\{A_s * A_D * A_r\}$$

$$\Phi_p = \{\Phi_0+\Phi_s+\Phi_D+\Phi_r\}$$

Frequency-response characteristics ($A_s$, $\Phi_s$) of probe tube system were measured with an apparatus for measurement of probe tube frequency-response characteristics. In the apparatus, the fluctuating pressure is made by the interaction between jet flow and a rotating disc with sinusoidal lobe shape and is injected into flow from opposite side of two transducers to make unsteady pressure in flow. Frequency of fluctuating pressure can easily be controlled by rotational speed of disc.

The frequency response characteristics of electronic data acquisition system, DC amplifier and Data Recorder are also measured with a function signal generator and an FFT analyzer.

Using 32 time-averaged transfer function data of blade oscillation signal and corrected time-dependent pressure signal, unsteady aerodynamic moment and chordwise distributions of unsteady pressure amplitude and phase lag referenced to blade oscillation, and element aerodynamic energy were calculated.

**Fourth Standard Configuration.**

*(Courtesy of D. Schläfli [28].)*

The unsteady data are low-pass filtered and then recorded on an analog tape recorder. By reproducing the data at a lower speed than recorded, this procedure allows the limitations of the analog-to-digital conversion speed on the computer to be overcome. The data reduction procedure is as follows. The frequency of the forced vibration is know. Thus the harmonic part of the signals can be evaluated straightforwardly by computing the first term of the corresponding Fourier series. In this case, the sampling frequency need not be an integer multiple of the signal frequency as required by ensemble averaging and FFT techniques.

The total recorded time of the digitized unsteady signals is split up in sections, for which amplitudes and phase angles in relation to a reference signal are computed. The result of each section is then considered as a single piece of data. These results are averaged in their turn to yield the final result (amplitude and phase angle). The variance of the section results is used to estimate a 95% confidence interval. Typical values are 2'560 samples per section and 10 sections per total record length (i.e. 25'600 samples per channel and per test).

With these settings, the 95% confidence limits are roughly twice the sample mean standard deviation (based on the elementary estimation theory, using Student's T-distribution) from the mean value.

The sampling frequency is selected at 10-15 times the fundamental of the signal frequency, in order to avoid aliasing problems.

**Fifth Standard Configuration.**

*(For convenience, this section of the present report has been copied from the the publication "A Straight Cascade Wind Tunnel Study Of Fan Blade Flutter inStarted Supersonic Flow", by E. Szechényi, I. Cafarelli, C. Notin, J. P. Girault [70].)*

Two distinct types of aeroelastic measurements are made: those giving "direct" coefficients (the case of forces acting on a vibrating blade with all other blades fixed) and those giving coupling coefficients (the influence of the vibration of neighboring blades).
Only one blade is instrumented to mesure aeroelastic coefficients but it can be placed in any position in the cascade. One of the blades is made to vibrate in either pitching or heaving. The pitching mode is usually about the mid-chord axis.
The aeroelastic force coefficients are determined as the transfer functions between the vibratory motion and the resulting lift or moment.
In this testing technique, the assumption is made that the direct and coupling terms combine linearly so that a vectorial addition can be made. Thus the total coefficient for a blade in an infinite cascade is:

$$c_{total} = \sum_{n=-\infty}^{+\infty} c_n \cdot e^{in\sigma}$$

where

- n is the blade index (n=0 is the vibrating blade, n<0 are the "upstream" blades, n>0 are the "downstream" blades)
- $c_n$ is the complex coefficient measured on blade n,
- $\sigma$ is the blade-to-blade phase angle.

The imaginary part of the coefficient, $c_{total}$, is a measure of aeroelastic damping. For $c_{total}<0$, aeroelastic damping is negative and flutter conditions exist.
The experimental verification of this assumption is reported in detail in [71].
From the above equation it is obvious that the total coefficient is to a great extent a function of $\sigma$. For a compressor cascade this blade-to-blade phase angle depends on the number of blades and on the normal mode of vibration. In order to have a valid stability criterion one calculates the minimum possible value that $c_{total}$ can attain for $0 \le \sigma < 2\pi$. The negative sign of this $c_{total(min)}$ then reveals possible flutter conditions.

**Sixth Standard Configuration.**

*(Idem fourth standard configuration.)*

**Seventh Standard Configuration.**

*(For convenience, this section of the present report has been copied from the NASA Contractor Report 159831 by R. E. Riffel and M. D. Rothrock [48].)*

The fundamental time-unsteady data of interest is the complex airfoil surface chordwise pressure distribution. This data, together with the airfoil motion data, determines the aerodynamic stability. The unsteady force (lift) and moment on the airfoil are calculated from this pressure and airfoil motion data.

The instrumentation used to acquire unsteady data are included in the following.

- Strain Gauges: Two per airfoil with one on either side of the tunnel.
- Kulite pressure transducers: Six flush-mounted per surface on center airfoil of the cascade (a total of twelve transducers on blade 3).
- Heated film gauges: Five surface-mounted per surface (a total of 10) on the center airfoil of the cascade.

The heated film gauges were used to qualitatively examine the transition and flow separation phenomena on the airfoil surfaces for the conditions where the measured unsteady work per cycle attains its maximum and minimum values. The dynamic characteristic of each heated film gauge at a particular operating point were determined from the taped oscilloscope traces of the blade motion as defined by the signals from the strain gauge and the particular heated film gauge. In addition, high speed Schlieren movies were taken.

The strain gauge and pressure transducer data was acquired simultaneously. The on-line analysis was performed on the strain gauge signals concurrent with the magnetic tape recording of the signals from the instrumented blade's strain gauge and pressure transducers. The on-line analysis involved eight channels of strain gauge data, two per airfoil. The twelve surface dynamic pressure signals, six from the pressure surface and six from the suction surface, along with the reference strain gauge signal from the instrumented blade were taped for each data point.

In this investigation an analog-to-digital converter having a rate of 100'000 points per second was used. Data, either real time or taped, was digitized and

stored on a magnetic disc for evaluation. An "n" cycle data averaging technique was adapted early in the test program to eliminate background noise from the unsteady pressure signal. The data is sampled at preset time, triggered by a square wave pulse supplied by the airfoil drive system computer. The analog-to-digital converter is triggered by the positive voltage at the leading edge of the pulse, initiating the acquisition of the unsteady pressure data. The data can be sampled for "m" ensembles and "n" cycles and an average data set obtained.

The data analysis comprised the following three techniques:

- Amplitude calculation
- Frequency calculation
- Phase calculation

In the amplitude calculation, a second order least square fit of the data on the positive and negative sides of the time axis was made for each half cycle of motion. The signal amplitude becomes the average of the positive peaks minus the average of the negative peaks.

The frequency of the time-dependent digital data was determined through the autocorrelation function. This function describes the dependence on the values of the data at one time, $X_i$, on the values at another time, $X_{i+r}$. The lag time, $\Delta T$, is inversely proportional to the rate at which the data are digitized. An autocorrelogram of the digitized data exhibits the features of a sine wave plus random noise. A second order least square fit function was fit to the data depicting the second positive peak of the autocorrelogram. The inverse of the time at which this least square function is a maximum is equal to the frequency, f, of the time-dependent data. Additionally, the frequency is known from the computer commanded input and an on-line, electronic counter.

The phase difference between the time-variant digitized signals was calculated through the cross-correlation function. This function, for two sets of data, $X_i$ and $Y_i$, describes the dependence of the values of one set of data on the other. As in the frequency calculation, a second order least square curve was fit to the data in the nearest to zero time positive peak of the cross-correlogram. The time, $t_p$, at which this least square function is a maximum was analytically determined. The phase difference, in degrees, was calculated as

$$\Phi_p = t_p \cdot f \cdot 360$$

where f is the frequency calculated for the airfoil motion from the strain gauge data.

The reference signal for all the phase angle determinations was a strain gauge signal from the instrumented airfoil. This signal was common in both the on- and off-line data acquisition.